Emissions Predictive Modelling and Simulation for a Plug-in Hybrid Electric Scooter

By

Wai Kean Yap

B. Eng. (Hons.), University of Tasmania, 2005

A Thesis Submitted in Fulfillment of the Requirements for the Degree of Doctor of Philosophy

School of Engineering, University of Tasmania

June 2010

Supervisory Committee:

Professor Vishy Karri, Australian College of Kuwait

Dr. Tim Gale, University of Tasmania

DECLARATION AND AUTHORITY OF ACCESS

This thesis contains no material that has been accepted for a degree or diploma by the University of Tasmania or any other institution, except by way of background information that has been duly acknowledged in this thesis, and to the best of the author's knowledge and belief no material has previously been published or written by another person except where due acknowledgement is made in text of this thesis, nor does the thesis contain any material that infringes copyright.

This thesis may be made available for loan. Copying of any part of this thesis is prohibited for two years from the date this statement was signed; after that time limited copying is permitted in accordance with the Copyright Act 1986.

Signed:_____

Date:_____

ACKNOWLEDGEMENTS

I would like to express my sincere gratitude to my principal supervisor, Professor Vishy Karri for his profound knowledge, inspiration and expert guidance on, not just on my research, but life in general. I'd known Professor Karri since my undergraduate days. During his tenure at the University of Tasmania, he approached each of my problems, either personal or work-related, with patience and dedication.

I would also like to thank my secondary supervisor, Dr. Tim Gale, for his assistance in all administrative-related problems I'd encountered during the course of my research at the university. Thanks also to Mr. Steven Avery, Mr. Andrew Bylett, Ms. Jennifer O'Donohue, Professor Michael Negnevitsky and Professor Chris Letchford for their assistance.

I would also like to thank Mr. Rob Warren of Reds Motorcycles for his assistance in operating the chassis dynamometer and his extensive knowledge on motorcycles and the Bike Ambulance for transporting the scooter efficiently and punctually.

Special thanks to my parents and I dedicate this thesis to them for their constant support in every way possible. Constant encouragements and phone calls proved invaluable to me and I'm greatly indebted to you.

ABSTRACT

This thesis presents a comprehensive study on emissions predictive control modelling for hybrid electric scooters. Two approaches were investigated on a constructed hybrid electric scooter. The first approach involves developing a hybrid electric scooter dynamic model using MATLAB-Simulink and the second involves the development of an Emissions Predictive Model using artificial neural network.

The hybrid electric scooter model was developed to further understand and analyze as well as to predict its performance and emissions before proper construction of the prototype begins. The MATLAB-Simulink model consists of four integrated models that formed the complete hybrid scooter model: Battery Model, Engine Model, DC Motor Model and the Vehicle Dynamics Model. The multi-mode controller predicts the required parameters to operate the scooter in an optimize condition. Experimental data were gathered and thus compared to the simulated data to check the model's feasibility and accuracy on four distinct driving cycles: Modified Urban Dynamometer Driving Schedule, New York City Cycle, European Driving Cycle and the Modified Highway Fuel Economy Driving Schedule. Results showed that the developed multi-state hybrid electric scooter model was accurate and feasible with predictive errors of ±10 % for emission levels and fuel economy on the European Driving Cycle. Simulated results were also compared to the existing literature and it was found that the qualitative trends were similar. By having a high-confidence simulation model, performance of the hybrid electric scooter were also simulated over the mentioned driving cycles demonstrating the optimization strategy of the multi-state control system.

For the second approach, the Emissions Predictive Model was then built using artificial neural network techniques to predict the following tailpipe emissions gases; CO, CO_2, HC and O_2. Three feed-forward neural network models were investigated and compared in this study; back-propagation, optimization layer-by-layer and radial basis function networks. Based on the experimental setup, the neural network models were trained and tested to accurately predict the effect of the engine operating conditions on the emissions by varying the number of hidden nodes. The selected optimization layer-by-layer network proved to be the most accurate and reliable predictive tool with prediction errors of ±5 %. The effect of the engine operating conditions on the tailpipe emissions for a scooter is shown to display similar qualitative and quantitative trends between the simulated and the experimental data.

Having accurate predictive models for emissions and fuel economy enable the hybrid electric scooter to be optimized via modelling and simulation before proper construction begins. The developed emissions predictive models could act as a virtual emissions sensor replacing costly hardware for the developed physical hybrid electric scooter. This study provides a better understanding in effects of engine process parameters on tailpipe emissions for the hybrid electric scooter as well as for general hybrid vehicular applications

FULL LIST OF PUBLICATIONS

1. **Yap, WK** & Karri, V 2010, 'Emissions predictive modelling by investigating various neural network models', *accepted for 2010 IEEE Vehicle and Propulsion Conference*, Lille, France.
2. **Yap, WK** & Karri, V 2010, 'Performance simulation and prediction model for a hybrid electric scooter drive ', *International Journal of Energy Research*, vol. 34, no. 1, pp. 67-83.
3. **Yap, WK** & Karri, V 2009, 'Performance modelling and simulation of a hybrid electric scooter', *International Journal of Electric and Hybrid Vehicles*, vol. 2, no. 1. pp. 43-63.
4. **Yap, WK** & Karri, V 2008, 'Modelling and simulation of a hybrid scooter', *International Journal of Electrical Power and Energy Systems Engineering*, vol. 1, no. 3, pp. 165-170.
5. Karri, V, **Yap, WK** & Titchen, J 2008, 'Simulation and configuration of hydrogen assisted renewable energy power system', *International Journal of Electrical Power and Energy Systems Engineering*, vol. 1, no. 3, pp. 171-178
6. **Yap, WK** & Karri, V 2008, 'Regenerative control system for plug-in hydrogen fuel cell scooter', *International Journal of Energy Research*, vol. 32, no. 9, pp. 783-792.
7. **Yap, WK** & Karri, V 2008, 'Modelling and simulation of a hybrid scooter', in *Proceedings of World Academy of Science, Engineering and Technology*, Paris, France, vol. 30, pp. 880-885.
8. Karri, V, **Yap, WK** & Titchen, J 2008, 'Simulation and configuration of hydrogen assisted renewable energy power system', in *Proceedings of World Academy of Science, Engineering and Technology*, Paris, France, vol. 30, pp. 886-893.
9. **Yap, WK** & Karri, V 2007, 'Control system for plug-in hybrid hydrogen fuel cell scooter', in *Proceedings of International Conference on Modelling and Simulation*, Coimbatore, India, pp. 31-36.
10. **Yap, WK** & Karri, V 2007, 'Regenerative control systems for plug-in hydrogen fuel cell scooter', in *Proceedings of 2007 International Conference on Engineering Sustainability*, Western Australia, Australia, pp. 195-196.

TABLE OF CONTENTS

LIST OF FIGURES

LIST OF TABLES

ABBREVIATIONS

AI	artificial intelligence
ANN	artificial neural network
BP1	back-propagation with 1 hidden layer
BP2	back-propagation with 2 hidden layers
BSFC	brake specific fuel consumption
CAFE	Corporate Average Fuel Economy
CL	clutch
CO	carbon monoxide
CO_2	carbon dioxide
DFV	dual-fuel vehicles
ECE-15	Standard European Cycle
EPM	Emissions Prediction Model
EC	energy source
ES	energy converter
EV	electric vehicle
FCV	fuel cell vehicles
HC	hydrocarbon
HEM	hybrid electric motorcycle
HES	hybrid electric scooter
HEV	hybrid electric vehicle
HWFET	Highway Fuel Economy Driving Schedule
I/O	input/output
ICE	internal combustion engine
LVQ	learning vector quantization
M/G	motor/generator unit
NO_3^-	nitrate
NOx	nitrogen oxides
NYCC	New York City Cycle
O_2	oxygen
O_3	ozone
OLL	Optimization Layer by Layer

Pb	lead
PGT	planetary gear train
PM	particulate matter
ppm	parts per million
RBF	Radial Basis Function
RBF+KOH	Radial Basis Function incorporating the Kohonen Network
RMS	root mean square
rpm	revolutions per minute
SC	state of charge
SLA	sealed lead acid
SO_2	sulphur dioxides
SO_4^-	sulphate
tce	trichloroethylene
TPS	throttle position sensor
UDDS	Urban Dynamometer Driving Schedule
US EPA	Environment Protection Agency
WOT	wide open throttle
ZEV	zero emissions vehicle

CHAPTER 1: INTRODUCTION

1.1 Introduction

Internal combustion engine (ICE) vehicles have been around a hundred and more years, almost as old as the automobile technology itself. The development of ICE vehicles, particularly in the automobile industry, is one of modern technology's greatest achievements. ICE vehicles provide many social and economic benefits, and this has enabled the rapid advancement of mankind from a primitive to a highly mobile and developed society. In addition, ICE vehicles alongside the automobile industry provide a backbone for most major world economies.

Unfortunately, the rapid growth of ICE vehicles generated massive environmental issues. Air pollution and the rapid depletion of the Earth's natural petroleum resources continue to be the major issues facing the world today. The increase in harmful tailpipe emissions generated by these automobiles is known to have adverse health effects to the human body.

1.2 Motor Vehicle and Emissions Growth

The transportation sector is one of the main contributors to air pollution and petroleum depletion. Since the 1970s, the global vehicle population has been growing steadily at a rate of about 12 million vehicles per year. This subsequently contributed to the rise of petrol prices and an increase in gas consumption [1].

The author will be focusing on motorcycles in relationship to this thesis. The term motorcycle will be used to represent two-wheeled vehicles throughout this thesis, unless stated explicitly (such as scooter).

The population of motorcycles is lowered compared to petrol-powered passenger cars in general. However in some countries, motorcycles appear to be one of the primary transportation options. An example is China where the motorcycle population is steadily approaching 100 million units [2]. It was estimated that this number will increase to 447 million in 2010 [3]. The related energy use from the increased motorcycle use was estimated to be about 98.29 million tce (which is equivalent to about 66.80 million tons of petrol) [3]. With close to 500 million motorcycles in China by the year 2010, the harmful emissions of motorcycle will be of concern especially in the rural and industrial areas where motorcycles

are poorly maintained. Motorcycles are also said to have replaced bicycles as the preferred substitute in China due to their low cost and flexibility in operation compared to four-wheeled vehicles.

In Switzerland, studies have indicated that motorcycles produced significantly higher emissions of all pollutants, with the exception to carbon dioxide (CO_2), compared to petrol-powered passenger cars in 2001. This comparison applies in direct comparison of mean unit emissions (in gkm^{-1}), mean yearly emissions (in kg/vehicle/year) and fleet emissions (in tons/year). Results showed that hydrocarbons (HC) and carbon monoxide (CO) emitted by motorcycles were all, and often significantly, higher [4].

In Australia, according to the Urban Pollutant Emissions from Motor Vehicles: Australian Trends to 2020 report released by the Bureau of Transport and Regional Economics in 2003, the projected growth for motor vehicle travel in Australia will reach up to 275 billion km travelled in 2020 [5]. This data applied for both four-wheelers and motorcycles in general. Motorcycles alone are estimated to contribute to 1.85 billion km travelled by 2020 though comparatively lesser to other type of motor vehicles, its emission contributions should neither be overlooked nor underestimated. Figure 1.1 shows the graph of projected growth of motor vehicles in Australia. With that, the projected usage of petrol for motorcycles in the year 2020 will reach 54.76 million litres, compared to 47.33 million litres during the year 2000, approximately 13 % growth [5]. Table 1.1 shows the comparison, between year 2000 and the projected year of 2020, of tailpipe emissions for motorcycles in Australia.

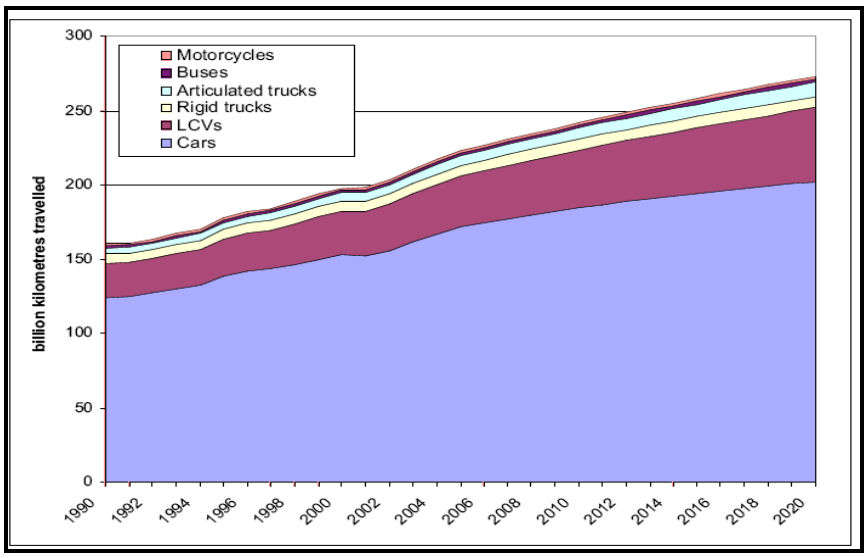

Figure 1.1: Base Case Projected Growth in Motor Vehicle Travel [5]

Year	NO_x	CO	VOC	PM	Pb
	thousand tonnes				tonnes
2000	0.8	24.0	5.3	0.10	1.0
2020	0.9	27.8	6.1	0.11	0.1

Table 1.1: Projected Emissions [5]

The most notable increase is in the amount of CO emitted, from 24 thousand tonnes in 2000 to an estimated 27.8 thousand tonnes in 2020. All major emission gases are projected to increase, with the exception to lead (Pb), where its concentration (as an additive) in petrol is being constantly regulated and minimized through laws and regulations.

A common public misconception of motorcycles not contributing as much emissions compared to passenger cars, and often overlooked by larger automotive manufacturers prioritizing manufacturing costs and profit margins. It is important to note that motorcycles do play an important role in tackling the issues of air pollution and greenhouse gas emissions. Highlighting the importance of motorcycles in being a significant contributor in air pollution and an environmental threat remains if measures are not introduced by governments and organizations to eliminate or minimize tailpipe emissions. The health and social impacts of harmful emissions will be discussed in the next section.

1.3 Emission Impacts on Human Health

ICE vehicles have demonstrated to be a major contributor to air pollution and their long term poses a major concern. This is attributed to the harmful gasses emitted during combustion of the ICE. Ideal ICE combustions yield CO_2 and water. CO_2 is an essential gas in vegetal life and this, together with water, is harmless to the environment (unless the concentration of CO_2 in the atmosphere is such that oxygen is almost absent).

However, the combustion of hydrocarbon fuel is never ideal in reality. Harmful by-products of fuel combustion produced are toxic to human health and the environment. These by-products include nitrogen oxides (NOx), sulphur doxides (SO_2), CO and HC. In addition, ozone (O_3) and particulate matters (PM) such as sulphates (SO_4^-) and nitrates (NO_3^-) are also sources of various health problems.

Reports indicate that the concentration of CO_2 in the atmosphere is rising rapidly and its concentration is now well over 380 ppm. According to the planet's history, the CO_2 level

has not exceeded 300 ppm [6]. Thus minimizing tailpipe emissions of ICE vehicles is of utter importance.

1.3.1 Carbon Monoxide

CO is an odorless, tasteless and colorless gas, easily absorbed through the lungs in to the blood stream of humans. CO is a highly toxic gas when combined with hemoglobin in the blood to form carboxy-hemoglobin, which will reduce the capacity of blood in carrying oxygen, affecting sensitive organs such as the brain and the heart [7].

1.3.2 Nitrogen Oxide

NOx react with ammonia, moisture, and other compounds to form nitric acid vapor and related particles. Effects on human health include respiratory problems, damage to lung tissue, and premature death. Small particles penetrate deeply into sensitive parts of the lungs and can cause or worsen respiratory disease, such as emphysema and bronchitis, and aggravate existing heart disease [8].

1.3.3 Ozone

Breathing O_3 can trigger a variety of health problems including chest pain, coughing, throat irritation, and congestion. Ground-level O_3 can also reduce lung function and inflame the linings of the lungs. Repeated exposure may permanently scar lung tissue. People with lung diseases, children, older adults, and people who are active can be affected when O_3 levels are unhealthy. Problems include airway irritation, coughing, and pain when taking a deep breath, wheezing and breathing difficulties during exercise or outdoor activities, aggravation of asthma and increased susceptibility to respiratory illnesses like pneumonia and bronchitis and more importantly permanent lung damage when exposed repeatedly [9].

1.3.4 Hydrocarbon

HCs such as benzene, toluene, xylene, 1, 3-butadiene, polycyclic aromatic HCs, formaldehyde and acetaldehyde are some of the by-products formed during engine combustion. Benzene and polycyclic aromatic HCs have fatal impacts on human health and is carcinogenic. Formaldehyde and acetaldehyde were said to have carcinogenic effects as well. Xylene is said to have a negative effect on human organs such as the lungs, skin, eyes, kidney

and possible the reproductive system [10]. Toluene, when inhaled, causes decreases in neurological function and irritation of the respiratory tract [11].

1.3.5 Particulate Matter

PM exposure can lead to a variety of health effects, both long-term and short-term. For exposures for long-terms, studies showed it reduces the lung function, development of chronic bronchitis and even premature death [12]. For short term exposures, asthma acute bronchitis may occur. This generally happens to older adults, children and heart and lung disease patients [12].

1.3.6 Sulphur Dioxide

Peak levels of SO_2 in the air can cause temporary breathing difficulty for people with asthma conditions and who are active outdoors. Longer-term exposures to high levels of SO_2 gas and particles may cause respiratory illnesses and aggravate existing heart diseases. Besides that, SO_2 also reacts with other chemicals in the air to form tiny sulphate particles. When these are breathed in, they gather in the lungs and are associated with increased respiratory symptoms and diseases, difficulty in breathing, and even premature death [13].

1.3.7 Lead

Lastly is Pb. Once induced into the body, it is distributed throughout the body through the bloodstream and thus accumulates in the bones. Depending on the level of exposure, it can affect the nervous system, kidney function, immune system, reproductive and developmental systems and the cardiovascular system. Pb exposures also affect the oxygen carrying capacity of the blood. The most common effects encountered in current populations are neurological effects in children and cardiovascular effects (e.g., high blood pressure and heart disease) in adults. Infants and young children are especially sensitive to even low levels of Pb, which may contribute to behavioral problems, learning deficits and lowered IQ [14].

1.4 Solutions Required

The health and environmental concerns lead to more research and development being devoted in producing cleaner and more efficient automobiles. Some of the alternatives include alternative fuels, using hydrogen as a fuel, zero electric vehicles (ZEVs) and hybrid electric

vehicles (HEVs). These alternatives are proposed to replace ICE vehicles in the future in efforts to eliminate tailpipe emissions.

1.4.1 Alternative Fuels

Alternative fuels such as biodiesel and ethanol were also proposed to minimize emissions. Biofuels, in general, are produced using natural oils such as vegetable oil or peanut oil. This looked promising as emissions are near zero when operating with biodiesel. Besides, diesel engines require minimal or no modifications at all to run on biodiesel.

However turning crops into biofuels has sparked numerous debates. It was published in a report by Cornell University in New York that growing crops for biofuel production not only ignores the need to reduce natural resource consumption, but also increases the severity of the global food crisis issue, especially in severely affected areas in parts of Asia, Africa and the Americas. The increase usage of biofuel will only further damage the environment and the food system, the report concluded [15]. Besides that, numerous papers published in the literature also stated the disadvantages and effects of biofuel. James et al. [16] and Josserand [17] argued that the diversion of food crops to produce biofuels had been blamed for the increase in cost of staple food crops such as maize and rice. Also, a recent report published by Crutzen et al. [18] suggested that certain biofuel production methods or pathways may lead to a net positive increase in greenhouse gas emissions. One example given is the conversion of carbon-rich peatland to oil-palm in Southeast Asia for biofuel production, which led to a net positive increase in emissions [18].

1.4.2 Zero Emission Vehicle

Due to various concerns outlined in the previous sections, it is vital to find solutions toward eliminating or reducing tailpipe emissions. One of the proposed solutions was the introduction of ZEVs, in the form of electric powered vehicles.

A typical ZEV consists of a traction motor and a power source, mainly batteries and/or ultracapacitors to supply power. The absence of an ICE would meant that fuel would not be required, hence eliminating harmful tailpipe emissions. Although this solution seems perfect, there are several disadvantages. Some of the disadvantages posed to ZEVs are their limited driving range and performance and high initial costs [19]. These disadvantages are mainly due to the slow progress in battery technology and research. Although great efforts and research are done in battery technology, the poor energy storage capacity per unit weight

and volume for batteries limits the capability of ZEVs. On top of that, studies showed that ZEVs will never be able to challenge petrol vehicles even with an optimum energy storage capacity [20].

Thus, this makes ZEVs impractical for commercial use and is only restricted to specific applications such as in airports or railroads.

1.4.3 Hydrogen as a Fuel

The next proposed solution was using hydrogen as a fuel. Hydrogen was originally introduced in fuel cell vehicles (FCVs). Fuel cells offer a lot of benefits over the ICE. One of them is having a high operating efficiency and its high efficiency is not constrained by the maximum Carnot cycle efficiency, unlike ICEs [20]. Fuel cells are capable of producing near-zero emissions with water being the by-product when reacting with oxygen.

Although the advantages are lucrative, there are many problems associated with hydrogen and fuel cells. The main problems with FCVs are the high cost of construction and optimizing the conditions for efficient reaction of the fuel cell.

Another solution involving hydrogen as a fuel proposed is the use of dual-fuel vehicles (DFVs). DFVs can be categorized into two categories; bi-fuel and flexible-fuel. Bi-fuel vehicles are vehicles that can only be operated on one type of fuel at a time. Flexible-fuel vehicles are vehicles that can be operated based on mixtures between the two fuels. Various researches have catered to hydrogen-fuel ICEs, in which the fuel could be biodiesel, diesel or just petrol [20-23]. While DFVs looked promising, a reduction in power could go up to 30% compared to conventional petrol ICEs [24].

One of the main problems in regard to hydrogen is the infrastructure and storage capabilities and the costs related to it. Fueling infrastructure is not readily available and hydrogen storage has its drawbacks in terms of safety and costs. These are just the problems that continue to hinder the development of hydrogen as a fuel. Thus hydrogen-powered vehicles still have a long way to go before it can be introduced commercially.

1.4.4 Hybrid Electric Vehicles

The concept of HEVs date back as early as the automobile technology itself. During those times, the electric motor was used as a power assist tool for the ICE as electric motor engineering was more advanced than ICE engineering. Because of this, emphasis on performance, rather than environmental concerns, is the main priority at that time.

One of the first HEV was designed and built on 4th May 1897 by Justus B. Entz, chief engineer of the Electric Storage Company in Philadelphia. Figure 1.2 shows the chalkboard with Entz's design.

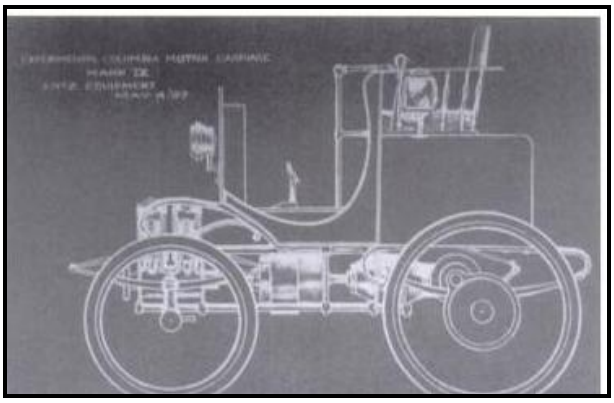

Figure 1.2: Justus B. Entz's Chalkboard Design [25]

Although HEVs were being built and designed, it is not until 1899 at the Paris Salon where two HEVs were presented. The two HEVs were built by the Pieper establishment in Liege, Belgium and the Vendovelli and Priestly Electric Carriage Company of France [26]. The two designs were shown in Figures 1.3 and 1.4.

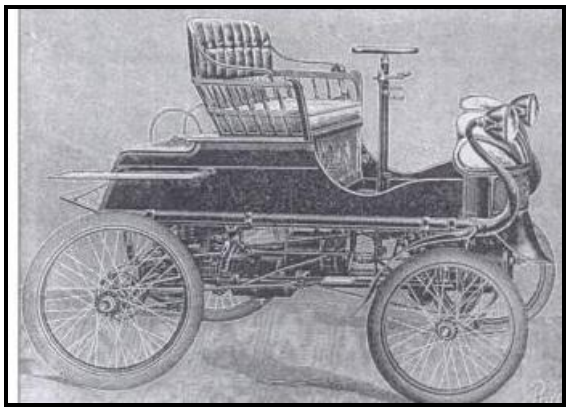

Figure 1.3: The Pieper Design [27]

The Pieper design shown in Figure 1.3 is a parallel HEV, with a small air-cooled engine equipped with an electric motor and lead-acid batteries. In addition to being one of the first two HEVs, and being the first parallel HEV, the Pieper was undoubtedly the first to use an electric starter [28]. The other HEV introduced by Vendovelli and Priestly is the world's first series HEV, with both rear wheels being powered by independent motors. Both HEVs

design has different approaches; the design by Pieper was used to supply more power and the Vendovelli and Priestly design mainly focus on the achievable ranges. Various HEVs were built during the period ranging from 1899 until 1914.

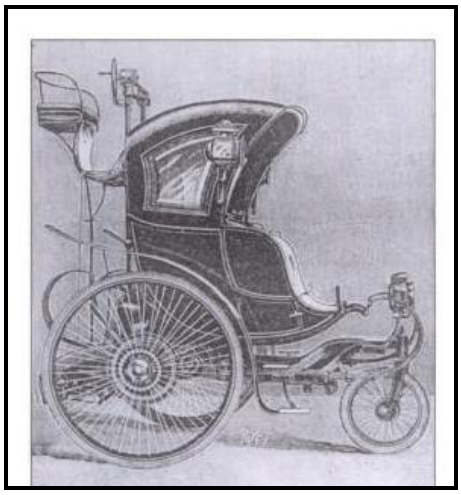

Figure 1.4: The Vendovelli and Priestly Electric Carriage Company Design [29]

One of the greatest problems faced during that time was the inability to properly control the electric machine i.e. the traction motor. This is because power electronics engineering was not available until mid-1960s. Because of this, the traction motors have limited operating ranges and low efficiencies.

Although the concept of HEVs is almost as old as the automobile itself, HEVs were normally overshadowed by the traditional petrol vehicles due to their production costs and power efficiencies. For example, the Volkswagen Taxi was introduced following the 1973 during the Arab oil embargo. This parallel hybrid vehicle logged over 13,000 km in test drives. The taxi was constantly featured in many automotive industry shows but never made it to the production stage [30]. Hybrid vehicle technology was slowly becoming dormant again.

Hybrid vehicle technology was revived again in 1975 when Dr. Victor Wouk built a Buick Skylark [31]. This parallel HEV has a top speed of just under 130 kmh^{-1} with an acceleration from 0 to 100 kmh^{-1} in 16 seconds. This was an impressive feat and this lead to Dr. Victor Wouk being dubbed as the "modern investigator of the hybrid electric vehicle movement" [31]. The advancement in power electronics also contributed to the rise of HEV technology.

With the growing concerns in air pollution, HEVs have been introduced into the automotive market again. HEVs had since been popularized by two major car giants, Honda and Toyota; the Honda Insight in 1999 and the Toyota Prius in 2000, were both sleek and well-designed. The HEVs offered petrol mileages exceeding the by the current Coporate Average Fuel Economy (CAFE) standard of the United States of 8.6 l/100 km [31].

With that, the market for HEVs continued to grow, with an estimated 345,000 units were sold in the United States alone in 2007, an increase of 35 % over the 2006 figure [32]. Toyota's hybrid range sales reached 1,000,000 units in 2007 and data showed (for 2006) for Prius, sales reached 500,000 units [33]. Toyota also pledged to produce 1 million HEVs a year by 2012 [34]. As for Honda, their hybrid range sales reach to 300,000 units in January 2009 [35]. The all-new 2010 Honda Insight hybrid also made its world debut at the North American International Auto Show in Detroit in January 2009. The five-passenger, five-door HEV went on sale in the spring of 2009 and is expected to have annual global sales of 200,000 units per year - approximately 100,000 in the North America [36]. General Motors (GM) also caught up with their company plans to introduce a new hybrid vehicle every three months from 2008 until 2012 [37].

1.5 Problem Statement and Contributions

This thesis deals with emissions predictive modelling applicable to classes of hybrid electric vehicles that employ multiple energy storage units. In particular, this thesis introduces two emissions predictive techniques applicable to hybrid vehicular applications, where using a hybrid electric scooter as a reference vehicle model. The majority of published works in the literature focusing on emissions predictive modelling are catered to four-wheelers. Minor considerations were given to motorcycles, especially in the effort in regulating and controlling the tailpipe emission levels. As a result, emissions from two-wheelers are often not addressed, although studies showed a significant contribution in harmful emissions produced from these vehicles.

As a novel approach, this work employed a multi-state control strategy on a hybrid electric scooter predictive model to simulate its performance, emissions and fuel economy. The multi-state control strategy demonstrated a more optimum vehicle system with emission levels, fuel economy and system performance are all optimized and accurately predicted and simulated. This forms a dynamic approach in system modelling and simulation. The second approach presented in this thesis is the use of artificial neural networks for emissions

predictive modelling. This approach exhibits a more control-oriented methodology, where emissions levels can be properly predicted and controlled accordingly and as requested. Thus having accurate control on the emissions enable strict adherence to emission laws and guidelines.

The key contributions as a result of this work are summarised below:

1. Emissions predictive modelling and control for hybrid electric scooter applications are rare in the literature. Regarding hybrid vehicle technologies, most of the researches were focused in system optimizations and performance improvements of the systems for four-wheelers. Emissions predictions and control were not focused, especially for two-wheelers. This thesis presents a fresh perspective in emissions predictions and control for two-wheelers.
2. This predictive tool can be used to analyze the interaction between sub-systems and evaluate vehicle performance using measures such as fuel economy, emissions contributions and drivability. Also, the multi-state control strategy employed in this research presents a novel control system for hybrid electric scooter applications.
3. The predictive models constructed enable various possible configurations to be systematically explored and simulated, creating a general model for hybrid electric vehicles. Hardware components can be added or removed from the model, giving it a higher flexibility.

1.6 Research Focus and Tools

Two approaches in emissions predictive modelling will be presented in this study. The specific objectives of this thesis can be summarized as follow:

1. Construct a simulation model on MATLAB-Simulink which properly simulates a hybrid electric scooter (HES). The measured variables will be the fuel economy and the tailpipe emissions. Simulating a worst case scenario for the HES, the ICE model will be verified in terms of fuel economy and emissions through experimental data. The HES model will then be verified from the literature. This approach uses dynamic modelling simulation techniques in emissions predictive modelling.
2. With the HES model, a physical HES will be constructed using the information from the HES Model. This is to mimic the HES model so that accurate results could be obtained, both experimentally and through simulation. Incorporating the multi-state control strategy,

the HES model was then simulated over four distinct driving cycles and the performance of the system were studied.

3. The second approach in emissions predictive modelling is to construct an Emissions Prediction Model (EPM) to accurately predict the tailpipe emissions based on the HES's operating conditions. This predictive approach, unlike the first approach using dynamic modelling and simulation, will be using artificial neural network (ANN) techniques. Various ANN models were used to choose the most suitable and accurate model for emissions prediction.

This thesis comprises of 7 chapters. Chapters 2 and 3 are literature surveys. Chapter 2 will discuss about hybrid electric vehicles including its designs and architectures. Several commercialized designs will be presented as well. Chapter 3 discusses about the essential knowledge about ANN and specific networks employed in this research. Past researches that are within the scope of this research found in the literature will be presented as well.

Chapter 4 can be divided into two parts; the first part will discuss about the construction and development of the MATLAB-Simulink HES model. The second part will discuss the physical construction of the actual HES. Chapter 5 will present the experimental and predictive results as well as the HES model appraisal in terms of fuel economy, emissions and performance.

Chapter 6 will show the construction of EPM using ANN techniques to predict the tailpipe emissions. Lastly, several proposed future work and final concluding remarks will be discussed in Chapter 7.

The computer modelling and simulation tools that will be used for this are from MATLAB. MATLAB is a software developed by MathWorks®. The MathWorks® family consists of two platforms, MATLAB and Simulink. MATLAB consists of stand-alone applications, various toolboxes and data access tools. Some key characteristics of MATLAB are its user-friendly interfaces with powerful, easy-to-use graphics and visualization techniques. Toolboxes (or third-party software) could be added to form a powerful tool. Simulink, on the other hand, is perfect for modelling, simulating and implementing dynamic and embedded systems. It uses a block interface, which is user-friendly and easy to be implemented in the Simulink environment.

For dynamic modelling and simulation of the HES, Simulink will be used to create a complete model of the HES scooter. Data will be obtained *via* simulation, all simulated under the MATLAB-Simulink environment. For the development of the EPM, the Neural Network

Analysis Package developed within the School of Engineering, University of Tasmania by the Hydrogen and Allied Research Technologies (HART) research team will be used. This package will be used for emissions predictive modelling for the second approach of this research project.

CHAPTER 2: LITERATURE SURVEY

2.1 Introduction

Chapter 2 presents a literature survey on hybrid electric vehicle (HEV) drivetrain architectures, with in-depth discussions on the 3 main types of HEV drivetrain designs: series, parallel and series-parallel drivetrains. Their architectures, advantages and disadvantages will be highlighted. Several patented and commercialized hybrid drivetrain designs and their respective control strategies will also be presented, showcasing the uniqueness and variability of each design.

This literature survey also discusses modelling techniques found in the literature. This gives an overview on the current modelling and simulation methodologies in terms of energy optimization and emissions control management of HEVs and, in particular, hybrid electric scooters (HESs). The final part of this literature survey discusses about the current emissions prediction techniques and methodologies found in the literature. This section summarizes the emissions predictive modelling techniques used in the past by various studies and researches.

2.2 Hybrid Electric Vehicle Drivetrain Architecture

Hybrid vehicles, as defined by the Official Journal of the European Union, are termed as "a vehicle with at least two different energy converters and two difference energy storage systems onboard for the purpose of vehicle propulsion" [38]. In common terms, a vehicle with two different propulsion sources (normally an internal combustion engine (ICE) and a DC traction motor) installed onboard operating the vehicle either independently or in parallel can be described as a hybrid vehicle.

A HEV drivetrain usually consists of no more than two powertrains. More than two powertrains in a drivetrain will often complicate the system. Figure 2.1 shows a general representation of a HEV drivetrain. Two powertrains are present in this case and was labeled in the figure.

ES and EC are defined as energy source and energy converter respectively. The non-dotted lines show the power flow during vehicle operation and the dotted lines show the charging operation. Powertrain 1 has a unidirectional power flow and Powertrain 2 has a bidirectional flow.

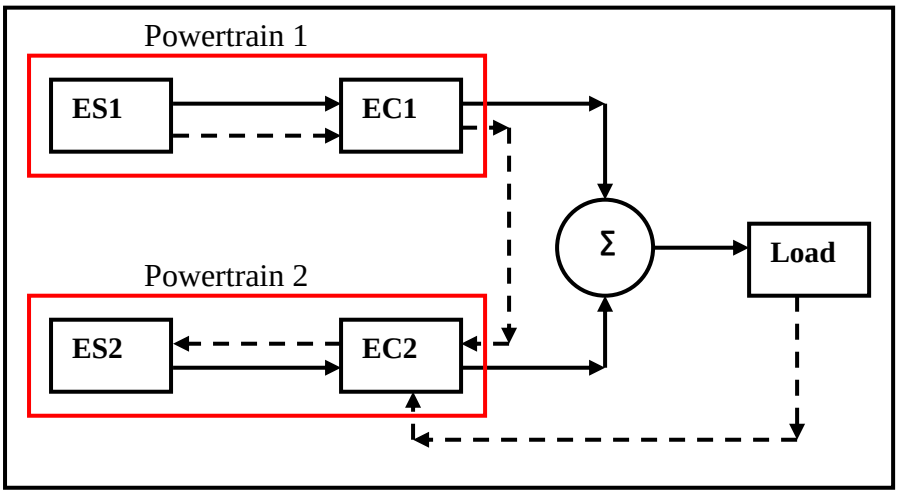

Figure 2.1: General Representation of a HEV Drivetrain

The power demanded from the load consists of two parts; the average power and the dynamic power as shown in Figure 2.2. The average (steady) power is normally provided by the ICE but fuel cells and Stirling engines are the other alternatives. The dynamic power is provided by the traction motor. The dynamic power source would normally be sealed lead acid (SLA) or lithium batteries. Besides batteries, ultracapacitors, flywheels or a combination of both may be used as well [39-41]. The power flow during operation is represented by the solid lines. Power flow from ES1 and ES2 are coupled before meeting the load demand. Normally a torque or speed coupler will be used.

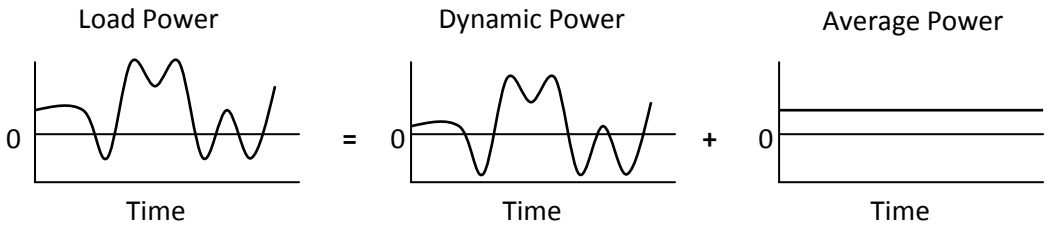

Figure 2.2: Load Power

The recharging procedure (as depicted in dotted lines in Figure 2.1) has two operations. The first operation is a regenerative braking operation where energy is captured during braking and was used to recharge ES2. This is depicted by the dotted lines from the load to EC2. Regenerative braking is only possible when ES2 is not at full charge or else mechanical braking will operate instead. Thus it is wise to keep the SC at an optimum level so that regenerative braking can occur every time braking occurs. This is to eliminate the

energy losses during braking as mechanical braking does not capture the braking energy. The second operation is where ES1 (normally the ICE) recharges ES2 (normally the batteries) while operating the vehicle or during idle conditions. This is depicted in Figure 2.1 by the power flow direction (dotted lines) from ES1 to ES2. This loop occurs when the vehicle is caught idling, during traffic jam or stop junctions. Another possible operation is a plug-in hybrid behavior where the energy source is charged using the main electricity grid. Vehicles of this type are normally referred to as plug-in HEVs where a standard electricity plug is installed onboard enabling electricity grid charging.

HEV drivetrains in general can be classified into three distinct categories based on their unique architecture and complexity. The three classes are a series hybrid, parallel hybrid and a combination of both, series-parallel hybrid. These three types of hybrid vehicles and their architectures are discussed in the sections below.

2.2.1 Series Architecture

A series hybrid vehicle architecture is shown in Figure 2.3(a). From the diagram it can be seen that a series configuration has two power sources feeding a single power plant, in this case a DC motor. This means that only the DC motor is propelling the vehicle and drawing power from either the ICE or the battery, making it quite similar to an electric vehicle (EV). A generator is present to recharge the battery when it is under a certain SC.

The battery's SC is an important variable as it determines the operating condition of the HEV. Depending on the load demands, a low SC would require battery charging and a high SC would enable the traction motor to operate the vehicle without the need of the ICE. Minimal usage of the ICE would subsequently reduce tailpipe emissions.

This series configuration has its advantages and disadvantages. One advantage is that it has a simple construction. This would ultimately lead to simple control strategies for this type of HEV. Another advantage is that the ICE and the generator can be located anywhere in the drivetrain. This provides a great flexibility during design and construction. Series hybrid vehicles are also suitable for short trips and in low-speed areas, especially urban areas. In this case, the HEV would act as a pure EV due to the low power demands (where power is not required from the ICE). Subsequently, tailpipe emissions would be lower as the ICE was not in use.

One disadvantage of the series hybrid is the need of three propulsion components; ICE, motor and generator. Because of this, the energy from the ICE was converted twice

(mechanically and electrically) and this contributes to a lower efficiency as power losses occur on the motor and the generator. Also, three propulsion units will increase the cost of construction as well as the weight of the vehicle. A heavier-weighted vehicle will lead to higher fuel consumption. Another disadvantage is that the motor have to be sized correctly according to the requirements of the vehicle. This is because the maximum attainable traction power of the vehicle is determined by its only propulsion source, the traction motor. For longer distance trips or high speed cruising, the battery will exhaust quickly and the vehicle will have to be powered by just the ICE, although the maximum vehicle traction power is determined by the motor's rating. Some of the most notable series HEV designs are the Mitsubishi ESR, the Volvo ECC and the BMW 3 Series [42].

Because of the advantages discussed above, manufacturers have started to show more interest in parallel HEVs as the need of a large sized motor would not be required. The next section discusses about the parallel drivetrain configuration.

2.2.2 Parallel Architecture

A parallel hybrid drivetrain is shown in Figure 2.3(b). In this instance, the ICE and the motor are providing propulsion power to the vehicle, unlike the series configuration where just the motor is providing traction power. The generator is not installed in this case. This is because the motor will act as a generator during battery charging and regenerative braking.

Some of the early developments of parallel HEVs include the BMW 518, the Citröen Xzara Dyn-active and Saxo Dynavolt, the Daimler-Chrysler ESX 3, the Fiat Multipla, and the Ford Multiplia and P2000 Prodigy [42]. The most well-known examples today are the Insight, Civic and Accord hybrids from Honda. Honda calls its technology Integrated Motor Assist (IMA) technology [43]. Parallel designs are also found in commercial hybrid vehicles from manufacturers such as Azure Dynamics and Nissan [44].

The variety of commercialized parallel HEVs produced demonstrates immense interest in parallel HEVs. This is due to parallel HEVs having many possible control strategies to increase its performance and minimize tailpipe emissions as well. For example, the parallel HEV can be operated only on motor during urban travel and on ICE during highway cruising. The ICE could be turned off when not in use. Turning the ICE off reduces emissions, fuel consumption and unwanted noise. Another option would be a hybrid approach where the motor and the ICE each play a role in operating the vehicle using various control

methodologies. The flexibility in design for parallel HEVs generates more interest when compared to series HEVs.

This parallel drivetrain configuration has several advantages and disadvantages. One of advantages is that a smaller rated ICE and motor can be used to deliver the same power ratings. This is because the two propulsion sources can be operated either independently or in a hybrid mode. Priority is generally given to the traction motor, with the ICE acting as an assisting propulsion source. The absence of a generator set reduces the weight of the vehicle and minimize production/assembly costs.

One of the disadvantages is that this configuration does not enable the ICE to recharge the battery during idle or low SC conditions. There are two ways to recharge the battery. Firstly is during the regenerative braking condition where the traction motor acts as a generator for battery recharging. This is similar to an alternator found in conventional cars. The second is to recharge the battery through the electricity grid. Only plug-in parallel HEVs are engineered to charge the batteries directly through the main electricity grid. Another notable disadvantage is the complex control methodology as the power flows have to be regulated and blended from the two parallel sources, making it time consuming and difficult. Lastly, the power blending from the ICE and the motor requires a complex mechanical device [45]. This mechanical device could be a torque coupler (gear transmission or a pulley and chain assembly) or a speed coupler (planetary gear trains (PGTs) and an electric motor with float stator). Both couplers could also be combined and incorporated into the drivetrain.

2.2.3 Series-Parallel Architecture

Although the parallel configuration offers more flexibility in design over the series configuration, car manufacturers soon realized the importance of the ICE recharging the battery for practical road usage. This lead to a series-parallel drivetrain design; where the series characteristics were incorporated into the parallel drivetrain. Series-parallel configuration adapts the concept of the ICE recharging the battery but retains a dual-propulsion system. The battery can be charged either from the main electricity grid, from the ICE or during regenerative braking.

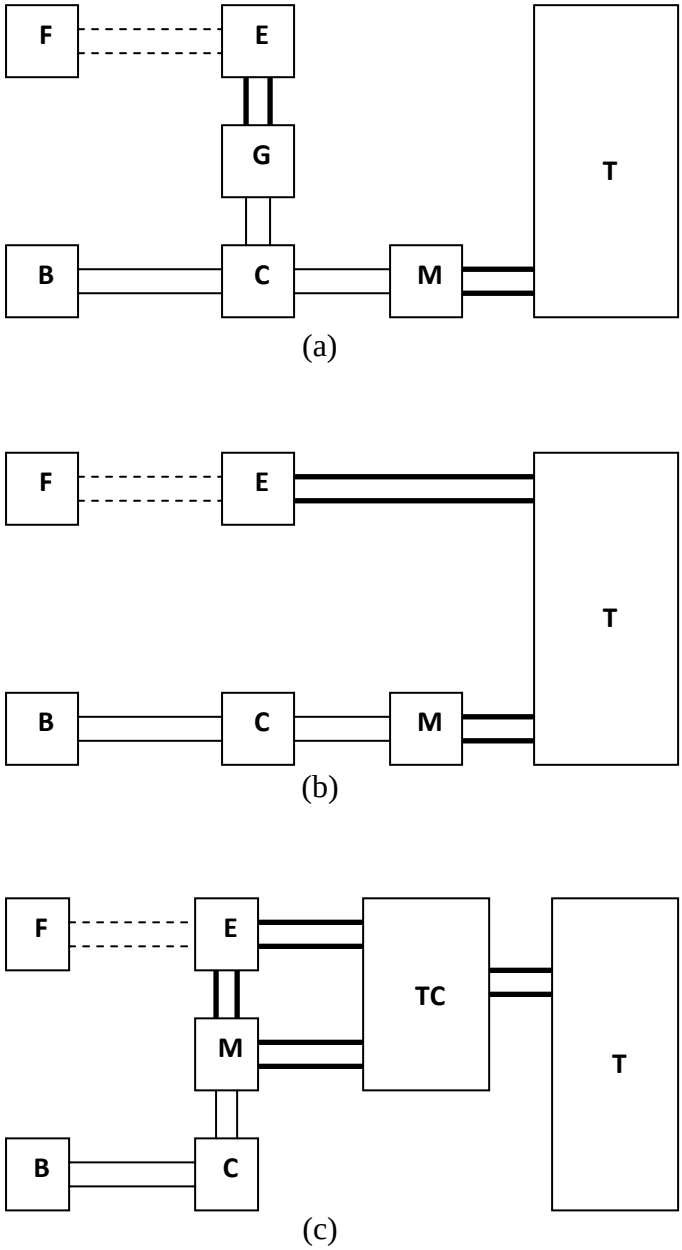

F: Fuel TC: Torque Coupler E: ICE T: Transmission

B: Battery G: Generator M: Motor/Generator C: Power Converter

Note that the bold lines represent mechanical links, the normal lines represent electrical links and the dotted lines represent hydraulic links between two components in the hybrid drive train.

Figure 2.3: (a) Series Hybrid Structure (b) Parallel Hybrid Structure (c) Series-Parallel Hybrid Structure

The component arrangement of a series-parallel hybrid is shown in Figure 2.3(c). A torque coupler device is present, either combining the torque of the ICE and the motor together or splitting the ICE torque into two parts; for propelling the vehicle and for charging the battery. The power flow of the ICE is uni-directional and for the motor is bi-directional. The ICE charging characteristic adapted enables battery charging to occur during engine operation or idling. The traction motor acts as a generator during charging and regenerative braking conditions. One famous commercialized series-parallel HEV is the Toyota Prius.

The use of the ICE should be minimized in order to maximize the efficiency of the drivetrain. This is because charging and discharging of the battery reduces the efficiency of the system. Energy is usually expended during the power flow through the power converter and the generator. One way to minimize energy losses is for the HEV to operate without its ICE or motor or both turned on until the battery is at a minimum acceptable SC (30 % - 40 %) before recharging.

2.3 Commercialized Multi-Mode Hybrid Vehicle Drivetrain Designs

Several multi-mode HEV drivetrain designs and their control strategies had been introduced and patented as researched and discussed in the literature. A total of five multi-mode HEV drivetrain designs are discussed in this section; General Motors, University of Michigan-Dearborn, Renault, Silvatech and Timken designs.

General Motors (GM) designed and patented several multi-mode drivetrains. Two patents (U.S. patents 5,558,588 and 5,571,058) were discussed to highlight the difference between the two designs. The first design, labeled as Design A in this thesis, is a two-mode design and Design B is a four-mode design. Two commercialized designs are also discussed and examined.

The drivetrain design by University of Michigan-Dearborn is very much similar to the design incorporated to the parallel HES. Although this design was applied to a four-wheeler (more specifically, the Toyota Prius), it provides a benchmark for future parallel hybrid two-wheeler development and research and the control strategy will be adopted in this study for the dynamic modelling approach (more in Chapter 4).

The remaining Renault, Silvatech and Timken designs are further examined and discussed to demonstrate its versatility and variability in multi-mode designs and hybrid drivetrain research, providing a more in-depth understanding of the current development in the HEV industry.

Note that the terms multi-mode and multi-state will be used constantly throughout this thesis. The term multi-mode refers to different power-split configurations for each drivetrain design. Multi-state refers to various operating states (or operating conditions) for the hybrid vehicle (more information will be presented later in Chapter 4).

2.3.1 General Motors Design

General Motors (GM) has around 33 U.S. patents involving designs on multi-mode hybrid drivetrains. The initial design that began the two-mode development will first be discussed. A four-mode design will then be examined to illustrate the differences in mode number. Subsequently, two designs that have been commercialized will also be examined

The first design to be discussed here was one of the earliest designs by Schmidt in 1996 with the U.S. patent number 5,558,588 [46]. This patent is important as it is one of the earliest designs that introduce multi-mode hybrid powertrains in the literature. This design has a two-mode architecture, which contains two planetary gears and three clutches, labeled as Design A shown in Figure 2.4. Note that the notations on the figures below are as follows: MGs represents motor/generator units, FD represents the final drive output, CLs are used to show clutches and the planetary gears are represented by the sun (S), carrier (C) and ring (R) respectively.

Figure 2.4 shows GM's two-mode hybrid design. This design is a series hybrid design. The ICE is connected *via* clutch CL3 to the first planetary ring gear, MG1 is connected mechanically to the first planetary carrier gear and MG2 is connected to the both sun gears. A control unit regulates power flow between the energy storage devices and the MGs as well as between the first and second MGs [46].

Operation in Modes 1 or 2 may be achieved by using the three clutches CL1, CL2 and CL3. For Mode 1, the output speed of the transmission is proportional to the speed of one MG; as for Mode 2, the output speed of the transmission is proportional to the speed of the other MG. For all of the configurations, when CL2 is on (and CL1 is off), Mode 1 of the power-split is selected, and when CL1 is on (and CL2 is off), Mode 2 is selected. When both CL1 and CL2 are on, the transmission is transitioning between the two modes.

This design is a multi-mode design; means that several power-split configurations can be present by controlling the clutches and assigning the electrical machines MG either as a motor, a generator or turned off. The modes include ICE only mode, motor only mode,

hybrid mode, charge mode, regenerative braking mode, engine braking mode and regenerative engine braking mode.

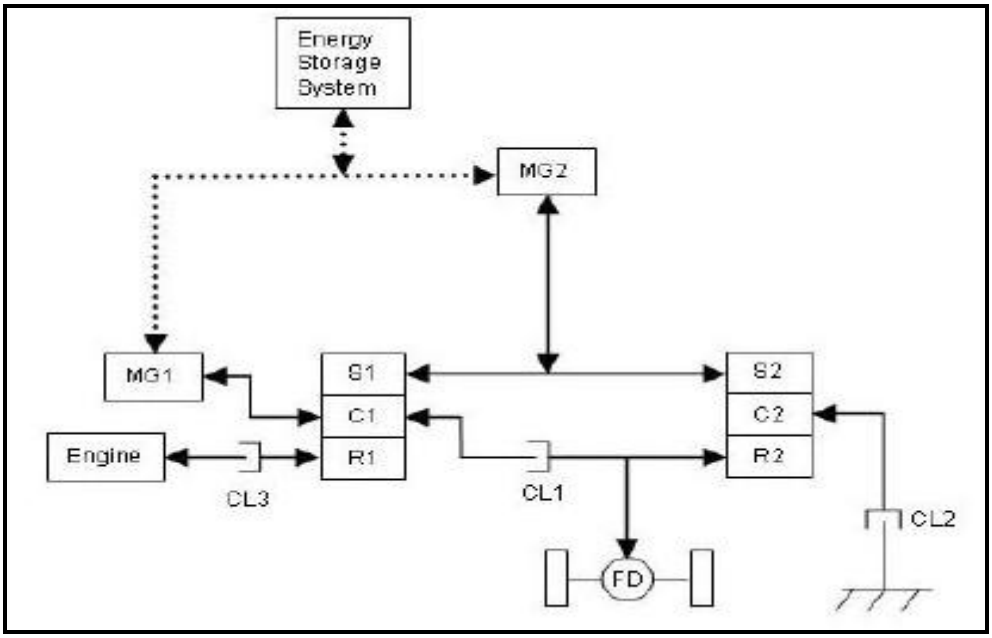

Figure 2.4: General Motors Hybrid Drivetrain Design A [47]

Table 2.1 below shows the operating conditions for each mode at various defined speeds [46]. The operating conditions are the behavior of the MGs (whether it is acting as a motor, generator or turned off) and the CLs (whether they are engaged or disengaged).

STATE	MG1	MG2	CL1	CL2	CL3
Motor State					
Slow	OFF	Motor	ON	ON	OFF
Fast	Motor	Motor	ON	OFF	ON
Hybrid State					
Very Slow	Generator	Motor	OFF	ON	ON
Slow	Motor	Generator	ON	OFF	ON
Medium	Motor	Motor	ON	OFF	ON
Fast	Generator	Motor	ON	OFF	ON
ICE State					
Slow	Generator	Motor	OFF	ON	ON
Medium	Motor	Generator	ON	OFF	ON
Fast	Generator	Motor	ON	OFF	ON

Charge State					
Mode 1					
Very Slow	Generator	Motor	OFF	ON	ON
Slow	Generator	Generator	OFF	ON	ON
Mode 2					
Medium	Motor	Generator	ON	OFF	ON
Fast	Generator	Generator	ON	OFF	ON
Very Fast	Generator	Motor	ON	OFF	ON
Regenerative Braking State					
Slow	Generator	Generator	ON	ON	OFF
Fast	Generator	OFF	ON	OFF	OFF
Engine Braking State					
Slow	Motor	Generator	OFF	ON	ON
Medium	Generator	OFF	ON	OFF	ON
Fast	Motor	Generator	ON	OFF	ON
Regenerative + Engine Braking State					
Very Slow	Motor	Generator	OFF	ON	ON
Slow	Generator	OFF	ON	OFF	ON
Medium	Generator	Generator	ON	OFF	ON
Fast	Motor	Generator	ON	OFF	ON

Table 2.1: Operating Modes and Conditions for GM Design A

GM Design A has seven states and each state has at least two different speed settings. The first four states are acceleration states. The motor state is where the ICE is off and the MGs are powering the vehicle. This state has two regions, slow and fast speeds. The second state is the hybrid state, where the ICE and MGs operate in a hybrid condition to power the vehicle. This state normally happens during high power demands. This state has four speeds, ranging from very slow to fast. For the ICE state, there are three speeds. For low speeds, Mode 1 is chosen. When the speed increases to medium, Mode 2 is selected. The charging state occurs when the SC is low and the ICE available power is higher than the demanded load. Mode 1 is selected for low speeds and Mode 2 is selected for high speeds.

The remaining three states are deceleration (or braking) states. The regenerative braking state occurs when the SC of the storage system is not in full charge. The ICE is off

(thus not absorbing energy) and only the momentum of the vehicle is used to charge the energy storage system. For slow speeds, Modes 1 and 2 are chosen and for faster speeds, only Mode 2 is selected. The next state is the engine braking state, where the momentum of the vehicle is absorbed by the ICE and none of the energy is used to charge the energy storage system. The energy storage system is off in this case. In this state, Mode 1 is chosen for slow speeds. Mode 2 is chosen as the speed increases. The last state of the GM Design A architecture is the combination of regenerative and engine braking. The vehicle momentum is partially employed to charge the energy storage system and partially absorbed by the ICE.

The second design to be discussed is another U.S. patent by Schmidt in 1996 (U.S. patent number 5,571,058) [48]. Design B has four power-split modes, as opposed to only two from Design A. The design is shown below in Figure 2.5. This is a four-mode input-split parallel hybrid transmission design.

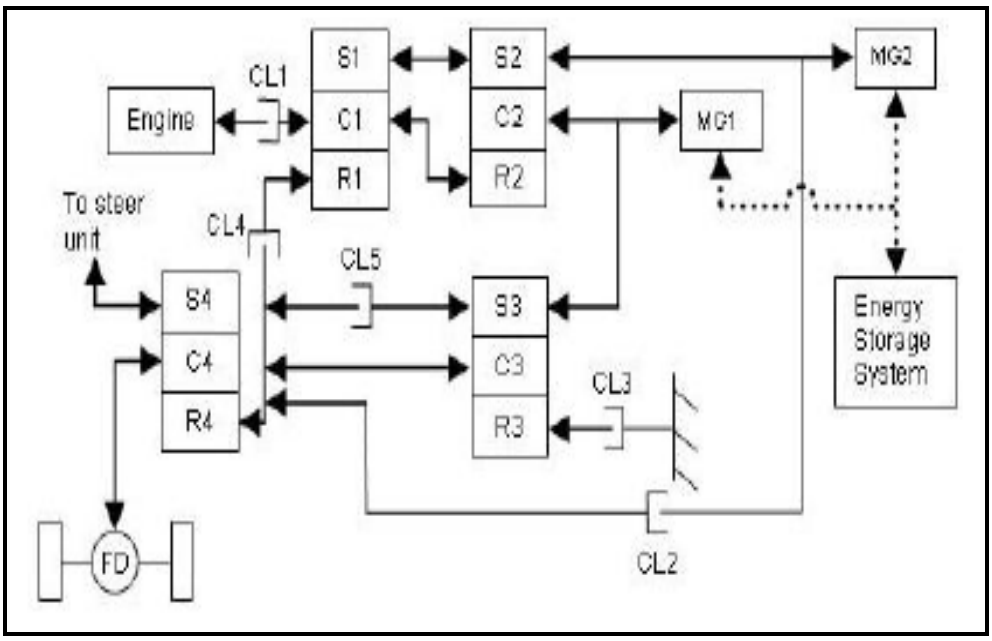

Figure 2.5: General Motors Hybrid Drivetrain Design B [47]

From Figure 2.5, this design has four PGTs and five CLs. The ICE is connected *via* CL1 to the first carrier, MG1 is connected to both the second carrier and the third sun gear, and MG1 is connected to the second sun gear and *via* CL2 to the intermediate shaft. The intermediate shaft is the point where the mechanical power from the first ring gear (when CL4 is engaged), third sun gear (when CL5 is engaged), the third carrier, and the sum of the second sun gear and MG2 is combined. The intermediate shaft delivers power to the fourth

ring gear, and this power is split between the wheels and a steer unit that is included since this design was specifically designed for track-driven vehicles; the steer unit regulates the speed of each track and allows the vehicle to pivot and turn [48].

MODE	MG1	MG2	CL1	CL2	CL3	CL4	CL5
Mode 1	Generator	Motor	ON	ON	OFF	OFF	OFF
Mode 2							
Slow	Motor	Generator	ON	OFF	ON	OFF	OFF
Medium	Motor	Motor	ON	OFF	ON	OFF	OFF
Fast	Generator	Motor	ON	OFF	ON	OFF	OFF
Mode 3							
Slow	Motor	Generator	ON	OFF	OFF	ON	OFF
Medium	Motor	Motor	ON	OFF	OFF	ON	OFF
Fast	Generator	Motor	ON	OFF	OFF	ON	OFF
Mode 4							
Slow	Motor	Generator	ON	OFF	OFF	OFF	ON
Medium	Motor	Motor	ON	OFF	OFF	OFF	ON
Fast	Generator	Motor	ON	OFF	OFF	OFF	ON

Table 2.2: Operating Modes and Conditions for GM Design B

Table 2.2 above shows the operating modes and their respective operating conditions for Design B. For Modes 2, 3 and 4, there are multiple output speed ranges for each mode. Mode 1 has only one speed range, and is used for starting the vehicle since it provides the highest tractive torque [49].

One commercialized design released by GM is the Two-Mode EVT (which stands for electronically variable transmission). This design was installed in transit buses. This design comes from patent number 5,931,757 granted to Schmidt and was assigned to General Motors in 1999 [50]. This is a two-mode design and is more suitable for heavy duty vehicles (HDV). The Two-Mode EVT architecture is shown in Figure 2.6. This drivetrain consists of three PGTs, two CLs and two MGs. MG1 is connected between the first sun and the second ring gear and MG2 is connected between the second and the third sun gears.

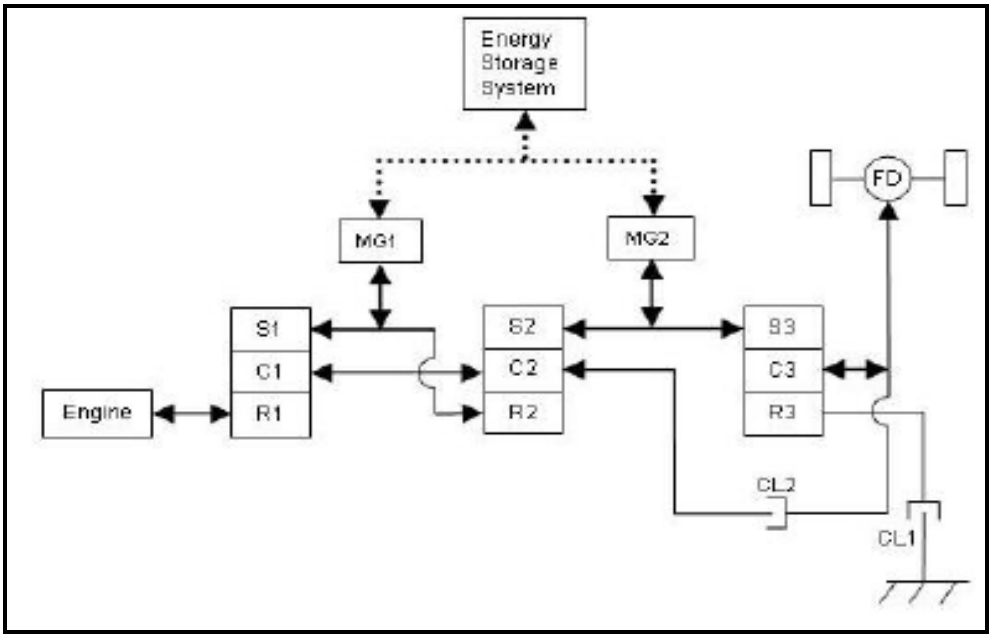

Figure 2.6: General Motors Two-Mode EVT Architecture [47]

The Two-Mode EVT design has various operating speeds with two modes. Mode 1 has three speeds. During stationary conditions, MG1 is off and MG2 operates as a motor to provide a high torque, suitable for vehicle start-ups. Slow speeds are about from 0 kmh^{-1} to 34 kmh^{-1} and fast speeds are 34 kmh^{-1} and above. For Mode 2, to make a transition from Mode 1, CL1 is disengaged and CL2 is engaged. The speed thresholds for medium and fast speed are 27 mph and 62 mph respectively, with the behavior of the MGs clearly illustrated in Table 2.3.

MODE	MG1	MG2	CL1	CL2
Mode 1				
Stationary	OFF	Motor	ON	OFF
Slow	Generator	Motor	ON	OFF
Fast	Motor	Motor	ON	OFF
Mode 2				
Transition	Generator	Motor	OFF	ON
Medium	Motor	Motor	OFF	ON
Fast	Motor	Generator	OFF	ON

Table 2.3: Operating Modes and Conditions for GM Two-Mode EVT Design [50]

For light duty vehicle (LDV) applications, GM introduced a series design called a Two-Mode compound-split hybrid architecture (U.S. patent 6,953,409) [51]. This design has four fixed-gear ratios, three PGTs, four CLs and similar to previous designs, two MGs. The ICE is connected to the first ring gear. MG1 is connected between the first sun and the second ring gear. MG2 is connected to the second ring gear *via* CL4, second and third sun gears. This design is illustrated in Figure 2.7.

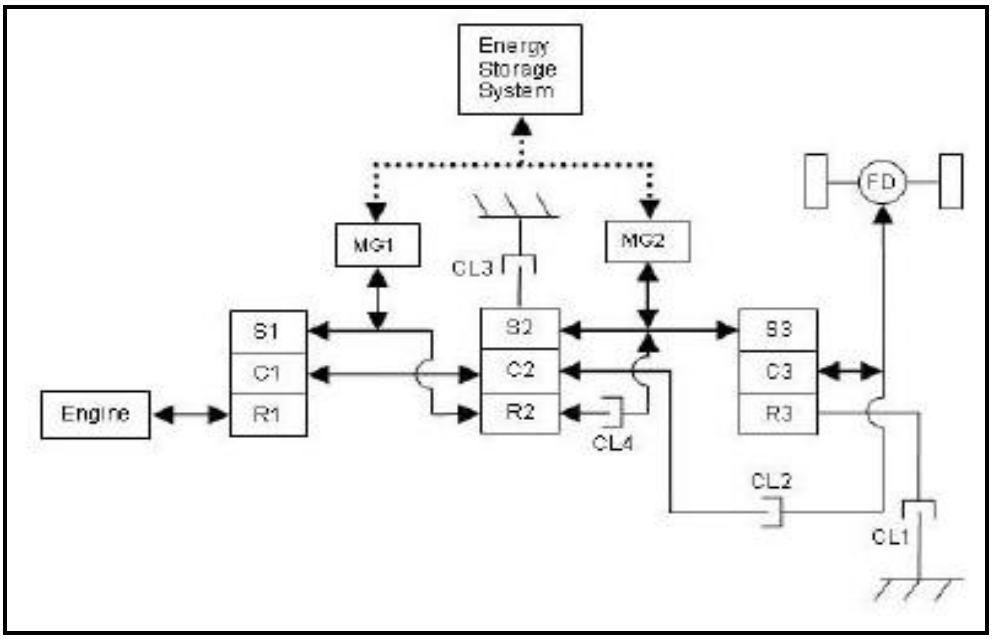

Figure 2.7: GM's Two-Mode Compound-Split Hybrid Design [47]

Table 2.4 shows the two operation modes for this architecture. CL1 is engaged to operate the vehicle in Mode 1. Mode 1 has three speeds. The stationary speed is for start-up conditions where MG1 is off. Slow speeds see MG1 acts as a generator and for faster speeds, MG1 acts as a motor. MG2 operates as a motor for Mode 1, where speeds ranging from 0 to about 113 kmh^{-1}. To make a transition from Mode 1 to Mode 2, CL2 is engaged and CL1 is disengaged. This state is for speeds ranging from 113 kmh^{-1} to about 142 kmh^{-1}. As the speed increases, MG1 and MG2 acts as motors and for fast speeds, MG2 acts as a generator.

MODE	MG1	MG2	CL1	CL2	CL3	CL4
Mode 1						
Stationary	OFF	Motor	ON	OFF	OFF	OFF
Slow	Generator	Motor	ON	OFF	OFF	OFF
Fast	Motor	Motor	ON	OFF	OFF	OFF
Mode 2						
Transition	Generator	Motor	OFF	ON	OFF	OFF
Slow	Motor	Motor	OFF	ON	OFF	OFF
Fast	Motor	Generator	OFF	ON	OFF	OFF

Table 2.4: Operating Modes and Conditions for GM's Two-Mode Compound-Split Hybrid Design

2.3.2 University of Michigan-Dearborn Design

Researchers at the University of Michigan-Dearborn introduced a novel multi-state hybrid drivetrain design, where further reading can be made from the following reference [52]. This design is originally called a multi-mode design, but the term multi-state was used to clear up confusions between this paper and the patents.

Figure 2.8 shows the University of Michigan-Dearborn design, where S, C and R represents the sun, carrier and ring gears respectively. From the figure, the design has three pair of clutches, one planetary gear train (PGT) and a lock for safety. It can be seen that the power from the ICE is split between the direct gear path and the PGT and then recombined at the gear input and this mini loop makes the PGT redundant in this case. This design is not efficient due of the inertias of the extraneous PGT [47].

This design was based on the concept of automated manual transmissions. The carrier of the planetary gear train (PGT) is connected with the engine shaft that picks up the ICE torque. The sun is connected with the motor shaft. One motor is used either as the driving assisting unit or as the generator in charging and energy recovery operations. State switching and gear shifting are done by actuating the clutches *via* computer-controlled step motors. This design is similar to an automated manual transmission. The operation states are described in Table 2.5 [52].

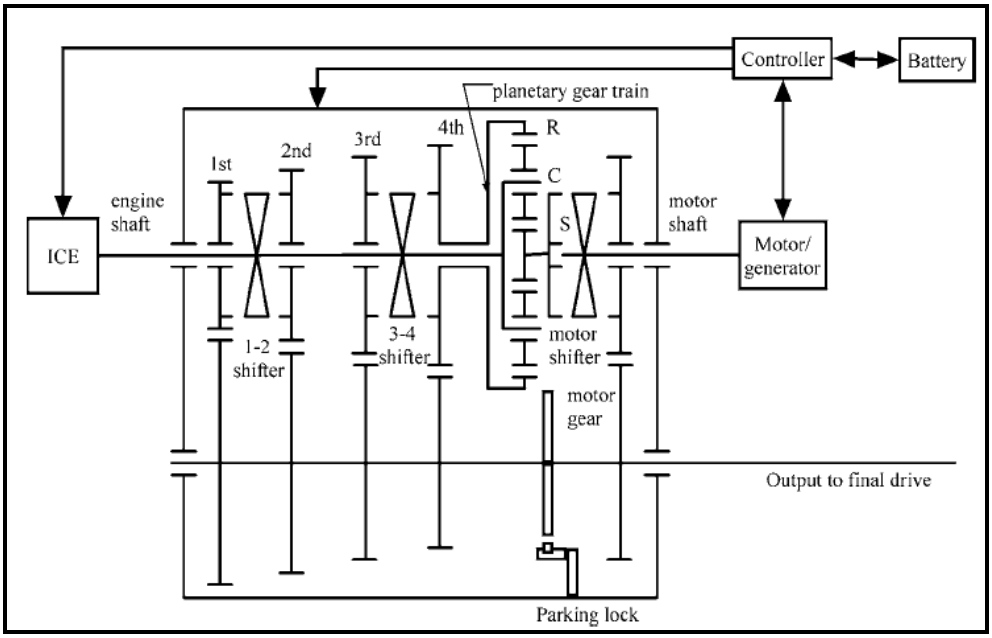

Figure 2.8: University of Michigan-Dearborn Hybrid Drivetrain Design [52]

STATE	MG	CL1	CL2	CL3
Motor Alone State	Motor	OFF	OFF	ON
Combined Power State	Motor	ON	OFF	OFF
Engine Alone State	OFF	ON	OFF	OFF
Electric CVT State	Generator	ON	OFF	ON
Energy Recovery State	Generator	ON	OFF	ON
Stand Still State	Generator	OFF	OFF	ON

Table 2.5: Operation Modes and Conditions for University of Michigan-Dearborn Design

Note that CL1, CL2 and CL3 represent the 1-2 shifter, 3-4 shifter and the motor shifter respectively. The highlighted columns are interchangeable i.e. CL1 and CL2 and be interchanged based on the gear number and vehicle speed.

2.3.3 Renault Design

The Renault design shown in Figure 2.9 below differs from GM's Design A as dog clutches were used instead. Dog clutches are a type of brake and its labeled B1 and B2 in the figure. Four PGTs were present, where the ICE is connected to the first carrier, MG2 connected to the fourth sun and MG1 connected to the second sun and third ring gears. The driveshaft is connected to the first ring and second carrier gears. B1 can lock the third carrier whereas B2

is able to lock the fourth ring and third sun gears. A summary of the operating modes are shown in Table 2.6.

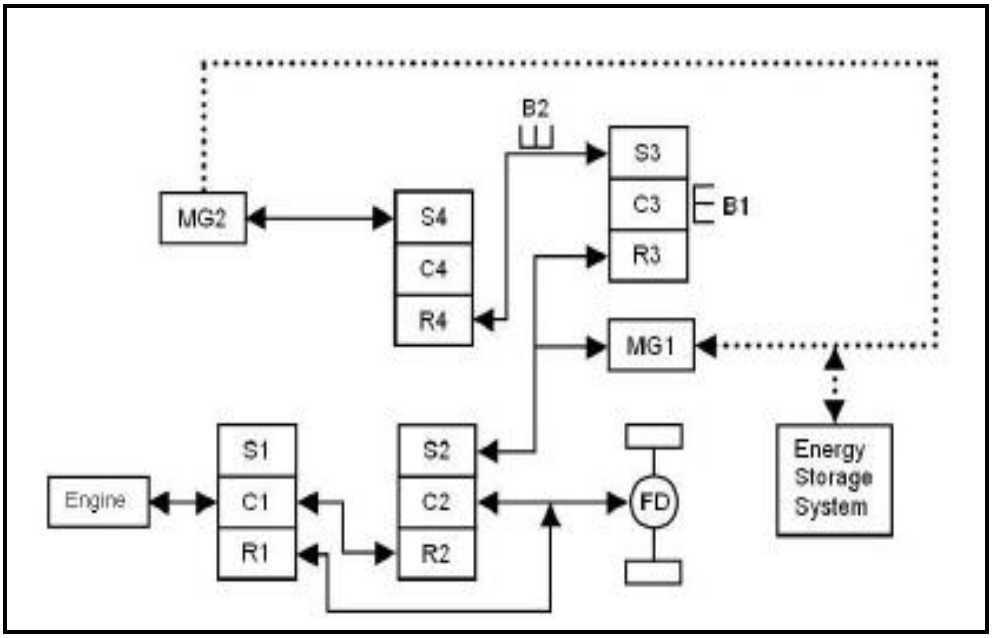

Figure 2.9: Renault Drivetrain Design [47]

MODE	MG1	MG2	B1	B2
Forward Mode				
Parallel Mode 1, Slow	Motor	Generator	ON	OFF
Parallel Mode 1, Fast	Generator	Motor	ON	OFF
Parallel Mode 2	Motor	Generator	OFF	ON

Table 2.6: Renault Design Modes

Initially, for low speeds, Mode 1 is activated. MG1 acts as a motor and MG2 acts as a generator. B1 is activated while B2 rotates freely. As the speed increases, MG1 and MG2 now act as a generator and motor respectively. The transition to Mode 2 occurs when the speeds of both MG1 and MG2 is zero. B1 was then deactivated and B2 is engaged. MG1 and MG2 acts as motor and generator respectively.

This architecture has a capability to operate in full electrical and ICE mode as well and could be implemented. However, this feature was not mentioned in reference [53].

2.3.4 Silvatech Design

This design was designed by Dyck et al. [54] and the patent was assigned to Silvatech Global Systems Ltd.. The U.S. patent number is 7,008,342. Figure 2.10 below shows the architecture of the hybrid drivetrain design containing five CLs, two MGs and a PGT. The ICE is connected directly to the sun gear and *via* CL1 and CL3 to MG1. MG1 and MG2 are connected together *via* CL4. The final drive is connected *via* CL5 to the ring gear. The energy storage system in this design consists of a capacitor bank and battery.

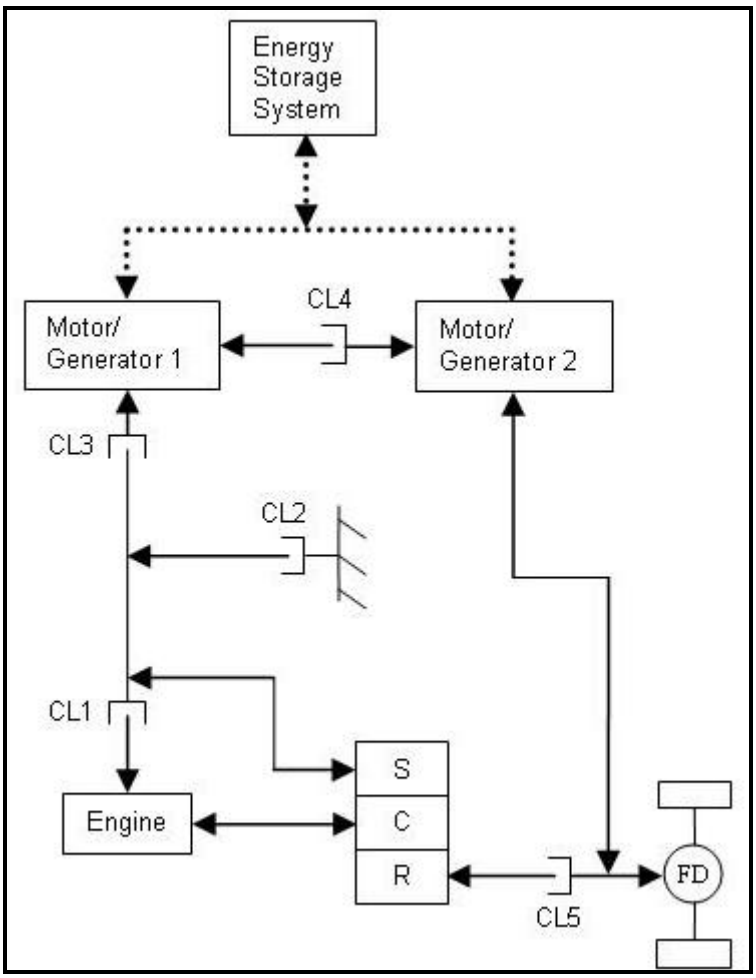

Figure 2.10: Silvatech Drivetrain Design [47]

Table 2.7 below shows the operation of the MGs and CLs over four modes: Forward, Reverse, Braking and Starting. The forward mode has five states: full and economy electrical (motor only state), full electrical + engine (hybrid state), parallel (ICE charge state – where the ICE is operating the vehicle whilst recharging the energy storage system) and full mechanical (ICE only).

For the reverse mode, three states are available: full and economy electrical (motor only) and parallel (hybrid). Note that the highlighted box was used to show that the MGs are operating in a reverse direction. The full electrical state is for reverse operations where high torque demand is required and the economy state is for reverse operations with low power demands.

For the braking mode, there are four different states: maximum regeneration, light regeneration, parallel and full engine. During maximum regeneration, the ICE is shut off and both MG1 and MG2 acts as a generator to recharge the energy storage system (provided the SC is not full). This state is suitable for sudden stop conditions (emergency braking, etc.). Light regeneration state is suitable for stop and go conditions (i.e. during traffic jams, etc.). Parallel and full engine states happened when the SC is fully charged. The parallel state is more suitable for light braking conditions (downhill on steep grades) and full engine state is suitable when maximum braking is required, similar to conventional engine braking.

The last mode is the starting mode where there are two states: stopped and output in motion. The stopped state is where startups required when the vehicle is in stationary and the output in motion state is where the vehicle is motion (during forward then reverse operations).

MODE	MG1	MG2	CL1	CL2	CL3	CL4	CL5
Forward Mode							
Forward Full Electrical State	Motor	Motor	OFF	OFF	OFF	ON	OFF
Forward Full Electrical+Engine State	Motor	Motor	ON	OFF	OFF	ON	ON
Forward Economy State	OFF	Motor	OFF	OFF	OFF	OFF	OFF
Forward Parallel State	Generator	Motor	ON	OFF	ON	OFF	OFF
Forward Full Mechanical State	OFF	OFF	OFF	ON	ON	OFF	ON
Reverse Mode							
Reverse Full Electrical State	Generator	Motor	OFF	OFF	OFF	ON	OFF
Reverse Economy State	OFF	Motor	OFF	OFF	OFF	OFF	OFF
Reverse Parallel State	Generator	Motor	ON	OFF	ON	OFF	OFF
Braking Mode							
Braking--Maximum Regeneration	Motor	Generator	OFF	OFF	ON	ON	OFF

Braking--Light Regeneration	Motor	Generator	OFF	OFF	OFF	OFF	OFF
Braking--Parallel	Generator	Generator	ON	OFF	OFF	OFF	OFF
Braking--Full Engine	Generator	Generator	ON	OFF	ON	OFF	OFF
Starting Mode							
Starting--Output Stopped	Motor	OFF	OFF	OFF	ON	OFF	ON
Starting--Output in Motion	Motor	OFF	OFF	OFF	ON	OFF	ON

Table 2.7: Silvatech Design Modes

2.3.5 Timken Design

This design was designed by Ai and Mohr and was assigned to the Timken Company with U.S. patent number 6,595,884 in 2000 [55-56]. The schematic of the design is shown in Figure 2.11. Two PGTs, MGs and CLs are present, with an additional of two brakes (labeled as B). The ICE is connected directly to the first ring gear. MG1 is connected to the first sun gear *via* brake and clutch B2 and CL2 to the second ring gear. MG2 is directly connected to the second sun gear. The second carrier is connected directly to the output shaft and the first carrier is connected to the output shaft *via* brake and clutch B1 and C1 respectively.

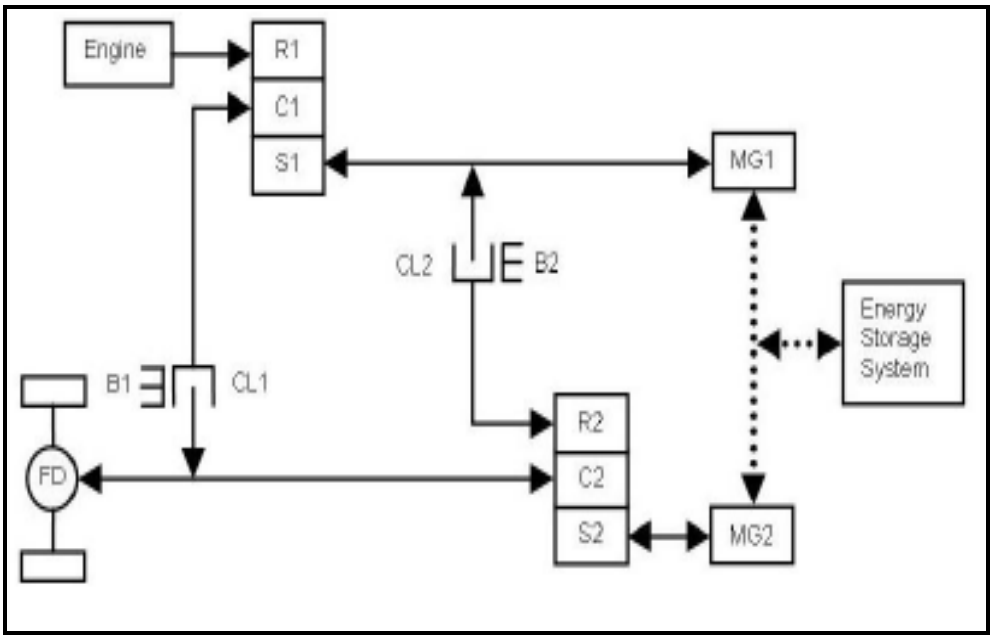

Figure 2.11: Timken Drivetrain Design [47]

MODE	MG1	MG2	CL1	CL2	B1	B2
Forward Mode						
Forward Full Electrical Mode, low power	OFF	Motor	OFF	OFF	OFF	ON
Forward Full Electrical Mode, high power	Motor	Motor	OFF	ON	ON	OFF
Forward Parallel Mode 1	Generator	Motor	ON	OFF	OFF	ON
Forward Parallel Mode 2, slow	Motor	Generator	OFF	OFF	OFF	OFF
Forward Parallel Mode 2, fast	Generator	Motor	OFF	OFF	OFF	OFF
Reverse Mode						
Reverse Full Electrical Mode	Generator	Motor	OFF	OFF	ON	ON
Reverse Parallel Mode	Generator	Motor	ON	OFF	OFF	ON
Stationary Mode						
Parking (ICE off)	OFF	OFF	ON	ON	ON	ON
Parking (ICE on)	Generator	Generator	ON	OFF	ON	OFF
Neutral	OFF	OFF	OFF	OFF	OFF	OFF
Starting Mode						
Starting--Output Stopped	OFF	Motor	ON	ON	OFF	ON
Starting--Output in Motion	Motor	OFF	OFF	OFF	ON	OFF

Table 2.8: Timken Design Modes

Table 2.8 shows the Timken Design Modes. For the Forward Mode, there are five different operations. There is Forward Full Electrical Mode (high and low power) and three Forward Parallel Modes. The high power Forward Full electrical Mode can only occur if the speed is not too large, since at high speeds of the first sun gear and carrier, the ring gear (and ICE) will begin to rotate. The Forward Parallel Modes allow for two node points, one in the low mode and one in high mode.

Besides the Forward mode, there also exist the Reverse, Stationary and Starting Modes. Table 2.8 shows a full summary along with the operating conditions for the motor/generator units (MG), the clutches and brakes.

2.4 Hybrid Vehicle Modelling and Simulation

This section presents a review on the current researches found in the literature for hybrid vehicle technology, highlighting the current methodologies and simulation tools used.

2.4.1 Modelling and Simulation Tools

Choosing an appropriate computer-aided modelling and simulation software/tool is very important in the design and analysis phase, especially with HEVs. This is because HEVs can have a variety of possible configurations, hardware components, control methodologies and designs. This shows modelling and simulation-based analysis and research are crucial to the development of hybrid vehicle design since design validation by hardware measurement is impractical prior to the costly prototype building.

One of the most popular HEV simulation modelling packages is the ADvanced VehIcle SimulatOR (ADVISOR), developed by the National Renewable Energy Laboratory (NREL). ADVISOR is designed for rapid analysis of the performance and fuel economy of conventional and advanced, light and heavy-duty vehicle models as well as hybrid electric and fuel cell vehicle models. It tests the effect of parameter changes in vehicle components (such as motors, batteries, catalytic converters, climate control systems, and alternative fuels) and other modifications that might affect fuel economy, performance or emissions [57]. Various researches are done in the past on HEVs using the ADVISOR tool and results showed a high feasibility in the models developed [52, 58-61].

Another popular HEV simulation software is the Partnership for a New Generation of Vehicles (PNGV) System Analysis Toolkit (PSAT) which was developed by the Argonne National Laboratory (ANL). The PNGV System Analysis Toolkit (PSAT) allows users to choose the appropriate configuration, component sizes, and technology and to optimize the control strategy in simulation for a wide range of HEVs but one of the most important characteristics of PSAT is that it is a forward-looking model, meaning PSAT allows users to model reality with real commands, in contrast with ADVISOR [62]. Besides ADVISOR, various researches on HEVs were done using PSAT and demonstrated the power of this tool [63-66].

ADVISOR and PSAT both are written in the MATLAB-Simulink software environment, as a third-party commercialised component. The original MATLAB-Simulink platform is also a powerful tool especially for modelling and simulation purposes. MATLAB itself is a high-level language and has an interactive environment that enables the user to

perform computationally intensive tasks faster than with traditional programming languages such as C, C++ and Fortran [67]. Simulink, on the other hand, is an add-on to MATLAB. Simulink is an environment for multi-domain simulations and model-based designs for dynamic and embedded systems. It also provides an interactive graphical environment and a customizable set of block libraries where the user will be able to choose block components in the library with ease [68]. Several research were done using the Simulink platform, and modelling and simulation results showed the flexibility of Simulink in terms of power management and optimization modelling of HEVs [52, 69-70].

Other modelling software used for HEV modelling and simulation purposes are Power Electronics Simulator (PSIM), LabVIEW and V-Elph. The PSIM software was made to simulate power electronic converters and motor drives for HEV applications. Literatures showed that PSIM was capable to not only simulate the electrical systems but also the mechanical and thermal systems as well [71-72]. LabVIEW was used as a tool as well, although not popular. Literature showed that LabVIEW was able to successfully study the power flows in drivetrains and corresponding component losses as well as to compare different drivetrain topologies [73].

Lastly is a third part Simulink software developed by the Texas A&M University, called V-Elph. V-Elph is a system-level modelling, simulation and analysis package developed to study issues related to EV and HEV designs such as energy efficiency, fuel economy and vehicle emissions [74-75]. The flexibility of V-Elph was demonstrated in studying various issues relating to EVs and HEVs [76].

2.4.2 Energy Control Management

The energy, fuel economy and emissions management for HEVs are correlated as an increase in fuel economy subsequently reduces emissions. Thus various researches were catered towards optimizing and minimizing the fuel economy. This was done by optimizing the energy control of the HEV system. In general, the energy control management strategies for HEVs in the existing literature can be classified into three broad categories; using AI methodologies, dynamic programming strategy and using optimal control theory.

The first type employs heuristic artificial intelligence (AI) control techniques such as control rules/fuzzy logic, artificial neural networks (ANN) and the neuro-fuzzy approach (ANFIS) for control algorithm development. Fuzzy logic control is a popular strategy in determining power-splits between the ICE and the traction motor of the HEV, by developing

a set of fuzzy rules governing the operation [77-81]. The ICE was optimized to operate at its optimum region and the load-levelling device (battery, ultracapacitors, etc.) to provide the remaining demanded torque or power. The fuzzy controller is optimized and several results especially in fuel economy and charge sustenance were achieved. ANNs were also discussed in the literature and this approach requires large experimental data sets for training, validation and testing of the ANN model. In the literature, the ANN approach is normally used to predict tailpipe emissions of the HEVs over a specific driving cycle [59, 82]. However, driving pattern recognition using ANN predictions were used to optimize the HEV as well [83]. Another literature presents a HEV equipped with ultracapacitors as an energy storage component. ANNs were then used to determine the ideal current the ultracapacitors must deliver to the HEV during the driving process [84]. Besides fuzzy logic and ANN, ANFIS was used as a control methodology as well but only one research was found in the literature, in terms of HEV energy control [85].

Another approach in power and energy management control for HEVs is the use of the dynamic programming approach. The dynamic programming method calculates the optimal control signals over a given fixed driving cycle [86-89]. This method is proven, in the literature, to properly optimize the fuel management and charge sustenance of the HEV. However, future information about the driving trip has to be provided (i.e. driving cycle, GPS signals, etc.) for proper control and optimization [90-91]. Issues faced by using this method are the huge amount of computer time required to obtain solutions and the need of future information where it is not feasible in real-time control.

To avoid the drawback faced by the dynamic programming method, the optimal control strategy was proposed by Delprat et al. [92] based on an existing optimal control theory proposed by Lewis and Syrmos [93] in the literature. The proposed control algorithm presented by [92] contributed in powertrain designs (for evaluating powertrain efficiencies) and the evaluation of real-time control strategies (for evaluating fuel consumptions and emissions). Optimal control strategies discussed in the literature were mostly designed around finding a global optimal solution to minimize the fuel consumption for HEVs [94-95].

2.4.3 Emissions Prediction Techniques

Most predictive modelling and simulation work proposed in the literature regarding emissions are normally catered for conventional vehicles; ICEs and diesel vehicles. Artificial neural network seemed to be a major methodology in emission predictions for conventional

vehicles as several papers were found in the literature [96-99]. Results showed that artificial neural network is a feasible tool in emissions predictive modelling as prediction errors were all below 8 %.

Predictive modelling of tailpipe emissions for HEVs are rarely found in the literature with the exception of papers published by Toth-Nagy et al. [59], Ao et al. [100] and Gray and Hentea [101]. Toth-Nagy et al. presented an artificial neural network model to predict emissions from heavy-duty trucks. Results showed accurate predictions for CO and NO as the truck duty (sizes) increase [59]. Ao et al. presents a HEV model with a dynamic-programming-based supervisory (DPBS) controller to properly predict and estimate the fuel economy and emissions [100]. Potential improvements were highlighted as the trade-offs were made between fuel consumption and NOx emissions using the DPBS controller. Gray and Hentea also published a paper to predict emissions by presenting 3 models; static engine maps, dynamic multiple regression linear model and time delay dynamic neural network model. In similar operating conditions the neural network model outperformed both the linear dynamical model and the static map in predicting CO, CO_2, NOx and HC emissions [101].

2.5 Summary

This chapter provided a comprehensive overview about HEVs and some of its commercialized drivetrain architectures and its respective control strategies. The architectures mentioned did not take into account the effects of fuel economy in transient ICE operations. The control strategy adopted for the dynamic modelling approach in emissions prediction in this research is the University of Michigan-Dearborn's strategy. This control strategy was incorporated into a Toyota Prius MATLAB model and was published scientifically in the literature. Other architectures were not widely published and most of them just remained as patented documents. Besides that, all the discussed drivetrain architectures do not investigate the tailpipe emissions, with focus only on power and energy management of the hybrid vehicle.

In addition, various methodologies used in the literature regarding HEV modelling were also explored. This survey includes past and current studies in energy management of HEVs as well as emission prediction techniques and modelling tools used. As discussed in Section 2.4, previous researches done in the field of emissions predictive modelling for HESs are minimal compared to HEVs. There are only a handful of published papers on emissions

predictive modelling but they are for HEVs instead of HESs. Thus emissions predictive modelling technology for HESs are still in its infancy stage.

Next chapter presents a review of artificial neural networks (ANN), the methodology used to construct the EPM, for emissions predictive modelling. Essential knowledge about ANN and its networks employed throughout the course of this research will be investigated.

CHAPTER 3: DEVELOPED ARTIFICIAL NEURAL NETWORK

3.1 Introduction to Artificial Neural Network

The exact mechanism on how the human brain actually works and performs is still a mystery. The human brain consists of approximately 10 billion information-processing units, called neurons, and 60 trillion connections between them [102]. An artificial neural network (ANN) is a type of artificial intelligence which attempts to mimic how the human brain works.

An ANN is an information processing paradigm that is inspired by the way biological nervous systems, such as the brain, learn and process information. The structure is composed of a large number of highly interconnected neurons working in unison to solve specific problems. An ANN is normally configured to cater for a specific application, such as pattern recognition or data classification, through a learning process. Learning in biological systems involves adjustments to the synaptic connections that exist between the neurons. This also holds true for ANNs as well.

A neuron consists of a cell body, called soma, a number of fibres called dendrites and a long single fibre called the axon. Figure 3.1 shows a schematic drawing of a biological neural system.

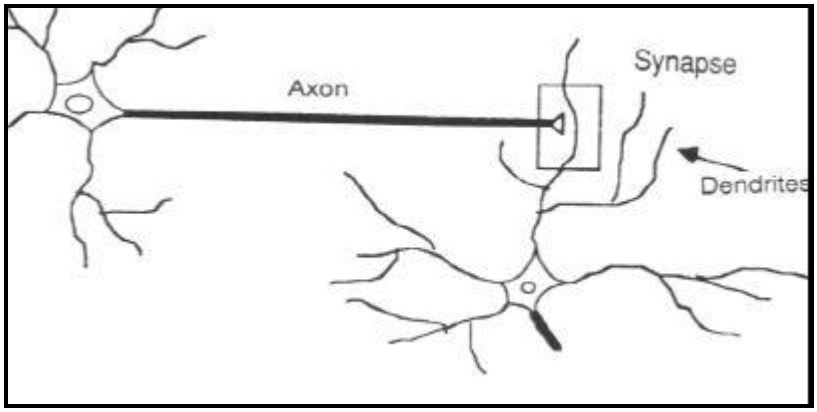

Figure 3.1: Biological Neural System

Signals are propagated between neurons by complex electrochemical reactions. Chemical substances are released from the synapses causing a change in electric potential. When the potential reaches a threshold, an electrical pulse is sent down through the axon

which then later reaches synapses and causes them to increase or decrease their potential [103]. Many synapses exhibit plasticity behaviour, that is, they can increase or decrease their strength and power under proper conditions [104-105]. Thus their weights vary. Each neuron can have up to 10^4 synapses [105].

Learning is one of the main features of the human brain. This is done by changing the synaptic weights of the synapses. Donald O. Hebb, the father in neurology, was one of the first people to postulate the learning mechanism of the human brain. Hebb postulated that when an axon of cell A is near enough to excite cell B or repeatedly takes part in firing it, some growth process and metabolic changes would occur in one or both cells [106]. These changes, in this case, would increase cell A's efficiency.

3.1.1 Artificial Neuron

An ANN consists of a number of simple and interconnected processors called neurons. This term is analogous to the biological neuron of the human brain. A neuron receives signals from its input links, computes a new activation level and sends the signal to its output links. This output signal could either be another input to another neuron or could be the final solution of the network. Figure 3.2 shows a representation of an artificial neuron structure.

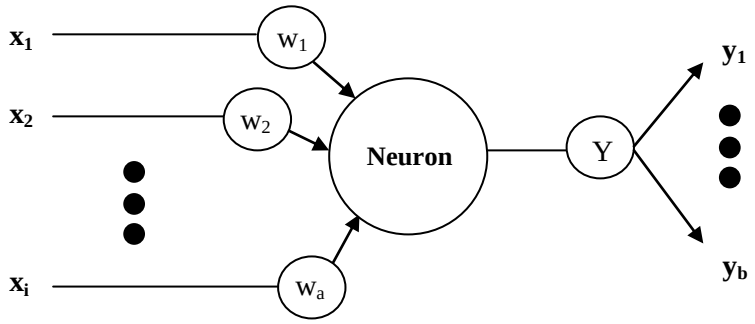

Figure 3.2: Artificial Neuron Structure

where $x_{1,\ldots,i}$ are the inputs to the networks, $w_{1,\ldots,a}$ are the weights and $y_{1,\ldots,b}$ are the neuron's outputs.

The neuron computes the weighted sum of the input signals and compared to a threshold value. A sign activation function is used in this case. If the net input is less than the threshold, the neuron's corresponding output is -1. If it is greater than the threshold value, the neuron becomes activated and the output is then +1 [107]. Thus, the neuron uses the following functions:

$$X = \sum_{i=1}^{I} x_i w_i \qquad \textbf{(3.1)}$$

$$Y = \begin{cases} +1 & if \;\; X \geq 0 \\ -1 & if \;\; X < 0 \end{cases} \qquad \textbf{(3.2)}$$

where X is the net weighted input, x_i is the input value, w_i is the weight associated with input x_i, I is the number of neuron inputs and Y is the neuron output.

Other activation functions such as log, sine, sigmoid or linear functions were commonly used as well, as depicted in Figure 3.3.

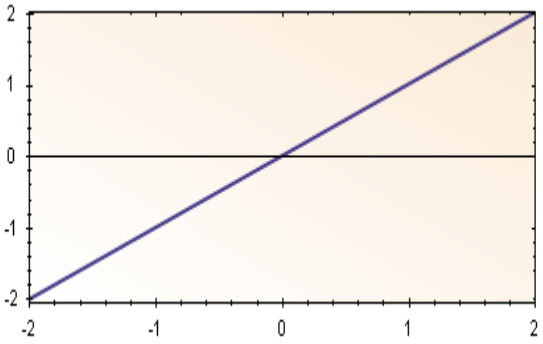

Linear Function

$y = x$

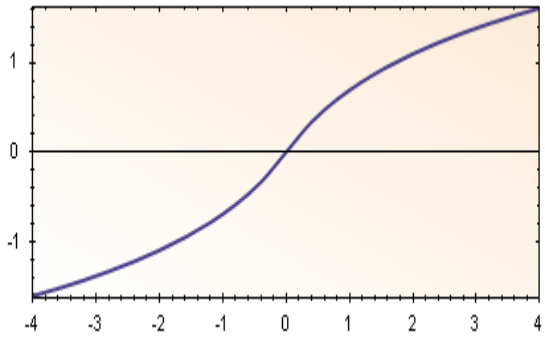

Log Function

$y = \log(1 + |x|)$

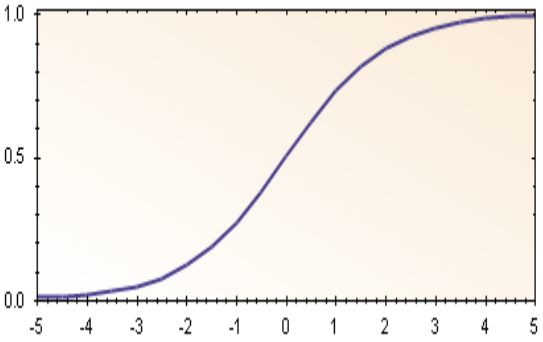

Sigmoid Function

$$y = \frac{1}{1 + e^{-x}}$$

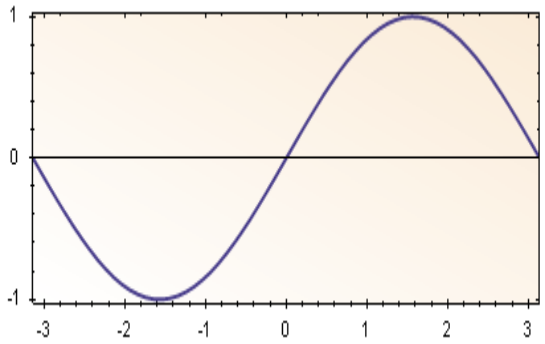

Sine Function

$y = \sin(x)$

Figure 3.3: Activation Functions

3.2 Neural Network Structures

3.2.1 Feed-forward Network

A feed-forward neural network is an artificial neural network where connections between the units do not form a directed cycle. Figure 3.4 below shows a feed-forward network structure with one input, hidden and output layer.

The feed-forward neural network was the first and arguably simplest type of artificial neural network devised. In this network, the information moves in only one direction, forward, from the input nodes (Layer 1) , through the hidden nodes (Layer 2) and to the output nodes (Layer 3). There are no cycles or loops in the network.

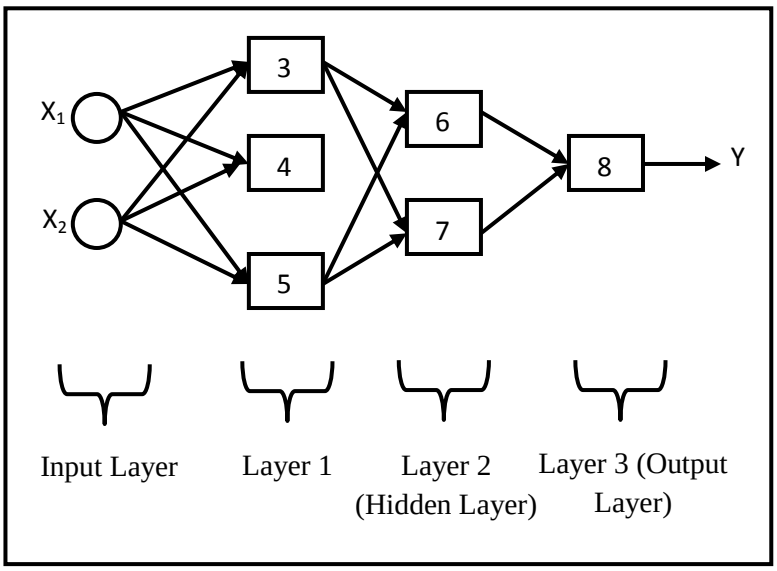

Figure 3.4: Feed-forward Neural Network

Examples of feed-forward networks include the back-propagation network [108], learning vector quantization (LVQ) [109], cerebella model articulation control (CMAC) [110] and the group-method of data handling (GMDH) network [111]. Feed-forward networks have the ability to perform static mapping; the output at any given instance is the function of the input at that instance.

3.2.2 Recurrent Network

Unlike the feed-forward network, the recurrent neural network has a feedback loop, as depicted in Figure 3.5 below. Recurrent neural networks are networks that feed the outputs

from neurons to other adjacent neurons, to themselves, or to neurons on preceding network layers. Thus signals are able to flow bidirectional.

For recurrent networks, after an input was applied, the network output is calculated and fed back to adjust the input. This process will then be repeated until the output becomes constant (or the network converges).

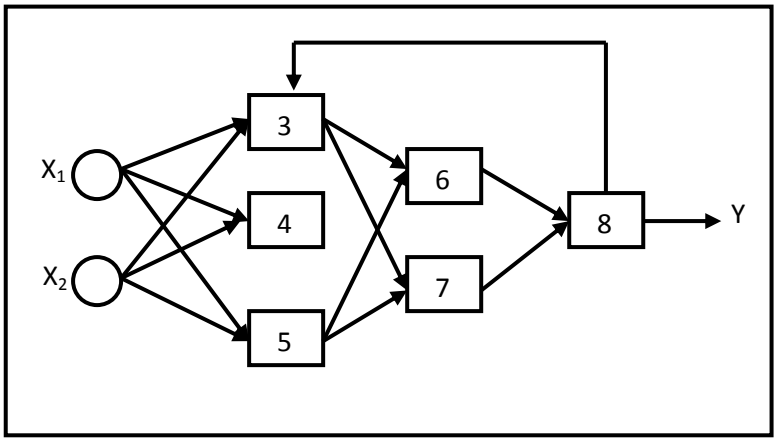

Figure 3.5: Recurrent Neural Network

Examples of recurrent networks include the Hopfield [112], Elman [113] and Jordan [114] networks. Recurrent networks have a dynamic memory; their outputs at any given instance reflect the current input as well as the previous inputs and outputs.

3.3 Normalization of Dataset

Normalization of the dataset is an extremely important step in artificial neural networks. The normalization process will convert the input and output values to the same order of magnitude. This step is critical because if the variables have a different order of magnitude, their respective influences to the predicted output might vary.

One common way to normalize the dataset is to convert the values within the range from 0 to 1 using the following Equation 3.3 below:

$$R_N = \frac{R_A - R_{\min}}{R_{\max} - R_{\min}} \qquad \textbf{(3.3)}$$

where R_A is the actual value, R_{min} is the minimum value of R, R_{max} is the maximum value of R and R_N is the normalized value of R which will be within the range from 0 to 1.

3.4 Neural Network Learning

Neural network learning consists of two algorithms; supervised and unsupervised learning. A supervised learning algorithm adjusts the strengths or weights of the inter-neuron connections according to the difference between the desired and actual network outputs. Thus, a supervised learning requires a teacher or an external supervisor to provide desired or target output signals.

Examples of supervised learning networks include the Widrow and Hoff (delta rule) [115], back-propagation algorithm [108], optimization layer-by-layer (OLL) network [116] and the LVQ network [109].

An unsupervised learning algorithm does not require any teacher or external supervisor for the network to learn. During training, the input patterns are presented to the network. The neural network automatically adapts the weights of its connections to cluster the input pattern into group with similar or same features.

Examples of unsupervised learning networks include the Kohonen network [109], and the Carpenter-Grossberg Adaptive Resonance Theory [117].

3.5 Neural Network Models

3.5.1 Back-propagation Neural Network

A Back-propagation Neural Network is a multi-layered feed-forward network. It is trained with a supervised training method called the error back-propagation procedure.

Figure 3.6 shows a back-propagation neural network model with 1 hidden layer with a neurons and output layer with b outputs. Note that for the entire thesis, the connection weights are depicted as w with the first index is the target neuron and the second index is the source neuron. The neurons in the layers perform 3 functions: input, activation and output function.

The input function is given by the sum of products of the inputs and their corresponding connection weights. The equation below shows the relationship:

$$X = \sum_{a=1}^{A} x_i w_{ai} \qquad \textbf{(3.4)}$$

where X is the net weighted input, x_i is input i to neuron a and w_{ai} is the connection weight from neuron i to a.

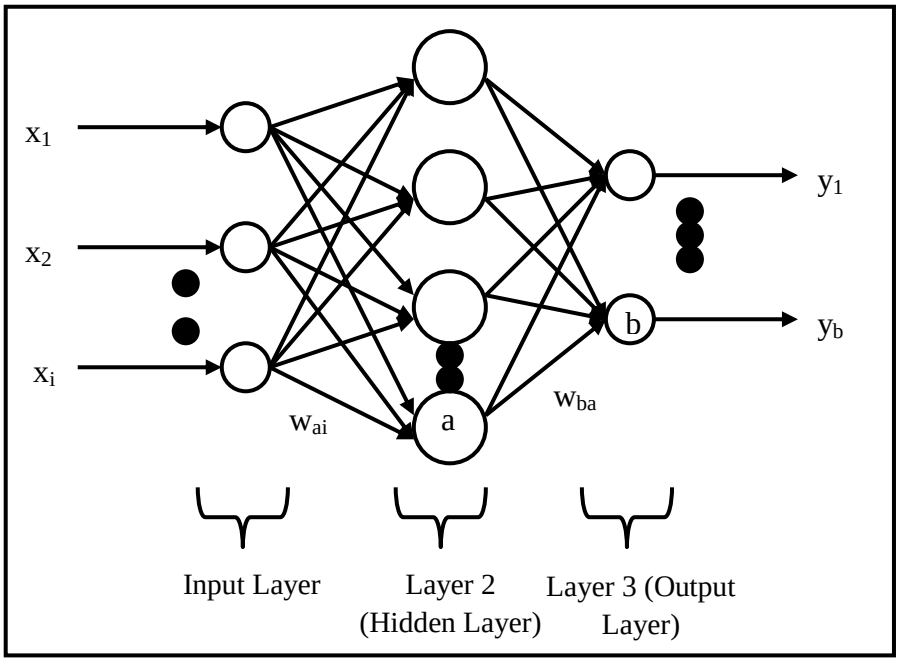

Figure 3.6: Back-propagation Neural Network Model with 1 Hidden Layer

The second function is the activation function. The typical activation function used is a sigmoid function:

$$X_A = \frac{1}{1+e^{-X}} \qquad \textbf{(3.5)}$$

The derivative of this function can be easily computed as well and guarantees that the output of the neuron is bounded within the range of 0 to 1.

Lastly is the output function. The output function simply passes the information to the connected neuron at the adjacent layer, depending on the direction. Typically, information and error signals propagate at opposite directions.

The error back-propagation training normally uses a gradient descent method [103]. In this training procedure, the error signals are calculated in the output layer working back to the hidden layer.

For errors in the output layer, the error value β_b is given by Equation 3.6 below:

$$\beta_b = X_A' \times (t_b - y_b) \quad \textbf{(3.6)}$$

where t_b is the target output of neuron b, y_b is the actual output of neuron b and X_A' is the derivative of the activation function X_A.

Moving back to the hidden layer, the error in the hidden layer can be calculated using Equation 3.7 below:

$$\beta_a = X_A' \times \sum_{b=1}^{B} \beta_b w_{ba} \quad \textbf{(3.7)}$$

where β_b is the error value in the hidden layer and w_{ba} is the connection weight between the output and the hidden layer.

Each interconnection weight is adjusted by considering the error term of the neuron that receives input from the connection. The adjustment is shown mathematically below [118]:

$$\Delta w_{ba} = \eta \beta_a x_i \quad \textbf{(3.8)}$$

where η is the learning rate constant ranging from 0 to 1. η is sometimes varied during training as a low η will slow the training process and a high η will cause instability during the training process. Starting with high values of η and gradually decreasing it during training might produce better performance [118].

Thus, a momentum constant is introduced to accelerate the training. The momentum constant is incorporated into Equation 3.7 and is shown below:

$$\Delta w_{ba}^{\ n} = \eta \beta_a x_i + \alpha \Delta w_{ba}^{\ n-1} \quad \textbf{(3.9)}$$

where $\Delta_{ba}^{\ n}$ and $\Delta_{ba}^{\ n-1}$ are weight corrections at the n^{th} and n^{th}-1 iterations respectively and α is the momentum constant. Typical values of α is set to 0.95 [103]. According to the literature, the inclusion of the momentum constant has a stabilizing effect on the training process [119-120]. From Equation 3.9, a portion of the weight adjustment ($\alpha\ \Delta_{ba}^{\ n-1}$) is not applied until the next iteration. This dampened the weight changes and thus better convergence is achieved.

To evaluate the success of the training process, the root mean square (RMS) error formula was used. The RMS error formula is commonly used as a measure of accuracy and it is shown below [118]:

$$\% \; RMS \; error = \frac{\sum_{p=1}^{P}\sum_{k=1}^{K}(t_{kp} - y_{kp})^2}{PK} \times 100\% \qquad \textbf{(3.10)}$$

where P is the number of training data, K is the number of output neurons, t_{kp} is the target output for neuron k after presentation of training data p and y_{kp} is the output value produced after presentation of training data p. Generally a % RMS error below 10 % for the system is considered acceptable.

Summarizing, the general algorithm for the back-propagation neural network is shown below:

1. Initialization. Connection weights are assigned to random numbers uniformly distributed over a small range.
2. Activation. The outputs are computed (Equation 3.4 and 3.5) and error values were calculated.
3. Weight Training. Weights are adjusted using Equation 3.8 and 3.9.
4. Compute Steps 1 – 3 with all input-output data. The training % RMS error was then calculated using Equation 3.10.
5. If error is in the desired range (< 10%), the training process was then terminated. If not, variables such as momentum and learning rate are then adjusted and repeat Steps 1 – 4.

3.5.2 Kohonen Neural Network

The Kohonen network is a self-organizing map (SOM). SOMs are types of artificial neural network that is trained using unsupervised learning to transform an incoming signal pattern of arbitrary dimension into a one or two-dimensional discrete map [109, 121].

Figure 3.7 above shows a basic structure of a Kohonen network. Unlike the back-propagation network, the Kohonen network has two layers, the input and output layer. Input layer has i neurons and the output layer has a neurons.

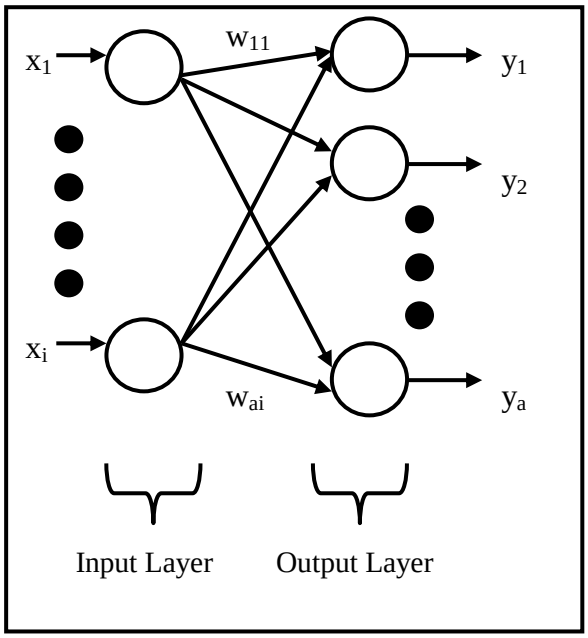

Figure 3.7: Basic Kohonen Neural Network Model

In a Kohonen network, neurons learn by shifting their respective weights from inactive connections to active ones. If at some particular point a neuron does not respond to a given input pattern, the learning cannot occur for that neuron. The weights associated with the neurons are updates and going through a specific number of iterations, the network weights will converge to a specific weight matrix.

The standard competitive learning rule defines the weight change, Δw_{ai}, applied to synaptic weight w_{ai} as

$$\Delta w_{ai} = \begin{cases} \eta(x_i - w_{ai}) & \text{if neuron } k \text{ wins} \\ 0 & \text{if neuron } k \text{ loses} \end{cases} \qquad \textbf{(3.11)}$$

where x_i is the input signal and η is the learning parameter.

The overall effect of competitive learning rule is to move the synaptic weight w_{ai} of the winning neuron k towards the input X. The matching criterion is equivalent to the minimum Euclidean distance between the vectors. The Euclidean criterion is shown below:

$$k_X = \min_k \left\| X - W_a \right\| = \left(\sum_1^i (x_i - w_{ai})^2\right)^{0.5} \qquad \textbf{(3.12)}$$

for k = 1,..., A

where k_X is the winning neuron.

The winning neuron will have the lowest Euclidean distance between the competing neurons. The winning neuron's corresponding weights will then be updates and the wining neuron will become closer to input vector X after each iteration.

Summarizing, the general algorithm for the Kohonen neural network is shown below:

1. Initialization. Initial weights are set to small random values between the range from 0 – 1. The learning rate parameter is defined.
2. Learning. The synaptic weights are updated after each iteration (Equation 3.11). The weight corrections are determines by the competitive learning rule.
3. Iteration. Iteration is increased, repeat steps 1 – 2 and continue until the minimum-distance Euclidean criterion is satisfied (Equation 3.12).

The accuracy of the Kohonen network depends on the number of iterations as well as the selection of parameters such as the learning rate parameter and the neighborhood function.

3.5.3 Radial Basis Function Neural Network

Radial Basis Function (RBF) networks are a type of ANN for applications to problems with supervised learning. In principle, RBFs could be employed in any sort of model (linear or nonlinear) and any sort of network (single-layer or multi-layer). However, RBF networks have traditionally been associated with radial functions in a single-layer network shown below [122].

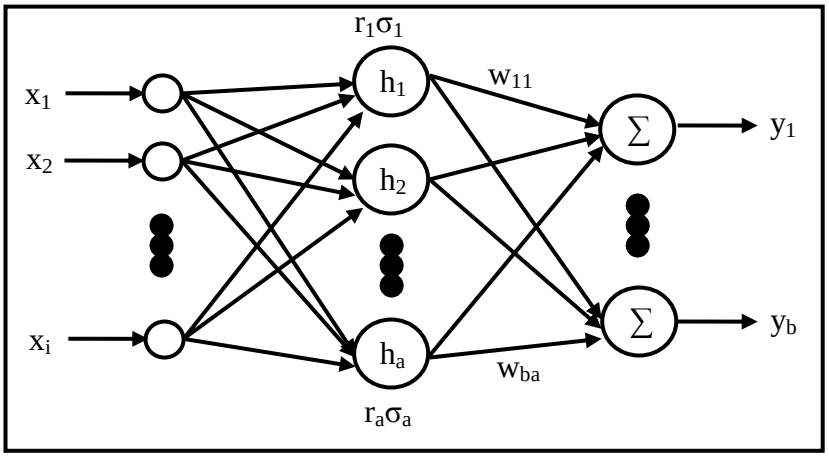

Figure 3.8: Basic Radial Basis Function Neural Network Model

The basic structure of a RBF network is shown in Figure 3.8. A Gaussian activation function is used and represented below:

$$h_a = \exp\left(-\frac{(x_i - r_a)^T (x_i - r_a)}{2\sigma_a^{\,2}} \right) \qquad \textbf{(3.13)}$$

where h_a is the output of the hidden neuron, r_a is the weight of the hidden layer, T is the matrix transpose operator, σ_a is the diameter of the receptive field. The Gaussian activation function is also shown in Figure 3.9 where u is the center of the function with width parameter σ_a.

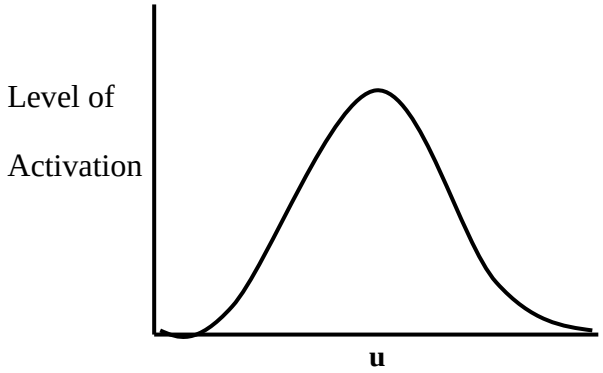

Figure 3.9: Gaussian Activation Function

Thus the output, y_b, can now be defined as:

$$y_b = \sum_{a=1}^{A} h_a w_{ba} \qquad \textbf{(3.14)}$$

The training of RBF networks generally consists of two steps. The first step includes finding the center u of the neuron and sigma (σ), which is the diameter of the receptive field. These two variables are very important during training. The second step is then applying the outputs to produce the network actual outputs.

Finding center u

Several popular methods were used to locate the center u. One of the most common methods is to divide the input vector, X, so some clusters and then locate the center of each cluster and

locate a hidden neuron at that point [123]. A Kohonen network is normally applied in this case. The Kohonen network clusters the training patterns to reduce the number of functioning centers. Because of this, this type of network is normally referred to as RBF networks incorporating Kohonen.

Finding diameter σ_a

The diameter sigma σ_a is an important variable that will have significant effect on the network. One of the most common approaches to find diameter σ_a is to cluster to data according to its similarities. That is, for each neuron in the hidden layer, the RMS distances between each neuron and its nearest neighbour will be calculated, representing the value σ_a [124].

Summarizing, the training algorithm for the RBF network incorporating Kohonen is shown below:

1. Initialization. The hidden-output layer weights are initialized at small random values. A suitable clustering technique (in this case, the Kohonen) is used.
2. Start the training cycle by exposing the input-output pairs to the network.
3. Using Equations 3.13 and 3.14, the network outputs are calculated.
4. The hidden-output layer weights are adjusted based on the error back-propagation procedure.
5. The RMS error (Equation 3.10) was then calculated. If the RMS error is within the desired range, the training process is then terminated. If not, repeat Steps 2-5.

3.5.4 Optimization Layer by Layer Neural Network

The Optimization Layer by Layer (OLL) neural network was proposed and developed by Ergezinger and Thomsen [116]. This method is based on the linearization of the activation function, thus leading to a linear optimization problem in each layer. The error made when linearizing the activation function is accounted for by introducing a penalty term. This penalty term, whose influence is varied, is to maintain optimum convergence for the network The OLL neural network is then optimized in an iterative procedure, where for each iteration, the corresponding weights are optimized by solving a set of linear equations. It was showed in the literature that the OLL neural network converge faster compared to the back-propagation algorithm [116]. This network also contained no parameters that can be interacted with by the user.

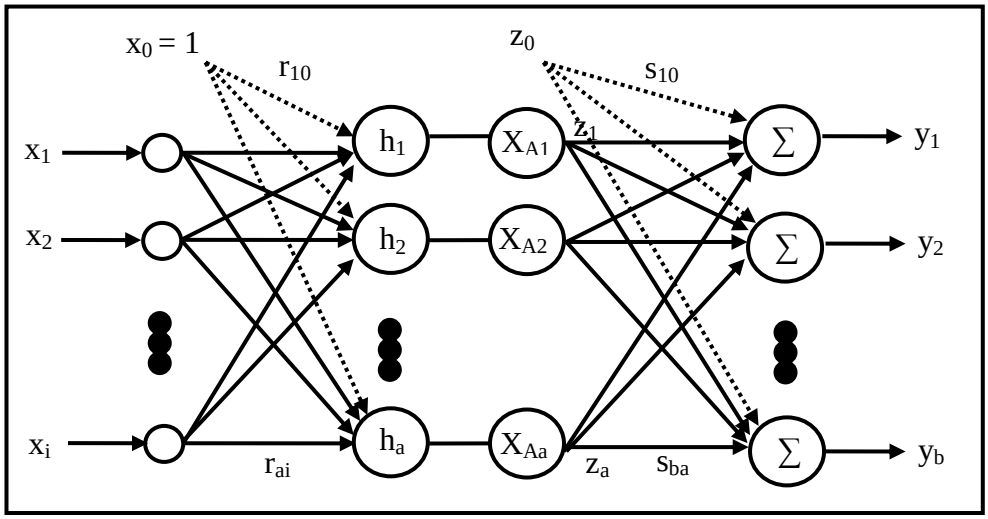

Figure 3.10: Optimization Layer by Layer Neural Network Model

Figure 3.10 above shows a basic OLL neural network structure. Inputs x_i are connected to the hidden layer with connect weights r_{ai} and the hidden neuron are connected to the output neurons with connection weights s_{ba}. The b neurons in the output layer have a pure linear activation function and hidden neurons have a sigmoid activation function:

$$X_A = \frac{1}{1+e^{-X}} \qquad \textbf{(3.15)}$$

Weight vectors R and S are to be optimized to minimize the error function. The mean squared prediction error is defined as:

$$E(R,S) = \frac{1}{p}\sum_{p=1}^{P}\frac{1}{2}(t^p - {y_b}^p)^2 \qquad \textbf{(3.16)}$$

where t^p is the target output, y_b^p is the network output, P is the number of training data, R and S are the weight vectors between the hidden-input and output-hidden layers respectively.

Optimization of the Output Layer

Adjustments of the weight matrices R and S is required for each layer. For the output layer, to adjust and find the optimum weight S for the output layer, Equation 3.16 is differentiated with respect to weight s to obtain the gradient:

$$\frac{dE}{ds} = 0 = \frac{1}{p}\sum_{p=1}^{P}(t^p - y_b{}^p)z^p \qquad \textbf{(3.17)}$$

where z^p is the scalar output of the hidden neuron of training data p. The output, y_b for training data p, is simply:

$$y_b{}^p = \sum_{a=1}^{A} s_{ba} z_b = S^T z^p \qquad \textbf{(3.18)}$$

where z^p is the scalar output of the hidden neuron for training data p.

Solving Equation 3.17 above generates the optimum weight for S for the output-hidden layer:

$$S^{optimum} = A^{-1} \bullet b \qquad \textbf{(3.19)}$$

where

$$A = \sum_{p=1}^{P} z_a{}^p z_j{}^p \quad a, j = 0,..., A$$

$$b = \sum_{p=1}^{P} z_a{}^p t^p \quad a = 0,..., A$$

Note that $S^{optimum}$ represents the optimal output layer weights for the current value R and R is the weight matrix of the output-hidden layer.

Optimization of the Hidden Layer

As mentioned previously, the layers are optimized independently of each other. Thus previously the network weights R are considered as constants as far as the optimization of weight S in the output layer is concerned.

Assuming the optimization of the hidden-input layer connections yield a weight change Δr_{ai}, the updated weight value can be computed as:

$$r_{ai} = r_{ai}{}^{old} + \Delta r_{ai} \quad a = 1,..., A \text{ and } i = 1,..., I \qquad \textbf{(3.20)}$$

To compute the effects of Δr_{ai} on the new network output y_b^{new}, the new outputs z_a^{new} of the non-linear activation functions have to be evaluated. By linearizing the sigmoidal activation function X_A, a linear correlation between Δr_{ai} and y_b^{new} can be achieved. This was done using the Taylor series expansion of X_a about the point h_a^{new}. The weight connections between the output-hidden layers are linearized:

$$S^{linearized} = X_{Aa}{}' s_j \qquad \textbf{(3.21)}$$

where $X_{Aa}{}'$ is the derivative of summation of weighted inputs to neuron h_a and s_j is the connection weights between neuron j and neuron in the output layer.

The change in network output can be written as:

$$\Delta y_b = \sum_{a=1}^{A}\left[S^{linearized} \times \sum_{i=0}^{I} \Delta r_{ai} x_i \right] \qquad \textbf{(3.22)}$$

Figure 3.11 below shows the resulted linearized network structure for the optimization of the hidden layer. Optimization of the hidden layer weight matrix is based on this structure. The modified error function for the hidden layer can be defined as [116]:

$$E^{hidden} = E^{linearized} + \mu E^{penalty} \qquad \textbf{(3.23)}$$

where

$$E^{linearized} = \frac{1}{p}\sum_{p=1}^{P}\frac{1}{2}\left(e_a{}^{old} - \Delta y_b\right)^2$$

$$E^{penalty} = \frac{1}{AB}\sum_{a=1}^{A}\sum_{b=1}^{B}\left|e_a s_{ba}\right|$$

where $E^{linearized}$ is the new cost function defined for the optimization of the linearized structure, $E^{penalty}$ is a penalty term introduced to estimate the quality of the linear approximation, μ is the weighting factor, e_a is the error, $e_a{}^{old}$ is the error of the original network and s_{ba} is the output weight. μ determines the influence of $E^{penalty}$ to $E^{linearized}$ and by multiplying $e_a s_{ba}$ in $E^{penalty}$, the influence of the linearization error on network output y_b is accounted for.

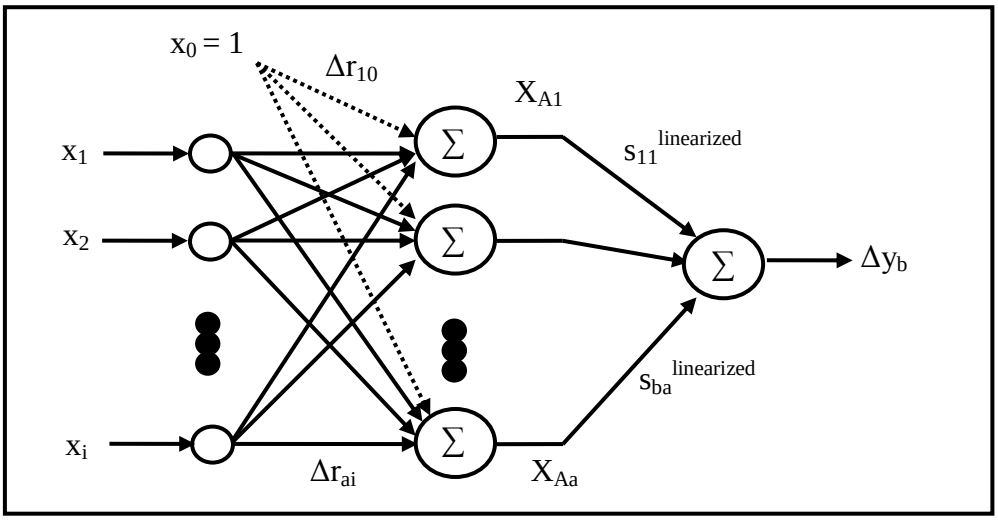

Figure 3.11: Linearized Network Structure for the Optimization of the Hidden Layer

Now, to find the optimal weight change $\Delta R^{optimal}$ for the hidden-input layer, all partial derivatives are set to 0:

$$\begin{aligned} \frac{dE^{penalty}}{d\Delta r_{ai}} &= 0 \\ \frac{dE^{linearized}}{d\Delta r_{ai}} &= 0 \\ \frac{dE^{hidden}}{d\Delta r_{ai}} &= 0 \end{aligned} \qquad \textbf{(3.24)}$$

This results in an optimal solution for weight change $\Delta R^{optimum}$:

$$\Delta R^{optimum} = \tilde{A}^{-1} \bullet \tilde{b} \qquad \textbf{(3.25)}$$

where

$$\text{for } a \neq h$$

$$\tilde{A} = \sum_{p=1}^{P} \sum_{b=1}^{B} \left[\left(x_i s_{ba}{}^{linearized} \right) \left(x_m s_{bh}{}^{linearized} \right) \right]$$

$$where\, i, m = 0, \ldots, I \;\; h = 0, \ldots, A$$

$$for\ a = h$$

$$\tilde{A} = \sum_{p=1}^{P}\sum_{b=1}^{B}\left[\left(x_i s_{ba}^{\ linearized}\right)\left(x_m s_{bh}^{\ linearized}\right) + \frac{\mu}{A}\left|s_{ba}^{\ linearized}\right|\left\|X_{Aa}^{\ "}\right|x_i x_m\right]$$

$$where\ i, m = 0,\ldots,I\ \ h = 0,\ldots,A$$

and

$$\tilde{b} = \sum_{p=1}^{P}\sum_{b=1}^{B}\left[(t^{p} - y_b)s_{bh}^{\ linearized} x_m\right]$$

$$where\ m = 0,\ldots,I\ \ h = 0,\ldots,A$$

where $s_{ba}^{\ linearized}$ and $s_{bh}^{\ linearized}$ are the linearized weights from neuron b of the output layer to neurons a and h in the hidden layer (of training data P), $X_{Aa}^{"}$ is the second derivative of the activation function X_{Aa}, s_{ba} and s_{bh} are the connection weights between the output-hidden layer and t^p is the target output.

Once $\Delta R^{optimum}$ is obtained, the new update weight can be defined as:

$$R = R^{old} + \Delta R^{optimum} \qquad \textbf{(3.26)}$$

Thus now the optimum weights S and R are defined for the OLL neural network. Summarizing, the overall algorithm for the OLL network is:

1. Initialization. Initial values for the weights R and S as well as the penalty constant μ. The number of iterations are defined as well.
2. Optimization of Output Layer Weights. $S^{optimum}$ is obtained using Equation 3.19. Update the weights S and calculate the RMS error.
3. Optimization of Hidden Layer Weights. The new updated weight R is then defined as R^{test}, as shown in Equation 3.25.
4. Test for Completion. RMS error, $E_{RMS}^{\ test}$, was then calculated comparing the R^{test} matrix with S or $S^{optimum}$ matrices calculated in Step 3.

   a. $E_{RMS}^{\ test} < E$

   The hidden layer weight matrix R is updated R= R^{test}. Decrease the influence of the penalty term by decreasing μ. Proceed to Step 5.

   b. $E_{RMS}^{\ test} \geq E$

Increase the influence of μ and repeat Step 4a.

5. If RMS error is not within the desired range, repeat Step 2, else the training process was then ceased.

3.6 Summary

There exist numerous applications for ANNs found in the literature. The problems treated ranged from finance to engineering to medical related applications. Within the scope of this research, the capability of ANNs in emissions predictive modelling was explored. As reviewed in Sections 2.4.2 and 2.4.3, there had only been a handful of studies investigating the potential usage of ANNs in emissions predictive modelling for HEV and HES applications. Promising results were achieved for all of the cases as presented.

In addition, only a few literatures for HEVs were found in the literature and none for HESs in terms of emissions predictive modelling. Among the literatures, none of them exhibited any control focus or using ANN as a predictive model focus. This is because ANN requires data for training, and by altering these operating conditions after training, emission levels could be predicted. By controlling the operating conditions, the emission levels can be controlled as well.

This chapter provided a general knowledge about ANN and its associated theoretical concepts. The neural network models used throughout the course of this research were reviewed and explained in detail. The neural network models discussed were the back-propagation, RBF incorporating Kohonen and the OLL network. Among the three networks, OLL is a fast-learning network.

Next chapter, Chapter 4, shows the first of the two approaches in emissions predictive modelling for HES. This approach uses a dynamic modelling approach. The second approach, the development of the emissions prediction model (EPM) using ANN and its associated results obtained will be discussed in Chapter 6. The neural network models examined above are targeted to perform the prediction task for tailpipe emissions for HESs.

CHAPTER 4: HES MODELLING AND CONSTRUCTION

4.1 Introduction

Chapter 4 consists of two main parts. The first part of this chapter introduces the development of a hybrid electric scooter (HES) dynamic model on the MATLAB-Simulink platform for predictive modelling of emissions and fuel economy. The dynamic model consists of two parts; the HES model and the Multi-State Controller. The HES model consists of the Vehicle Dynamics Model, DC motor Model, Battery Model, Internal Combustion Engine (ICE) Model and Emissions Model. The Multi-State Controller present a dynamic control strategy to control the power splits between the two propulsion sources based on the vehicle speed and the state of charge (SC) of the energy storage system (the battery). Threshold and boundary points are defined in the multi-state controller. Each operating state of the HES is then chosen according to the defined points. The multi-state control strategy defined is similar to the University of Michigan-Dearborn Design presented in Section 2.3.2.

This first part of Chapter 4 comprises of four sections. The first section discusses the past and current research work done in the area of HES. The second section discusses the modelling of the HES model itself. Several sub-models are present and will be discussed. The third section introduces a multi-state control algorithm to the model to control and optimize the hybrid scooter according to operating conditions and driving demands. The final section of this chapter summarizes the HES model, including its functionality and usage as a simple and basic tool to predict the fuel economy and emissions for generic HES applications.

4.2 Previous Research

Previous researches focusing on HES and hybrid electric motorcycles (HEM) development found in the literature were minimal compared to research conducted on hybrid four-wheelers. Only a handful of research papers had been published in the past that discussed HES technology.

Numerous journal papers were found in the literature regarding the development of transmissions and drives for hybrid scooters, which were mostly by the same author, Sheu et al. [125-128] and Chen and Cheng [129]. The literatures by Sheu et al. focused mainly on theoretical concepts behind drivetrains and transmissions technology of HEMs. Chen and Cheng, on the other hand, presents a bidirectional DC/AC converter for a HES drive system.

Chen and Cheng focused on the designing phase of the HES. Important variables such as energy management were not presented nor discussed. No modelling or simulation techniques were used to justify the transmission and drive systems proposed. The actual construction of the HEM and HES using the techniques proposed in the literature were not introduced (and for Chen and Cheng, were not discussed thoroughly, just a note stating the construction had begun). The mathematical models developed remained just as that.

In regards to simulation and modelling techniques, not many simulation and modelling papers on the development of HES were found in the literature; Ceraolo et al. [130], Shao et al. [69] and Khateeb et al. [131]. Ceraolo et al. presented an innovative drivetrain design for HESs. Simulation results showed improvements in fuel economy but the development of the physical HES was not discussed thoroughly. Shao et al. presented a HEM model developed on MATLAB. This is basically the only 'pure' modelling and simulation paper found in the literature for hybrid scooters or motorcycles. Shao et al. developed a HEM model to analyze the design issues such as emissions, fuel economy, and energy and power efficiencies. No prototypes were built to justify the results obtained in the MATLAB simulation, especially in terms of emissions. Regenerative braking was not mentioned in the paper [69]. Although that was the case, Shao et al. demonstrated the importance of modelling and simulation in HES technology. Khateeb et al. did some modelling and simulation work on HES technology by presenting a Li-ion battery model for HES applications. Khateeb et al. presented a battery model for HESs but actual field validations were not carried out to justify the simulated outputs. Thus the models remained just as that.

Thus, in conclusion, research and development on HES and HEM technology are still in its infancy stage especially in the field of emissions predictive modelling. Simulation and modelling techniques are still extremely important in predicting the behavior of the hybrid vehicle before proper construction of the actual prototype begins.

4.3 HES Model Development

The modelling of the HES consists of a few sub-models integrated together. The sub-models consist of the Vehicle Dynamics, ICE, Motor and the Battery Models. Constructed under the MATLAB-Simulink platform, block components can be inter-connected together to construct a parallel HES configuration. Each sub-model is discussed in the sections below.

4.3.1 Vehicle Dynamics Model

The Vehicle Dynamics Model models the vehicle dynamics in the form of road load characteristics as well as various constants such as air density and scooter frontal area. This mathematical model, equating the dynamics of the scooter, predicts the demanded road torque and power for the HES at any specific speed.

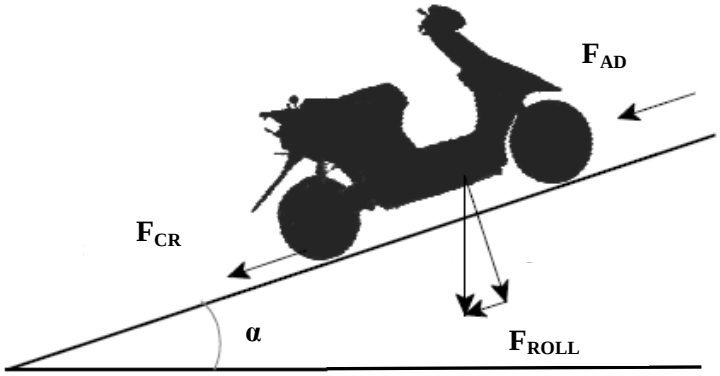

Figure 4.1: Scooter Free Body Diagram

Taking a free body diagram analysis (Figure 4.1) of the vehicle, the summation of forces are shown in Equation 4.1 below:

$$F_{RL} = F_{ROLL} + F_{CR} + F_{AD} \qquad \textbf{(4.1)}$$

where F_{RL} is the road load force, F_{ROLL} is the rolling force. F_{CR} is the climbing resistance and F_{AD} is the aerodynamic forces. Expanding each term in Equation 4.1 and defining each corresponding forces to define the road load force:

$$F_{CR} = mg\sin\alpha \qquad \textbf{(4.2)}$$

$$F_{ROLL} = C_r mg\cos\alpha \qquad \textbf{(4.3)}$$

$$F_{AD} = \frac{1}{2}\rho C_D A_F (V_x + V_o)^2 \qquad \textbf{(4.4)}$$

where m is the total mass of the vehicle in kg, g is the gravitational constant (9.81 ms^{-2}), C_r is the rolling coefficient resistances (Table 4.1 for typical C_r values), α is the road inclination angle, ρ is the air density in kgm^{-3}, C_D is the aerodynamic drag coefficient (dimensionless and

typical values range from 0.2 to 0.4; typical value are for motorcycles is between 0.6 to 0.7 [28]), A_F is the equivalent frontal area of the vehicle, V_x is the velocity and V_o is the head-wind velocity, which has a positive sign when this component is opposite to the vehicle speed and a negative sign when it is the same direction of the vehicle speed. The term $C_r mg$ from Equation 4.3 is the maximum rolling resistance of the vehicle at standstill.

Conditions	Rolling Resistance Coefficient
Car tires on concrete or asphalt	0.013
Car tires on rolled gravel	0.02
Tar macadam	0.025
Unpaved Road	0.05
Field	0.1-0.36
Truck Tires on concrete and asphalt	0.006-0.01
Wheels on rails	0.001-0.002

Table 4.1: Rolling Resistance Coefficient [28]

Substituting Equations 4.2, 4.3 and 4.4 into 4.1, Equation 4.5 shows the road load force derived from Figure 4.1.

$$F_{RL} = C_r mg\cos\alpha + mg\sin\alpha + 0.5\rho C_D A_F (V_x + V_o)^2 \qquad \textbf{(4.5)}$$

With the road load forces now defined, the demanded tractive torque is calculated using Equations 4.6 and 4.7.

$$T_{Load} = F_{TR} d \qquad \textbf{(4.6)}$$

$$F_{TR} = F_{RL} + K_m m \frac{dV_x}{dt} \qquad \textbf{(4.7)}$$

where T_{Load} is the tractive torque (torque required), d is the wheel radius, velocity V_x, ω_{wheel} is the angular velocity of the wheel, F_{TR} is the tractive force and K_m is simply a dimensionless constant for rotational inertia (typical values ranging from 1.08 to 1.1 [45]). Equation 4.6 indicates that the required vehicle torque for a corresponding vehicle speed can be

mathematically determined using three dynamic variables; tractive force, vehicle horizontal velocity and wheel angular velocity. Tractive force is defined in Equation 4.7, where road load forces are defined in Equation 4.5. Substituting Equations 4.5 and 4.7 to Equation 4.6, the required vehicle tractive torque:

$$T_{Load} = \frac{C_r mg\cos\alpha + mg\sin\alpha + 0.5\rho C_D A_F (V_x + V_o)^2] + [K_m m\frac{dV_x}{dt}]}{\omega_{wheel}} \quad \textbf{(4.8)}$$

$$d = \int v_x dt = \iint a_x dt \quad \textbf{(4.9)}$$

Equations 4.8 and 4.9 show the outputs (required torque and distance travelled) of this model. The total power must be delivered by the propulsion unit was determined using Equation 4.10 below:

$$P_{Load} = F_{TR} V_x \quad \textbf{(4.10)}$$

$$P_{Total} = \frac{P_{Load}}{\eta_{Drivetrain}} + P_{Auxilary} \quad \textbf{(4.11)}$$

where P_{TR} is the tractive power calculated on the wheels derived using Equation 4.10. $P_{Auxilary}$ is the power needed by the scooter original system (headlights, dashboard, etc). The efficiency of the scooter drive-train is to be accounted for. Finally the tractive energy, e_{TR}, can be calculated over a driving cycle is [45]:

$$e_{TR} = \int P_{Load} dt \quad \textbf{(4.12)}$$

The input/output (I/O) functions of this model are shown in Equation 4.13, where the torque and power demanded is a function of vehicle speed. Figure 4.2 shows a graphical representation in MATLAB-Simulink model, in terms of a flow diagram, the I/O of the Vehicle Dynamics Model.

$$T_{Load}, P_{Load} = f(V_x) \quad \textbf{(4.13)}$$

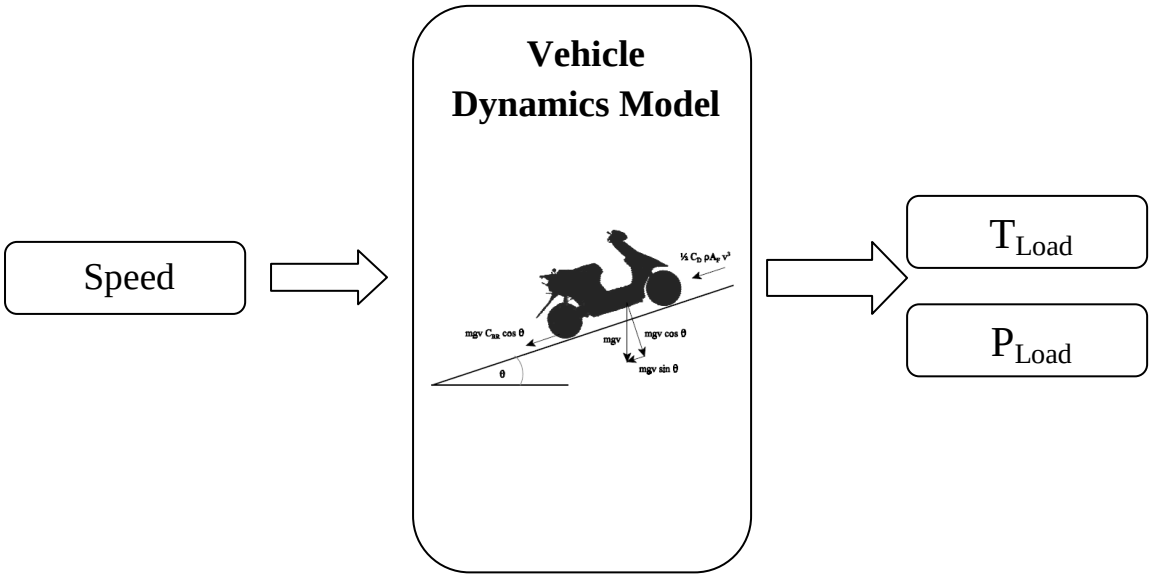

Figure 4.2: I/O Flow Diagram for Vehicle Dynamics Model

The developed MATLAB-Simulink block model for the vehicle dynamics and its structure is shown in Figures 4.3 and 4.4 below. The speed value for the vehicle was obtained from the driving cycle profile and the slope angle was obtained from the road profile, both during simulation of the model. The corresponding outputs are the torque (T_{Load}) and power (P_{Load}) demanded (road).

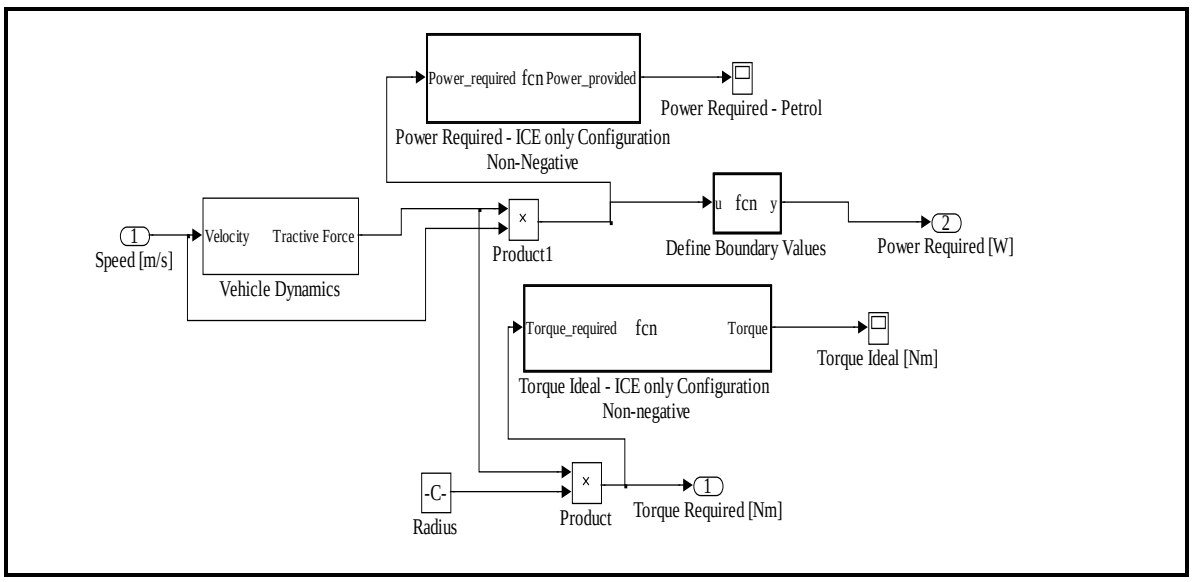

Figure 4.3: MATLAB-Simulink Vehicle Dynamics Block Model – Level 1

From the diagram, it can be seen that T_{Load} and P_{Load} are derived from the output of the Vehicle Dynamics block (on the left), which is the tractive force. The Power Required and Torque Ideal function codes are written to define the boundary conditions of the model.

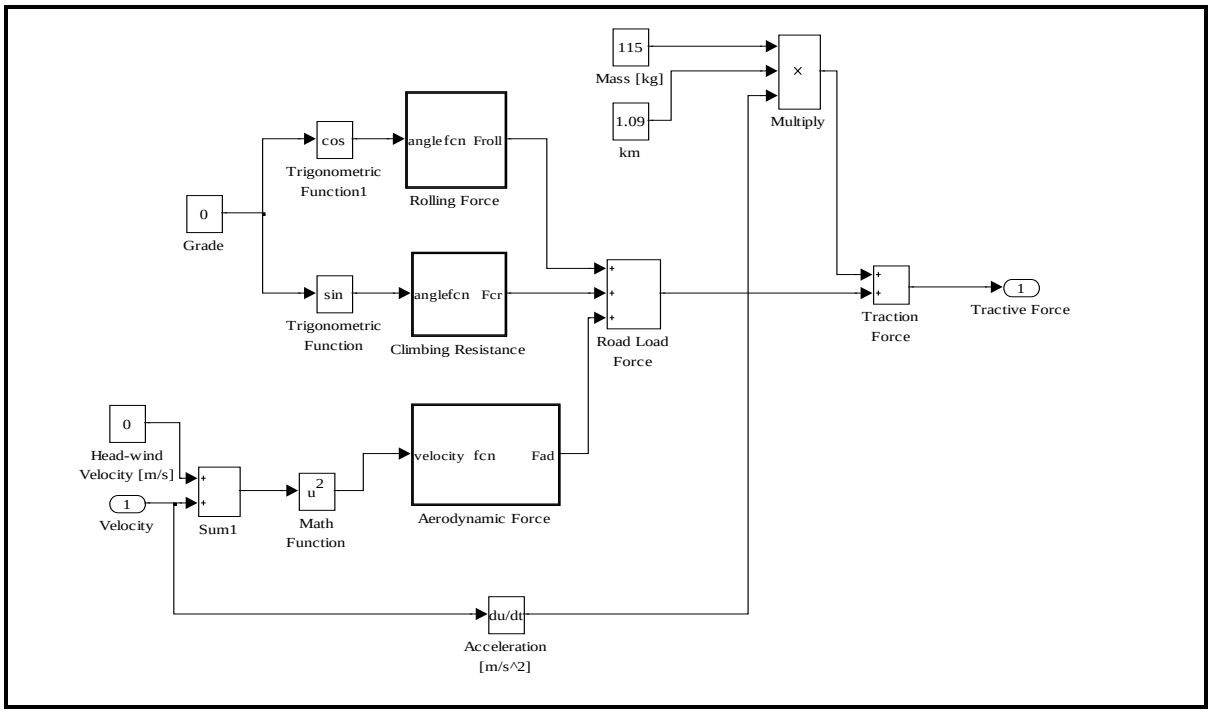

Figure 4.4: MATLAB-Simulink Vehicle Dynamics Block Model – Level 2

Figure 4.4 is the final level of the block, which zooms in how the tractive force is calculated. Three functions were defined; Rolling Force, Climbing Resistance and Aerodynamic Force (in the middle of the diagram) based on Equations 4.1 to 4.7. All the written codes (function block) of this model are attached in Appendix A.

4.3.2 Hub Motor Model

The hub motor chosen for modelling is a GL2 hub motor developed by Island Earth. Further information regarding this hub motor will be presented later in the chapter. The motor model was developed based on the motor's experimental data provided by the manufacturer shown in Figure 4.5. From the figure, variables power input, power output, RPM and efficiency are all graphed and plotted based on the motor's torque values. The maximum efficiency of the motor is 84.89 % at 12.38 Nm.

The demanded torque (T_{Load}) and the instantaneous battery's SC are the input variables to model. The corresponding outputs from the hub motor model are the motor's

available torque and power. By interpolating between the manufacturer's data shown in Figure 4.5, the motor's available torque and power can be obtained. The general equation that describes the linear interpolation method is shown in Equation 4.14:

$$y = y_0 + (x - x_0)\frac{y_1 - y_0}{x_1 - x_0} \qquad \textbf{(4.14)}$$

where y is the unknown value for the corresponding value x.

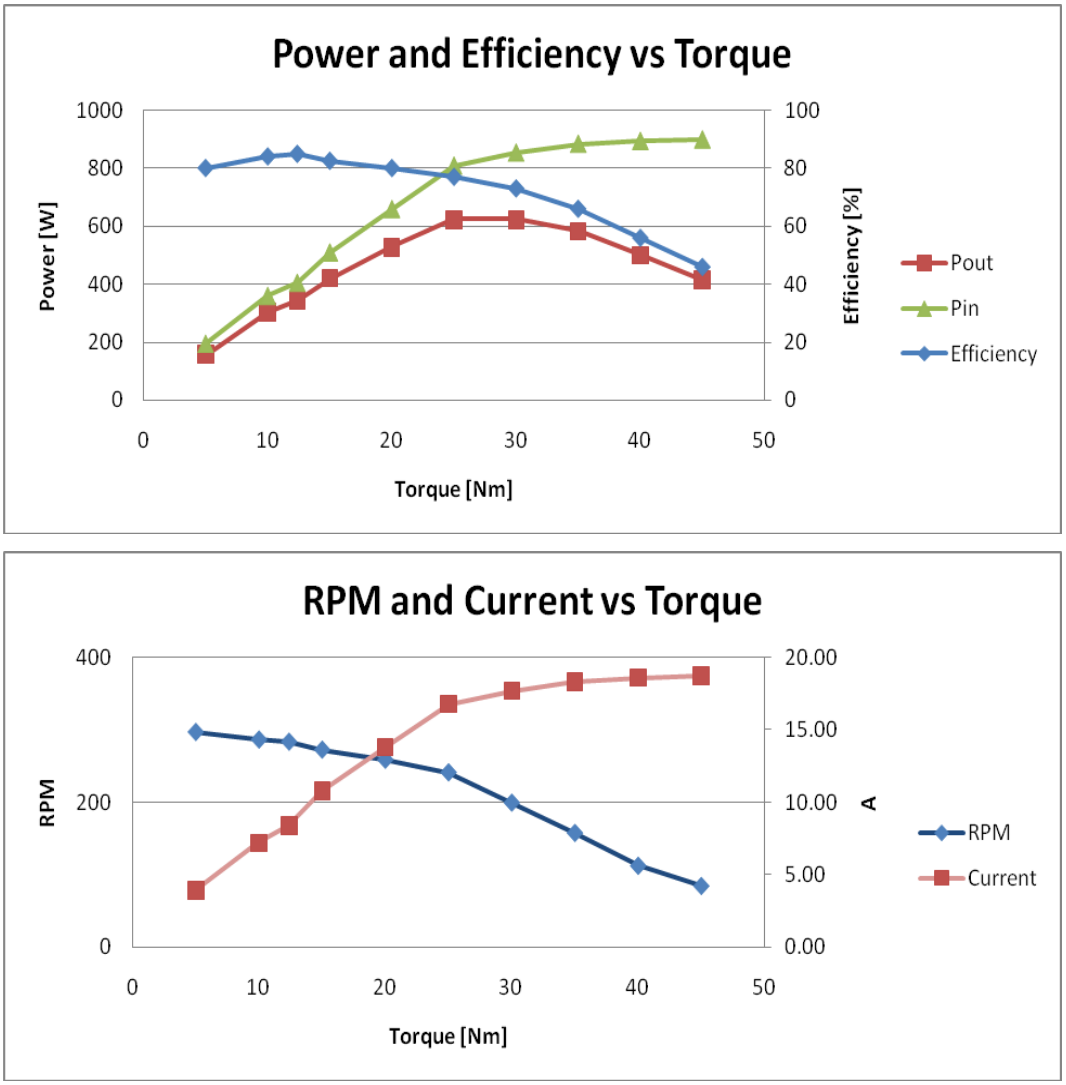

Figure 4.5: Island Earth GL2 Hub Motor Characteristics [132]

Each output corresponds to each speed value, which is shown in Equation 4.15. The flow diagram depicting the I/O of the model is shown in Figure 4.6, where the value of T_{Load} was obtained from the Vehicle Dynamics Block and SC is the battery's state of charge.

$$T_{motoravail}, P_{motoravail} = f(T_{Load}, SC) \quad \textbf{(4.15)}$$

Using the linear interpolation method described in Equation 4.14 above enables the available motor torque ($T_{motoravail}$) and power ($P_{motoravail}$) to be calculated using the manufacturer's data provided. Knowing the instantaneous motor torque and power available is extremely important to determine whether the demanded load can be met by the motor or additional power is needed. The input SC must be kept at a high level to ensure the motor is enable to operate most of the time (to reduce the ICE operation time) for a cycle.

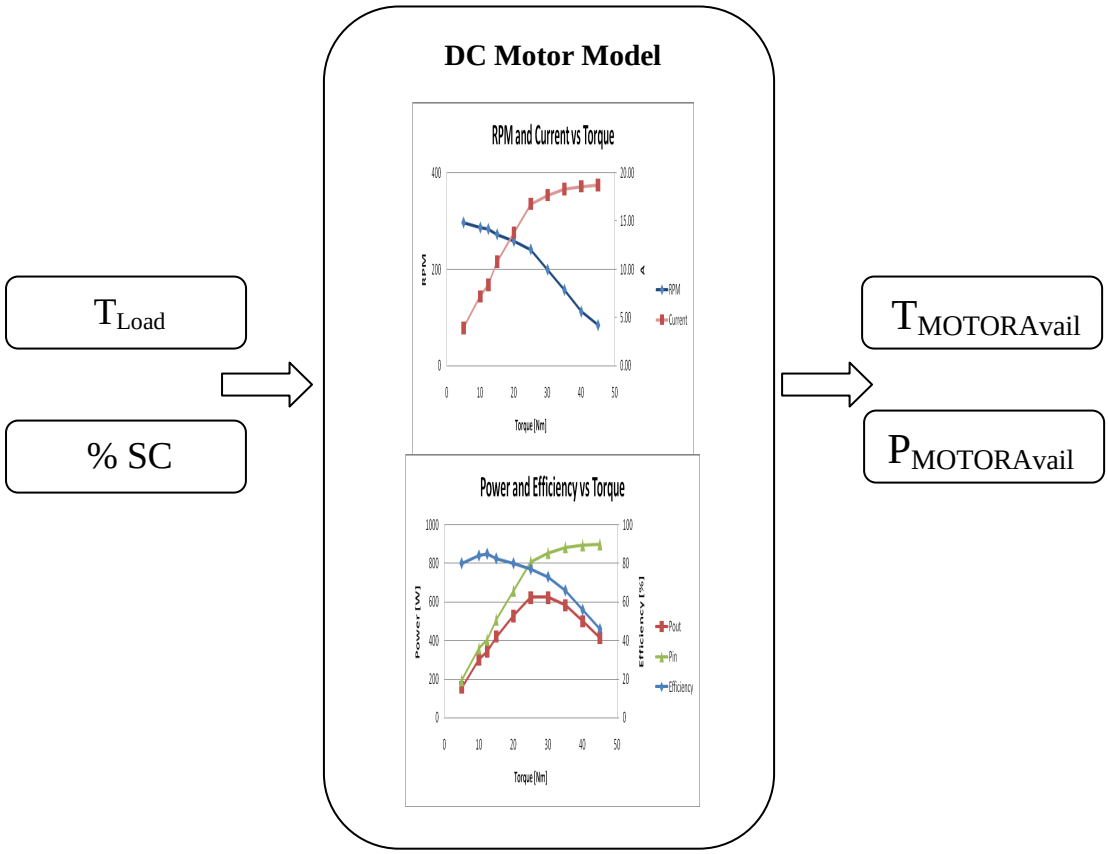

Figure 4.6: I/O Flow Diagram for Hub Motor Model

Figure 4.7 shows the structure of this model. The Linear Interpolation Code function basically interpolates between plots (Figure 4.5) to obtain the desired power and torque

outputs. The net propulsion torque was also modeled for testing and simulation purposes. The linear interpolation code is attached in Appendix A.

The All Electric Drive System (AED) (highlighted in orange) represents a pure electric scooter environment, equipped with only the hub motor as the propulsion source. The outputs are the torque and power provided and the efficiency curves over a driving cycle. This is an additional feature to the HES model to investigate an all-electric scenario for the scooter, using the same motor and battery source. This enables future expansion on the model when an AED vehicle is simulated and comparisons can be made with the existing HES model.

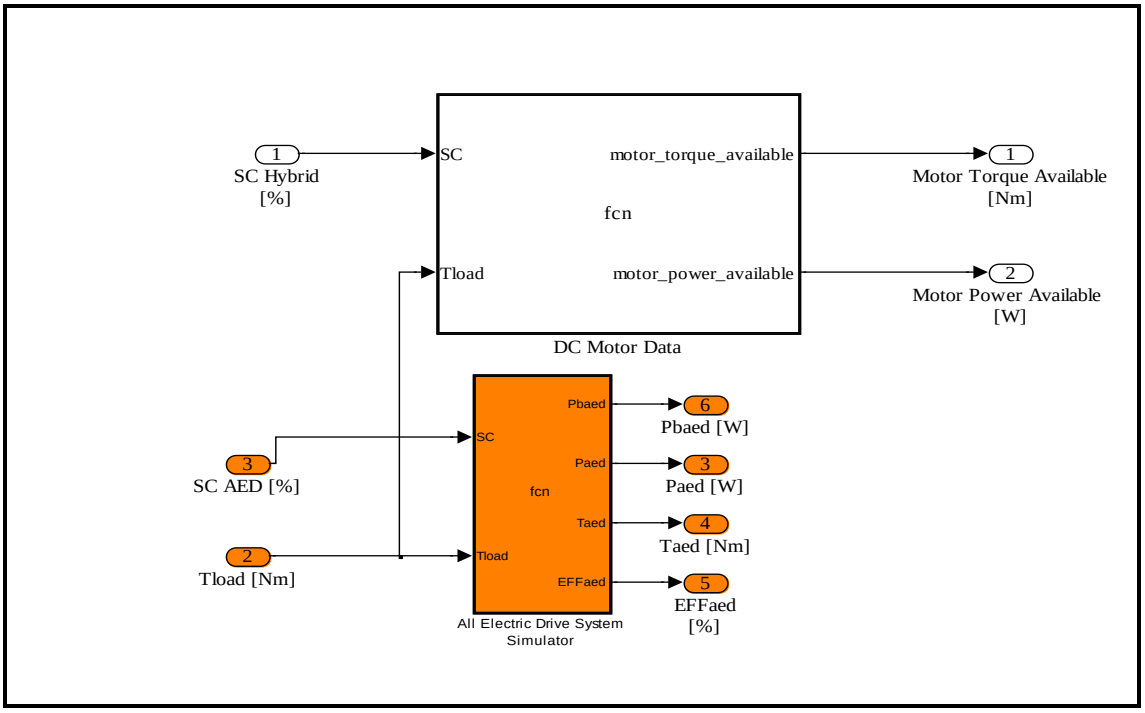

Figure 4.7: MATLAB-Simulink Hub Motor Block Model – Level 1

4.3.3 Battery Model

A 48 V 6 Ah sealed lead acid battery was used as a modelling reference for the hybrid electrical scooter's physical model. The battery model was modeled, theoretically, in terms of energy and charge of the batteries provided.

The main objective to develop this model is to properly predict or monitor the battery's instantaneous SC. Knowing the amount of energy left in a battery compared with the energy it had gives a good indication of how much longer the battery will continue to discharge during operation before recharging is needed. The % SC of the battery must stay

within predetermined threshold values so that there will always be room for regenerative braking. However, the % SC also has to be high enough so that the motor is able to boost the propulsion power when the ICE no longer has the ability to support the demanded power.

The % SC was calculated based on the charging and discharging power, where a negative current was assigned for a charging condition, and a positive current was assigned for a discharging condition. An initial condition of the battery must first be specified in the model as a constant. The % SC can be calculated using the variables initial charge, current charge (instantaneous charge) and the battery's rated capacity, as shown in Equation 4.16.

$$\%\,\mathrm{SC} = \frac{\text{Initial Charge} - \text{Current Charge}}{\text{Battery Capacity}} \times 100\% \qquad \textbf{(4.16)}$$

The % SC predicted is determined by the net power drawn by the battery (or the net power requested by the motor). Net power is defined as:

$$\mathrm{P_{Net}} = \mathrm{P_{Drawn}} - \mathrm{P_{Regen}} \qquad \textbf{(4.17)}$$

where P_{Net} is the net power drawn from the battery source, P_{Drawn} is the power required by the propulsion unit (motor) and P_{Regen} is the regenerative braking power to recharge the battery. Thus two constants are defined to get the initial and current charge (Equation 4.16); the theoretical initial energy of the battery before each driving schedule and the maximum energy of the battery. Both can be calculated by the following:

$$E_T = V_b Q_T \qquad \textbf{(4.18)}$$

where E_T is the theoretical stored energy, V_b is the battery's terminal voltage, Q_T is the theoretical capacity in Coulombs (C), 1 Ah = 3600 C and 1 V is equivalent to 1 Joule (J) of work required to move 1 C. Using Equation 4.18, the initial stored energy and the battery's maximum energy can be calculated. As for the model, the battery's SC was calculated in terms of energy and the net input power, P_{NET}, was inputted to the Battery Model. The current energy required (E_{req}) from the battery could be calculated by:

$$E_{req} = \int_{t_1}^{t_2} P_{NET}\, dt \qquad \textbf{(4.19)}$$

Using Equation 4.16 similarly, the instantaneous SC can be obtained. The battery's SC is a function of the net power drawn from the battery source, as shown below:

$$\%\, SC = f\left(P_{Net}\right) \qquad \textbf{(4.20)}$$

The Battery Model is shown in Figure 4.8. Note that the methodology used to calculate the battery's SC is impractical, as building an accurate battery model to determine its SC is extremely complex. As the focus of this project is not on this scope, the Battery Model developed should not be affecting the results that much later on.

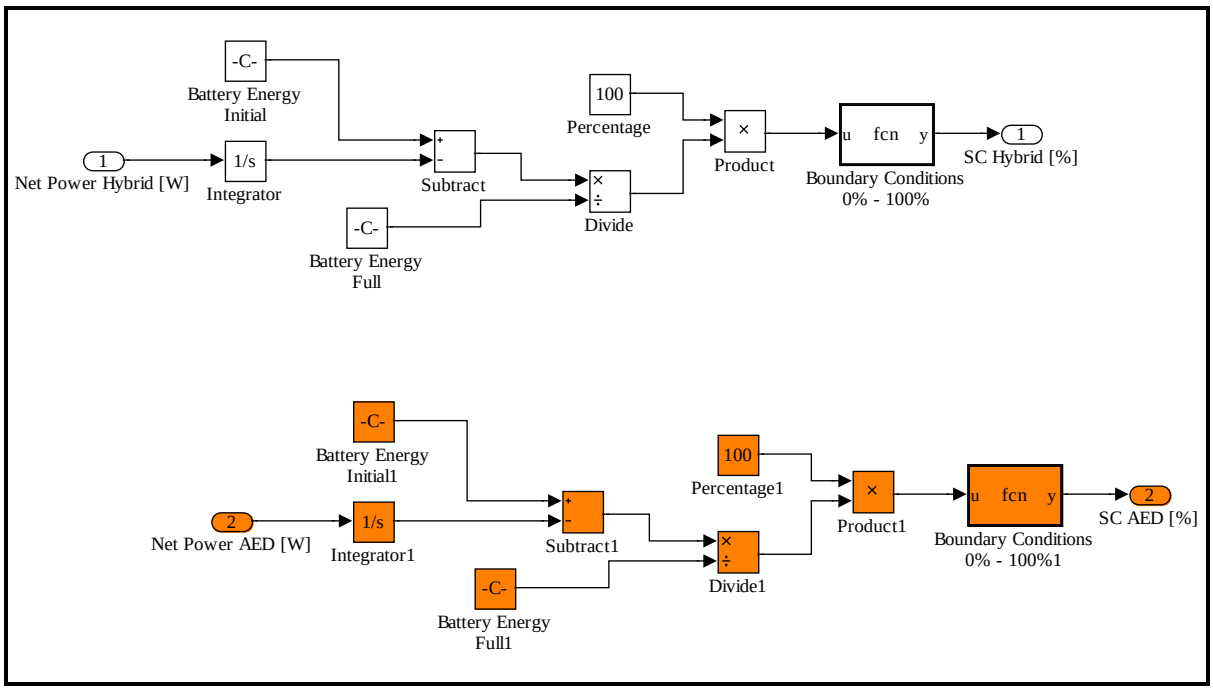

Figure 4.8: MATLAB-Simulink Battery Model – Level 1

Using Equations 4.16 to 4.19, the model shown above is constructed. The Boundary Conditions function is written to ensure that the SC can only be in the range from 0 % to 100 %. The highlighted structure is similar to the HES model, but this is applied to the AED model, where the SC is an input variable to the hub motor model.

4.3.4 Internal Combustion Engine Model

4.3.4.1 Chassis Dynamometer Testing

Before constructing the ICE Model, information about the ICE has to be gathered experimentally as no manufacturer's data for this scooter was provided. The chosen scooter is a Bug Escape 83 cc Scooter shown in Figure 4.9 and the specification is presented in Table 4.2.

Figure 4.9: 83 cc Bug Escape Scooter [133]

Engine	2 stroke air-cooled
Displacement	83 cc
Transmission	Auto CVT
Starting System	Electric kick
Fuel Capacity & Type	5.5 litres, Unleaded Gasoline
Wheels/Tyres Front	120/70-12
Read	130/70-12
Brakes F/R	Disc/Drum
Suspension Front	Hydraulic Damper
Rear	Adjustable Coil Spring
Weight	85 kg
Wheel Construction	Alloy
Head Lamp	Halogen

Table 4.2: 83 cc Bug Escape Scooter Data [134]

For experimental data collection, the scooter was tested on a chassis dynamometer shown in Figure 4.10 below. Information regarding the dynamometer unit can be found in the following reference [135].

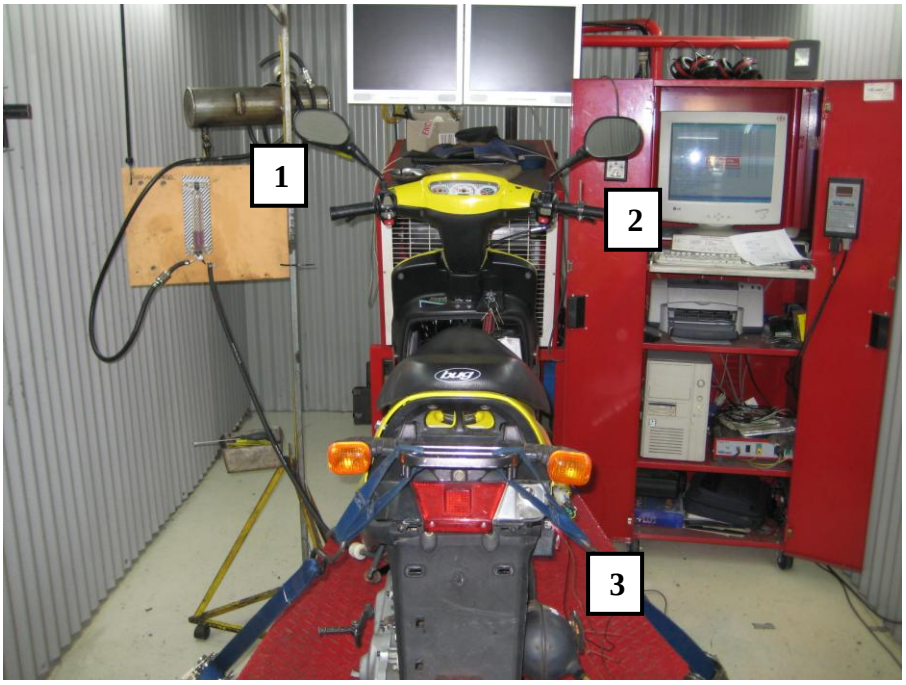

Figure 4.10: Scooter on the Chassis Dynamometer

An alternative fuel tank was used. The scooter's original fuel tank was disconnected. The alternative fuel tank was equipped with a test tube with a maximum volume of 100 ml (labeled 1). The fuel consumption was then measured by taking the fuel used for each test. A throttle position sensor (TPS) was installed on the scooter's throttle, labeled 2. The TPS functions as a throttle sensor by acting just like a potentiometer, with an output electrical signal showing the throttle position. Labeled 3 at the bottom of Figure 4.10 is where the input to the gas analyzer was attached, at the output of the tailpipe.

Figure 4.11: Gas Analyzer Setup

An AutoLogic Silver Series 5 Gas Analyzer was used to measure the emissions from the HES during experiment testing. Some important features of this analyzer [136]:

- Measures hydrocarbons (HC, ppm), carbon monoxide (CO, %), carbon dioxide (CO_2, %), oxygen (O_2, %), Air/Fuel (A/F) ratio and Lambda
- Meets or exceeds industrial standards BAR97, ASM, OIML Class 1, BAR90 and IM240
- Real-time data can be displayed in multiple formats and could be logged and automatically saved.

The analyzer set is shown in Figure 4.11. The analyzer is connected to a computer which displays the real-time gas values. The results are stored automatically, which made reviewing easy. Before performing the tests, the analyzer was calibrated against the calibration gasses provided by the manufacturer to ensure more accurate readings.

Three tests were performed for experimental data collection; throttle test, ramp test, and the modified ECE-15 cycle test. Four determined throttle positions, 25%, 50%, 75% and wide open throttle (WOT) were used for all the tests. The test data is important for verifying the model and training the neural network emissions model, which will be discussed in the later chapters.

To construct the model, throttle test was used to construct the MATLAB-Simulink model. The modified ECE-15 cycle test was used to verify the ICE Model. The measured variables for all the tests were:

- Throttle position
- Vehicle speed

- Tractive force
- Power
- Specific Emissions
- Fuel consumption

The throttle test involves holding the throttle constant and increasing the speed by 10 kmh^{-1} until maximum achievable speed. The second test involves simulating the scooter up a ramp, at each throttle position, from idle to the maximum achievable speed. By holding the throttle constant, the dynamometer load is then increase at an acceleration rate of 9 kmh^{-2} until achievable maximum speed. The last and final test is to run the scooter in a simulated driving cycle, a modified Standard European Cycle (ECE-15) cycle. The only difference from the original ECE-15 cycle is that the speeds are constant instead of decelerating to idle. Figure 4.12 shows the modified ECE-15 driving cycle profile. The duration of this cycle is 212 s. The total distance is 1.57 km. The maximum speed is 14 ms^{-1}.

Each test was simulated under laboratory conditions for five times to ensure accuracy and repeatability.

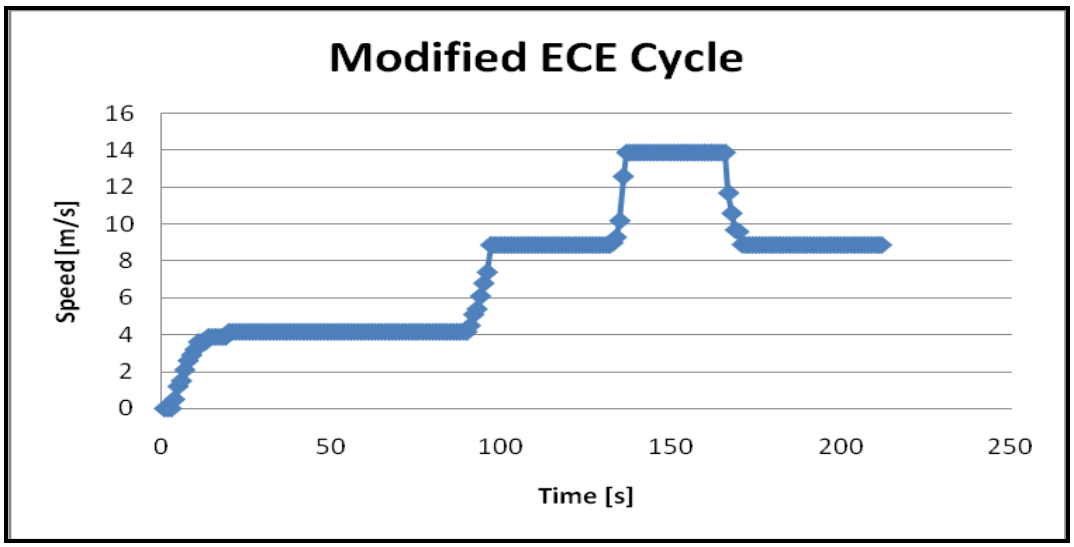

Figure 4.12: Modified ECE-15 Cycle

The obtained results are shown in Appendix B, and their graphical representation is shown in the next section. The emissions results in graphical representation will be in Section 4.3.5. The modified ECE-15 cycle test data was used to verify the HES Model in terms of fuel economy and emissions.

4.3.4.2 ICE Model

The first part of the ICE model is to map the ICE based on the scooter's experimental data. The scooter was tested on a chassis dynamometer to map the ICE's performance under laboratory conditions. The torque and power characteristics are shown in Figure 4.13 below.

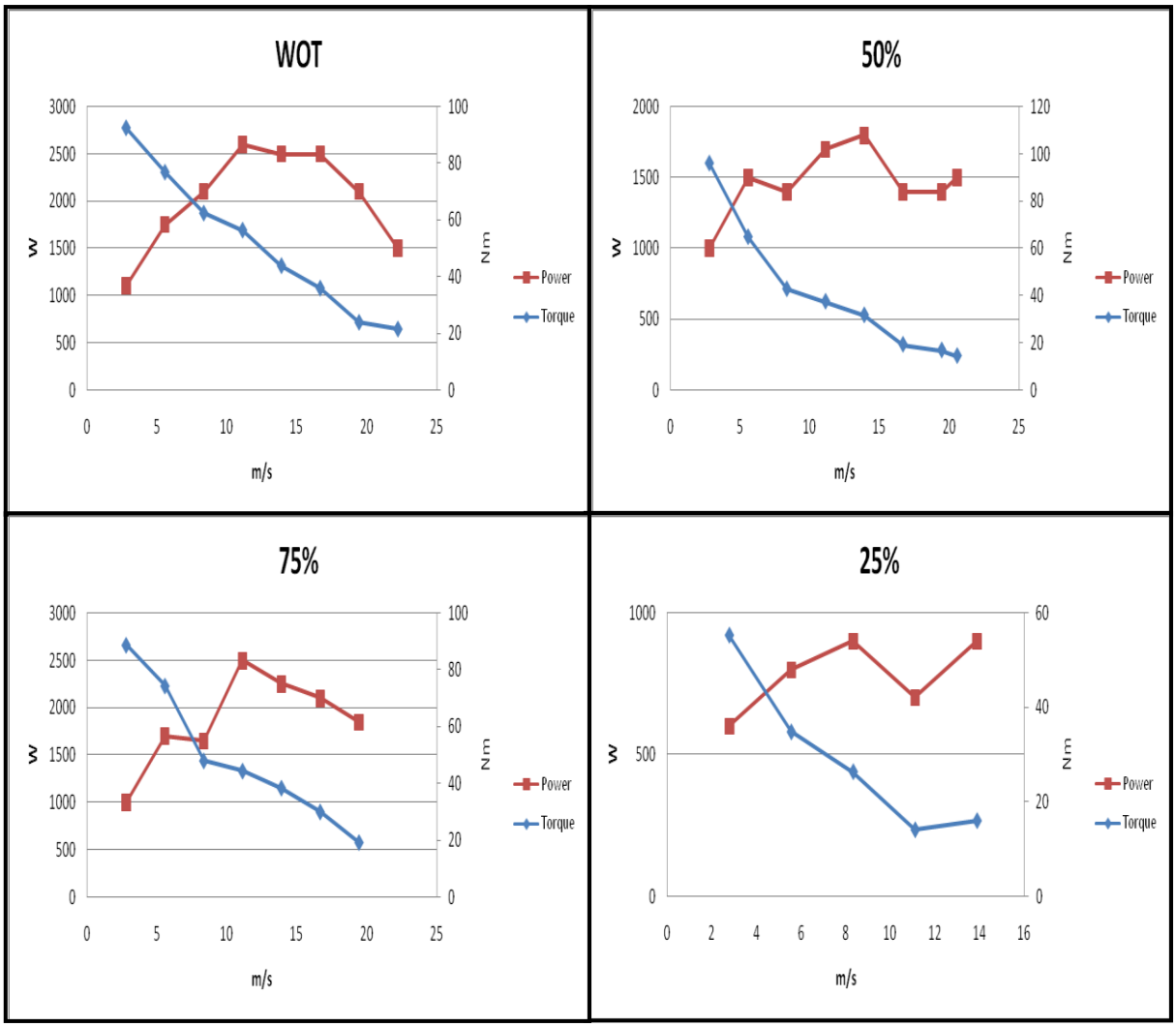

Figure 4.13: ICE Maps for Each Throttle Openings

Similar to the hub motor model, each available torque and power values are obtained using Equation 4.14 for each throttle opening. The I/O for the first part of this model is

$$P_{ICEavail}, T_{ICEavail} = f(v_x, P_{Load}, T_{Load}) \qquad \textbf{(4.21)}$$

where $P_{ICEavail}$ and $T_{ICEavail}$ are the engine's available power and torque respectively. The flow diagram for this part of the ICE model is shown in Figure 4.14. Note that the maximum available ICE torque and power lies on the wide open throttle (WOT) curve shown in Figure 4.13.

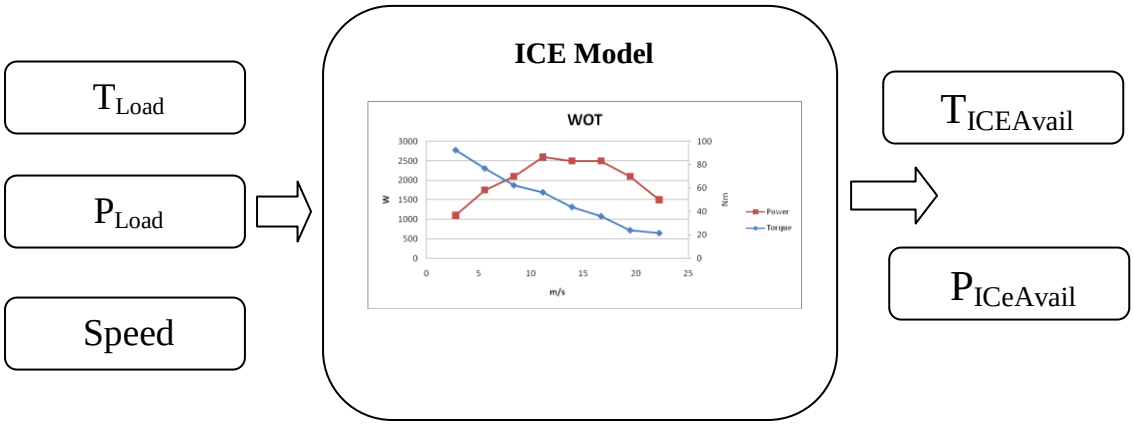

Figure 4.14: I/O Flow Diagram for ICE Model 1

The second part of the ICE model is the determination of the fuel economy over a simulated cycle. Four engine throttle openings are tested and simulations will be based on the four defined throttles; 25%, 50%, 75% and wide open throttle (WOT) openings, shown in Figure 4.13.

The brake specific fuel consumption (BSFC) map was obtained experimentally and is shown below in Figure 4.15. BSFC is a measure of fuel efficiency of an ICE, which can be calculated using the following equation:

$$BSFC = \frac{1}{LCV \times \eta_{th}} \qquad \textbf{(4.22)}$$

where LCV is the lower calorific value of petrol (44 $MJkg^{-1}$) and η_{th} is the thermal efficiency of the ICE. The thermal efficiency can be calculated using the equation below:

$$\eta_{th} = \frac{Power\ Output\ (ICE)}{Power\ Input\ (fuel)} = \frac{P_{DYNO}}{LCV \times \dot{V} \times \rho} \qquad \textbf{(4.23)}$$

where P_{DYNO} is the engine power reading obtained using the dynamometer (which is also the engine power), $\dot{V}$ is the volumetric flow rate of the fuel and ρ is the density of fuel (737.22 kgm^{-3}).

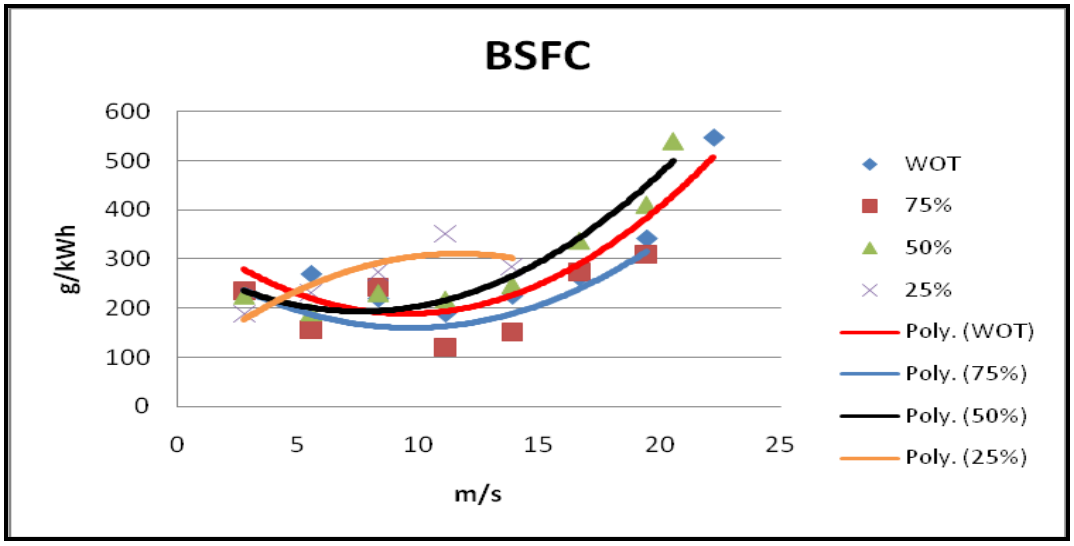

Figure 4.15: ICE BSFC Map

The corresponding fuel used in litres is then calculated in Equation 4.24 by converting grams to litres:

$$Fuel = P_{DYNO} \times \frac{BSFC}{3600} \times \frac{1.3564}{1000} \qquad \textbf{(4.24)}$$

The I/O for the second part of the ICE model is shown below:

$$Fuel, BSFC = f(throttle\ angle, P_{ICEFinal}, T_{ICEFinal}) \qquad \textbf{(4.25)}$$

where Fuel is the fuel usage (in litres), throttle angle represents the current throttle angle, $P_{ICEFinal}$ and $T_{ICEFinal}$ are the final power and torque values sent from the controller to operate the HES. Figure 4.16 is the flow diagram representing the second part of the ICE model in MATLAB-Simulink.

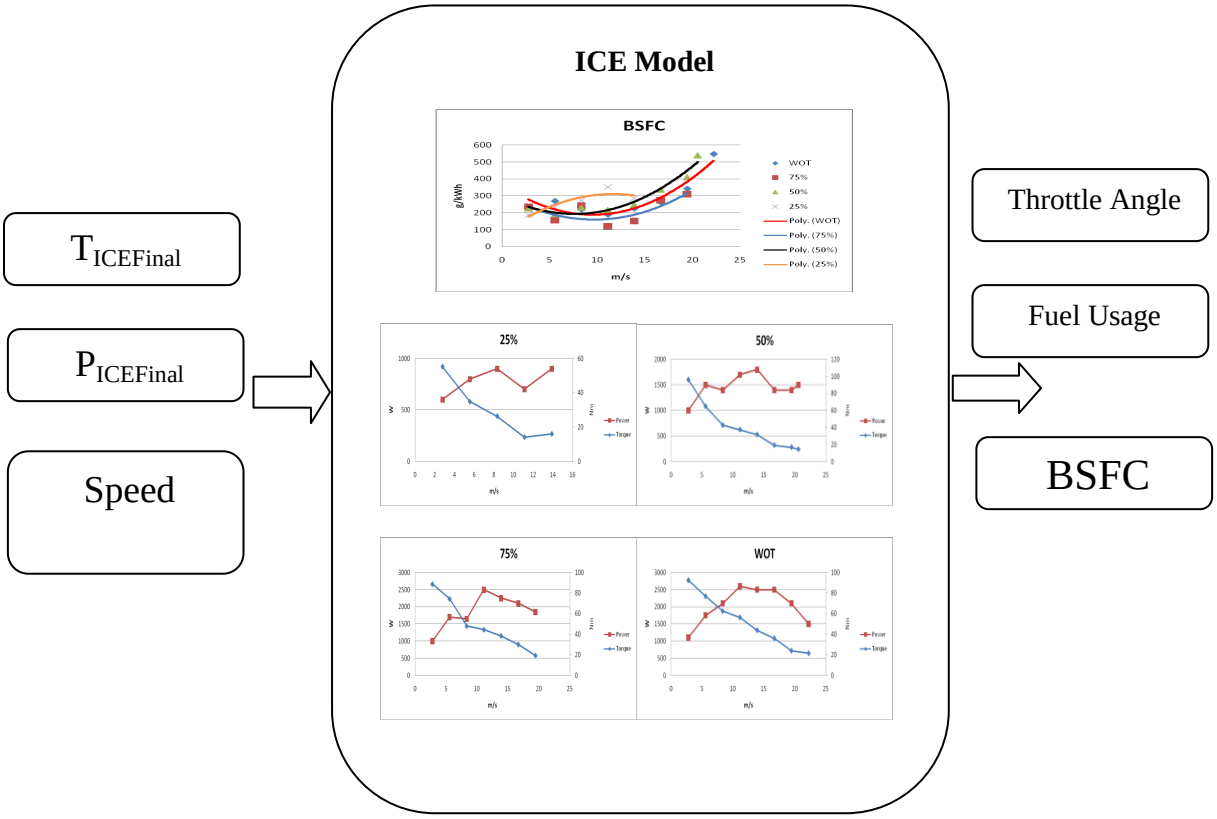

Figure 4.16: I/O Flow Diagram for ICE Model 2

Figure 4.17 shows the ICE model constructed in MATLAB-Simulink. Firstly, the blue highlighted an additional model created (similarly with the AED) to simulate a conventional petrol ICE scooter. The non-highlighted blocks are the main HES scooter blocks in the ICE model. The only difference is that the power and torque available signals will be sent to the controller first to determine a new power and torque level based on the controller's decision. The conventional scooter model does not have this feature.

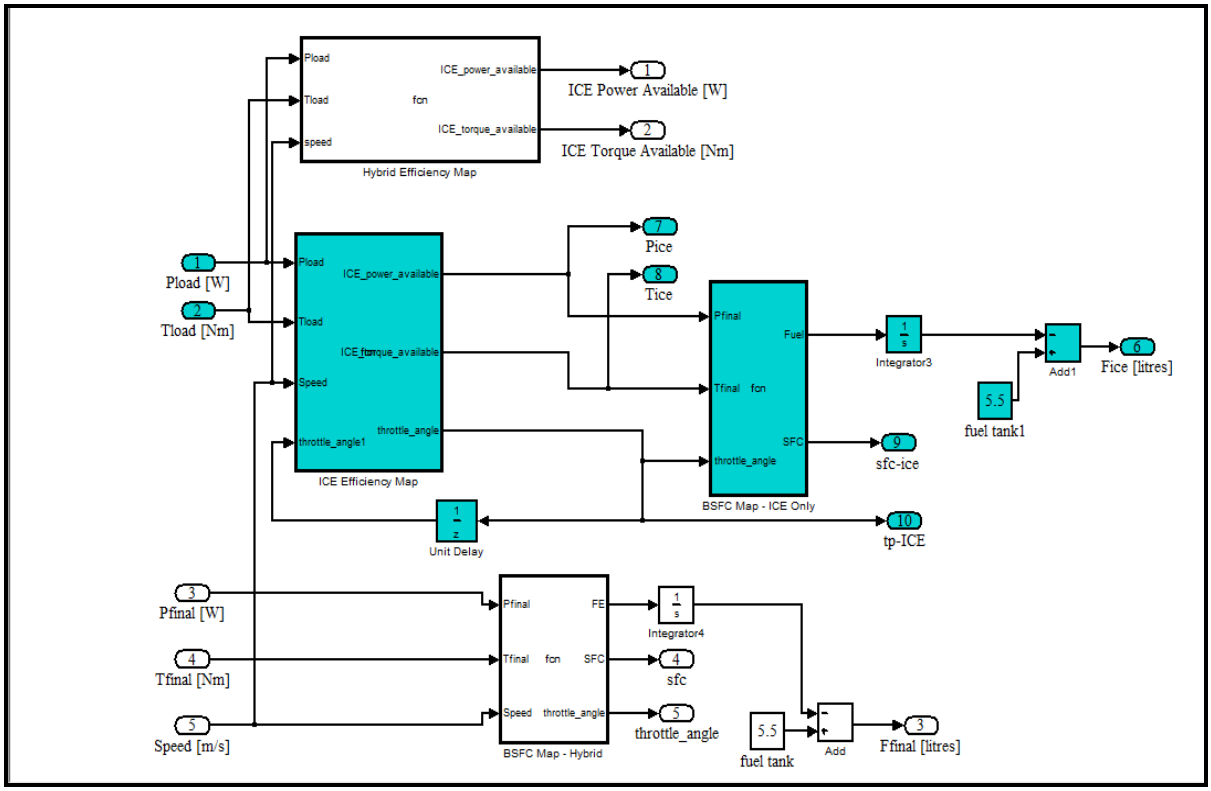

Figure 4.17: MATLAB-Simulink ICE Model – Level 1

4.3.5 Emissions Model

The incorporation of the Emissions Model to the HES model was based on experimental data obtained from the chassis dynamometer. For each of the three tests performed, the emissions for each throttle; CO, CO_2, O_2 and HC, together with the A/F ratio was recorded. Figure 4.18 shows the emission results obtained from the throttle test. The results will be used to construct the emissions model.

The I/O for this model is shown in Equation 4.26 and the flow diagram for the Emissions Model in MATLAB-Simulink is depicted in Figure 4.19.

$$Fuel\ Economy, Emissions = f(Fuel, BSFC, throttle\ angle, Speed) \qquad \textbf{(4.26)}$$

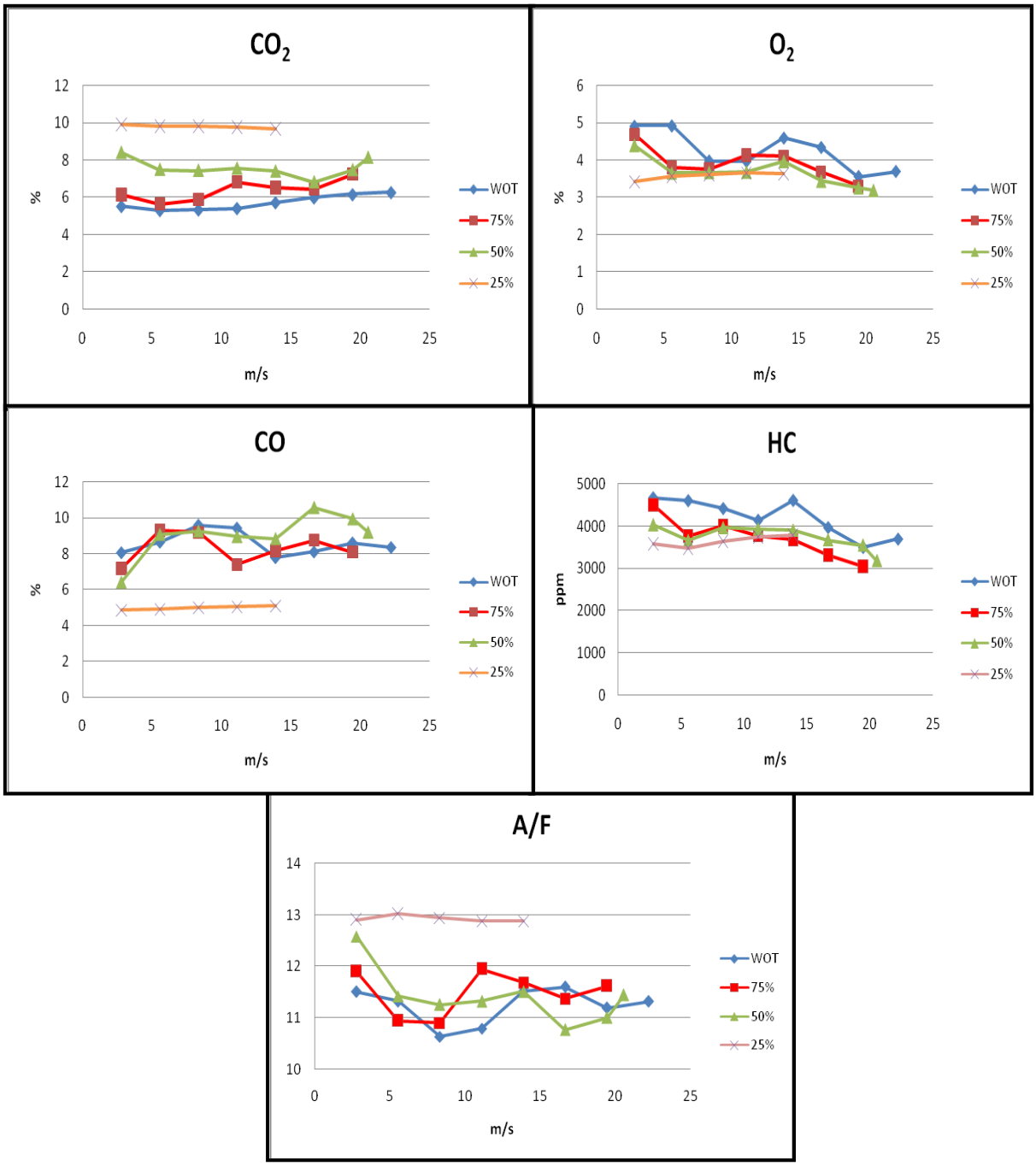

Figure 4.18: Emissions Data for Each Throttle

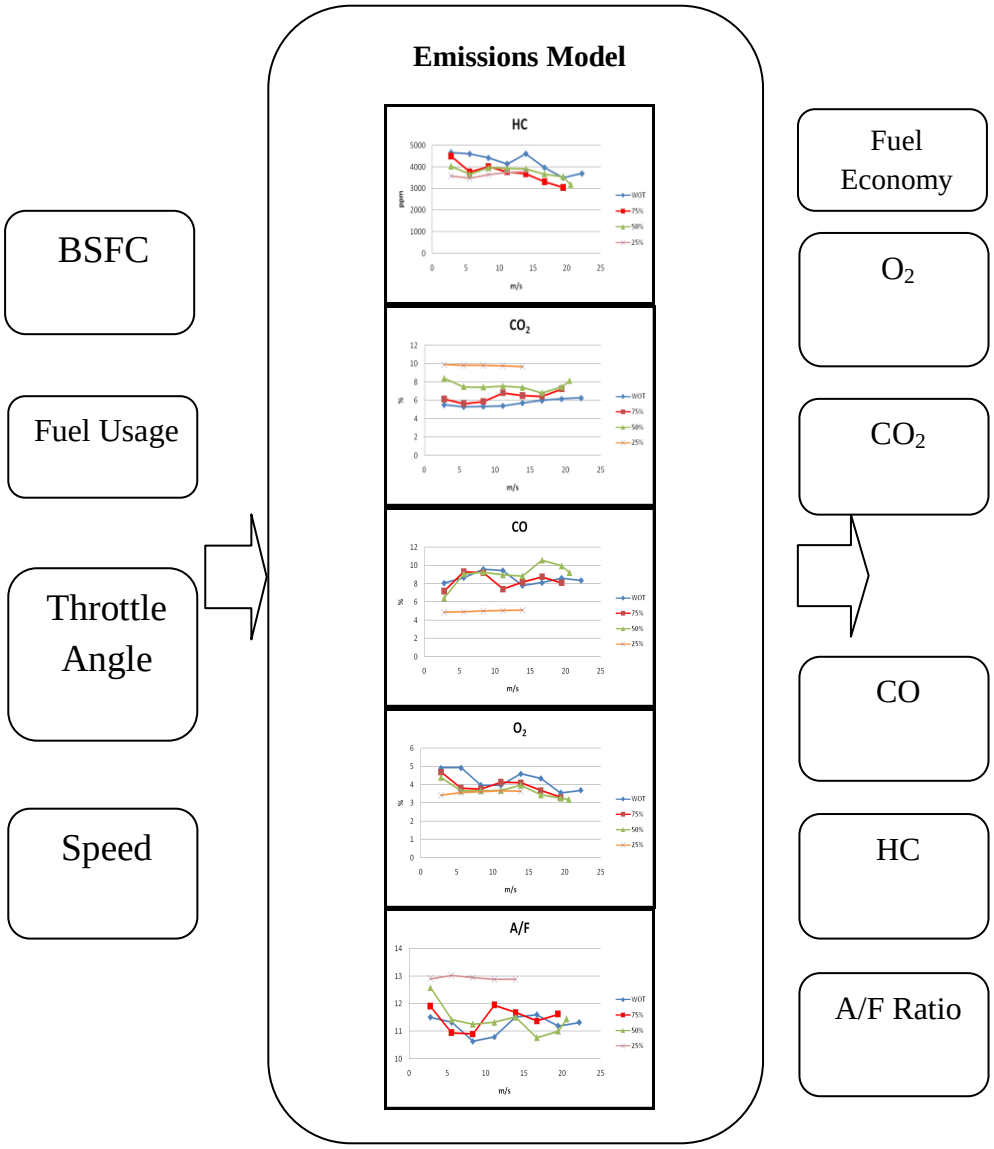

Figure 4.19: I/O Flow Diagram for Emissions Model

4.4 Multi-State Control System Model

The control system model and its algorithm are discussed in this section together with the MATLAB-Simulink model. The control strategy proposed for the hybrid electric scooter model is a multi-state approach. The multi-state approach control methodology defines several operating conditions for the two propulsion units and power sources. This control strategy has a proper set of defined static thresholds or values over the entire operating range for each propulsion unit. Each defined state will operated based on the thresholds defined.

Various operation states are determined in this control system model, based on the horizontal speed (V_x) of the scooter and the SC of the battery. The states are developed where the hub motor is given a priority as the primary propulsion system to the ICE. The reduction

in usage of the ICE will lower the petrol consumption and eventually reduces the harmful emissions produced. The 6 operation states realized are described in the following below with the power distribution equations governing the power for each propulsion source; ICE power, motor power and battery power:

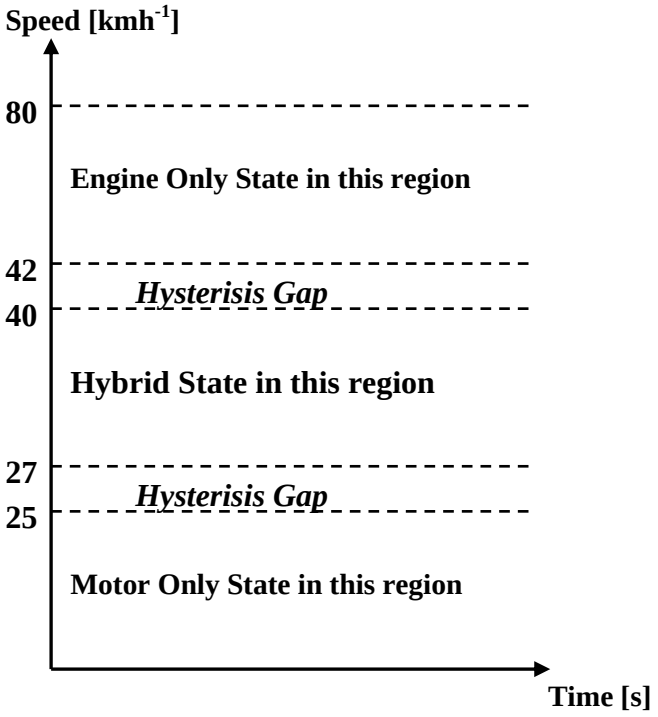

Figure 4.20: Speed Threshold Values for Each Propulsion Source

Engine Charge State. This state is where the ICE is operating the scooter, while recharging the set of battery through the DC generator on board. This state is the most efficient state for highway-cruising, as well as speeds just below 40 kmh^{-1} (especially in urban areas). The batteries' SC upper and lower thresholds are defined in Figure 4.21 which makes the selection of this state easier.

Hybrid State. The hybrid state is used when a high power demand is required in situations such as acceleration grade climbing. In this state, the two sources (ICE and the hub motor) are coupled to increase the scooter's power, thus increasing the rpm and torque of the motor. Basically, if the demanded torque for propulsion exceeds the maximum torque limit defined for the hub motor, the remaining power demanded is supplied by the ICE, or vice-versa.

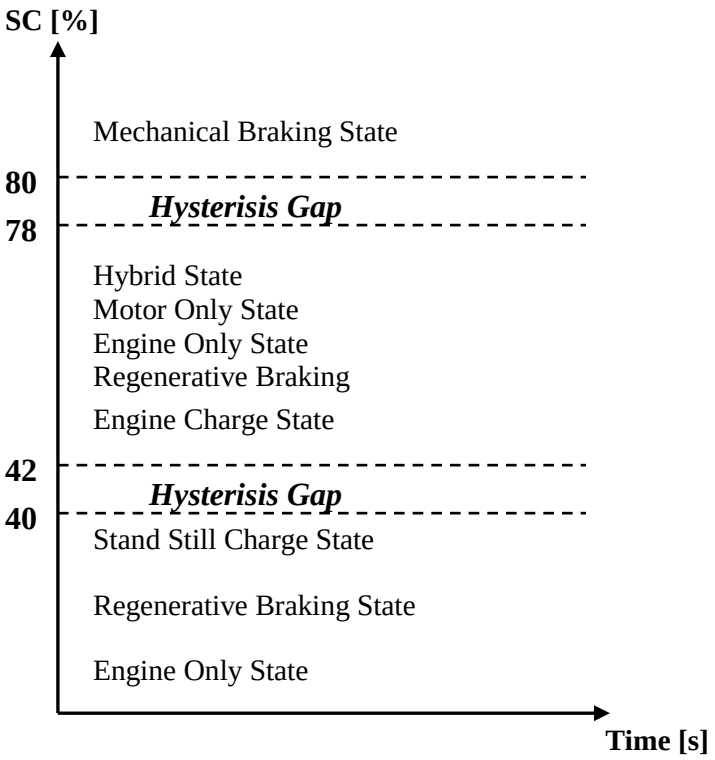

Figure 4.21: SC Threshold Values during Vehicle Operation

Motor Only State. This state operates during start-up conditions of the scooter. The maximum speed achievable by the Bug Escape Scooter in this state is 25 kmh^{-1}. Therefore this state is also suitable for speeds less than or equals to 25 kmh^{-1}. Although the boundary conditions are mainly governed by the speed of the vehicle, the battery's SC percentage plays a big part when choosing this state. A low SC (40 %) would not operate this state, as battery recharging is required. Refer to Figure 4.21 to check the threshold values for the battery's SC. These values provide a 'switch' between states when the threshold SC values are reached.

Idle Recharging State. This state operates when the hybrid electric scooter is not operating *i.e.* at idle conditions. This state basically recharges the batteries *via* a battery charger installed on board when a low SC (40 %) was detected in the system.

Engine Only State. This state is to be used as minimal as possible, which in turn reduces the emissions and the fuel consumption of the hybrid electric scooter system. This state is used when the torque and speed demand exceeds the maximum torque and speed available of the hub motor and the hybrid state. In this case, only the ICE power is needed.

Regenerative Braking State. This operation state can only occur in two cases; when the batteries are not over the upper threshold limit; in this case is 80 % of the full charge and

the demanded braking power is less than the maximum regenerative braking power. When determining the maximum desired braking power a number of factors must be considered. The first of these is how the regenerative braking is going to be used.

The new design it is to be used for both slowing the scooter when braking and also for charging the batteries from the ICE. If a large amount of charging occurred then the rider would be able to notice the reduction in performance of the scooter. This implies that small currents should be used. When considering the use of regenerative braking for the slowing of the scooter it is to be remembered that the control signal received from the rider is binary. To determine whether the rider is trying to brake gently or an emergency stop requires instantaneous signals and this is impossible in reality. As such the regenerative braking power should be low enough that it does not prevent the rider from gently applying the brakes. Once again, this implies that small current should be used. The final and most important consideration is safety. Since the regenerative braking is being applied to the front wheel of the scooter, it is essential that every endeavor be made to ensure that the wheel does not lock up. Such an event would cause a loss of control of the scooter.

To ensure that all the requirements were met, it was decided that a maximum current limit of 2 A be set. This sets the maximum braking power to be approximately 100 W. This power was considered to be small enough to meet all of the stated requirements.

From the speed threshold plot (Figure 4.20), the threshold values are defined for each propulsion unit on when to begin operation. The first speed threshold value (approximately 28 kmh^{-1}) was defined by realizing the maximum achievable motor speed (by referring to the given manufacturer's data). A hysteresis gap ($\pm$ 2 kmh^{-1}) was defined between the first and second threshold values. This hysteresis gap was defined to eliminate both the ICE and hub motor cycling on the on and off states. This unwanted effect might be present due to the noises generated during operation. Between the third threshold (40 kmh^{-1}) and the hysteresis gaps, the hybrid state propulsion system operates. Another hysteresis gap was introduced to eliminate the engine cycling effect. The Engine State was then to operate up to the maximum rated engine speed of 80 kmh^{-1} (maximum speed achievable by the engine).

Each possible operation state was defined in Figure 4.21, based on the SC level of the battery unit. A 40 % SC constitutes to a low SC and an 80 % SC constitutes to a maximum SC of the battery. Again, the hysteresis gaps are present to eliminate cycling charging at boundary points and conditions. Possible states (governed by the battery's SC) that can present during vehicle operation are shown in Figure 4.21. For low SCs, only three states can

be present; regenerative state, engine only state and stand still charge state. This is somewhat logical as a low SC shouldn't be operating the motor, instead generates enough energy to recharge the battery. Between the hysteresis gaps, several states are realized, as the SC is neither in full charge nor low charge, so mostly all states could happen during this time except the mechanical braking state. The mechanical braking state only happens when the battery is fully charged and no further energy is needed to recharge the battery.

Figure 4.22 shows the Controller Model developed. There are 2 user-defined codes; State Selector and Hybrid Optimizer functions. The state selector functions by analyzing threshold values based on Figures 4.20 and 4.21. It outputs the chosen state. The Hybrid Optimizer function is written to act as a controller, where for each state selected, the corresponding power and torque values are determined for the ICE and the motor based on the road load demands.

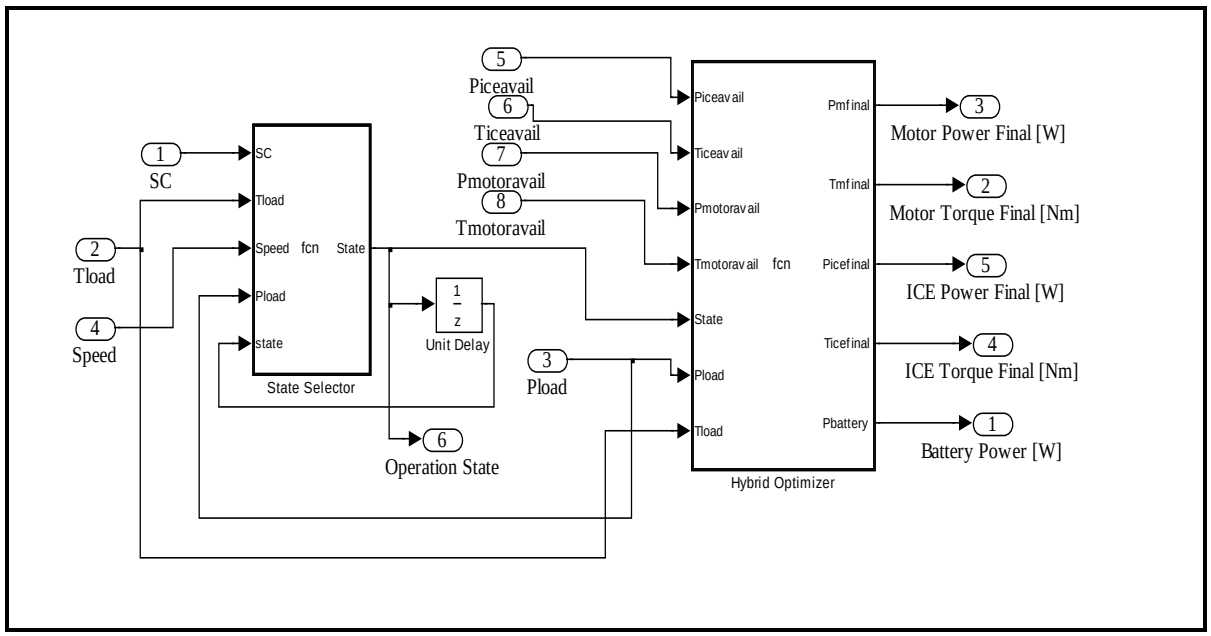

Figure 4.22: MATLAB-Simulink Controller Model – Level 1

Figure 4.23 shows a summary in terms of flow diagram for Figures 4.20 and 4.21. This was incorporated as a flow diagram in the State Selector Function This flow diagram clearly shows how the states are chosen based on logical expressions. For example, for a braking state to happen, the required torque (T_{Load}) must be less than zero and with a SC of less than 80 %, the regenerative braking state happens. If the battery does not requires any more energy, mechanical brakes are activated, to slow down the vehicle.

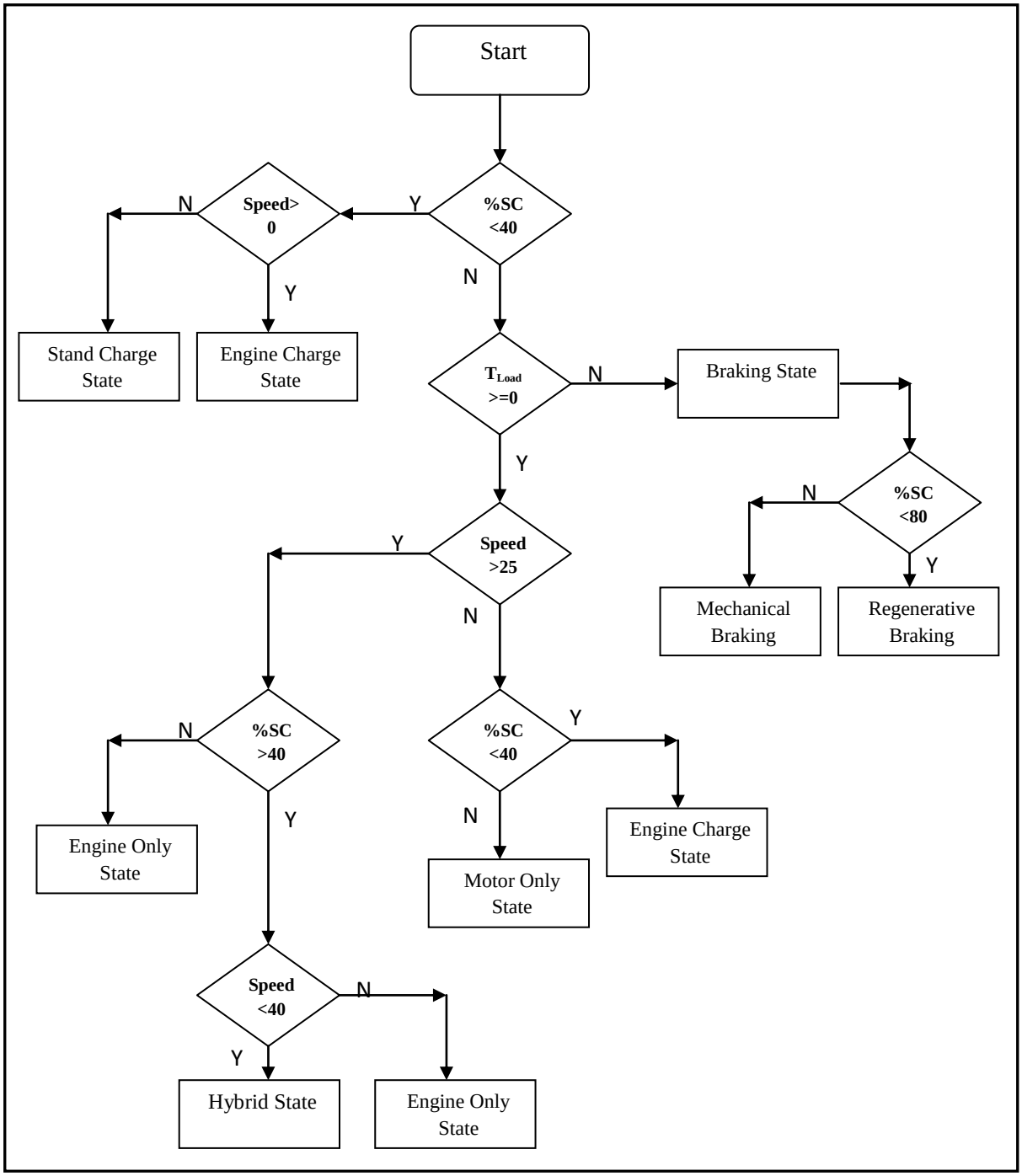

Figure 4.23: Control Block Diagram

Summarizing, the electrical hub motor provides propulsion for the hybrid electric scooter system during low-speeds, low-torques, and vehicle start-ups and provides extra power during accelerations. During highway cruising and deceleration, it will in turn recharge the battery *via* the generator on-board. The ICE provides propulsion during high-speeds, high torques as well as cruising conditions. Thus the states are operated (or 'switched') between each other based on two variables, the battery's SC and the vehicle speed. Figure 4.24 shows

the I/O of the controller of the Multi-State Controller Model implemented in MATLAB-Simulink.

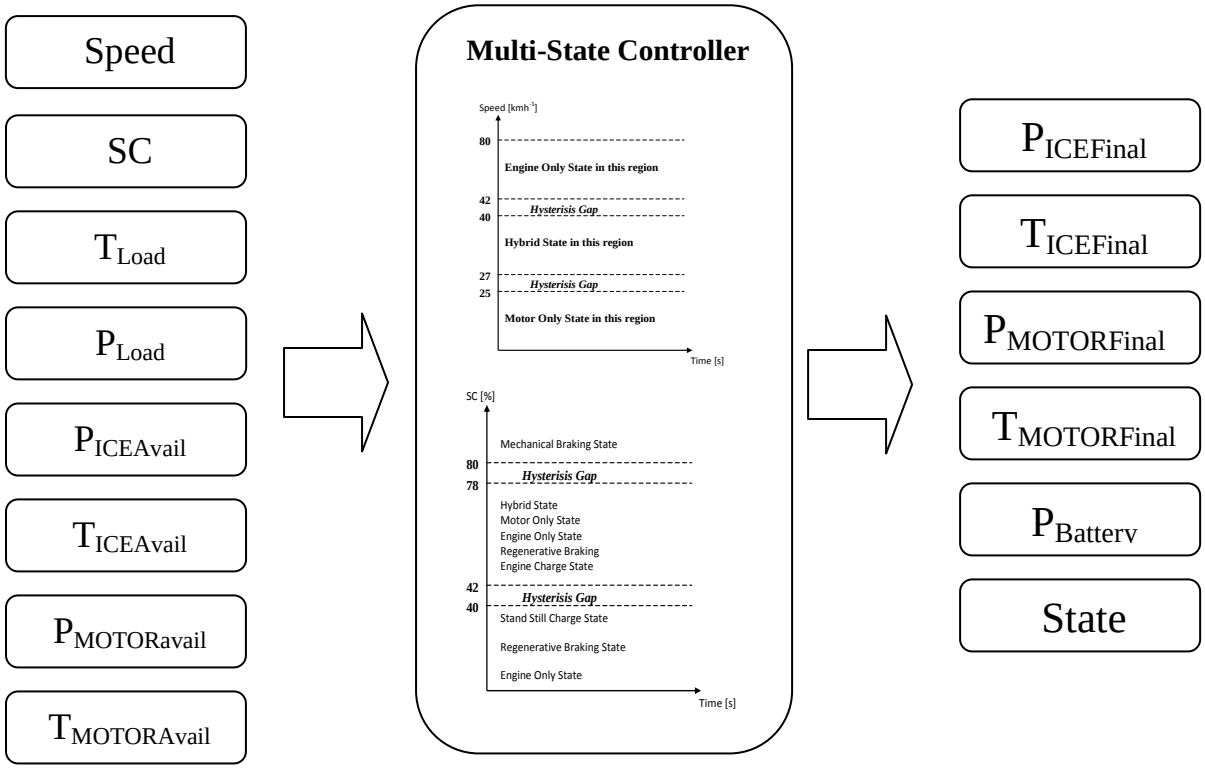

Figure 4.24: Control Operation Parameters

4.5 Overall Integration of HES Model

The main HES model and its flow as constructed in MATLAB-Simulink is shown in Figure 4.25 below. The figure is basically a summary of all the sub-models integrated together to form a complete HES Model. More in-depth discussion about the driving cycles used for this simulation will be outlined in the next chapter.

The input to the MATLAB-Simulink model is the vehicle speed where the speed was defined by the driving cycle. For every speed, the HES' road load torque and power demand are calculated in the Vehicle Dynamics Model. With the load power and torque demand known, the power and torque available for both the ICE and motor can be calculated. The available power and torque for both the ICE and motor together with the battery's instantaneous SC, speed and load power and torque demands are inputs to the multi-state controller.

The controller determines the optimum state the HES should be in and outputs the ICE and motor's power and torque levels. The engine control unit (ECU) will then control the

system based on the outputs of the controller. The system's emissions and fuel consumption were determined as well. Table 4.3 shows the descriptions of the labeled numbers.

The black dotted lines represent the MATLAB-Simulink flow for a conventional ICE scooter. Note that the ICE-only power and torque levels do not go through the controller as the controller was modelled for a hybrid configuration. The blue dotted lines represent an AED scooter flow in MATLAB-Simulink. The battery power was directly imputed to the Battery Model to get the battery's instantaneous SC. In another words, the conventional scooter was modelled based on the ICE data and the AED scooter was modelled using the hub motor as the propulsion unit. The ICE only and AED configurations are to enable the author to check how the propulsion systems react for the two types of scooters. Figure 4.26 shows the constructed HES model in MATLAB-Simulink. The orange results are for the AED and the blue one is for the ICE-only configuration.

No.	Description	Units
1	Speed	ms^{-1}
2	Power Demand	W
3	Torque Demand	Nm
4	ICE Power Available	W
5	ICE Torque Available	Nm
6	Motor Power Available	W
7	Motor Torque Available	Nm
8	State of Charge	%
9	ICE Final Power	W
10	ICE Final Torque	Nm
11	Motor Final Power	W
12	Motor Final Torque	Nm
13	Battery Power	W
14	Throttle Position	%
15	BSFC	g/kWh
16	Fuel Used	litres
17	CO	g
	CO_2	g
	O_2	g
	HC	g
	A/F Ratio	-
	Fuel Economy	g
18	ICE-only Power and Torque Final	W
19	AED Battery Power	W

Table 4.3: Overall HES Model Flow Diagram Description

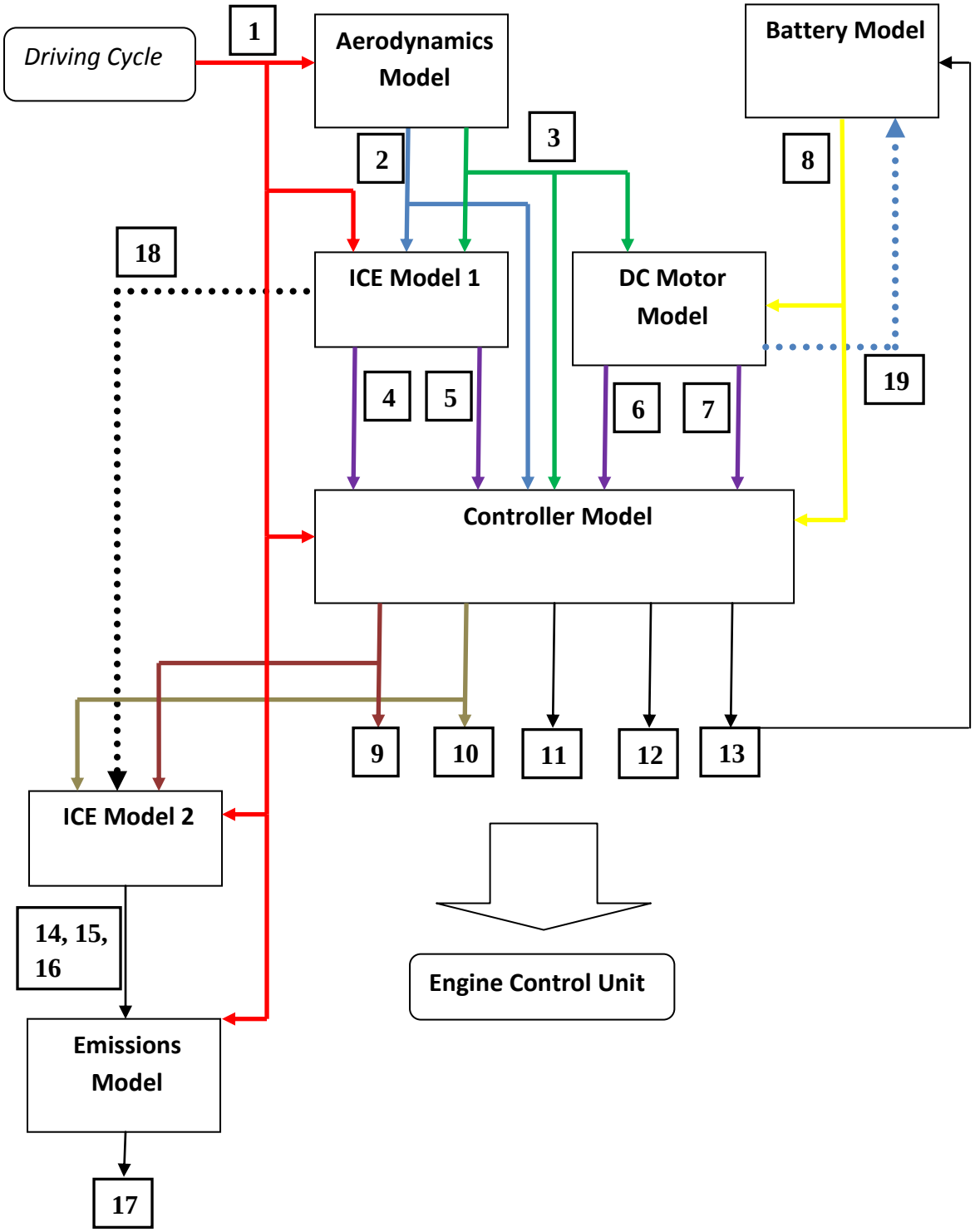

Figure 4.25: Overall HES Model Flow Diagram

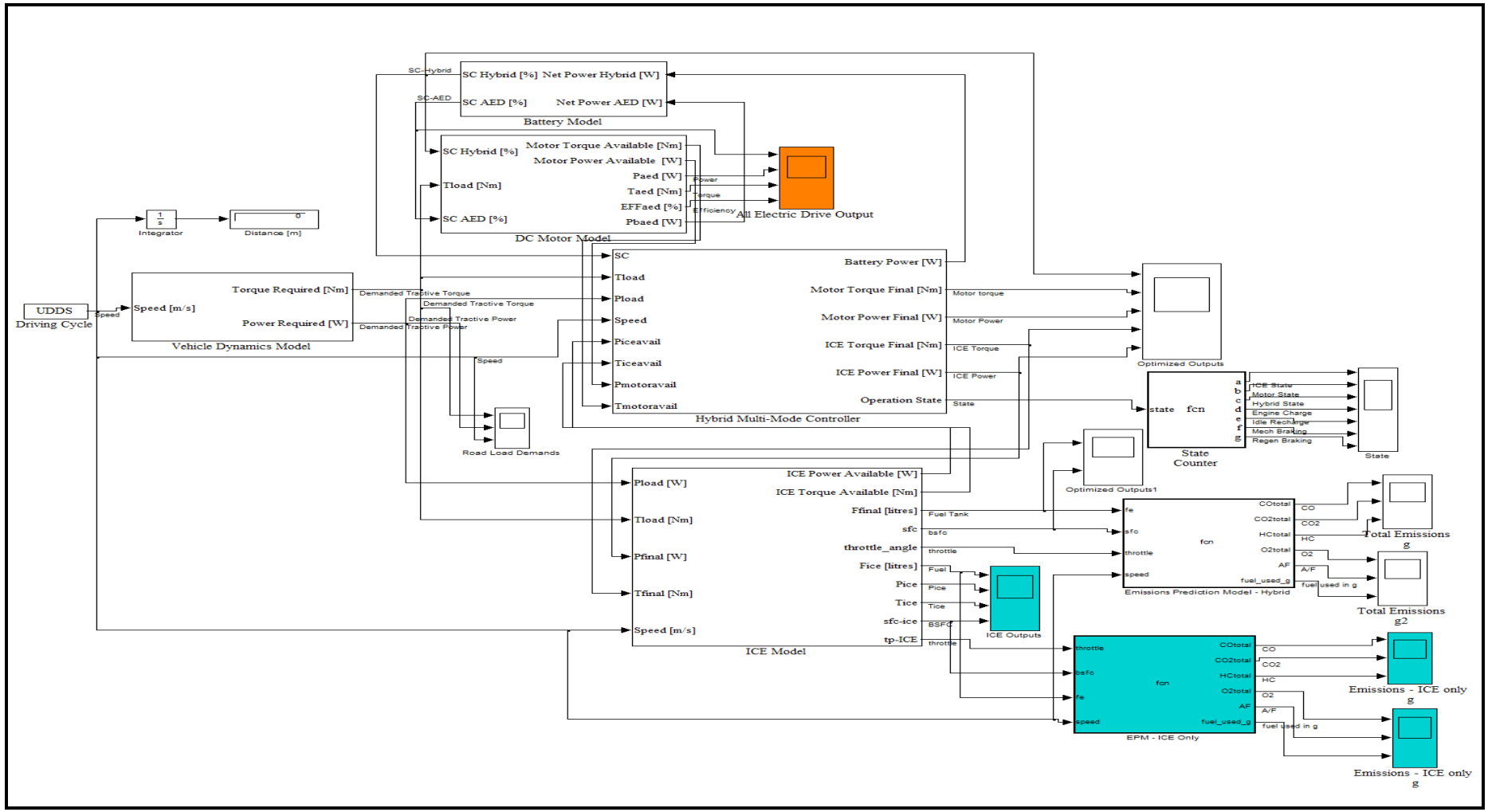

Figure 4.26: MATLAB-Simulink HES Predictive Model

4.6 HES Development

The second part of this chapter introduces and discusses the conversion of a conventional petrol scooter to a plug-in HES based on the MATLAB-Simulink model designed. Parallel hybrid scooters (or motorcycles in general) are extremely crucial in the reduction of harmful emissions. Applying the multi-state control strategy, a further reduction of the petrol consumption is believed to be possible, as modelling and simulation results showed. This step of the project is a crucial one as it is a physical representation of the author's model.

The second part of Chapter 4 comprises of four main sections. The first section is an introduction of the HES's architecture. The second section presents the development of the HES where a conventional petrol scooter was converted to a plug-in HES. The third section discusses the development of the multi-state controller based on the MATLAB-Simulink design. The last section presents some useful information about the constructed HES.

4.7 HES Model Architecture

Figure 4.27 below shows the HES model architecture and power flow. The solid lines are the possible power flows when operating the HES and the dotted lines are possible power flows during recharging procedures. This design also exhibits a plug-in feature where the battery can be charged on the electricity grid. This is suitable for overnight charging where the electricity tariff is lower compared to the day.

This drivetrain design can be termed as a plug-in series-parallel hybrid architecture. The DC motor is referred as the primary propulsion unit and the ICE is referred as the secondary propulsion unit. The two propulsion units may operate either together (in hybrid state) or independently (motor state or ICE state). For energy recovery and recharging purposes, a battery charger was installed to recharge the battery. The charger may be powered either by the ICE, during regenerative braking or by the electricity grid. During idle recharging and charging states, the charger is powered by the ICE whilst meeting the vehicle's load demands (if any). The regenerative braking state will recharge the battery as well. This is done by turning the motor to a generator. The captured braking energy will be used to recharge the battery.

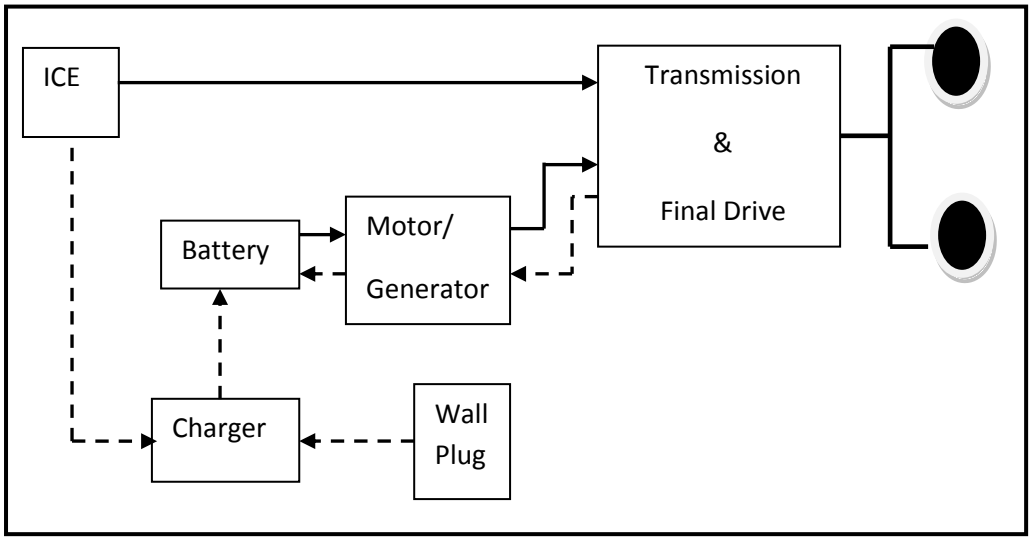

Figure 4.27: HES Architecture and Power Flow

4.8 HES Construction

This section discusses the physical conversion of a traditional petrol scooter to a plug-in hybrid electric scooter, with focus on selection of some selected components; the petrol scooter, DC motor, battery source and the incorporation of torque restrainers on the wheels. The constructed HES will be the platform for verifying our constructed emissions predictive models as well as for experimental data collection purposes. Each component mentioned is described below.

4.8.1 Scooter Selection

There were two main criteria for the selection of the base scooter. They were:

- That the scooter was able to freewheel without the ICE needing to rotate. This was intended to minimize the friction generated for the electric motor, as overcoming this friction and other external forces acting on the scooter would require extra energy.
- Sufficient storage room available for the addition of batteries and control equipment.

The chosen scooter was a Bug Escape 83 cc Oil Injected Two Stroke as shown in Figure 4.9. This vehicle was chosen due to its commercial availability in the market. The large amount of available storage space available under the seat was spacious enough to accommodate the battery, circuitry and cooling components. This scooter also had more open space around the rear wheel compared to other commercially available scooters. The scooter was tested on the chassis dynamometer during the modelling phase of this project.

4.8.2 DC Motor Selection

An electric hub motor was selected for this conversion. This selected permanent magnet DC hub motor met the following criteria outlined:

- Had power that was a significant fraction of the ICE (the majority of commercially available hub motors are under 200 W to allow unregistered and unlicensed use).
- Could be mounted in the front wheel where the diameter should be as closed as the original specification.
- Fitted between the forks of the scooter.
- Had (or could be adapted to have) a mechanical breaking system.

Finding a suitable motor had proved to be difficult and trade-offs were made. An unfortunate compromise that had to be made was the reduction in width of the front tire from 120 mm to 57 mm, as shown in Figure 4.28. This was due to the fact that no other suitable hub motors could be found which had a wider tire surface at the desired diameter.

Figure 4.28: Reduced Tire Surface Width from 120 mm to 57 mm

The chosen hub motor was a GL2 developed by Island Earth. The attached hub motor at the front wheel is showed in Figure 4.29. The motor's specifications are shown in Table 4.4. From this information the hub-motor has approximately one sixth of the power and torque of the ICE.

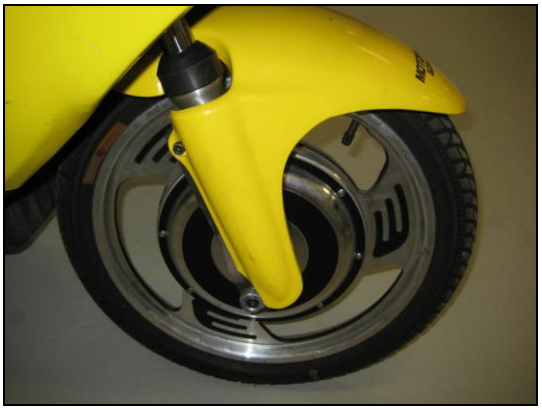

Figure 4.29: Attached Hub Motor

Max. Torque	48.42 Nm
Max. Power Ouput	642 W
Max. Speed	320 rpm
Max. Efficiency	84.89 % @ 12.38 Nm

Table 4.4: Island Earth GL2 Hub Motor Summary

4.8.3 Battery and Charger Selection

A sealed-lead acid (SLA) battery was chosen for this operation. The chosen battery is a connection of four 12 V 6 Ah (1 hour rate) batteries in series to give a 48 V 6 Ah battery setting, similar to the HES model presented in the first part of this chapter. The expected capacity is approximately half this value as a much heavier current was drawn. At maximum current and maximum speed, this gives an approximate scooter range of about 4 km. The data sheet for the SLA batteries are shown in Appendix C.

The location of the battery and other parts are located under the seat of the HES, below the fan, shown in Figure 4.30. The fan installed onboard was to maintain the temperature at a minimum as heat could easily build up in the compartment area under the seat, especially during charging.

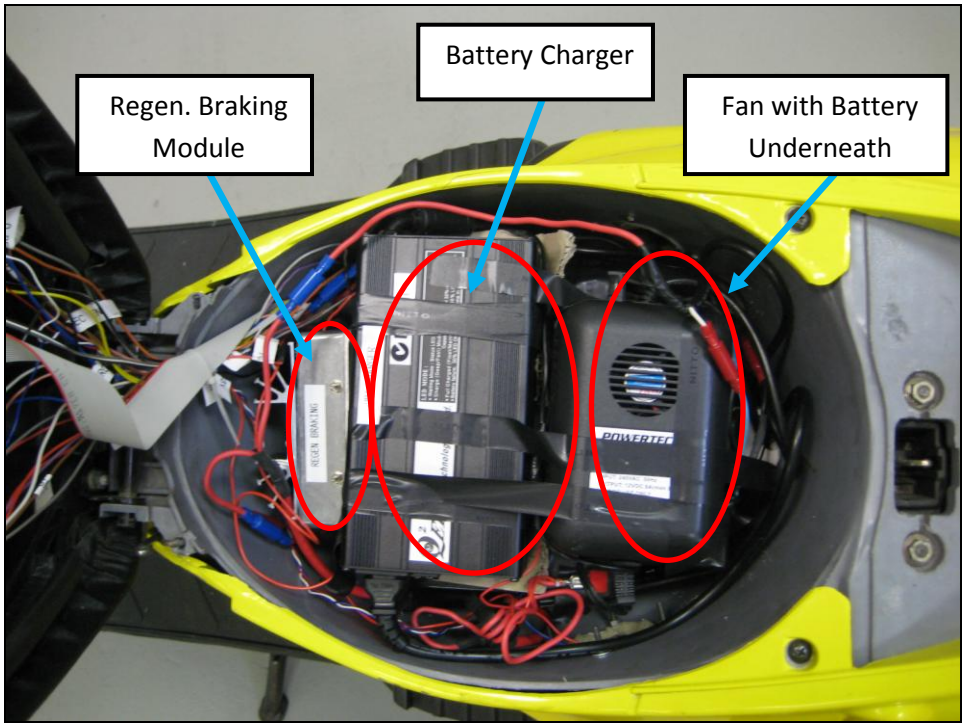

Figure 4.30: Underneath the Seat Compartment

The 48 V SLA battery charger used is developed by Quawin Electronics Co. Ltd. with an 81 % charging efficiency. This charger has a high frequency design which requires less power consumption. Another feature is that it has over-voltage protection, short-circuited protection and over-power protection, which is important in vehicular applications.

4.8.4 Torque Restrainer

The electric hub motor rotates around the axis and thus required to have a mechanical restrainer to prevent the axle from rotating when torque is applied. This mechanical restrainer is called a torque restrainer (or torque arm).

There are two sources of this torque. The first is the accelerating torque from the motor itself and the second is the braking toque derived from the disc brakes. Assuming the torque to be equivalent to the weight of the vehicle being applied at a distance of 0.1 m (radius of disc brake) [133]:

$$Torque_{Braking} = Mass \times Gravitational\ Acceleration \times BrakeDisc\ Radius = 147\,Nm \quad \textbf{(4.27)}$$

$$Force_{Braking} = \frac{Torque_{Braking}}{Axle\ Radius} = \frac{150 \times 9.8 \times 0.1}{0.01} = 14.7kN \qquad \textbf{(4.28)}$$

which is equivalent to 10 times the braking force. To counteract this force a strong torque restrainer was needed. As such, three 4 mm thick mild steel bars were attached to the front axle to prevent its rotation. Two of these torque restrainers are shown in Figure 4.31.

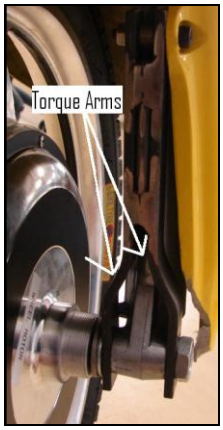

Figure 4.31: Torque Restrainers [133]

4.9 Controller Development

This section presents the other part of the HES development; the circuitry and the multi-state controller development, which is the 'brain' of the entire HES's operation and other issues such as power management, regenerative braking and mains charging. The control flow diagram of the physical HES is shown below in Figure 4.32.

As labeled, the dotted lines are control signals and the dark lines are physical connection lines. The 48 V battery is the main source to the primary propulsion unit, the electric hub motor. The 12 V battery is used to power the ICE. Both batteries can be charged in the mains electricity grid. Regenerative braking controller determines the regenerative current and is able to recharge the 48 V battery. Finally the rider will give user-driven signals such as start, stop, brake and acceleration to the multi-state controller.

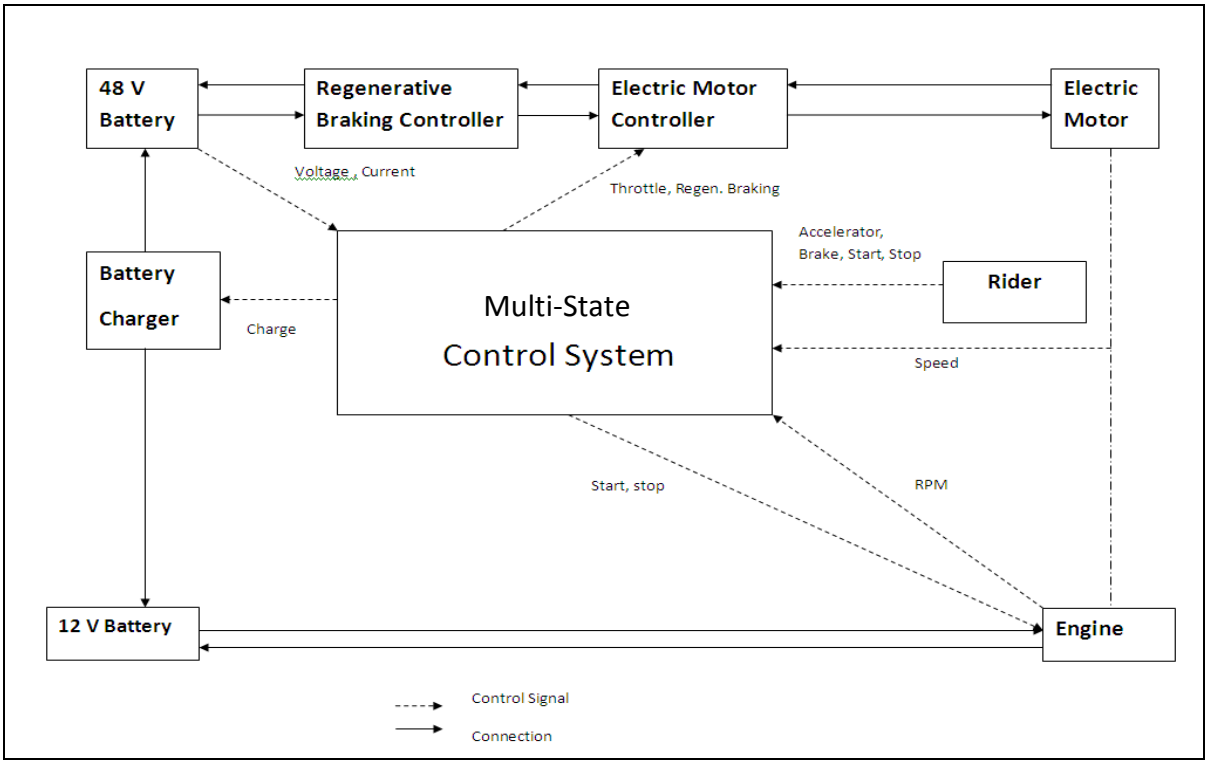

Figure 4.32: HES Control Signal Flow Diagram

4.9.1 Microcontroller Selection

A programmable PIC18F4520 (Figure 4.33) microcontroller was used. Some of the key features of the PIC18F4520 are shown in Table 4.5. This microcontroller was chosen because of the following advantages:

- Large amount of memory available,
- Available number of I/O pins and
- Resolution of the analogue to digital (A/D) converters.

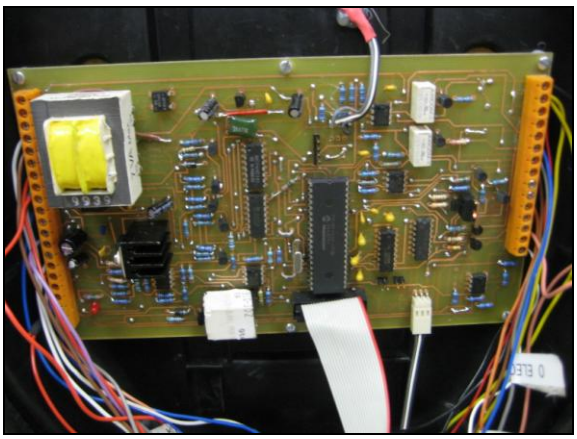

Figure 4.33: PCB Board under the HES's Seat

Device	Program Memory		Data Memory		I/O	10-bit A/D (ch)	CCP/ ECCP (PWM)	MSSP		EUSART	Comp.	Timers 8/16-bit
	Flash (bytes)	# Single-Word Instructions	SRAM (bytes)	EEPROM (bytes)				SPI	Master I^2C			
PIC18F4520	32K	16384	1536	256	36	13	1/1	Y	Y	1	2	1/3

Table 4.5: Summary of PIC18F4520 Features [137]

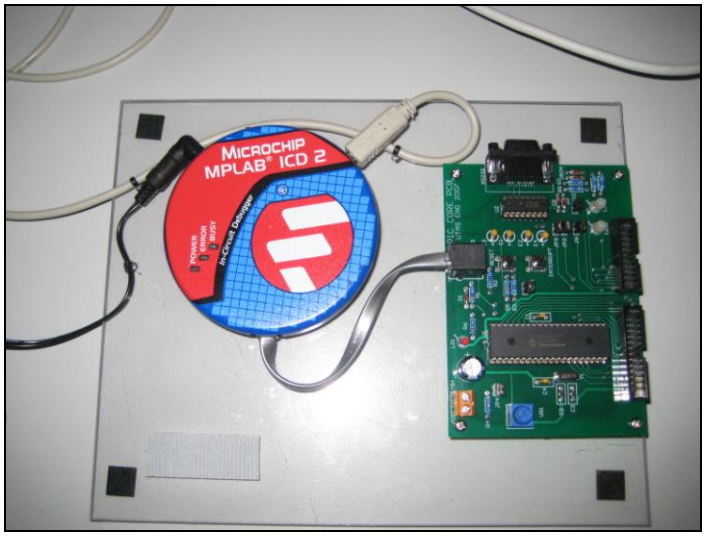

Figure 4.34: Microchip ICD 2 Programmer

The programmer software available for this device is the Microchip MPLAB ICD2 (Figure 4.34). This programmer has the dual functionality of also being able to behave as a debugger [137]. This tool allows execution of each line in the code for error checking purposes. This additional functionality also increases the speed of development since the process of debugging code is much simpler. Unfortunately, this extra functionality comes at the cost of the reservation of a number of memory locations and also three of the I/O pins of the controller. The use of an external crystal oscillator reduces the I/O count by a further two since it uses two of the I/O pins as the timing inputs to the controller. Thus the total number of available pins is down to 31.

The requirements for the multi-state control system are summarized in Table 4.6. From this table it can be seen that the total number of I/O pins required is 33. Clearly since only 31 I/O pins were available, an 8:1 multiplexer was used. Through the use of an 8:1 multiplexer the number of I/O pins required are now reduced to 29 I/Os (an 8:1 multiplexer requires three control pins plus the data signal), leaving 2 pins free for future expansion. Each I/O component is described in the following sections below.

Name	I/O	Type	Interrupt/Polled	Range
48 V Battery Current	I	Analogue	Polled	-10 to 25 A
48 V Battery Voltage	I	Analogue	Polled	25 V to 70 V
12 V Battery Voltage	I	Analogue	Polled	8 V to 18 V
Accelerator Position	I	Digital	Polled	0 V to 5 V
Engine Throttle Feedback	I	Digital	Polled	0 V to 5 V
Battery Temperature	I	Digital	Polled	0 C to 80 C
Electric Enable	I	Digital	Polled	
Petrol Enable	I	Digital	Polled	
Brake On	I	Digital	Polled	
Start Button	I	Digital	Polled	
Charger Connected	I	Digital	Polled	
Ignition On	I	Digital	Polled	
Kill Switch	I	Digital	Polled	
Fan OK	I	Digital	Polled	
Starter System OK	I	Digital	Polled	
Wheel Speed	I	Digital	Interrupt	0.2 Hz to 20 Hz
ICE Tachometer	I	Digital	Interrupt	1 Hz to 200 Hz
Regenerative Braking	O	Digital		
Electric Enable	O	Digital		
Electric Controller Throttle	O	PWM		
Start Engine	O	Digital		
Enable Charging	O	Digital		
Running Indicator	O	Digital		
Serial Data Transmit	O	Digital		once every second
Petrol Kill	O	Digital		
Run Fan	O	Digital		
LCD Control	O x 7	Digital		once every second

Table 4.6: Summary of I/O Requirements [133]

4.9.1.1 48 V Battery Current

The battery's charge and discharge current are monitored closely with the use of a hall-effect current sensor. The purpose of monitoring this current is to correctly determine the actual power flow in the scooter.

The current is measured using an analogue LOHET 650-554 hall-effect sensor. Based on Equation 5.3 and assuming a peak current of 30 A, a total of 4 turns of the power supply wiring were ran through the sensor to give a wide voltage output, V_{out}.

$$V_{out} = V_{offset} \pm k\left(\frac{0.00364NI}{I_g}\right)\frac{V_{cc}}{12} \qquad \textbf{(4.29)}$$

where I_g is the flux gap in toroid (in inches), V_{cc} is the supply voltage, I is the current through the conductor, N is the number of turns required, K is the correction factor (which is approximately equals to 1) and V_{offset} is the offset voltage (which was estimate to be half of V_{cc}).

The circuitry required for the sensor is a 9 V regulated power supply and the use of an operational amplifier summing circuit to remove the DC offset and hence makes the voltage level to the desired range. The power supply for the current sensor is shown in Figure 4.35 and the signal conditioning circuit is shown in Figure 4.36.

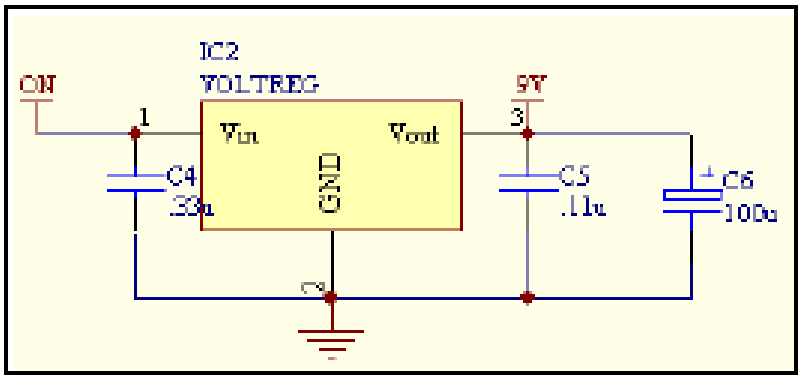

Figure 4.35: Current Sensor Power Supply [133]

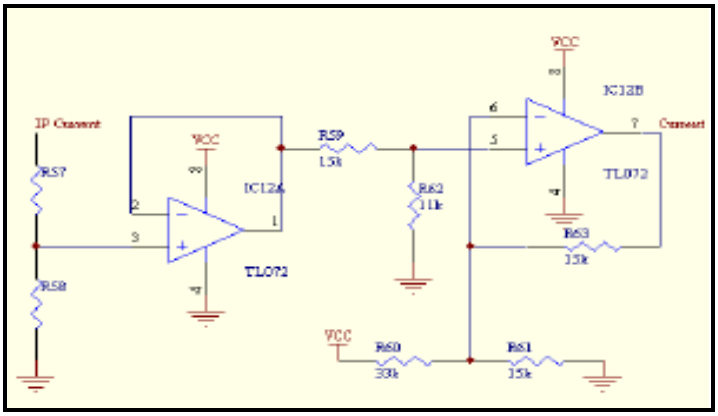

Figure 4.36: Current Sensor Signal Conditioning [133]

4.9.1.2 48 V and 12 V Battery Line Voltages

The 48 V battery voltage line was used for determining the SC of the battery system. This is a critical function of the multi-state control system since knowledge of the SC allows the controller to make decisions about which suitable mode to choose to operate the scooter.

The 12 V battery voltage line on the other hand is used to inform the rider about the condition of the 12 V battery. This information is critical since the HES relies on the battery for both powering the control system electronics and for starting the ICE. Thus, having ample knowledge about the battery's instantaneous conditions are critical. To sense these voltages, an operational amplifier was used. This summing circuit is to remove the DC offset and scale the signal according to the desired voltage range. The designed circuit is shown in Figure 4.37.

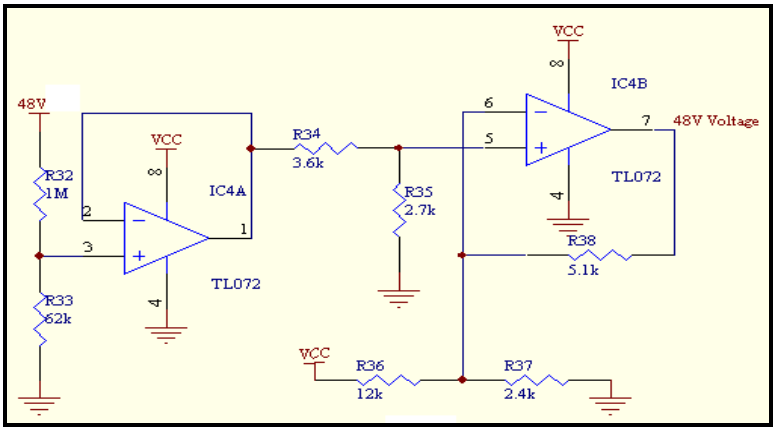

Figure 4.37: Battery Voltage Sensor Circuit [133]

4.9.1.3 Accelerator Position

The HES has retained the original twist grip throttle of the existing scooter. It has however, been adapted such that as well as directly providing the original cable throttle system to the ICE, it also gives an electric signal proportional to the position of the throttle. This electrical signal is produced by a potentiometer mounted in the end of the twist grip. This sensor installed will give information about the instantaneous throttle position, which is a critical variable during experimental testing.

The body of the potentiometer is restrained to the handlebars, while the adjustment knob is attached to the twist grip. The potentiometer's supply voltage is 5 V. An operational amplifier summing circuit would be implemented so that better resolutions could be obtained from the sensor. This was required since the potentiometer does not sweep the full scale when the accelerator is twisted and as such the output signal is not spread as widely as it should be. The circuit for the accelerator position sensing is shown in Figure 4.38.

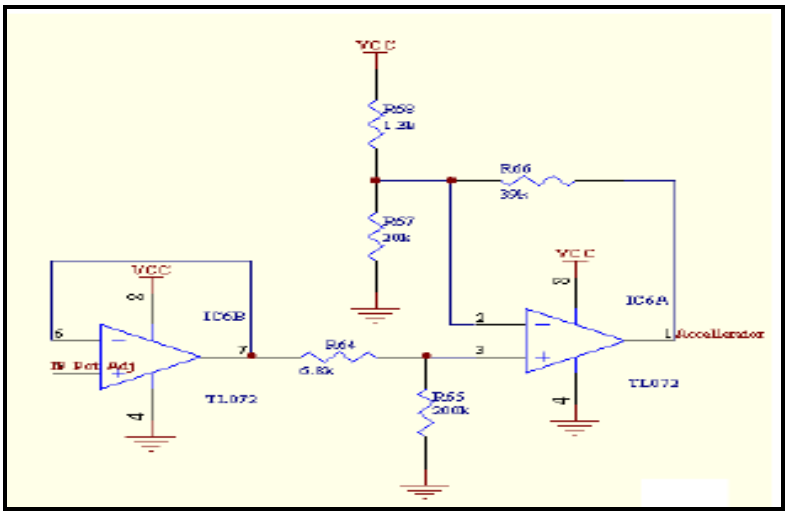

Figure 4.38: Throttle Sensor Circuit [133]

4.9.1.4 Battery Temperature

The storage region under the seat contains a number of components that could generate a significant amount of heat. As such, a temperature sensor was installed so that if the temperature gets to a certain threshold, the fan would operate to cool down the area. Any further temperature increase will enable the system to shut down itself. The fan operates automatically as well during idle charging (or overnight charging).

The temperature sensor is a LM335. LM355s provide a linear signal with slope of 10 mVK^{-1} [138]. This signal was put through a summing circuit as the approximate range of the signal was known and this enable a better understanding by increasing the resolution over this range. The full circuit for the temperature sensor is shown in Figure 4.39.

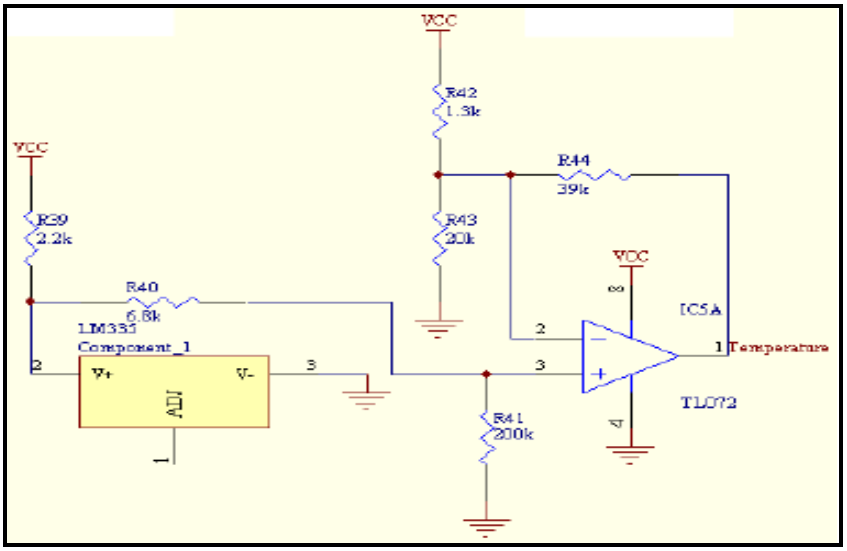

Figure 4.39: Temperature Sensor [133]

4.9.1.5 Electric and Petrol Enable

Specifically, the HES will be able to select between motor, ICE and hybrid modes. The design of the HES enables the rider to choose between motor, ICE and hybrid modes.

Figure 4.40: Electric, Petrol and Hybrid Modes Switches

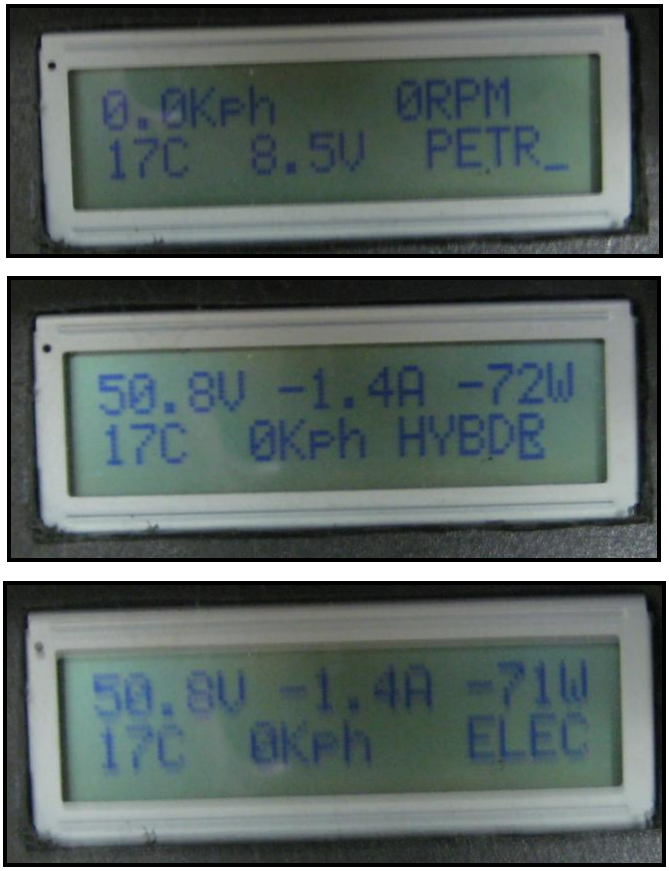

Figure 4.41: Dashboard Display

The selection of mode was implemented by two switches installed on board (Figure 4.40), one for electric and one for petrol. If both switches are turned on, the hybrid mode will come into effect. The dashboard displays accordingly to the mode chosen, shown in Figure 4.41. The design of this circuit is shown in Figure 4.42. The selected mode is then summarised in Table 4.7.

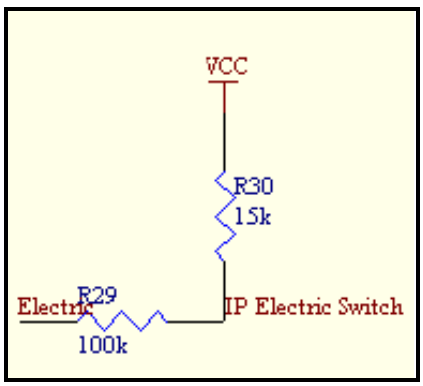

Figure 4.42: Manual Electric, ICE and Hybrid Mode Circuit [133]

Petrol Switch	Electric Switch	
	On	**Off**
On	*Hybrid*	*ICE*
Off	*Motor*	*Off*

Table 4.7: Switch Configuration

4.9.1.6 Kill Switch

The kill switch signal was used to know if the rider wishes to stop power being supplied from all power sources. Original configuration of this switch was to switch only the signal for shutting down the ICE. Unfortunately this signal was not suitable to use as an input to the controller, since the switch was used for pulling a floating wire to ground.

Fortunately, the switch was found to be of type dual pole, single throw, which allows connection of another signal to the same switch. This signal was then used to indicate to the controller that the rider wishes to stop all power sources. The design of the kill switch is shown in Figure 4.43.

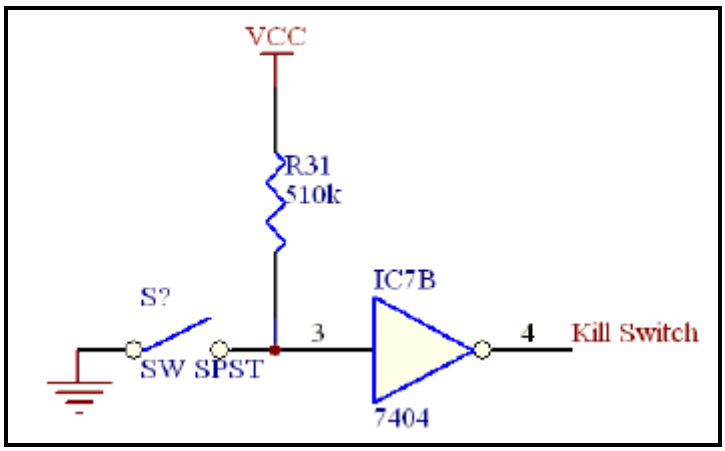

Figure 4.43: Kill Switch Circuit [133]

4.9.1.7 Petrol Kill

On the original scooter, whenever the kill switch was positioned in the ‘stop engine’ position the timing signal was removed from the ICE and it was stopped. As discussed in Section 4.9.1.6, the ‘stop engine’ signal corresponded to the input to the timing unit being connected to ground, while if the input was floating, the engine could run. This is poor design since all that needs to occur for the system to stop working is for the wire to get disconnected from the

timing unit and the engine could no longer be stopped (even turning the key off would not stop the engine since it uses the same method of switching this signal to the timing unit to ground to stop the engine.) This poor design could not be fixed since it is an intrinsic feature of the original scooter.

This same control signal was used for stopping the ICE when moving between different hybrid modes. To achieve this, a relay was used to switch the timing unit control wire to ground whenever it was required. As an attempt to increase the reliability and safety of the scooter, two relays were connected in parallel with each other and both switched to ground as required. This results in a system where if one of the relays fails in the open position (engine able to run) then the other switch is still able to control the scooter. However, in the extent that both relays failed (which is highly unlikely), the rider still has the kill switch and ignition switch option to turn off the ICE.

However, this is acceptable since it leaves the scooter in a safe state. When the control system is turned off the relays get left in the 'engine can run' position. This allows the rider to kick start the engine in the situation that the power supply to the control system fails. The control circuit for the relays is shown in Figure 4.44.

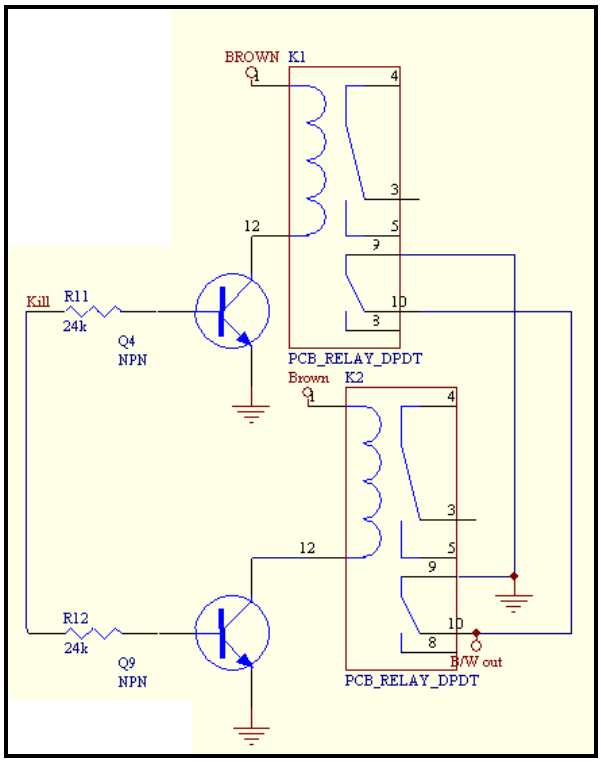

Figure 4.44: Petrol Kill Circuit [133]

4.9.1.8 Brake On and Ignition On

These signals are of common form. The brake on signal is derived from the existing signal on the scooter that is used for illuminating the brake lights. It signals that the rider has activated the brakes. This signal is used by the control system for turning off the electric motor control signal while braking and then enabling the regenerative braking.

The ignition on signal is used by the controller for knowing that the user has turned the key to the on position. This signal is then used as a requirement for the continued running of the scooter. All of these signals ranged from 12 V to 0 V (12 V for on and 0 V for off). The PIC18F4520 has a maximum input voltage of 5 V. As such we need to translate the voltage down to this level. This is done by using a bipolar junction transistor (BJT) as a switch to select between 0 and 5 V signals. The full circuit and design is shown in Figure 4.45.

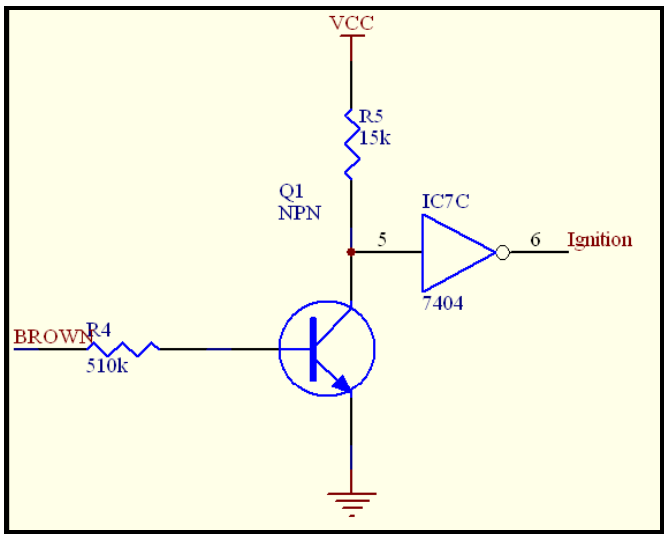

Figure 4.45: Brake On and Ignition On Circuit [133]

4.9.1.9 Start Button

The switch was wired so that when it was pressed, a 12 V signal was fed to the controller. This 12 V signal is derived from the ignition and as such adds the condition that for the controller to receive a start signal, the rider must have first turned the key on. This input signal is conditioned in the same way as the Brake On and Ignition On signals shown in Figure 4.45.

4.9.1.10 Charger Connected

This control signal was used to detect if the scooter has been plugged into a mains electricity supply for overnight charging. This is then used for disabling the scooter from being able to run when connecting the chargers to the batteries for charging. The sensing of the 240 V signal is done by first transforming the voltage down, rectifying it and creating a logic level signal. Since the charger could be connected whenever the ignition is turned off, it also desired that the logic signal could turn power back on to the controller. This was achieved *via* a relay.

A major concern when introducing a mains power supply to the system is safety. To make the scooter as safe as possible, the frame of the scooter has all been grounded. In addition to this, on the control circuit PCB, the signal ground and power ground have been connected together. Figure 4.46 shows the 240 V mains detection circuit. Figure 4.47 shows the switching circuit.

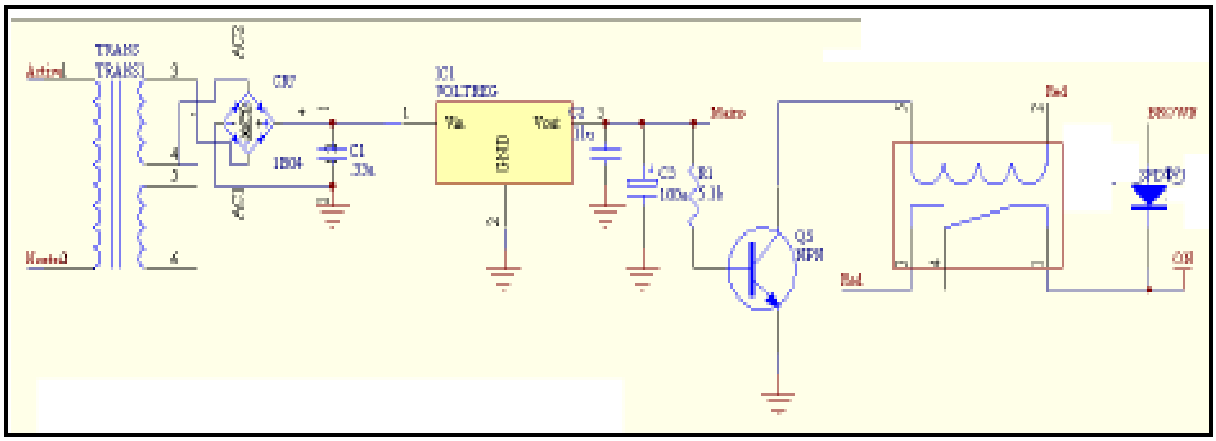

Figure 4.46: 240 V Mains Detection Circuit [133]

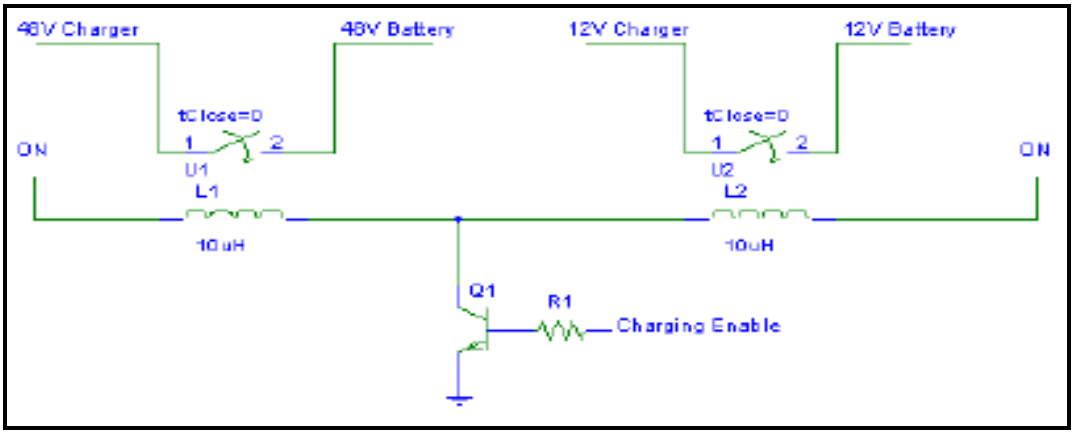

Figure 4.47: Switching Circuit [133]

4.9.1.11 Run Fan

To enable more cooling in the storage compartment, which houses the batteries and control system, an extraction fan has been installed. With a requirement to minimise power usage, the control system will start the fan only when it is required. This is done by switching the power supply to the fan on only when it is needed.

4.9.1.12 Wheel Speed

The speed of the vehicle determines which power source to use when it goes into hybrid mode. It is also used for displaying the speed information to the rider and for calculating the total distance travelled.

The existing scooter had an analogue cable driven speedometer which was connected to the front wheel. Since this wheel was replaced with the hub-motor, the system could no longer be used. As such a speedometer system based on passing a magnet past a digital hall-effect sensor was used. When designing this system the required number of magnets are to be mounted on the rear wheel such that enough pulses are able to be received for accurate calculations of the vehicle. The time, in seconds, between pulses is calculated by:

$$T = \frac{dN}{v} \tag{4.30}$$

where d is the perimeter of wheel in m, v is the vehicle speed in ms^{-1} and N is the number of magnets required.

From this calculation it was required that at least two magnets were required so that speeds of down to 5 kmh^{-1} could be determined. The hall-effect sensor used gives a logic level output that is 5 V when the south magnetic pole is in front of the sensor and 0 V when the south magnetic pole is not present in front of the sensor. It also contains a Schmitt trigger to prevent multiple pulses coming from the sensor when the magnetic field is changing. This results in the digital hall-effect sensor being very easy to interface to. The only additional circuitry for the sensor to work properly is a filter capacitor at the input to the microcontroller. This capacitor is required since the cabling to the speedometer passes close to the spark plug causing significant noise to be introduced which resulted in false speed readings. A 0.1 µF ceramic capacitor was connected between the microcontroller input and the ground to minimize the noise.

With that, the speed was then calculated by using the speedometer as the HES is normally operating at low speeds. At these speeds the time between pulses is relatively large and the slower update rate of the process of counting pulses in a fixed period becomes negligible.

The mounting of the wheel speed sensor was quite innovative. To simplify the installation of the magnets, they were mounted into wheel balancing weights which could then be simply installed onto the scooter. This makes the addition of more magnets for better resolution much easier since the magnets can be moved if required. The hall-effect sensor was mounted inside a bolt. Firstly, the bolt protects the sensor from damage, secondly this allows for the simple adjustment of the distance between the sensor and the magnets. The system is shown in Figure 4.48 with the sensor circled in red.

Figure 4.48: Wheel Speed Sensor

4.9.1.13 ICE Tachometer

The control system required the inclusion of a tachometer since it needs to know whether the engine is running. The designed tachometer takes advantage of the existing electronic timing unit from the scooter.

When observing this signal, it was noted that for low engine RPMs, the signal was approximately 20 V peak to peak, with symmetry around zero volts. As the engine RPM increases, this signal becomes larger and at maximum RPM, it was estimated to be 100 V

peak to peak. The signal also contains a large amount of noise and ripple. Clearly this signal is not suitable for direct interfacing to the control system. As such a circuit was created to condition this signal into logic level pulses that can be used by the microcontroller, as shown in Figure 4.49. The determination of engine RPM can be calculated in the same way as the wheel speed by counting the number of pulses in a fixed interval.

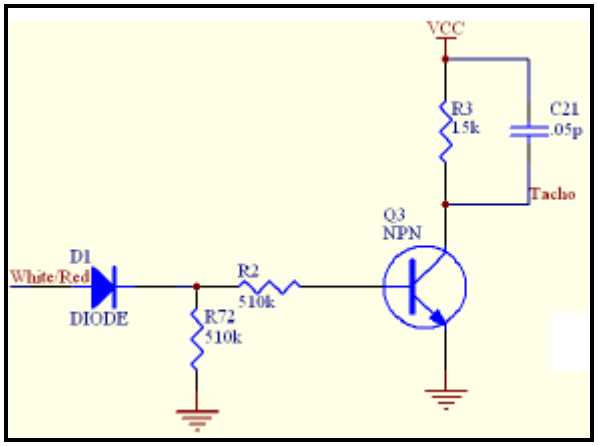

Figure 4.49: ICE Tachometer Circuit [133]

4.9.1.14 Electric Motor Enable

This signal is used for switching power to the electric motor controller. The microcontroller wiring diagram provided by the manufacturer was attached in Appendix C. By switching off the power to the electric motor controller, the motor will not be able to run and this increases the safety of the rider.

There are three requirements for the power to be turned on to the electric motor controller. Firstly, the ignition must be turned on, the rider has completed the required combination of brake and start button and electric mode must have been selected. The last two of these requirements are completed in coding form (as well as the ignition being checked to be on). However, the requirement that the ignition is on is also completed in hardware by the power to the relay being supplied by the ignition. Figure 4.50 shows the diagram from the controller output to the electric motor enable relay. The circuit for the switching of power to the electric motor is shown in Figure 4.51.

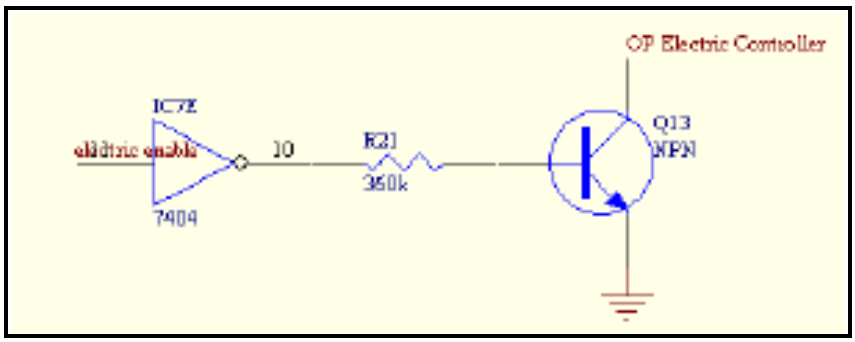

Figure 4.50: Controller Output to Relay [133]

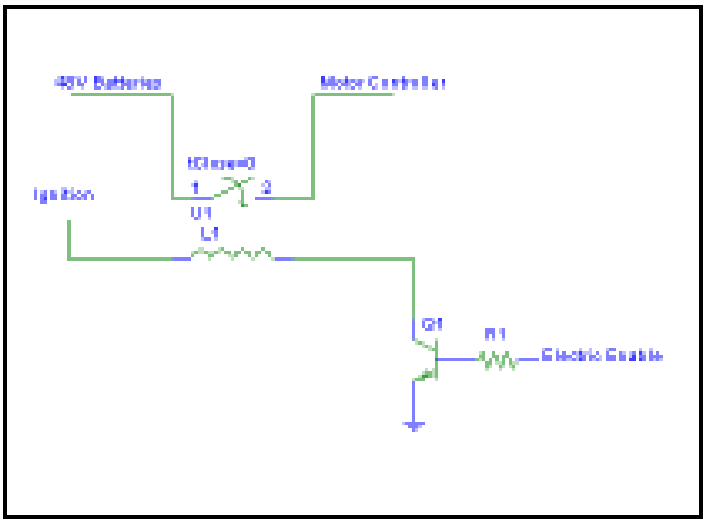

Figure 4.51: Switching Circuit [133]

4.9.1.15 Electric Controller Throttle

The electric motor controller takes a voltage signal in the range from 1 V to 4 V to control the power output of the motor, with the 1 V signal constituting to a minimum power and 4 V being the maximum power. This signal is normally generated from a twist throttle that is directly connected to the controller. However, the control system must be able to select the power produced by the electric motor. This, for example, allows the power control signal to be increased at times when it is determined that motor torque is needed, even when the rider has selected a position that would produce lower power if a direct connection to the controller from the accelerator had been made.

Unfortunately, the PIC18F420 cannot produce an analogue output signal. As such, the analogue signal has to be converted from the digital. The designed circuit is shown in Figure 4.52.

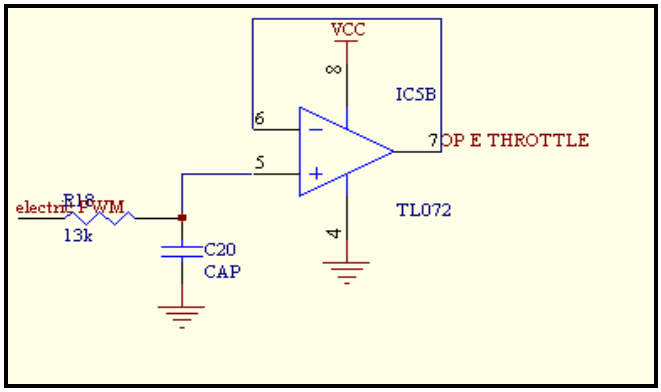

Figure 4.52: Electric Controller Circuit [133]

4.9.1.16 Start Engine

The existing engine starting system uses a relay to switch power to the starter motor. To start the engine on the original scooter, the user needed to apply the brake while pressing the start button. This system worked by the brake signal providing 12 V to one side of the relay and pressing the start resulted in the other side being grounded.

It was originally intended that this relay would be replaced with an N-type MOSFET on the ground return from the starter motor. However, on investigation of this design, it was found that this ground wire was the ground line to the frame of the scooter and also for the spark plug. As such placing an N-type MOSFET in this circuit would result in the scooter no longer working. An alternative to this approach would be to place a P-type MOSFET in the 12 V supply, however, none with a suitable current rating were available at the time. As such an alternative system that kept the relay was developed. Instead of switching the power to the motor directly as originally intended, we instead switched the current to the relay using an N-type MOSFET.

This system worked well until during testing when the MOSFET failed as a short circuit causing power to be supplied to the starter motor which started the engine. Although this problem occurred during an unusual fault, it was decided that the safety of the scooter should be increased by adding a second N-type MOSFET in series with the control MOSFET. This MOSFET is to be switched by the ignition signal so that the condition of having to have the key turn on for the motor to start is enforced.

4.9.1.17 Running Indicator

Due to the silent nature of the electric motor and the scooter's nature of having the engine turned off when sitting still in hybrid mode, we need some form of indication that the scooter is running and will supply power if the accelerator is twisted.

This indication is to be done visually using a light emitting diode (LED). Ideally this indication would be done both visually and audibly so that the rider is aware of the scooters state without the need to look at the indicator light. It was decided however that visual indication would be adequate for the purposes. To ensure that the visual indication is easy to observe the LED was placed close to the start button on the right handlebar on the scooter.

4.9.1.18 Serial Data Transmit

To allow simple data logging, an RS232 compatible serial port was added to the scooter. This allows the user to plug in a computer and obtain information about the current state of the scooter. This is useful for debugging purposes and also for testing the scooter.

The development of the RS232 interface is made simple on the PIC18F4520 by the use of the onboard universal synchronous, asynchronous receiver transmitter (USART). Since transmission of serial data is a common task, the USART is a common feature of modern microcontrollers. To transmit serial data using the USART we initially configure the settings for the serial port, then simply pass data to the serial port which is then processed and sent.

Figure 4.53: RS232 Serial Port

The data is transmitted at 9600 baud, 8 data bits with 1 stop bit, no parity and hardware flow control. To enable simple manipulation of the data when received a comma

delimited format with line brakes to terminate each line was used. This makes the output compatible with the standard comma separated variable (CSV) file type and allows the data to be quickly imported into Microsoft Excel.

4.9.1.19 LCD Control

The control of the LCD requires seven I/O pins of the microcontroller. Four of these are for the transmission of data, one for LCD enable, one for selecting which register to write to and another for selecting the read/write mode. The control code for the LCD and the LCD PCB used for the project were both the University of Tasmania's School of Engineering standard design and are not detailed here. The reader should refer to the School's documentation for the design and use of these components [139].

4.9.2 Mains Battery Charging

The HES has a grid charging ability, straight from a standard power point. This enables the rider to recharge the 48 V battery when a power point is present. This was achieved using a standard battery charger directly connected to the batteries. Of course, the battery charge should not be left directly connected to the charger during usage to prevent static discharge through the charge. Figure 4.54 shows the charging plug installed in the lower right of the HES.

Figure 4.54: Charge Plug Installed

4.9.3 Manual Start Requirement

Due to the freewheeling nature of the scooter, the ICE cannot be started automatically unless the existing starting system is working (primarily the greatest source of possible malfunction

is the starter battery). If the ICE starting system failed then the control system is unable to automatically start the engine. To still allow maximum usability of the scooter, if the starting system is detected to be not working, the user can either continue to ride under only electric power, or may choose to manually start the scooter. The control system is designed in a way that if started manually, the ICE will not be stopped unless explicitly requested by the user (kill switch or ignition switch).

4.10 HES Operation Procedures

This section briefly explains the required steps to be follow in order to start, stop and charge the HES. Also, information about long term storage of the HES was discussed as well. Figure 4.55 displays the parallel plug-in HES developed based on the mathematical MATLAB-Simulink model.

Figure 4.55: Parallel Plug-in Hybrid Electric Scooter

4.10.1 HES Startup Procedure

The startup procedures for the designed HES are shown below:

1. Select desired driving mode using “Electric” and “Petrol” switches as shown in Table 4.7
2. Turn the ignition key to the “on” position.
3. Turn kill switch to run.
4. Engage brakes while pressing start button (red) on right handlebar.

5. Red LED will turn flash to show that scooter is running. If ICE mode is selected, the ICE will start.
6. Twist throttle to start riding as normal.

Note that if petrol or hybrid mode is selected then scooter can also be kick started after Step 3. The rear brake needs to be adjusted to suit the rider's weight. Adjust before riding by turning nut at rear brake arm clockwise for lighter riders, anticlockwise for heavier riders. When set correctly rear brake should activate after small amount of movement of the brake handle.

4.10.2 HES Stopping Procedure

There are three primary methods to stop the HES during operation. They are:

1. Move kill switch upwards to don't run position.
2. Turn the ignition to off.
3. Power is also removed from the scooter if off mode is selected on the switches.

4.10.3 HES Charging Procedure

When the HES is not in use, it can be charged from a power point using the provided power cord. The charging procedures are:

1. Check that mode switches are both set to off and that the kill switch is onto prevent scooter from running.
2. Open front glove box.
3. Plug power cord into socket (with the power cord adapter) and turn on power point.
4. A number of fans will start running on scooter indicating charging has started. Note that there is an indicator light on the 48 V battery charger showing charging process and the charging percentage (located at the side of the charger).

Note that the HES can be left charging indefinitely without damage. To stop charging reverse Steps 1-4.

4.10.4 Long Term Storage

Before long term storage the batteries should be fully charged. Ignoring this will certainly reduce the life of the batteries. After charging, remove the positive terminal from both 48 V battery and starter battery (behind panel at right side of scooter) to prevent natural discharge.

4.11 Conclusion

The first part of this chapter discusses about the construction of the HES predictive model using the MATLAB-Simulink platform. The second part of this chapter introduces and discusses the results and model appraisal for the HES model developed. Having a feasible and accurate computer model of the physical hybrid scooter is important as troubleshooting can be done in the design phase instead after the prototype was built, in order to minimize cost. The user-defined codes of the MATLAB-Simulink models are attached in Appendix A at the end of this research thesis.

Having the HES properly constructed (as detailed in the second part of this chapter) provides a platform in tailpipe emissions modelling and fuel economy predictions for HES applications. The HES provides a link between modelling using MATLAB-Simulink and ANN for emissions prediction for a better understanding of the accuracies and predictability. This is because the MATLAB-Simulink HES model simulates the fuel economy and the emissions based on the driving cycles and the ANN model simulates emissions based on the HES's operating conditions. Thus the constructed HES, after verification with the MATLAB-Simulink model, enables the MATLAB-Simulink and ANN models to be simulated in parallel to better understand, not just the fuel economy and emissions, but also the necessary operating conditions of the HES. The relevant datasheets are attached in Appendix C.

Having constructed the HES model on MATLAB-Simulink, Chapter 5 will present the simulation results of the HES model. The accuracy and robustness of the HES model will be simulated and the simulated results are then compared to experimental results to validate the HES model.

CHAPTER 5: HES PREDICTIVE MODEL APPRAISAL AND SIMULATION RESULTS

5.1 Introduction

This chapter presents the model appraisal and simulation results of the hybrid electric scooter (HES) model developed in MATLAB-Simulink discussed in the previous chapter. Driving cycles were used to simulate the HES model for fuel economy and emission levels.

This chapter comprises of two main sections. The first section (Section 5.3) is the HES model appraisal results. This section discusses the validity and accuracy of the developed HES model by comparing experimental data with the computer simulated data. The ICE data were compared to the experimental data in terms of fuel economy and emissions over a modified driving cycle. The HES model was then simulated under the Standard European Driving Cycle (ECE-15) driving cycle and the results are compared to the literature for further validation of the HES model's feasibility. Error analysis and appraisal of the model are also discussed.

The second section of this chapter shows further simulation results for the other 3 driving cycles; Modified Urban Dynamometer Driving Schedule (UDDS), New York City Cycle (NYCC) and Modified Highway Fuel Economy Driving Schedule (HWFET). This section (Section 5.4) demonstrates, by having an accurate HES model, the torque splits between the power sources as well as the emissions and fuel consumption can be properly predicted and analyzed. The fuel economy and emissions of the HES can be modelled and observed over the four distinct driving cycles.

5.2 Driving Cycles

Driving cycles are standardized driving patterns produced by different countries and organizations to assess the performance of a vehicle, which can describe by a speed-time plot. The performances assessed are normally the fuel consumption and tailpipe emissions. These performances are assessed on a chassis dynamometer. The four driving cycles applied during model simulation in this project are briefly discussed below.

5.2.1 Standard European Driving Cycle

The Standard European Cycle (ECE-15) is a European driving test schedule. This driving cycle represents urban driving in European countries. It is characterized by low vehicle speed, low engine load, and low exhaust gas temperature. This driving cycle has a peak speed of nearly 14 ms^{-1}. The average speed of this cycle is 4.95 ms^{-1} with a duration of 200 s. The total distance is just less than 1 km. The speed *vs* time plot is shown in Figure 5.1.

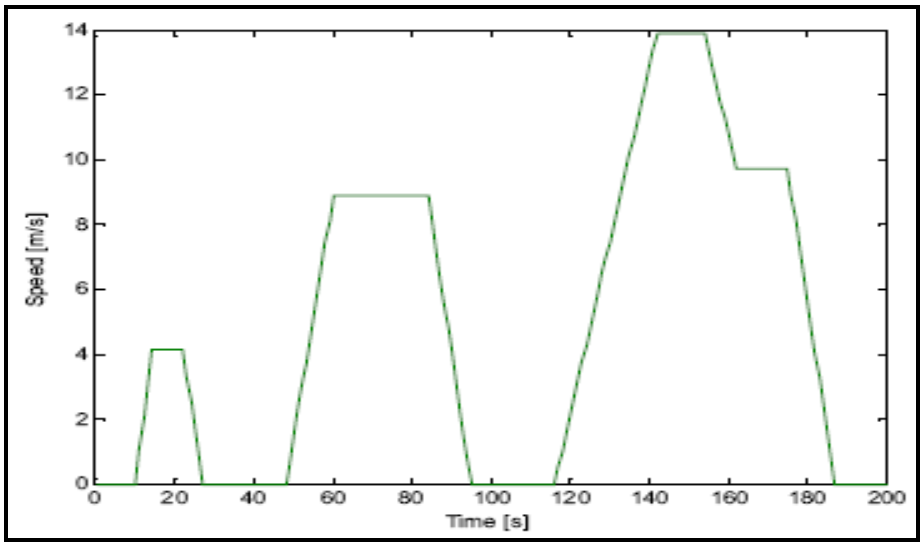

Figure 5.1: ECE-15 Driving Cycle

5.2.2 Modified Urban Dynamometer Driving Schedule

The modified Urban Dynamometer Driving Schedule (UDDS) is an American driving cycle standard. This driving cycle presented to simulate the HES MATLAB-Simulink model is a modified UDDS cycle. It still retains the original UDDS cycle characteristics of simulating an urban route with frequent stops and go. The difference is that the maximum speed (happens between 200 s to 400 s) is lowered to cater for the HES, which has a maximum speed of just about 22 ms^{-1}. The total distance is 10.98 km. This driving cycle is normally applied for light-duty vehicles. Alternative terms used for the UDDS cycle include the AD27 driving cycle (in Australia) and the CVS cycle (in Sweden). Maximum speed is just over 16 ms^{-1}, average speed of 8.0 ms^{-1} with the duration of 1400 s. This driving cycle is shown in Figure 5.2.

5.2.3 New York City Cycle

The New York City Cycle (NYCC) driving cycle was chosen due to its stop and go characteristics. It is used to simulate urban driving similar to New York City in the United

States. This driving cycle features low speed traffic conditions. The maximum speed is just over 12 ms^{-1}. The average speed is 3.16 ms^{-1} with a duration of 600 s. The total distance is 1.89 km. The plot is shown in Figure 5.3.

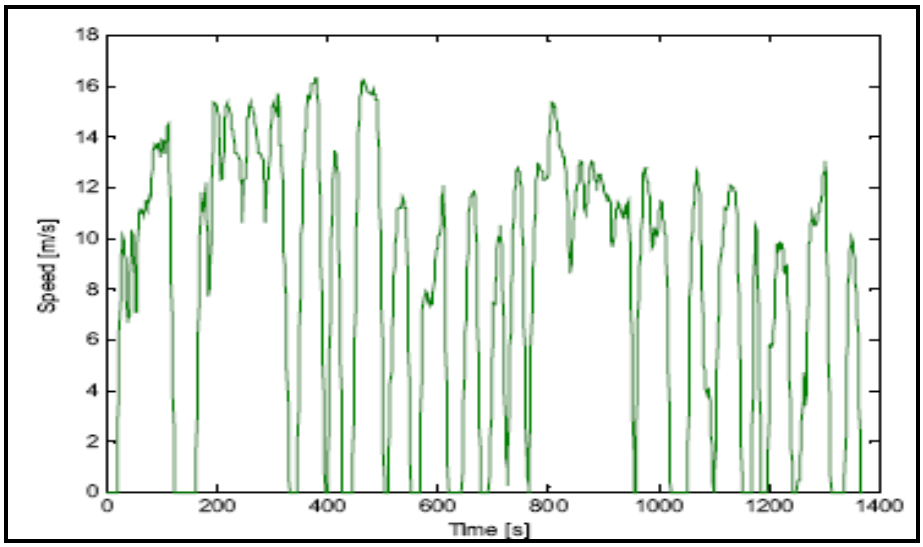

Figure 5.2: Modified UDDS Driving Cycle

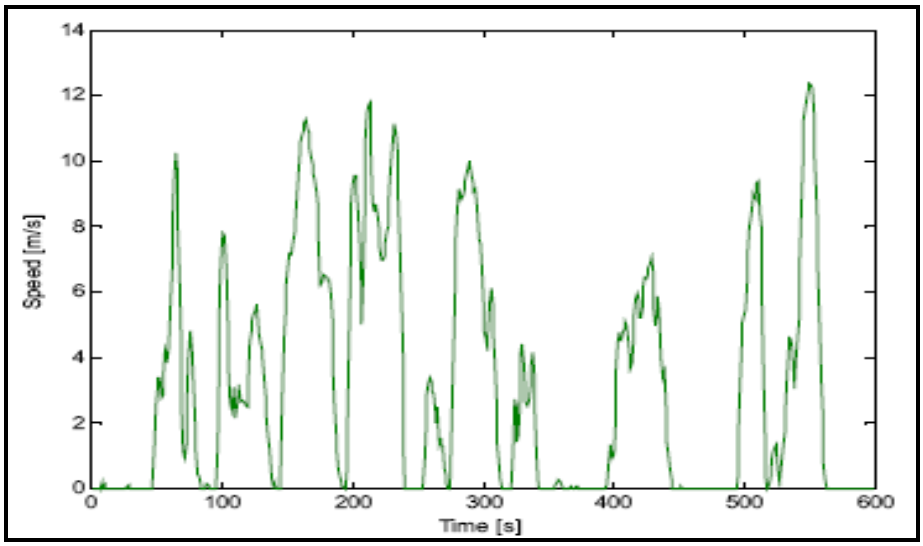

Figure 5.3: NYCC Driving Cycle

5.2.4 Modified Highway Fuel Economy Driving Schedule

The modified Highway Fuel Economy Driving Schedule (HWFET) is a chassis dynamometer driving schedule, developed by the US EPA for the determination of fuel economy for light duty vehicles in a highway condition. The only modified characteristic is that a maximum speed limit threshold of the HES had been incorporated to the original HWFET cycle. For

speeds below 20 ms^{-1} follows the original HWFET. For speeds over 20 ms^{-1}, the speed is set constant. This constant speed depicts an ideal highway condition with the maximum speed being limited to the HES's. The modified HWFET has a peak speed of 20 ms^{-1}, average speed of 18.92 ms^{-1} with a duration of 799 s. The total distance is 14.51 km. Figure 5.4 shows the driving cycle plot.

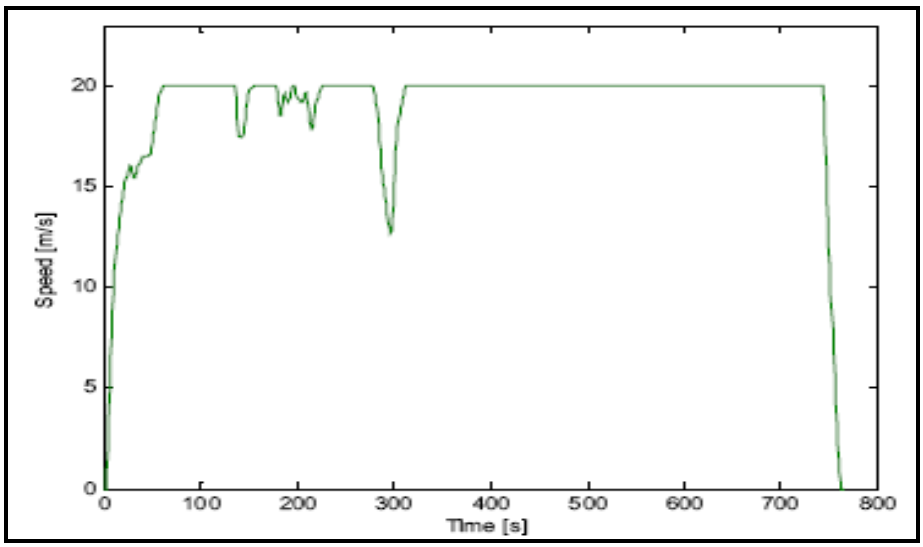

Figure 5.4: Modified HWFET Driving Cycle

5.3 HES Model Appraisal

This section shows the verification of the HES model against experimental data collected. This section also discusses about the validation of the ICE Model by investigating the four experimentally-measured throttles. This verification also provides a worst case scenario for a HES, in terms of fuel economy and emissions.

The ICE Model was verified in terms of fuel economy and emissions. The test involved is the fuel economy test where the model was simulated using the modified ECE-15 driving cycle depicted in Figure 4.12. The four tested throttle openings are 25 %, 50 %, 75 % and wide open throttle (WOT). The measured variables are the fuel economy and the total emissions over the driving cycle.

Figure 5.5 shows the simulated fuel economy for the modified ECE-15 driving cycle. The total fuel used for WOT is 76.10 ml, 75 % throttle is 73.40 ml, 50 % throttle is 59.30 ml and 25 % throttle is 44.80 ml. For low throttles, 25 % and 50 %, the actual speed was not achieved fast enough as the low throttles produced a low acceleration rate. In another words, the speed was limited for lower throttles.

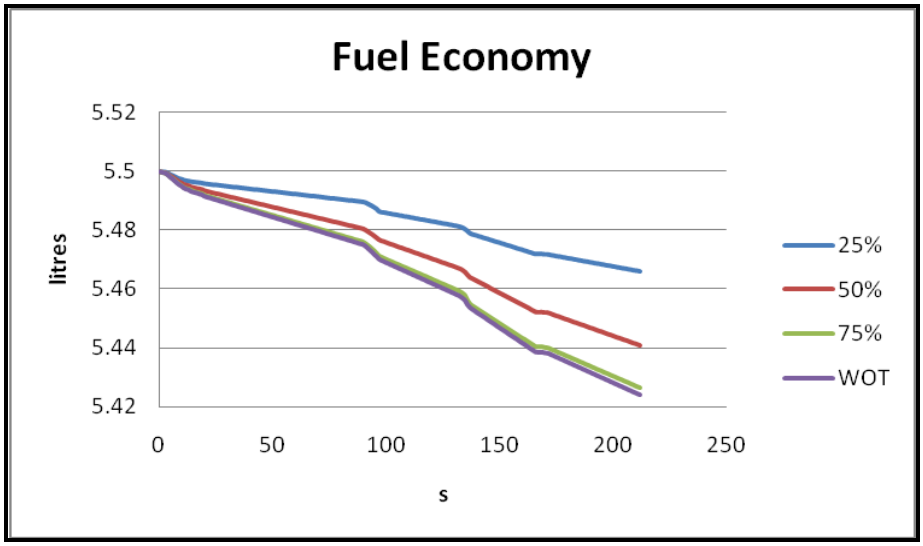

Figure 5.5: Fuel Economy for the Modified ECE-15 Cycle

Figure 5.6 shows the brake specific fuel consumption (BSFC) for the 4 throttles over the modified ECE-15 cycle. It can be seen that for 25 % throttle, the BSFC stay fairly constant at around 250 g/kWh. The recomended BSFC value for SI engines is between 200 g/kWh to 300 g/kWh [28]. From the figure, lower throttles have a lower average BSFC. Alhough that is the case, lower throttles have a lower acceleration rate, hence to achieve the desired speed requires a longer time. This is not feasible in the real world as the desired speed have to be achieved following the rider's throttle request.

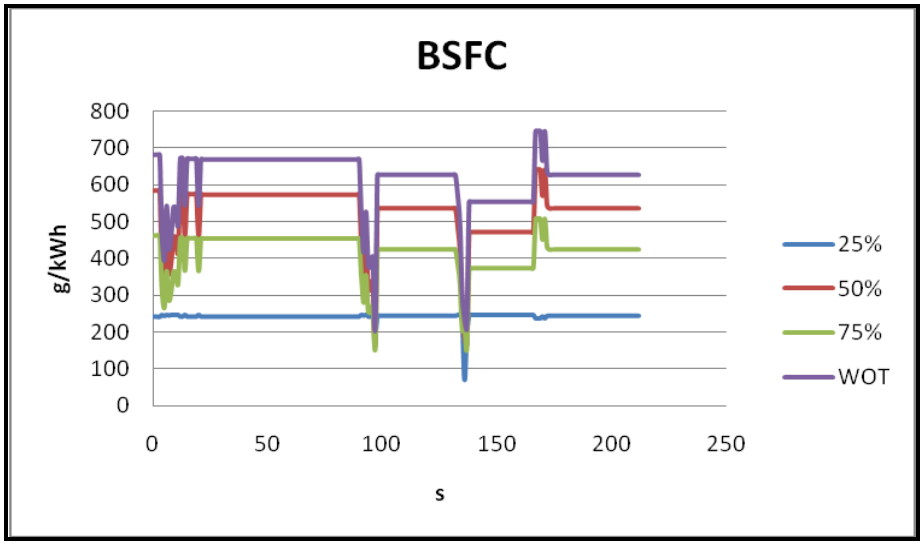

Figure 5.6: BSFC for the Modified ECE-15 Cycle

Note that the 50 % throttle has a higher average BSFC value compared to the 75 % throttle. WOT presents the highest average BSFC value. Thus it was observed that always running the ICE between 50 % to 75 % throttle would be the most optimum choice. This is because BSFC and fuel economy has an inverse relationship; a low BSFC value contributes to better fuel economy.

The emissions, CO, CO_2, HC and O_2, are shown in Figures 5.7 to 5.10 respectively for each throttle position. The emissions simulated are converted to grams. The results are then recorded and compared with the experimental data to check for the model's accuracy.

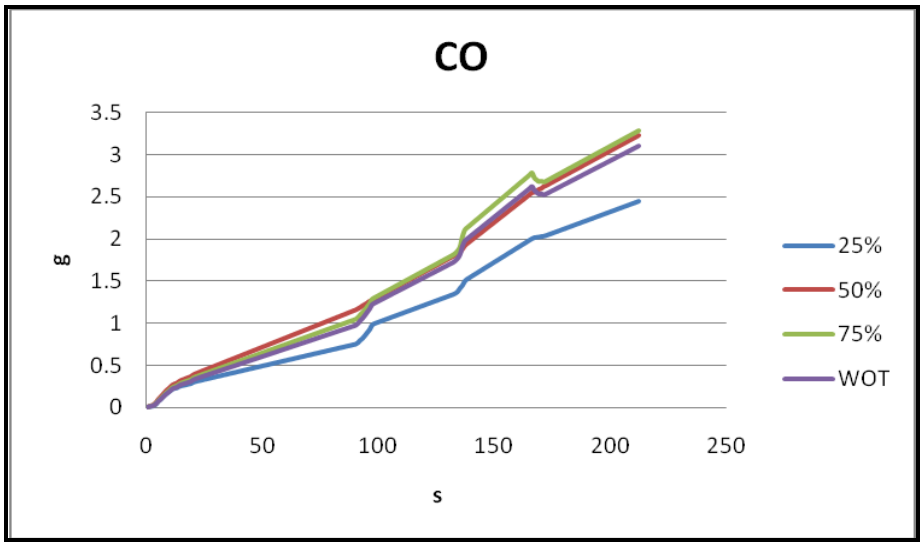

Figure 5.7: CO Predictions for the Modified ECE-15 Cycle

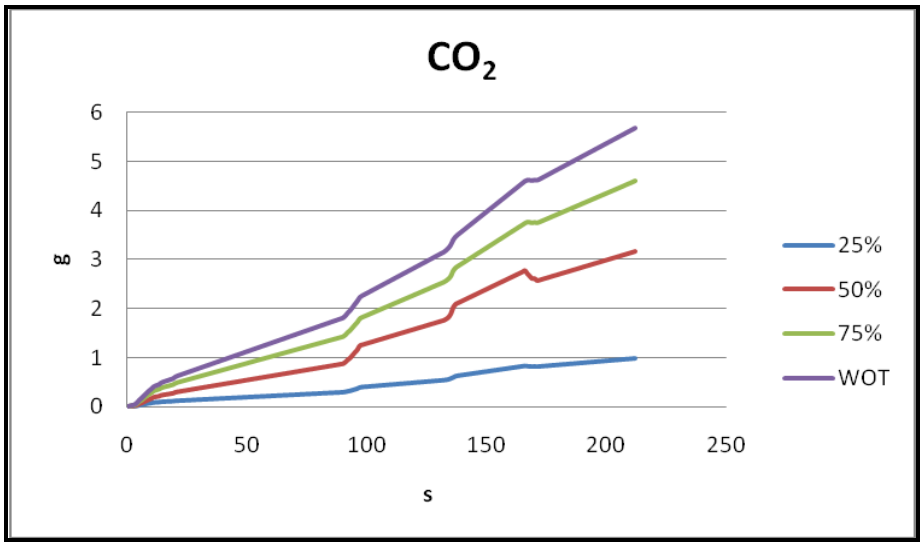

Figure 5.8: CO_2 Predictions for the Modified ECE-15 Cycle

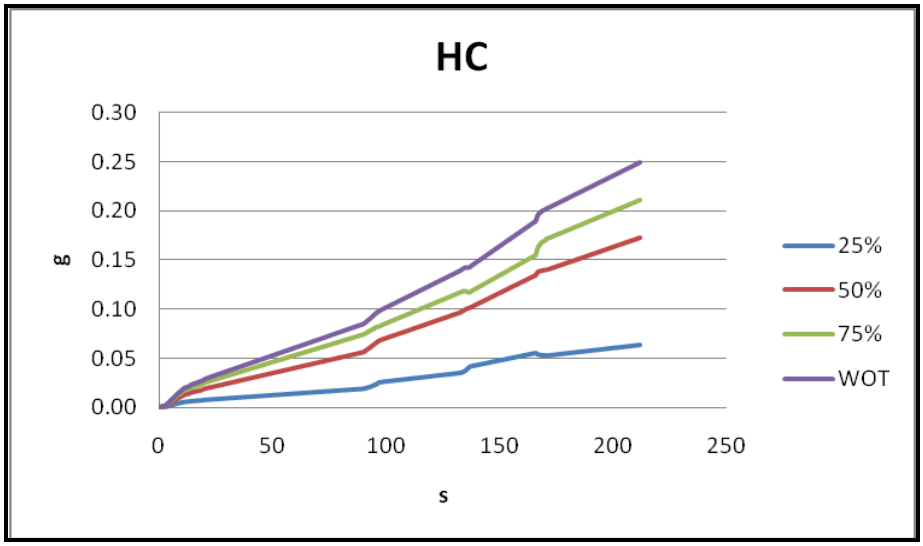

Figure 5.9: HC Predictions for the Modified ECE-15 Cycle

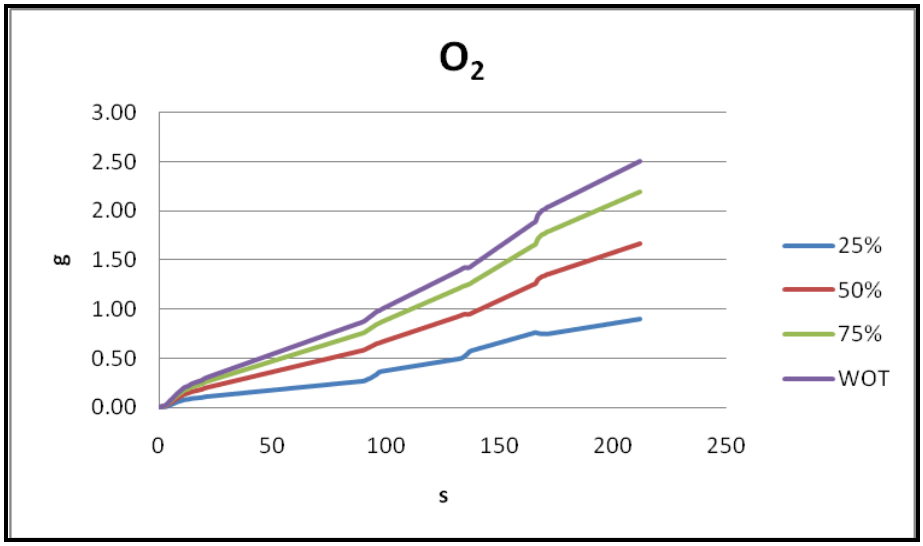

Figure 5.10: O_2 Predictions for the Modified ECE-15 Cycle

To verify the model, the simulated results for the fuel economy and emissions must be compared to the experimental data to show the model's feasibility and accuracy. Note that the experimental data are attached in Appendix B. Tables 5.1 and 5.2 show the comparison between the simulated and experimental data in terms of fuel usage and emissions respectively for the ECE-15 driving cycle. The errors, in percentage, were also calculated.

	Total Fuel Usage [ml]			
Throttle	**WOT**	**75%**	**50%**	**25%**
Simulated Results	76.10	73.40	59.20	33.80
Measured Results	81.50	72.00	58.00	36.00
Error %	**6.63**	**1.91**	**2.03**	**6.11**

Table 5.1: Results and Errors for Fuel Usage Simulation for ECE-15 Cycle

	Total Emissions for Modified ECE-15 Cycle				Total Fuel Usage	
Emissions	**CO**	**CO_2**	**HC**	**O_2**	**Fuel Economy**	
Throttle	**g**	**g**	**g**	**g**	**ml**	**g**
WOT						
Simulated Results	3.11	5.68	0.24	2.50	76.20	56.12
Measured Results	3.37	5.63	0.24	2.39	81.50	60.08
Error %	**7.79**	**0.89**	**0.88**	**4.29**	**6.50**	**6.58**
75 %						
Simulated Results	3.29	4.60	0.21	2.18	73.40	54.13
Measured Results	3.25	4.57	0.20	2.05	72.00	53.08
Error %	**1.16**	**0.47**	**4.12**	**6.02**	**1.91**	**1.94**
50 %						
Simulated Results	3.22	3.16	0.17	1.66	59.20	43.60
Measured Results	3.31	3.24	0.16	1.67	58.00	42.75
Error %	**2.70**	**2.58**	**1.57**	**0.62**	**2.02**	**1.92**
25 %						
Simulated Results	2.44	0.99	0.063	0.89	33.80	25.00
Measured Results	2.69	1.02	0.069	0.97	36.00	26.54
Error %	**9.29**	**2.92**	**8.69**	**7.89**	**6.11**	**5.80**

Table 5.2: Results and Errors for Emissions and Fuel Economy Simulation

For the fuel economy comparison (Table 5.1), all the errors between the simulated and experimental data are all below 7 %. This proves that the model accurately predicts the fuel usage of the ICE with an error of 7 %, which the author deemed feasible. The emissions were also measured experimentally and compared to the simulated results. The emissions obtained and the fuel economy comparison results have errors below 10 %. CO_2 error results are below 3 % over the four throttles.

The accuracy of the ICE model predicting fuel economy and emissions are acceptable with error results below 10 %. Properly mapping the ICE enable proper and more accurate fuel economy and emissions prediction, which further inject confidence on the HES model.

5.4 HES Model Simulation Results

Having a feasible model enabled the authors to predict how the HES's propulsion units (ICE and DC motor) interact with one another when each driving cycle is applied to the model. For any given driving cycle, the required torque and the required power can be estimated. The hybrid multi-state controller could properly predict the optimized power splits, the batteries' SC and the fuel consumption of the HES. The emissions were also estimated using this predictive HES model.

Thus, the performance of the HES model can be predicted over the four mentioned driving cycles. This will give the author a good estimate of the behavior of the HES for different driving conditions on the power demands as well as the fuel consumption. Note that for the state plots below, each number corresponding to a driving state chosen by the controller; ICE Only State (1), Motor Only State (2), Hybrid State (3), Idle Recharging State (4), Mechanical Braking State (5), Regenerative Braking State (6) and Engine Charge State (7). Below are the simulation results and discussion.

5.4.1 ECE-15 Cycle

This is an urban European driving cycle and it was applied to the developed model. The demanded torque and power are shown in Figure 5.11.

The demanded torque and power are calculated from the vehicle dynamics model in the HES model. Comparing to the paper published by Shao et al. [69], the demanded torque and power trends shown in Figure 5.11 matched the trends published. The published data by Shao et al. displays similar qualitative trends for the simulated power and torque. This adds further confidence to the HES model.

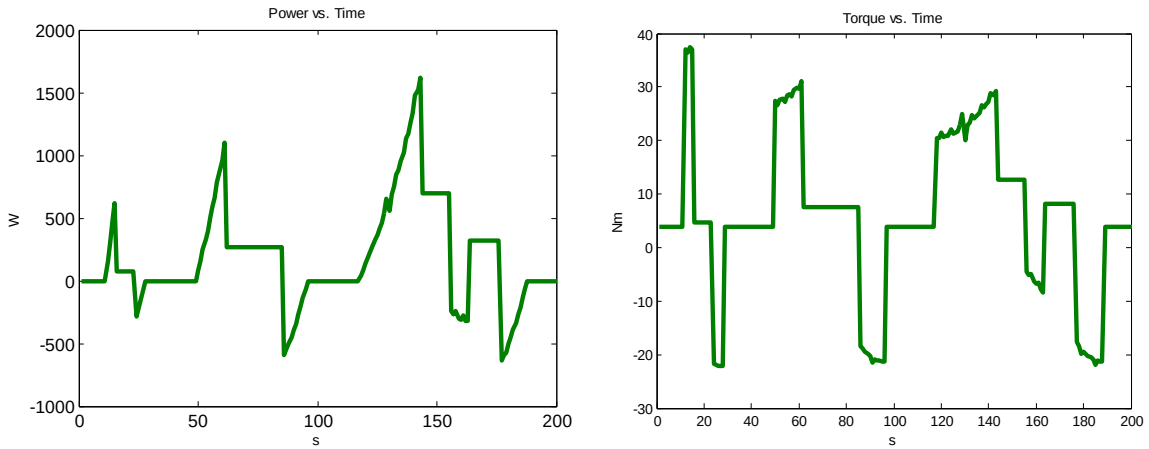

Figure 5.11: Demanded Torque and Power for the ECE-15 Cycle

The HES model outputs the optimized power splits between the two propulsion system, the SC of the battery, the fuel economy and the emissions. Figure 5.12 shows the simulated ICE and motor torque provided throughout the cycle. Most of the time during the entire driving cycle, hybrid state and motor state are working, with of course the regenerative state during braking which recharges the batteries. This is what was expected; to put priorities for the motor and hybrid state and minimize the ICE usage to minimize fuel consumption. During braking conditions, the regenerative braking state should be activated provided the SC of the battery is not full.

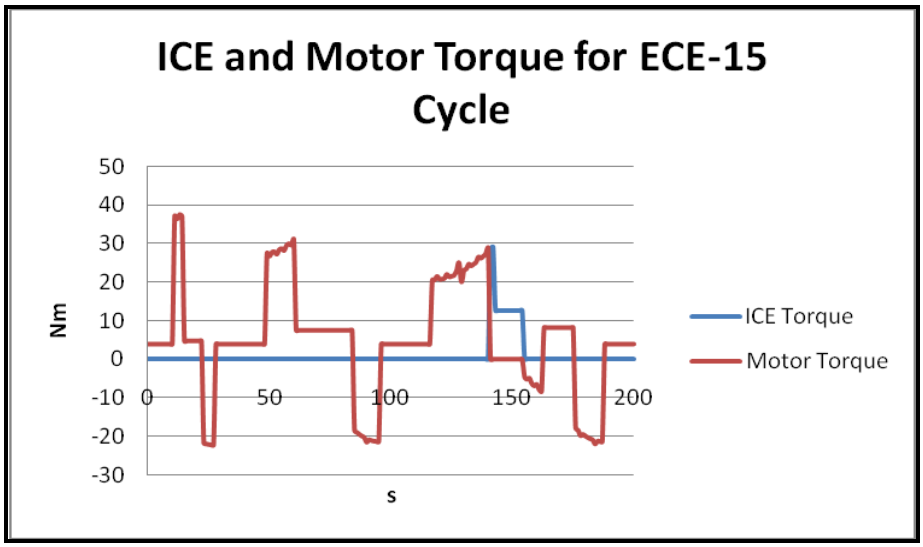

Figure 5.12: ICE and Motor Torque Provided for the ECE-15

The fuel economy and SC are depicted in Figure 5.13 below. The battery's SC assumed an initial charge of about 77 %. At the end of the driving cycle, the SC was discharged to about 75.75 %. The SC was more or less kept to a constant value by the regenerative braking state. This amounted to a 1.25 % SC loss. The petrol consumption for this cycle is 6.4 ml.

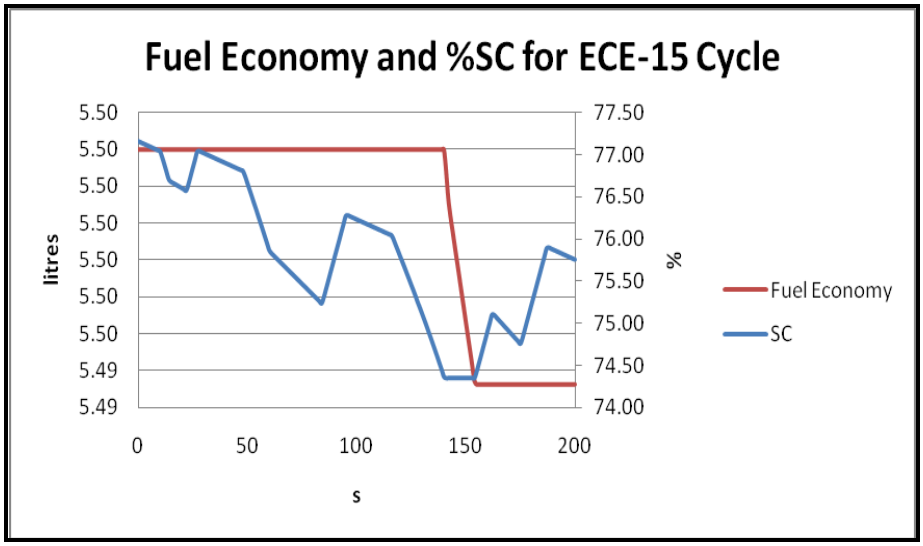

Figure 5.13: Fuel Economy and SC for the ECE-15

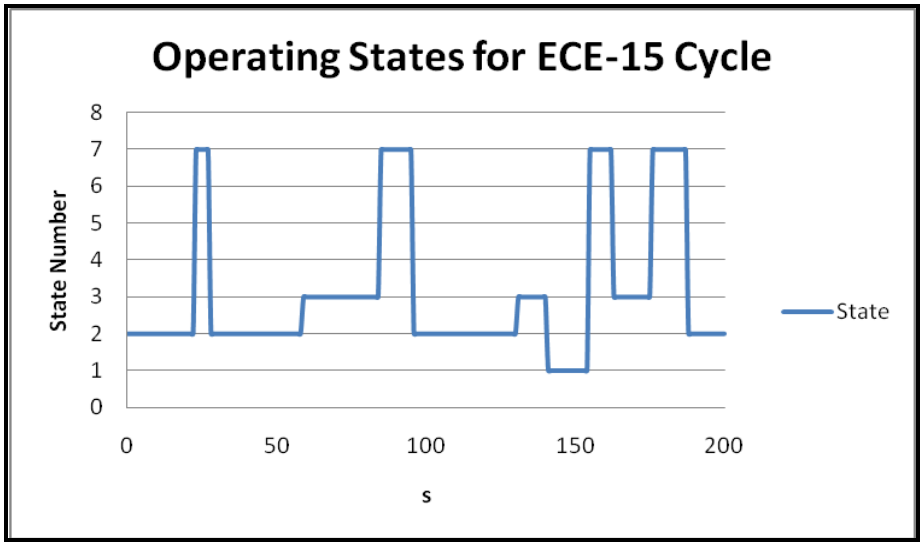

Figure 5.14: States Transition for the ECE-15 Cycle

Figure 5.14 shows the states transition throughout the entire cycle. From the figure, the ICE was in operation alone for about 7.4 % of the total time during the cycle. The priority was given to the motor and hybrid states. This reduces the ICE's operation and thus increases fuel economy. This will subsequently reduces emissions. Further analysis about the states will be presented in the next section.

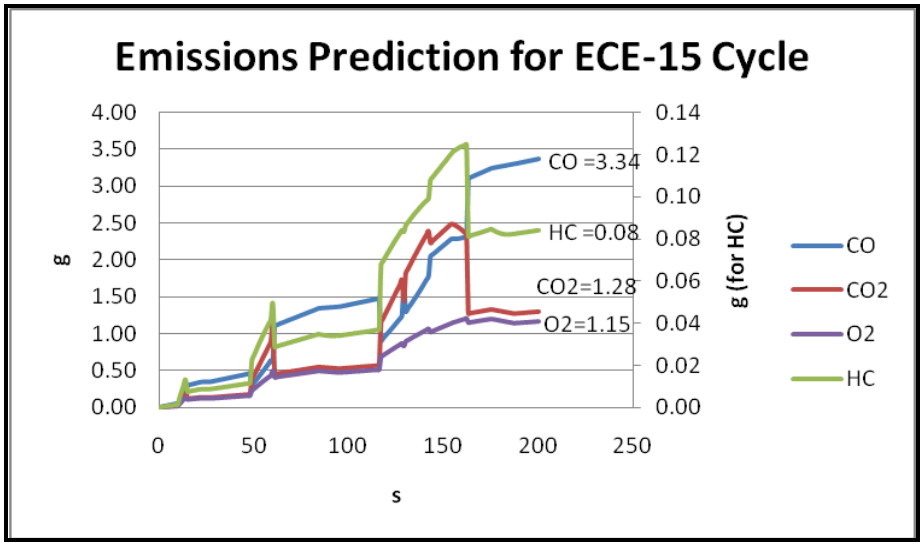

Figure 5.15: Accumulative Emissions for the ECE-15 Cycle

The accumulative emissions for this cycle are shown in Figure 5.15. The total emissions are labeled in the plot, where the amount of total CO emitted is 3.34 g, HC is 0.08 g, CO_2 is 1.28 g and O_2 is 1.15 g. Further analysis and errors about the emissions will be presented later in the chapter.

5.4.2 Modified UDDS Cycle

Having a feasible model, simulating the HES model on the modified UDDS cycle would give a better understanding of the behavior of the model and the HES. Figure 5.16 shows the demanded torque and power simulated for the modified UDDS speed profile.

Figure 5.17 shows the torque splits for the two propulsion units through the cycle. Again, from observation, the hub motor provided most of the demanded tractive torque, which reduces the usage of the ICE. This will eventually increases fuel economy and lower the emissions. Initial SC was set to 77 %, and after the cycle, the SC was reduced to just over 64 %. This gives a 12.38 % SC loss for this cycle. The petrol consumed for this drive cycle is 93.80 ml.

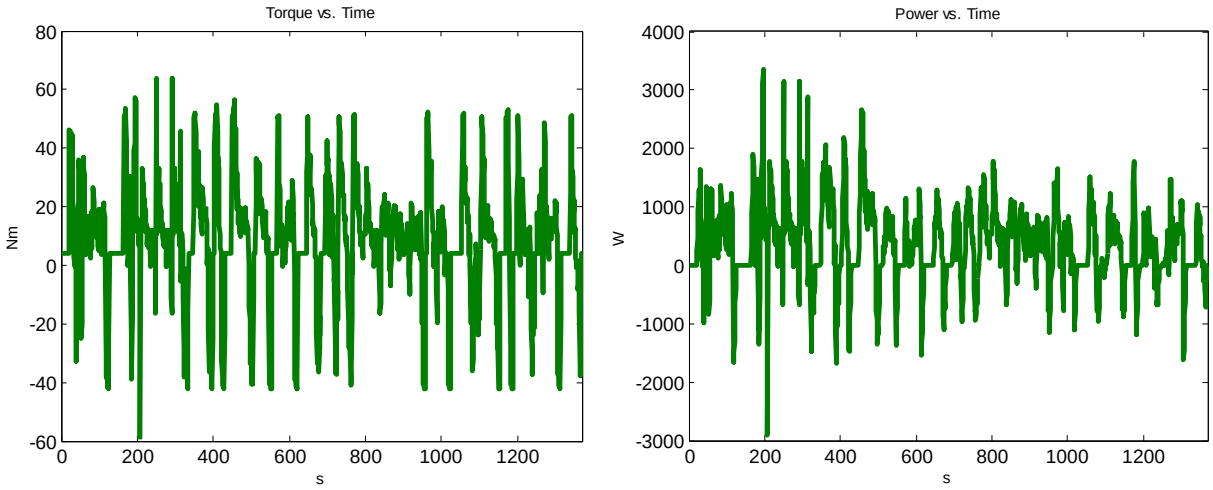

Figure 5.16: Demanded Torque and Power for the Modified UDDS Cycle

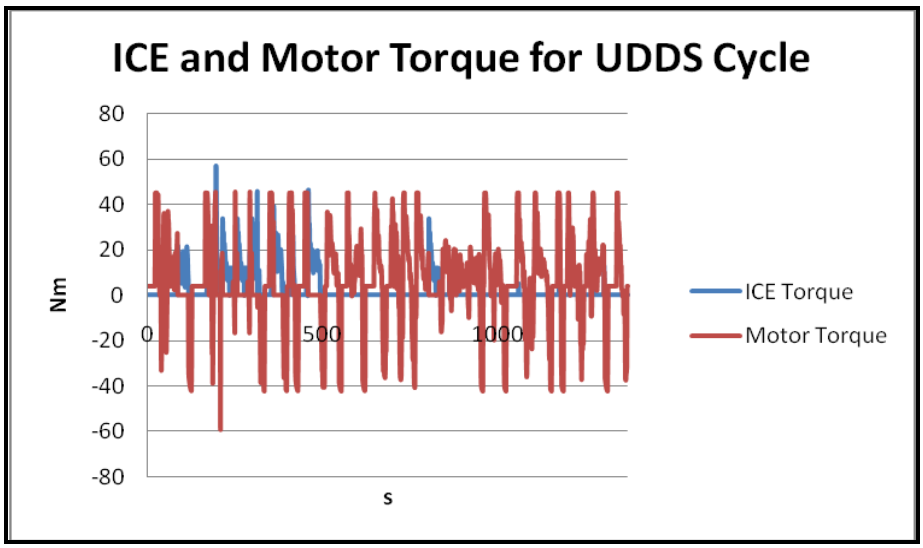

Figure 5.17: ICE and Motor Torque Provided for the Modified UDDS Cycle

Figure 5.18 shows the fuel economy and SC over the UDDS cycle.

The operating states and emissions simulated are shown in Figures 5.19 and 5.20 respectively. The total CO emitted is 27.86 g, HC is 0.73 g, CO_2 is 11.59 g and O_2 is 10.24 g. Further analysis for the states and emissions will be presented later in the chapter.

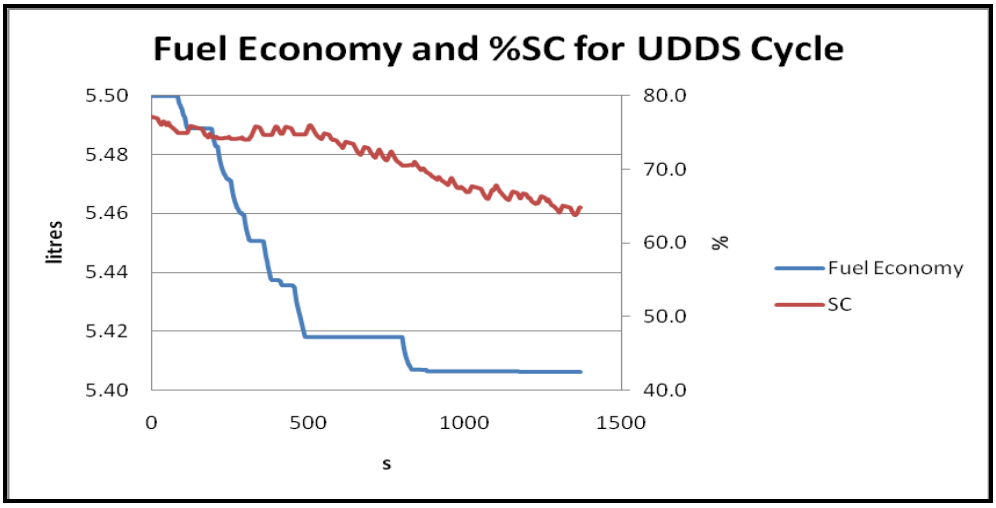

Figure 5.18: Fuel Economy and SC for the Modified UDDS Cycle

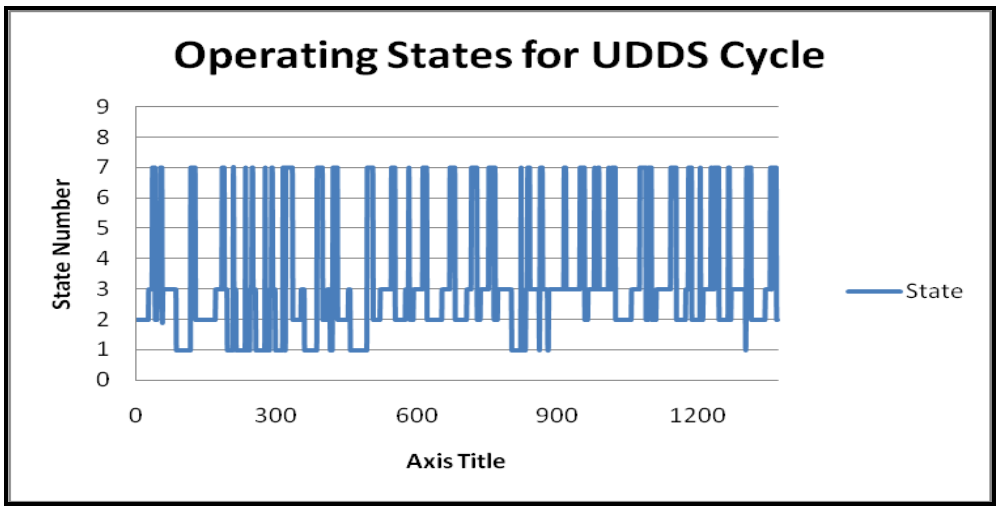

Figure 5.19: States Transition for the Modified UDDS Cycle

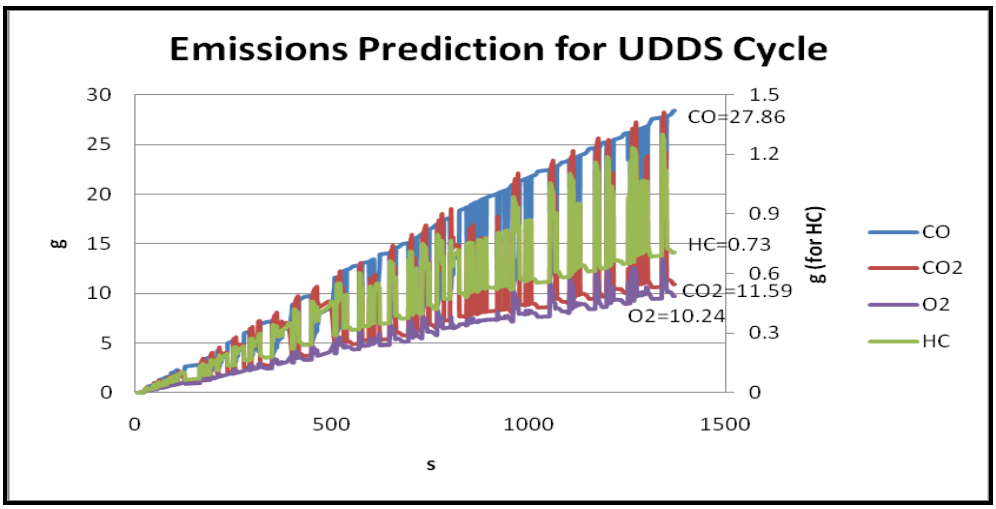

Figure 5.20: Accumulative Emissions for the Modified UDDS Cycle

5.4.3 NYCC Cycle

Now simulating the model on the NYCC cycle, the demanded tractive torque and power are shown in Figure 5.21. The torque splits between the ICE and motor for the cycle is shown in Figure 5.22. What is interesting with this cycle is that the ICE was never in operation alone. The motor-alone and hybrid states operate mostly for this cycle. This shows again that emissions were lowered as the fuel consumption is minimal.

The initial SC of the battery was set to 77 %. After simulation, the SC remained at the constant 77 % charge. The SC was maintained for this cycle by the regenerative braking state. Regenerative braking state is operating throughout the entire cycle as this driving cycle features a stop-and-go characteristic. Petrol consumption for this cycle is 2.5 ml. The fuel economy and SC is shown in Figure 5.23 below.

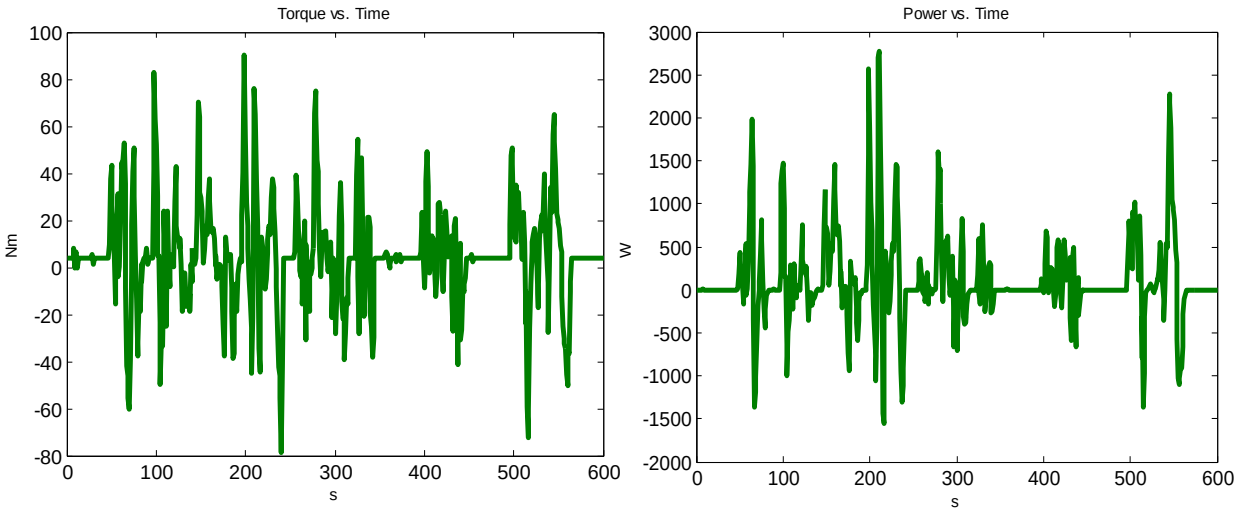

Figure 5.21: Demanded Torque and Power for the NYCC Cycle

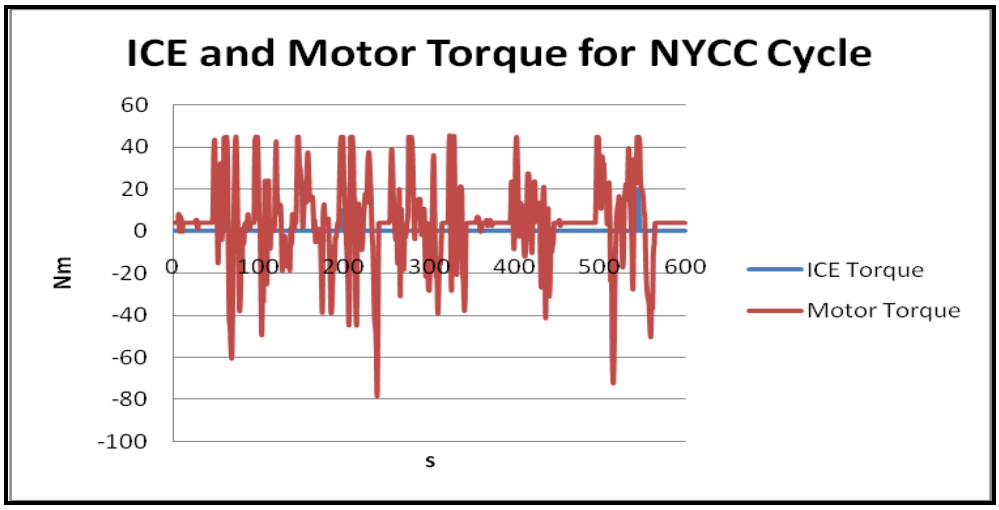

Figure 5.22: ICE and Motor Torque Provided for the NYCC Cycle

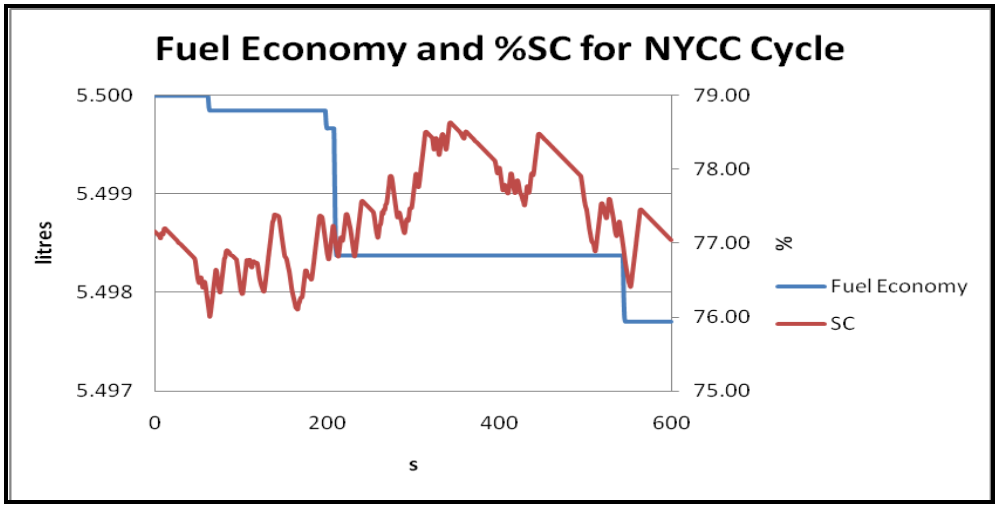

Figure 5.23: Fuel Economy and SC for the NYCC Cycle

The states transition is shown in Figure 5.24 and the total accumulative emissions are shown in Figure 5.25. Total CO emitted is 8.89 g, HC is 0.22 g, CO_2 is 3.42 g, O_2 is 3.04 g. Further analysis regarding the states and emissions will be presented later in this chapter.

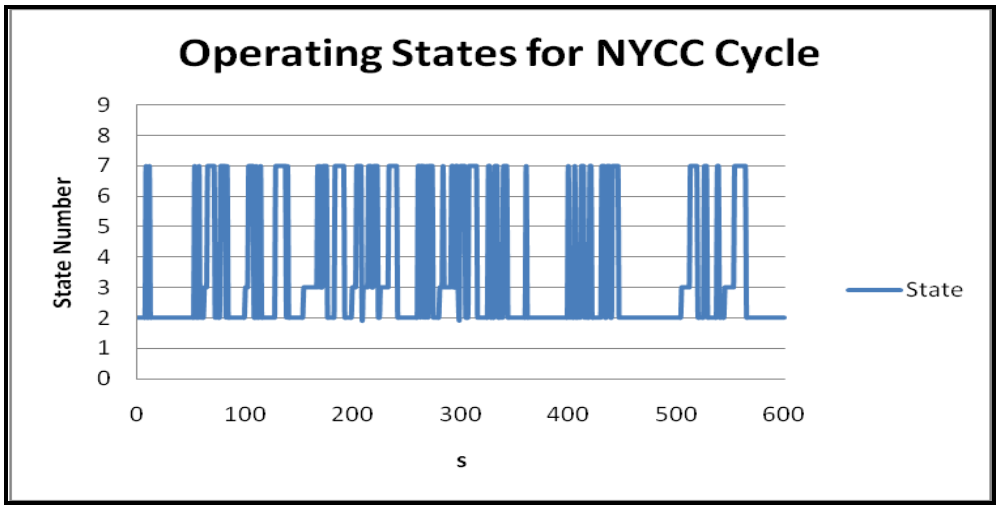

Figure 5.24: States Transition for the NYCC Cycle

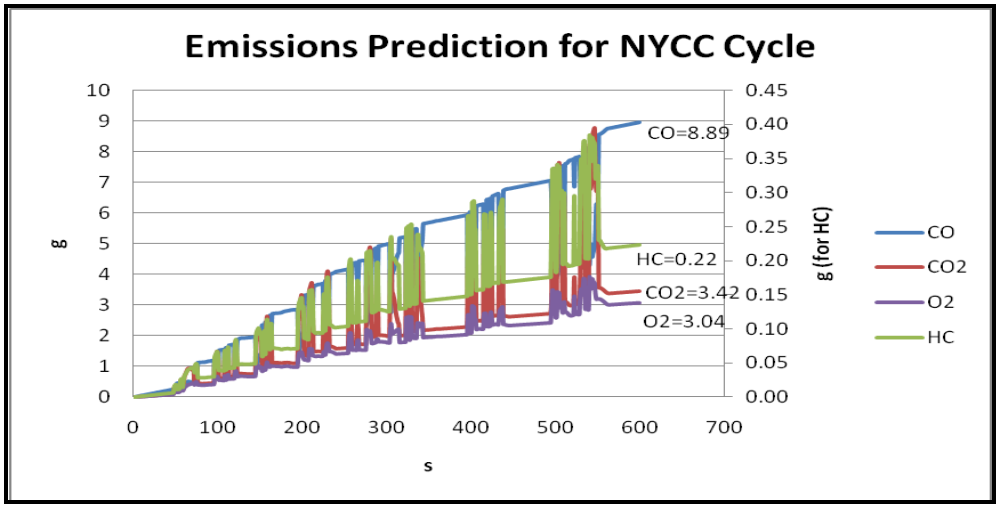

Figure 5.25: Accumulative Emissions for the NYCC Cycle

5.4.4 Modified HWFET Cycle

This highway cycle was chosen to simulate how the HES reacts when travelling in a highway. It was predicted that the ICE operates most of the time, while recharging the set of batteries. The battery provides auxiliary power to the HES. This strategy leads to low fuel consumption, as the ICE is running is its most optimum region. Figure 5.26 shows the demanded variables for this driving cycle and Figure 5.27 shows the torque split between the propulsion units of the HES for this cycle.

From the power split plot, the motor was rarely used during the modified HWFET cycle. Because the ICE is primarily running the HES, the motor was used to startup the vehicle and for accelerations. After that, during highway cruising, the ICE operates alone for most of the time, which is what was predicted in the beginning. The SC of the battery was monitored constantly and if it is below the threshold value set, the ICE will run the generator to recharge the batteries whilst cruising on the highway. Throughout this cycle, the SC was more or less constant between 77 % to 78 % with the petrol consumption of 476 ml, as shown in Figure 5.27.

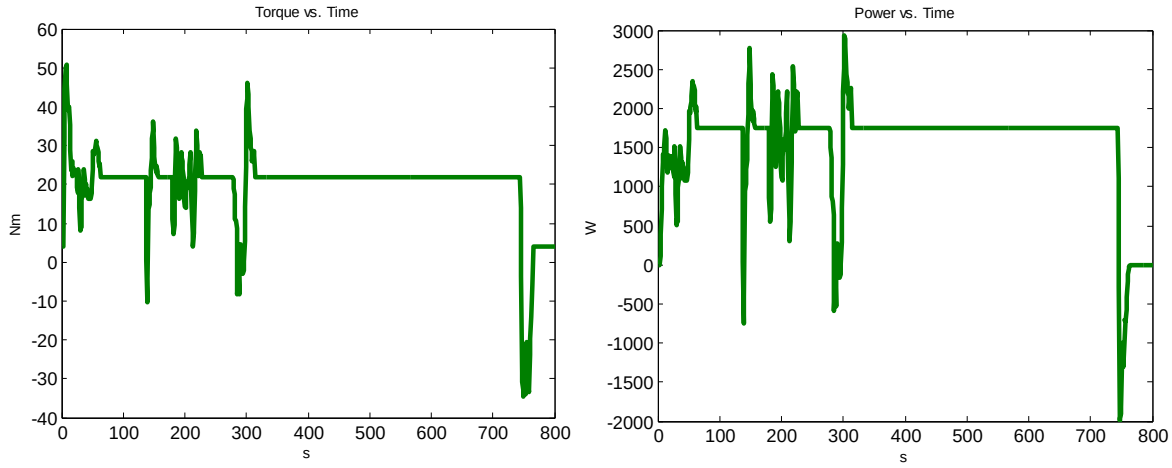

Figure 5.26: Demanded Torque and Power for the Modified HWFET Cycle

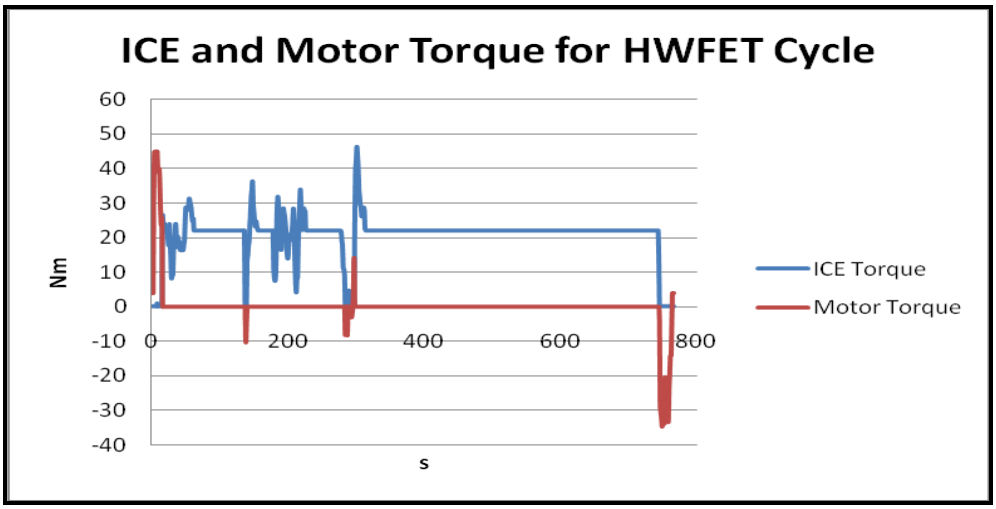

Figure 5.27: ICE and Motor Torque Provided for the Modified HWFET Cycle

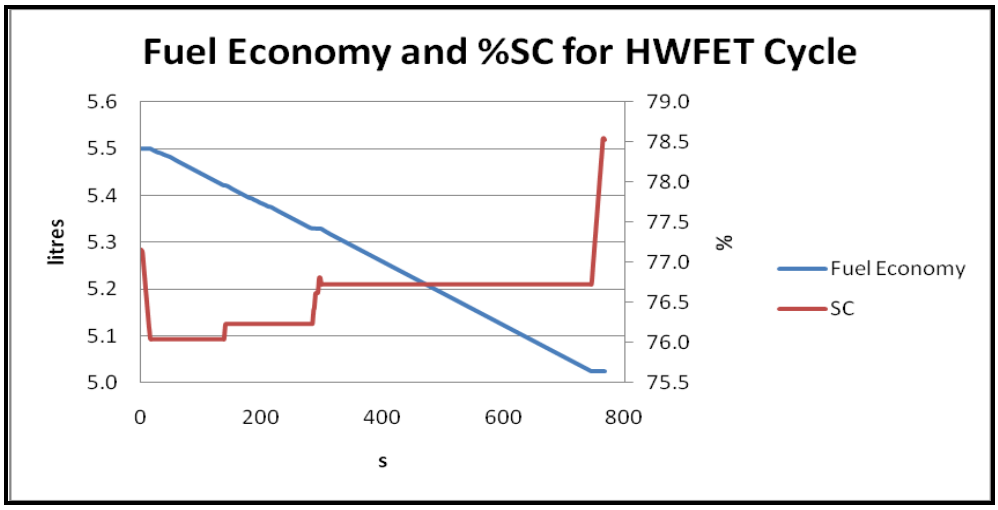

Figure 5.28: Fuel Economy and SC for the Modified HWFET Cycle

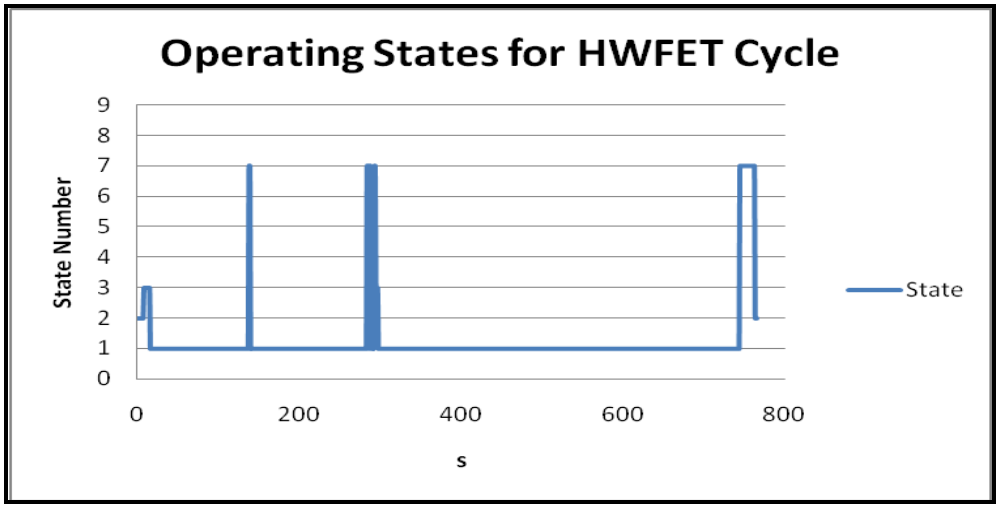

Figure 5.29: States Transition for the Modified HWFET Cycle

Figure 5.29 shows the states for the modified HWFET cycle. As observed, the entire cycle was operated on the ICE-only state, which was expected. Figure 5.30 shows the total emissions for this cycle. Total CO emitted was 35.7 g, HC was 0.89 g, CO_2 was 13.8 g and O_2 was 12.3 g. The analysis and discussion of the states and emissions will be presented in the next section.

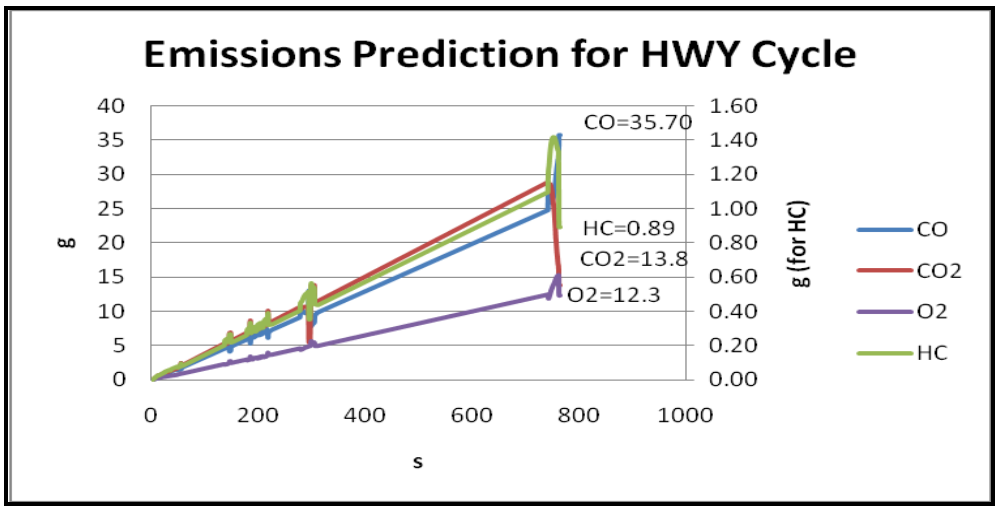

Figure 5.30: Accumulative Emissions for the Modified HWFET

5.4.5 States Analysis

Sections 5.4.1 to 5.4.4 discusses how the demanded tractive power and torque are met by showing how the two power sources interact based on the threshold values set in the control system for 4 driving cycles.

The percentage usage for each state for each individual driving cycle was determined, and showed in Table 5.3. As shown, it can be seen that the dependence on the ICE propelling the HES was significantly reduced with the presence of the motor state and the hybrid state. Two phenomena were observed from Table 5.3, mainly the HWFET and the NYCC cycle. The HWFET cycle has a high Engine State usage (94.7 % throughout the entire driving cycle). This was expected as for highway cruising, as high speeds are normally required. As for the NYCC cycle, an interesting phenomenon was observed. The ICE was never operated alone and this further reduces the fuel consumption for this driving cycle.

	1 Engine State	**2** Motor State	**3** Hybrid State	**4** Idle Recharging State	**5** Mechanical Braking	**6** Regenerative Braking	**7** Engine Charge State	**Total** %
UDDS	15.5	25.5	37.8	0.0	0.0	19.9	0.0	98.7
ECE-15	7.5	49.5	24.5	0.0	0.0	17.0	0.0	98.5
HWFET	94.7	1.1	1.3	0.0	0.0	2.4	0.0	99.5
NYCC	0.0	59.8	14.5	0.0	0.3	22.5	0.0	97.1

Table 5.3: Summary of State Usages

The total percentage will never achieve 100 % as there is a small time delay during simulation. This time delay usually happens during state changes. The more state changes expected in a driving cycle, the more delay is present. This time delay contributes to a maximum of 4.5 % for the four driving cycles, which the authors deemed feasible.

5.4.6 Fuel Economy and Emissions Analysis

The fuel economy for each driving cycle simulated is summarized below in Table 5.4. The total fuel used for the simulated HES model is converted to $mlkm^{-1}$ for comparative purposes. Using the multi-state control system proposed in this thesis, it can be seen that the modified HWFET cycle produced a high fuel consumption as the ICE was operating almost 94 %

throughout the cycle compared to the other three cycles where the ICE was shut off when not in used.

		ECE-15	Modified UDDS	NYCC	Modified HWFET
Fuel	ml	6.40	93.80	2.50	476.00
	$mlkm^{-1}$	6.43	8.54	1.32	32.81

Table 5.4: Summary of the Simulated Fuel Economy

The emissions prediction of the HES simulated presents an assistive tool in tuning and understanding the behavior of the HES. Table 5.5 shows the summary of the total emissions simulated on the HES model. The respective important emissions are converted to gkm^{-1} for comparative purposes.

		ECE-15	Modified UDDS	NYCC	Modified HWFET
CO	g	3.340	27.860	8.890	35.700
	gkm^{-1}	3.360	2.537	4.704	2.460
CO_2	g	1.280	11.590	3.420	13.800
	gkm^{-1}	1.288	1.056	1.810	0.951
HC	g	0.080	0.730	0.220	0.890
	gkm^{-1}	0.080	0.066	0.116	0.061

Table 5.5: Summary of the Simulated Total Emissions

As expected, the total emissions produced are all significantly higher for the modified HWFET cycle for all CO, CO_2 and HC compared to the other three cycles.

5.5 Conclusion

This chapter discusses the modelling and simulation results of a hybrid electric scooter model built on the MATLAB-Simulink platform. By comparing the simulation data and results with the literatures by Shao et al., there is a high confidence that the HES model developed is accurate [69]. The motorcycle presented by Shao et al. is very much similar to the scooter this thesis was proposing, although regenerative braking was not mentioned [69]. This thesis uses the multi-state approach incorporating the regenerative braking state.

The conventional petrol scooter, or a worst case scenario of the HES in terms of fuel economy and emissions, was verified with the experimental data. Results obtained between the simulated data and the experimental data has errors less than 10 %. This adds confidence

to the predictive capability of the HES model. The HES model was further verified when simulated under the ECE-15 cycle (Section 5.4.1) by comparing the simulated data with the results obtained in the literature. The qualitative trends of the simulated data matched the trends published. Quantitative trends do not match as different type of motorcycle was modeled. This further adds confidence to the predictability of the HES model.

With that, the proposed multi-state approach is suitable not only for four-wheeled vehicles but also for small two-wheeled and urban vehicles. Having a feasible HES model enable further analysis to be carried out and the emission impacts (which is one of the important impacts especially with HESs) can be examined *via* modelling and simulation, before the final prototype building begins.

The model was validated using experimental data to check for the HES model's feasibility and accuracy. The HES model is then simulated under 4 different and distinct driving cycles; ECE-15, Modified UDDS, NYCC and Modified HWFET. Results showed that the multi-state HES model accurately predicts the performance of the HES. This further demonstrates the predictive capabilities of the multi-state controller application for hybrid two-wheelers, in terms of power management, fuel economy and emissions.

CHAPTER 6: ANN EMISSIONS PREDICTIVE MODEL

6.1 Introduction

This chapter presents the development of an Emissions Prediction Model (EPM). The EPM was built around the HES discussed in previous chapters. Unlike the MATLAB-Simulink HES model, the EPM predicts the emissions by applying artificial neural network (ANN) methodologies. Experimental data gathered on the chassis dynamometer were used for training and testing the EPM. The predicted results will be then used to compare with the actual experimental results for error analysis.

This chapter presents the general procedures and its corresponding simulated results for each predicted emission; CO, CO_2, HC and O_2. Assessment of the various neural network models will be conducted and based on the errors generated, the most suitable model for each emission gas is selected for the EPM. Results and the EPM appraisal will then be presented for each emission component followed by summary and concluding remarks.

6.2 Emissions Predictive Model

The Emissions Predictive Model (EPM) is a model which consists of four different neural network models; representing each network for each emission gas. Thus, three different neural network models were investigated for each emission component to determine the most suitable model for each component prediction. The general structure is shown in Figure 6.1.

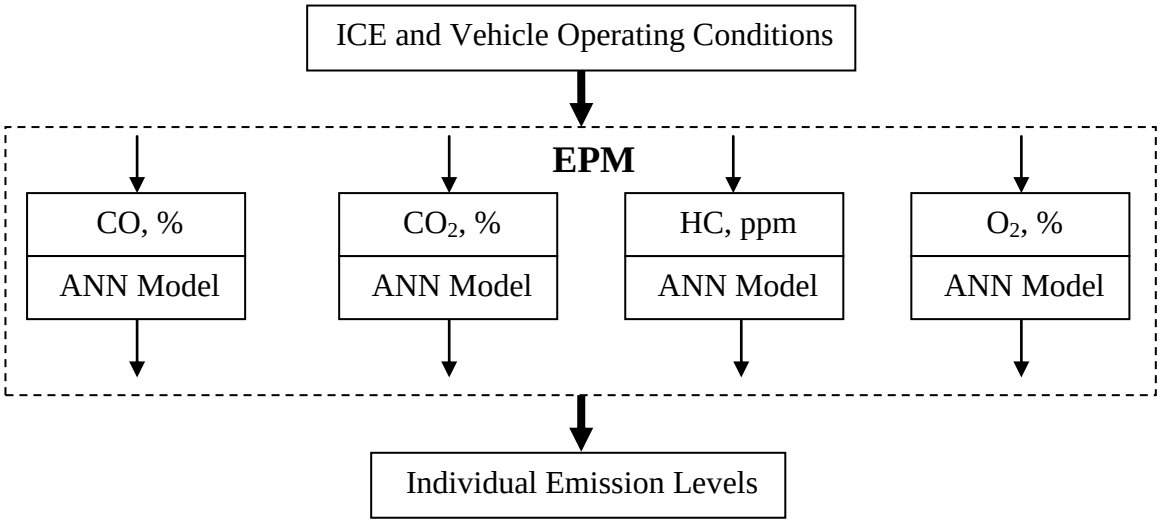

Figure 6.1: EPM Structure

The EPM was implemented using the Neural Network Analysis Package tool. This tool was developed by the HART Research Team from the School of Engineering, University of Tasmania. This section presents a summary of the relevant information of the Neural Network Analysis Package. Further reading can be made from the following references [140-142].

6.2.1 Neural Network Analysis Package

The Emissions Prediction Model (EPM) was constructed using the Neural Network Analysis Package. The Neural Network Analysis Package was developed based on Visual Basic macros running in the background of Microsoft Excel. The kernel that does most of the Neural Network processing tasks are coded using Pascal. Below is a summary describing the processing stages of this tool:

1. Neural Network Analysis Package's user interface was coded around the Microsoft Excel application. Spreadsheets are opened ready to be filled with test data.
2. Test data was then inserted to the spreadsheets by defining the number of inputs, outputs and the number of test data.
3. Data was then normalized from 0 to 1 and auto-saved without altering the original test data. The test data was then separated into training data and test data.
4. For each application, a neural network model is chosen from the list shown in Figure 6.2. For each neural network model chosen, its parameters such as number of hidden nodes, iterations, etc.

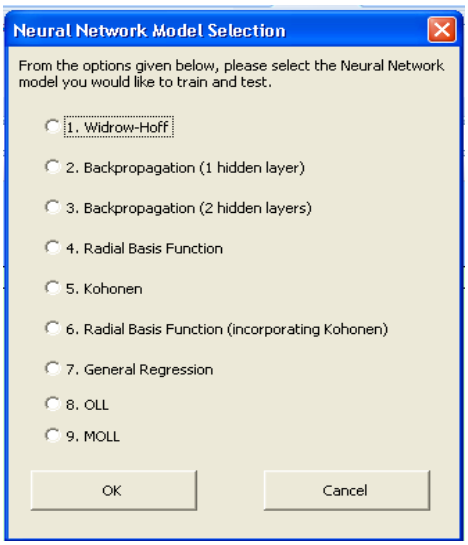

Figure 6.2: Neural Network Model List

5. Network training and testing are performed based on the chosen neural network and its parameters. Separate output files are generated.
6. Results are then uploaded and the outputs such as the average RMS errors and graphical plots can be viewed after uploading.

6.2.2 General Procedures of the Emissions Predictive Model

Exhaust emissions was measured and was discussed in Section 4.3.4.2. The predicted emissions are CO (%), CO_2 (%), HC (ppm) and O_2 (%). Each of these gasses was modeled based on the experimental data collected. The general neural network structure, showing the inputs and outputs, is depicted in Figure 6.3.

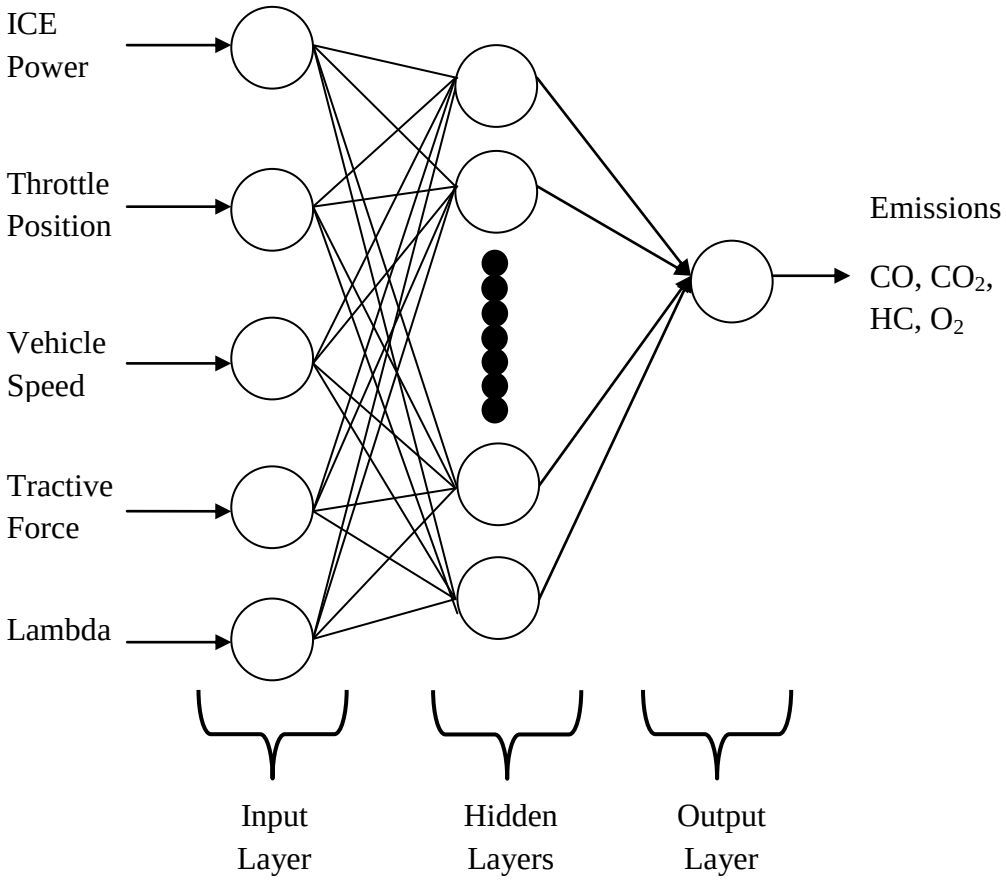

Figure 6.3: Neural Network EPM Structure

For each gas, three different neural network models described in Chapter 3 was applied. The three different neural network models are applied and the one that exhibits the best performance is selected. The three different neural network models are;

1. Back-propagation with 1 and 2 hidden layer(s) (BP1 and BP2)
2. Optimization layer by layer (OLL)
3. Radial Basis Function incorporating Kohonen (RBF+KOH) with sigma, σ_A, values of 0.3 and 0.5.

Using the Neural Network Analysis Package tool, the modelling of the EPM was accomplished by following the procedures below:

1. Data Processing
2. Network Training and Testing
3. Network Selection

Data Processing

A total of 588 data was collected during the experimental phase under different operating conditions. This data set was then normalized to the range 0 to 1 using Equation 3.3. After the normalization process, 10 % (59) of the total dataset was reserved for network testing and the rest will be used to train the neural network model.

Network Training and Testing

The network is then trained and tested against the actual testing data. The network then yields a root mean squared (RMS) error. This RMS error (in this case, training RMS error and testing RMS error) can be calculated based on Equation 3.10. Note that a RMS error of less than 0.1 (10 %) is considered acceptable.

Network Selection

A suitable neural network model has to be selected for each gas emission. The selection of the best network to predict each gas is based on the testing RMS error. The RMS testing error validates the model between the simulated data and the experimental data. Thus, the neural network model that has the lowest testing RMS error will be chosen to for each individual gas.

6.3 Results and Model Appraisal

6.3.1 CO

From Figures 6.4 and 6.5, it can be seen that for the model to properly predict the CO emission, the most suitable neural network models are the BP1, BP2 and OLL. These three models give an average RMS error of less than 7 %. The RBF+KOH models gives huge and unacceptable errors ranging from 60 % up to 140 %.

Figure 6.6 showed the prediction results using the OLL model with 9 hidden nodes. The OLL model with 9 hidden nodes gives the lowest error , which is just over 3 % for the training and testing data respectively. The plot gives a good estimation as the trends and the values matched between the experimental and predicted data. This further concludes that the OLL neural network model with 9 hidden nodes gives the best CO prediction with errors less than 4 % and thus this neural network model is selected for the EPM.

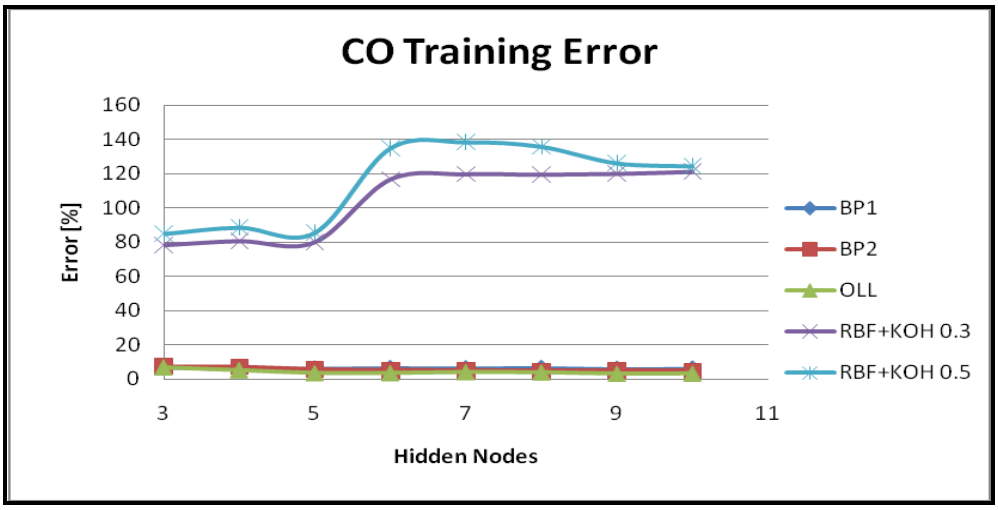

Figure 6.4: CO Training Error

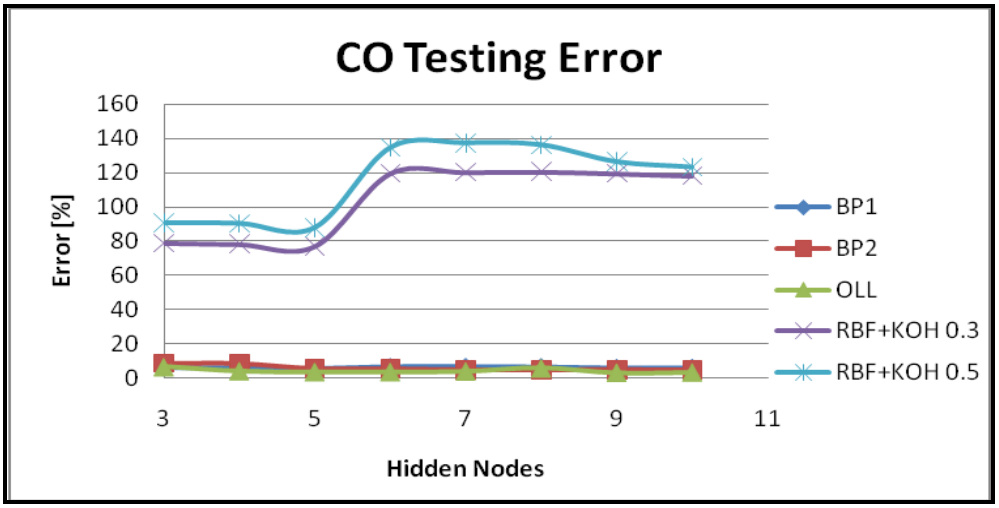

Figure 6.5: CO Testing Error

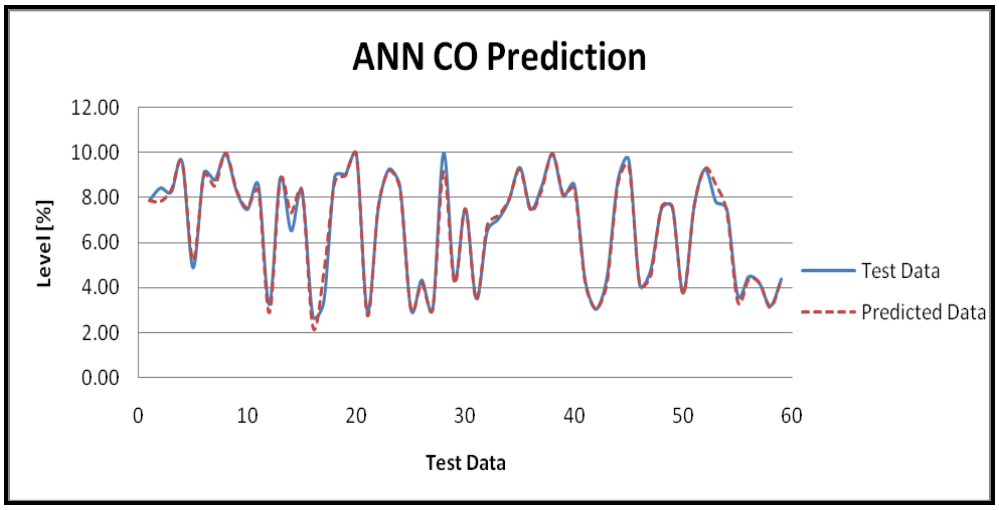

Figure 6.6: CO Prediction Results

6.3.2 CO_2

Similar to the CO prediction, OLL gives the lowest RMS error with 10 hidden nodes. The BP1 and BP2 models give acceptable errors of just under 9 %. The RBF+KOH neural network models give a maximum error of just over 25 %, which is unacceptable.

Figures 6.7 and 6.8 show the graphical representation of the relationship between the hidden nodes and RMS errors for each neural network model. From the figures itself, OLL with 10 hidden nodes gives the lowest error.

Thus the best neural network model selected is the OLL model with 10 hidden nodes, which gives an average RMS training error of 2.27 % and average RMS testing error of 3.69 %. Hence, this model is selected for the EPM. Figure 6.9 shows the prediction results when

using the OLL model with 10 hidden nodes. The qualitative and quantitative trends between the test and predicted data match entirely and this prediction was deemed accurate.

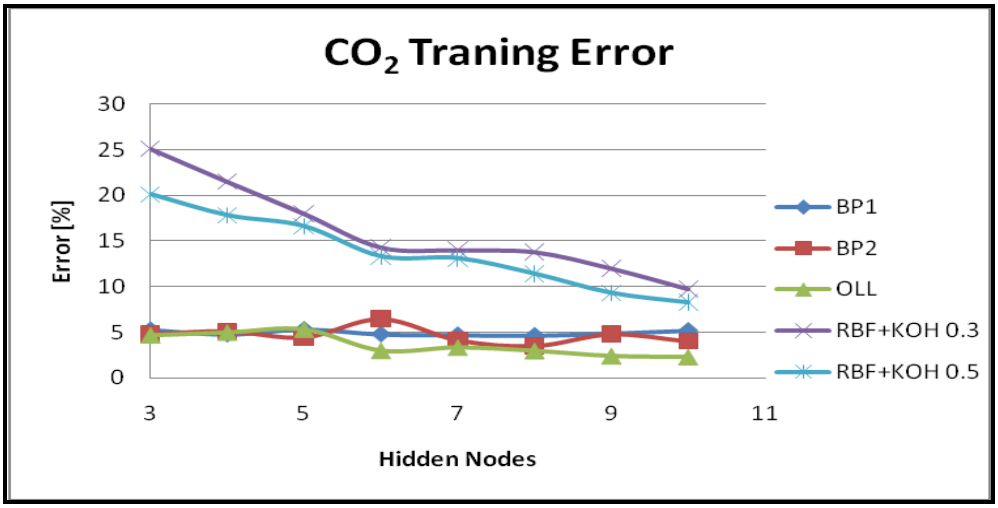

Figure 6.7: CO_2 Training Error

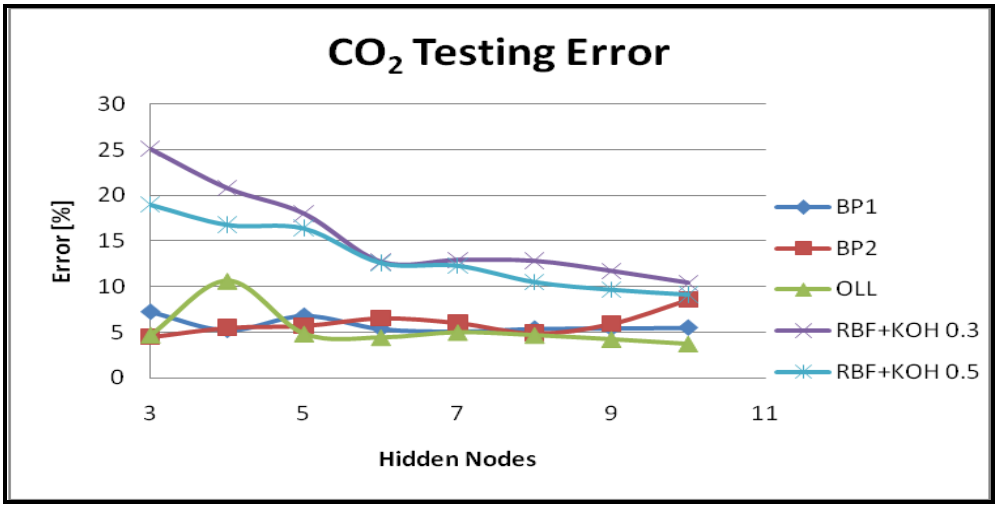

Figure 6.8: CO_2 Testing Error

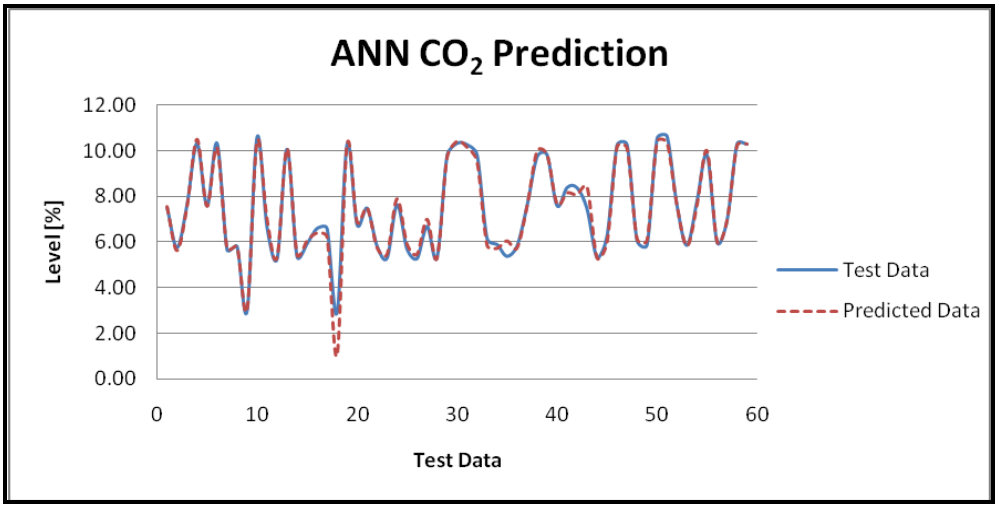

Figure 6.9: CO_2 Prediction Results

6.3.3 HC

For HC predictions, the same three neural network models are employed and the training and testing errors are recorded for each model with increasing hidden nodes. The BP1 network has errors ranging from 9 % to 13 %. BP2 have high errors as well with a maximum of just below 16 %. OLL presents the lowest errors among the three networks with maximum errors of 11 %. The RBF+KOH models with σ_A values 0.3 and 0.5 gives relatively high errors, which is depicted in Figures 6.10 and 6.11.

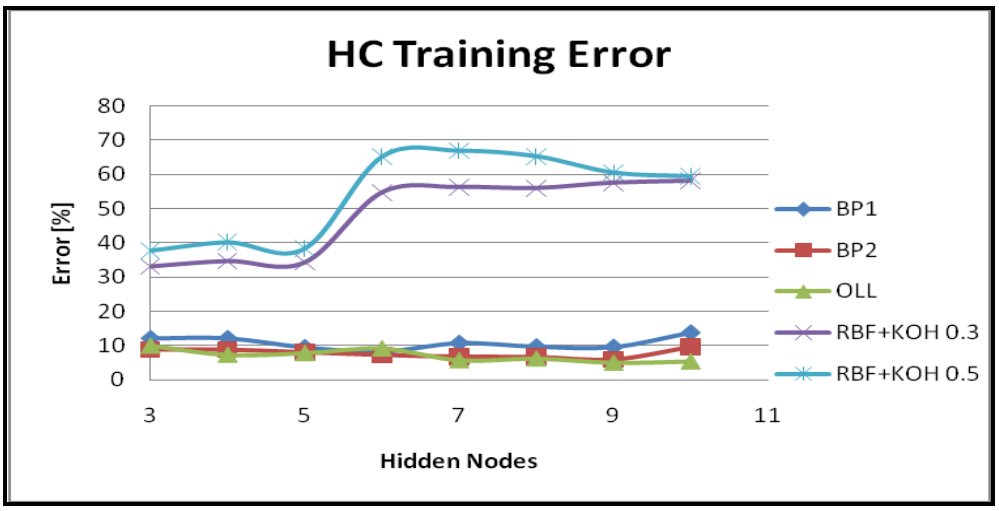

Figure 6.10: HC Training Error

The optimum OLL network selected for the EPM in HC predictions is the OLL model with 10 hidden nodes. This was chosen as it has the lowest testing error and besides that, the

maximum error is just 6 %. The predicted results comparing to the test data is shown in Figure 6.12 below. Again, the qualitative and quantitative trends between the predicted and actual data matched.

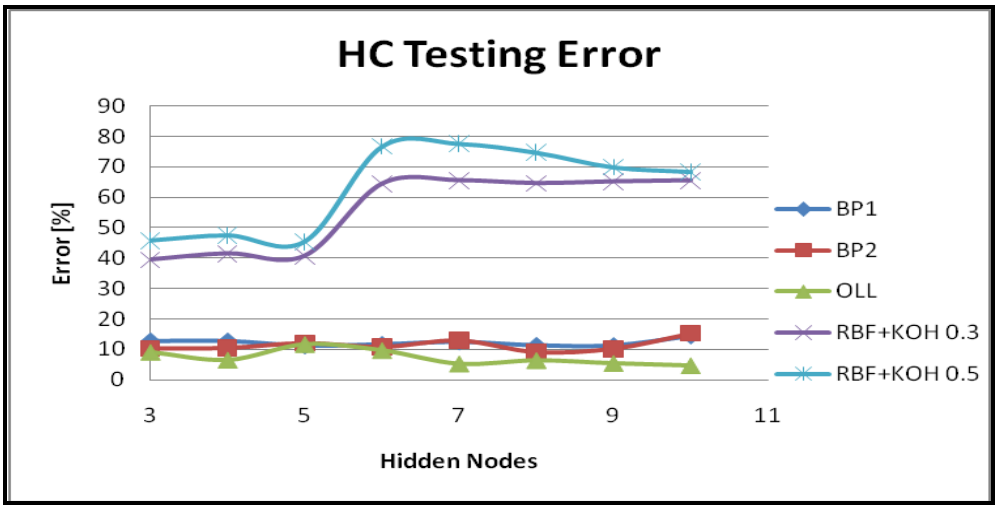

Figure 6.11: HC Testing Error

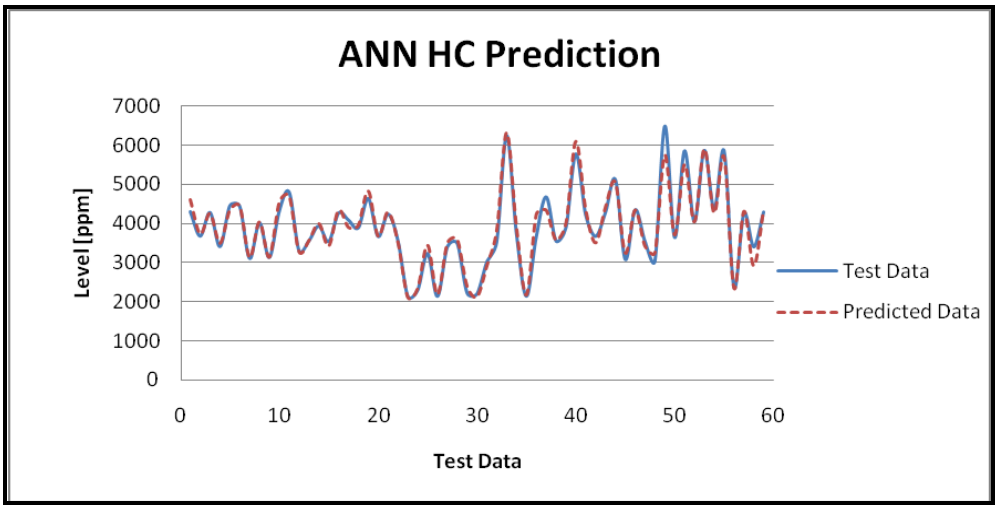

Figure 6.12: HC Prediction Results

6.3.4 O_2

Lastly, for O_2 predictions, again the OLL with 10 hidden nodes gives the best prediction results with an average RMS training and testing error of 2.79 % and 3.11 % respectively. Although that was the case, it was observed that the BP1 network also gives acceptable and constant errors of just under 5 %. Of course, the aim is to select the most accurate model for

online vehicle tuning; the most suitable O_2 model for the EPM is, again, the OLL model with 10 hidden nodes.

Figures 6.13 and 6.14 show the errors distribution with increasing hidden nodes for each neural network model.

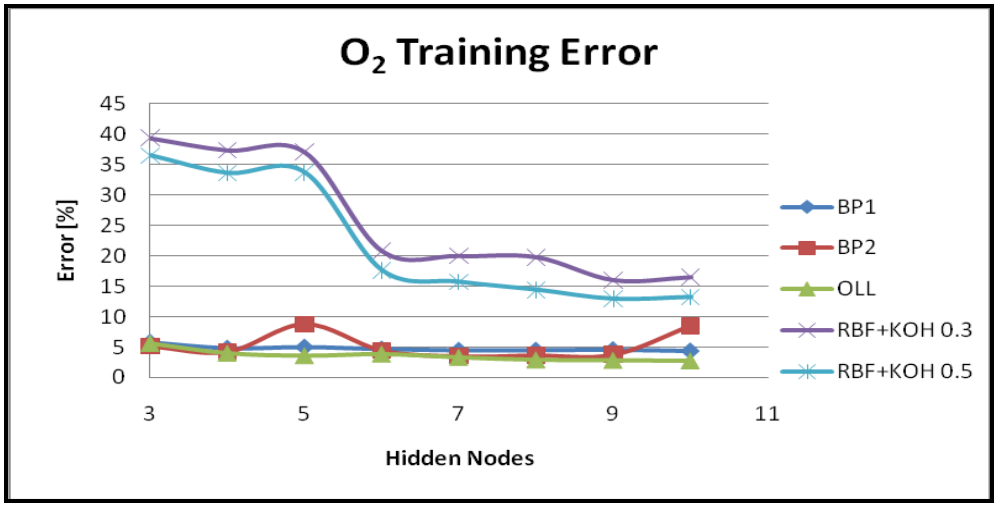

Figure 6.13: O_2 Training Error

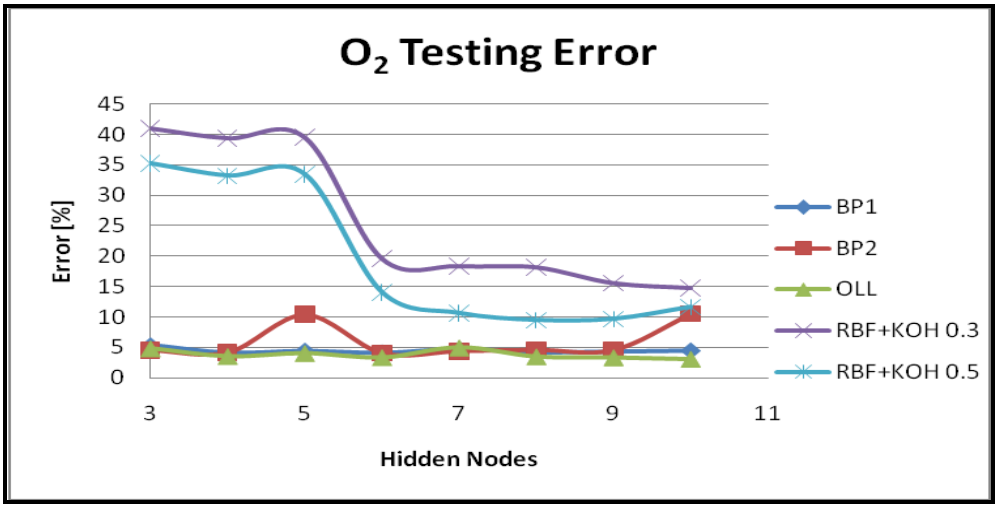

Figure 6.14: O_2 Testing Error

Having determined the optimum model for O_2 predictions, the predicted results of the OLL model with 10 hidden nodes is shown in Figure 6.15 below. Again, the qualitative and quantitative trends are similar, exhibiting errors just over 3 %.

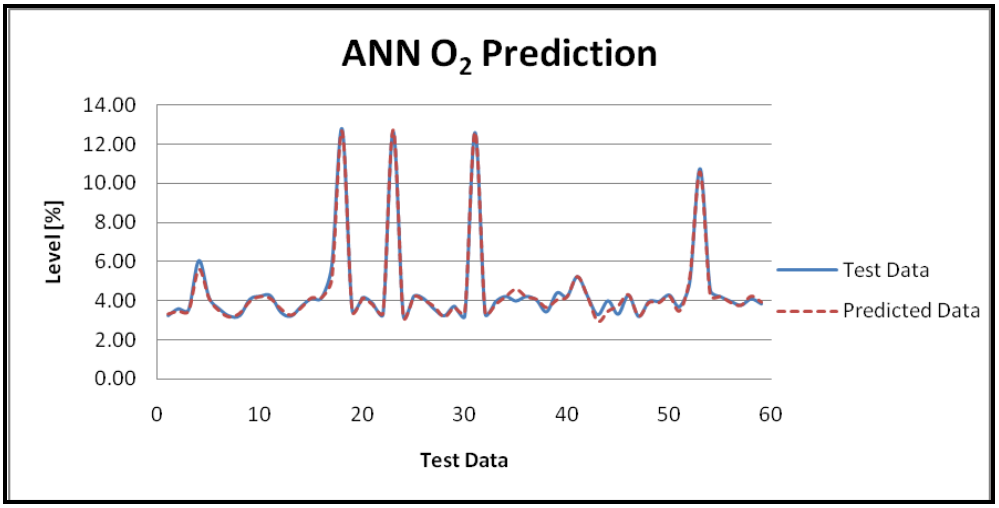

Figure 6.15: O_2 Prediction Results

6.4 Conclusion

Through the investigation and studies of various neural network models into four specific emissions; CO, CO_2, HC, O_2, some models are very accurate with low RMS errors. Having an accurate EPM gives a high confidence when adopted online to the HES model and the HES itself.

For CO prediction, the most suitable neural network model is the OLL model with 9 hidden nodes. For CO_2 prediction, the most suitable network is the OLL model with 10 hidden nodes, which gives an average RMS training error of 2.27 % and average RMS testing error of 3.69 %. For HC prediction, the OLL model with 10 hidden nodes was chosen as it has the maximum error of 6 %. Lastly, for O_2 prediction, the most appropriate neural network model selected for the EPM is also the OLL model with 10 hidden nodes. Average RMS errors for this model is below 3 %. Table 6.1 below shows the summary of the results.

Emission Gas	**RMS Testing Error %**	**RMS Training Error %**	**Best Network**
CO, %	3.32	3.01	OLL with 9 hidden nodes
CO_2, %	3.69	2.27	OLL with 10 hidden nodes
HC, ppm	5.34	4.74	OLL with 10 hidden nodes
O_2, %	3.11	2.79	OLL with 10 hidden nodes

Table 6.1: Summary of Results

This study presents a different approach in emissions predictive modelling as discussed in the earlier chapters. The HES model (discussed in Chapter 4) predicts the emissions by utilizing a mathematical approach where operating conditions are first determined whereas the EPM uses the operating conditions to predict the emissions. The incorporation of the ANN EPM provides another methodology in emissions predictive for HES applications.

From this study, the EPM can be constructed using the OLL network with 10 hidden nodes, which gives the most accurate prediction. This structure and configuration gives accurate prediction of the emissions and could also act as a ‘virtual sensor’ for the HES, replacing costly hardware.

CHAPTER 7: FINAL CONCLUDING REMARKS AND RECOMMENDATIONS

Two approaches on predictive modelling of emissions were presented in this thesis. The first approach in emissions prediction is to construct a dynamic hybrid electric scooter model to simulate and predict the emissions and fuel economy. The hybrid electric scooter model was constructed using MATLAB-Simulink and consists of several sub-models integrated together. These sub-models include Vehicle Dynamics, Battery, ICE, Emissions and the Motor Model. A Multi-State Controller, based on one control strategy discussed in the literature survey, was adopted for modelling and simulation. The Multi-State Controller was incorporated in the hybrid electric scooter model to optimize the system.

A hybrid electric scooter was then constructed accordingly to the model. A 90 cc Bug Escape Scooter was modified with a DC hub motor attached to the front wheel, acting as the primary propulsion unit. For experimental data collection, the hybrid electric scooter was laboratory-tested on a chassis dynamometer. A 5-gas analyzer was used to measure the tailpipe emissions of the scooter. The predicted emissions were CO, CO_2, HC and O_2.

Experimental data gathered was then used to construct and verify the hybrid electric scooter model in terms of emissions and fuel economy. The comparison between the simulated and experimental results for the ECE-15 cycle showed maximum errors of 7 % and 10 % for fuel economy and emissions predictions respectively. With the overall errors all under 10 %, the hybrid electric scooter model was deemed feasible and accurate and its performance using the multi-state control strategy was simulated over the NYCC, modified UDDS and HWFET cycle.

The second approach in emissions prediction is to construct an Emissions Predictive Model (EPM) to predict the tailpipe emissions. The EPM was constructed using artificial neural network techniques. 3 neural network models were investigated for each gas to determine the most accurate model for each gas to make up the EPM. The three investigated neural network models are the Back-propagation, Optimization Layer-by-Layer and Radial Basis Function incorporating the Kohonen network.

Experimental data gathered from the chassis dynamometer were used to train and verify the neural network models for each gas. Throttle position, engine power and tractive

force, Lambda (A/F ratio) and vehicle speed are the operating conditions that govern the predicted tailpipe emissions for the neural network model.

For CO prediction, the most suitable model that gives the highest accuracy was the Optimization Layer-by-Layer model with 9 hidden nodes. The average RMS training and testing error is 3.01 % and 3.32 % respectively.

For CO_2 prediction, the neural network model selected is the Optimization Layer-by-Layer model with 10 hidden nodes, which gives an average RMS training error of 2.27 % and an average RMS testing error of 3.69 %.

For HC prediction, the neural network model selected for the EPM for HC detection is similar with the CO_2 model, an Optimization Layer-by-Layer model with 10 hidden nodes. This gives an average RMS training error of 5.34 % and an average RMS testing error of 4.74 %.

Lastly, for O_2 prediction, an Optimization Layer-by-Layer with 10 hidden nodes was again the most accurate model with an average RMS training error of 2.79 % and an average RMS testing error is 3.11 %.

In conclusion, both approaches exhibit excellent predictions. The first approach in emissions predictive modelling gives maximum prediction errors of 7 % and 10 % for fuel economy and emissions respectively. For the second approach, given the mentioned operating conditions, the most suitable neural network model for each gas that makes up the EPM is the Optimization Layer-by-Layer model with 9 hidden nodes for CO and 10 hidden nodes for CO_2, HC and O_2. The overall obtained errors are below 6 %.

From the background setup of this study, several recommendations were identified:

Model Implementation

Both models can be implemented to the constructed hybrid electric scooter shown in Figure 4.55. The MATLAB-Simulink hybrid electric scooter model can be use as a predictive tool to optimize HES system and the EPM can act as a ‘virtual sensor’ or predictive tool to predict the emission levels of the hybrid electric scooter. By changing the operating conditions on the MATLAB-Simulink model, the emissions levels can be predicted using the EPM and thus the system can be optimized in such a way where the emission levels are minimized.

Model Integration

The EPM presents a more accurate tool in predicting emissions but do not predict fuel economy. Thus by incorporating the EPM to the HES model, the operating conditions (inputs to the EPM) will be controlled by varying operating parameters in the HES model. As the HES model was developed using dynamic modelling techniques, the operating conditions of the HES can be controlled to get the desired emission levels and fuel economy accurately.

Besides that, by having accurate predictive and simulation models, this study can also be expanded to optimizing the energy and power flow of the hybrid electric scooter system based on emission levels and fuel economy.

Online Control

The HES model and the EPM performed accurate predictions and simulations offline, where driving schedules (for HES model) and the experimental training data (EPM) were first presented. The accuracy of the models were discussed and published in the literature by the author. With the hybrid electric scooter readily available, both the HES model and the EPM can be incorporated online *i.e.* during real-time driving conditions. Control algorithms for both the models and the hybrid electric scooter have to be modified to cater for online data processing.

To adhere to more stringent regulations such as the introduction of the Euro IV and V regulations, the EPM will also have to be modified by which the emissions are to be read in real-time. In order for emission levels to comply under the regulations, the operating conditions (input parameters) have to be optimized and changed online.

Model Incorporation

The models developed using MATLAB-Simulink and ANN can also be applied, as a predictive tool, to not just for hybrid electric scooters, but other hybrid electric motorcycles as well. The HES model, with proper modification, can be used to model and simulate other types of motorcycles and scooters; being either hybrid, electric or petrol. Both the HES model and the EPM can also be used as a predictive tool in emissions prediction and modelling and simulation tool before physical prototype construction work begins. This will eventually reduce cost and time. The predictive models can also be incorporated to other hybrid vehicle systems, either online or offline, with proper modification to the code and algorithm.

LIST OF REFERENCES

[1] WRI calculation based on compiled data from various editions of: International Energy Agency, Energy Statistics and Balances of Non-OECD Countries and Energy Statistics and Balances of OECD Countries (Organization for Economic Co-Operation and Development, Paris, various editions).

[2] ACTAS Children Orphaned by Traffic Accidents Support Association, viewed 20 November 2008, <www.actas.org>.

[3] Wei, YM, Liu, LC, Fan, Y & Wu, G 2007, 'The impact of lifestyle on energy use and CO_2 emission: an empirical analysis of China's residents', *Energy Policy,* vol. 35, no. 1, pp. 247-257.

[4] Vasic, AM & Weilenmann, M 2006, 'Comparison of real-world emissions from two-wheelers and passenger cars', *Environmental Science and Technology*, vol. 40, pp. 149-154.

[5] Bureau of Transport and Regional Economics, 2003, *Urban Pollutant Emissions from Motor Vehicles: Australian Trends to 2020*, Bureau of Transport and Regional Economics, Canberra.

[6] Silver, J 2008, *Global Warming and Climate Change Demystified*, McGraw-Hill.

[7] Bascom, R, Bromberg, PA, Costa, DA, Devlin, R, Dockery, DW, Frampton, MW, Lambert, W, Samet, JM, Speizer, FE & Utel, M 1996, 'Health effects of outdoor air pollution: Parts I and II', *American Journal of Respiratory Critical Care Medicine*, vol. 153, pp. 447-498.

[8] Environmental Protection Agency 1998, *NOx – How Nitrogen Oxides Affect the Way We Live and Breathe*, EPA-456/F-98-005.

[9] Environmental Protection Agency, 1999, *Ozone and your health*, EPA-452/F-99-003.

[10] Carpenter, CP, Kinkead, ER, Geary, DL Jr, Sullivan, LJ & King, JM 1975, 'Animal and human response to vapors of mixed Xylenes - Petroleum hydrocarbon toxicity studies V', *Toxicology and Applied Pharmacology*, vol. 33, no. 3, pp. 543-558.

[11] Anderson, I, Lundqvist, GR & Molhave, L 1983, 'Human response to controlled levels of toluene in six-hour exposures', *Scandinavian Journal of Work, Environment and Health*, vol. 9, pp. 405-418.

[12] Environmental Protection Agency 2003, *Particle Pollution and Your Health*, EPA-452/F-03-001.

[13] Environmental Protection Agency 2009, *Health and Environmental Impacts of SO_2*, viewed 24 February 2009, <http://www.epa.gov/air/urbanair/so2/hlth1.html>.

[14] Environmental Protection Agency 2009, *Health and Environmental Impacts of Pb*, viewed 24 February 2009, <http://www.epa.gov/air/lead/health.html>.

[15] Pimental, D, Marklein, A, Toth, MA, Karpoff, MN, Paul, GS, McCormack, R, Kyriazis, J & Krueger, T 2009, 'Food versus biofuels: Environmental and economic costs', *Human Ecology*, vol. 27, pp. 1-12.

[16] James, WE, Jha, S, Sumulong, L, Son, HH, Hasan, R, Khan, ME, Sugiyarto, G & Zhai F 2008, 'Food prices and inflation in developing Asia: Is poverty reduction coming to an end?', in *Asian Development Bank*, Manila, Philipinnes.

[17] Josserand, H 2008, *Crop Prospects and Food Situation*, in Global Information and Early Warning Service – Food and Agriculture Organization of the United Nations, Rome, Italy, viewed 28 August 2009, <ftp://ftp.fao.org/docrep/fao/010/ai465e/ai465e00.pdf 2008>.

[18] Crutzen, PJ, Mosier, AR, Smith, KA & Winiwarter, W 2008, 'N_2O release from agro-biofuel production negates global warming reduction by replacing fossil fuels', *Atmospheric Chemistry and Physics*, vol. 8, no. 2, pp. 389-395.

[19] Chau, KT & Wong, YS 2002, 'Overview of power management in hybrid electric vehicles', *Energy Conversion and Management*, vol. 43, pp. 1953-1968.

[20] Gao, Y & Ehsani, M 2002, 'An investigation of battery technologies for the army's hybrid vehicle application', in *Proceedings of the IEEE 56th Vehicular Technology Conference*, Vancouver, Canada.

[21] He, X, Maxwell, T & Parten, ME 2006, 'Development of a hybrid electric vehicle with a hydrogen-fueled ICE engine', *IEEE Transactions on Vehicular Technology*, vol. 55, no. 6, pp. 1693-1703.

[22] Kim, YY, Lee, JT & Caton, JA 2006, 'The development of a dual-injection hydrogen-fueled engine with high power and high efficiency', *Journal of Engineering for Gas Turbines and Power – Transactions of the ASME*, vol. 128, no. 1, pp. 203-212.

[23] Karim, GA 2003, 'Combustion in gas fueled compression: Ignition engines of the dual fuel type', *Journal of Engineering for Gas Turbines and Power – Transactions of the ASME*, vol. 125, no. 3, pp. 827-836.

[24] Nguyen, V 2007, 'Study of predictive models for emissions in hydrogen assisted dual fuel internal combustion engine', PhD. Thesis, School of Engineering, University of Tasmania.

[25] Maxim, HP 1937, *Horseless Carriage Days*, 2nd edn., Harper & Brothers, New York.

[26] Wakefield, EH 1998, *History of Electric Automobile: Hybrid Electric Vehicles*, Society of Automotive Engineers.

[27] *Scientific American Supplement* 1899, vol. XLVIII, no. 1235, pp. 19795.

[28] Ehsani, M, Gao, Y, Gay, S & Emadi, A 2006, *Modern Electric, Hybrid Electric, and Fuel Cell Vehicles: Fundamentals, Theory and Design*, CRC Press.

[29] 'Paris automobile and cycle show' 1901, *Scientific American Supplement*, vol. LI, no. 1310, pp. 21142.

[30] *Hybrid vehicle history: More than a century of evolution and refinement* 2006, viewed 20 September 2006, <http://www.hybrid-vehicle.org/hybrid-vehicle-history.html>.

[31] *Hybrid cars comparison chart* 2006, viewed 27 August 2006, <http://www.fueleconomy.gov/feg/hybrid_sbs_cars.shtml>.

[32] Associates, JPA 2007, 2007 U.S. Hybrid Vehicle Forecast Second Quarter Update', JD Power and Associates.

[33] Toyota Corporation Japan 2007, *Toyota Chronology 1918 – 2007*, viewed 3 January 2009, <http://www.toyota.co.jp/en/about_toyota/in_the_world/pdf2008/40chronology.pdf>.

[34] Miller, J 2006, 'Hybrid electric vehicle propulsion system architectures of the e-CVT type', *IEEE Transactions on Power Electronics*, vol. 21, no. 3, pp. 756-767.

[35] Honda Corporation 2009, *Honda Reaches 300,000 units in Cumulative Global Sales of Hybrid Vehicles*, viewed March 2009, <http://world.honda.com/news/2009/4090218Hybrid-Vehicles>.

[36] Honda Corporation 2009, *2010 Honda Insight Hybrid to Make World Debut at the North American International Auto Show*, viewed 1 March 2009, <http://corporate.honda.com/press/article.aspx?id=4886>.

[37] HybridCarBlog.com 2008, viewed 5 January 2009, <http://www.hybridcarblog.com/2008/01/new-gm-hybrid-every-3-months.html>

[38] European Union 2007, 'Regulation (EC) No 715/2007 of the European Parliament and of the Council', *Official Journal of the European Union*, pp. L171.

[39] Ehsani, M, Butler, KL, Gao, Y, Rahman, KM & Burke, D 1998, 'Towards a sustainable transportation without sacrifice of range, performance, or air quality: the ELPH car concept', in *Automotive Congress, International Federation of Automotive Engineering Society*, Paris, France.

[40] Ehsani, M, Butler, KL, Gao, Y & Rahman, KM 1998, 'Next generation passenger cars with better range, performance, and emissions: the ELPH car concept', in *Horizon in Engineering Symposium*, Texas A&M University Engineering Program Office, College Station, TX.

[41] Ehsani, M 1996, *The Electrically Peaking Hybrid System and Method*, United States Patent Office 5,586,613.

[42] Westbrook, M 2001, *The Electric Car: Development and Future of Battery, Hybrid and Fuel-Cell Cars*, Institution of Electrical Engineers, London, United Kingdom.

[43] Honda Worldwide 2009, *The Honda Hybrid System: The Engine is the Main Power Source*, viewed 25 February 2009, <http://world.honda.com/automobile-technology/IMA/ima02/>.

[44] ABI Research 2006, 'Commercial hybrid vehicles: Market analysis for series, parallel, hydraulic, and electric drive systems', ABI Research Technical Reports.

[45] Husain, I 2003, *Electric and Hybrid Vehicles – Design Fundamentals*, CRC Press.

[46] Schmidt, MR 1996, *Two-mode, Input-split, Parallel, Hybrid Transmission*, United States Patent Office 5,558,588.

[47] Wishart, JD 2008, 'Modelling, simulation, testing and optimization of advanced hybrid vehicle powertrains', PhD. Thesis, Department of Mechanical Engineering, University of Victoria.

[48] Schmidt, MR 1996, *Four-mode, Input-split, Parallel, Hybrid Transmission*, United States Patent Office 5,571,058.

[49] Grewe, T, Conlon, B & Holmes, A 2007, 'Defining the General Motors 2-mode hybrid transmission', in *Proceedings of the 2007 SAE World Congress*, Detroit, MI.

[50] Schmidt, MR 1999, *Two-mode, Compound-split Electromechanical Vehicular Transmission*, United States Patent Office 5,931,757.

[51] Schmidt, MR, Klemen, D, Nitz, L & Holmes, A 2005, *Two-mode, Compound-split, Hybrid Electro-mechanical Transmission Having Four Fixed Ratios*, United States Patent Office 6,953,409 B2.

[52] Zhang, Y, Lin, H Zhang, B & Mi, C 2006, 'Performance modelling and optimization of a novel multi-mode hybrid powertrain', *J*ournal of Mechanical Design, vol. 128, no. 1, pp. 79-89.

[53] Villeneuve, A 2004, 'Dual mode electric infinitely variable transmission', in *International CVT and Hybrid Transmission Congress*, Davis, CA.

[54] Dyck, G, Dries, P, Bagherpour, M & Czepak, J 2006, *Electro-mechanical continuously variable transmission*, United States Patent Office 7,008,342 B2.

[55] Ai, X, Mohr, T & Anderson, S 2004, 'An electro-mechanical infinitely variable speed transmission,' in *Proceedings of the 2004 SAE World Congress*, Paper No. 2004-01-0354, pp. 27-40.

[56] Ai, X & Mohr, T 2003, *Continuous Variable Transmission*, United States Patent Office 6,595,884

[57] National Renewable Energy Laboratory 2009, *ADVISOR*, viewed 4 March 2009, <http://www.avl.com/wo/webobsession.servlet.go?app=bcms&page=view&nodeid=400030459>.

[58] Gao, DWZ, Mi, C & Emadi, A 2007, 'Modelling and simulation of electric and hybrid vehicles', Proceedings of the IEEE, vol. 95, no. 4, pp. 729-745.

[59] Toth-Nagy, C, Conley, JJ, Jarrett, RP & Clark NN 2006, 'Further validation of artificial neural network-based emissions simulation models for conventional and hybrid electric vehicles', *Journal of Air & Waste Management Association*, vol. 67, no. 7, pp. 898-910.

[60] Williamson, SS, Lukic, SM & Emadi, A 2006, 'Comprehensive drive train efficiency analysis of hybrid electric and fuel cell vehicles based on motor-controller efficiency modelling', *IEEE Transactions on Power Electronics*, vol. 21, no. 3, pp. 730-740.

[61] Bhatikar, SR, Mahajan, RL, Wipke, K & Johnson, V 2001, 'An artificial neural network module for simulation of the energy storage system of a hybrid electric vehicle', Proceedings of the Institution of Mechanical Engineers – Part C – Journal of Mechanical Engineering Science, vol. 215, no. C8, pp. 919-932.

[62] Rousseau, A & Pasquier M 2001, 'Validation of a hybrid modelling software (PSAT) using its extension for prototyping (PSAT-PRO)', in Global Powertrain Congress, Detroit, MI.

[63] Rousseau, A, Sharer, P & Besnier, F 2004, 'Feasibility of reusable vehicle modelling: application to hybrid vehicles', in *Proceedings of the SAE World Congress*, Detroit, MI.

[64] Rousseau, A, Pagerit, S & Monnet, G 2001, 'The new PNGV system analysis toolkit PSAT V4.1 – Evolution and improvements," in *Proceedings of Future Transportation Technology Conference*, Costa-Mesa, CA.

[65] An, F & Rousseau, A 2001, 'Integration of a modal energy and emission model into the PNGV vehicle simulation model: PSAT', in *Proceedings of the SAE World Congress*, Detroit, MI.

[66] Rousseau, A & Larsen, R 2000, 'Simulation and validation of hybrid electric vehicles using PSAT', in *Proceedings of the Global Powertrain Congress*, Detroit, MI.

[67] MathWorks 2008, *MATLAB – The language of technical computing*, viewed 3 March 2009, <http://www.mathworks.com/products/matlab/>.

[68] MathWorks 2008, *Simulink – Simulation and model-based design*, viewed 3 March 2009, <http://www.mathworks.com/products/simulink/>.

[69] Shao, DG, Li, YB, Wang, XY & Jiang, JZ 2003, 'A Matlab-based simulation for hybrid electric motorcycle', *Journal of Shanghai University (English Edition)*, vol. 7, no. 2, pp. 178-184.

[70] Khateeb, SA, Farid, MM, Selman, JR & Al-Hallaj, S 2006, 'Mechanical-electrochemical modelling of Li-ion battery designed for an electric scooter', *Journal of Power Sources*, vol. 158, pp. 673-678.

[71] Onada, S & Emadi, A 2004, 'PSIM-based modelling and automotive power systems: Conventional, electric and hybrid electric vehicles', *IEEE Transactions on Vehicular Technology*, vol. 53, no. 2, pp. 390-400.

[72] Onada, S, Lukic, SM, Nasiri, A & Emadi, A 2002, 'A PSIM-based modelling tool for conventional, electric and hybrid electric vehicle studies', *IEEE Vehicular Technology Conference*, vol. 3, pp. 1676-1680.

[73] Mierlo, JV & Maggetto, G 2001, 'Vehicle simulation program: a tool to evaluate hybrid power management strategies based on an innovative iteration algorithm', *Proceedings of the Institution of Mechanical Engineers*, vol. 9, no. 215, pp. 1043-1052.

[74] Stevens, KM 1996, 'A versatile computer model for the design and analysis of electric and hybrid drive trains', MSci. Thesis, Texas A&M University.

[75] Butler, KL, Stevens, KM & Ehsani, M 1997, 'A versatile computer simulation tool for design and analysis of electric and hybrid drive trains', in *SAE Proceedings in Electric and Hybrid Vehicle Design Studies*, Detroit, MI, pp. 19-25.

[76] Butler, KL, Ehsani, M & Kamath, P 1999, 'A Matlab-based modelling and simulation package for electric and hybrid electric vehicle design', *IEEE Transactions on Vehicular Technology*, vol. 48, no. 6, pp. 1770-1778.

[77] Schouten, NJ, Salman, MA & Kheir, NA 2002, 'Fuzzy logic control for parallel hybrid vehicles', *IEEE Transactions on Control Systems Technology*, vol. 10, no. 3, pp. 460-468.

[78] Kheir, NA, Salman, MA & Schouten, NJ 2004, 'Emissions and fuel economy trade-off for hybrid vehicles using fuzzy logic', *Mathematics and Computers in Simulation*, vol. 66, pp. 155-172.

[79] Pu, JH, Yin, CL & Zhang, JW 2005, 'Fuzzy torque control strategy for parallel hybrid electric vehicles', *International Journal of Automotive Technology*, vol. 6, no. 5, pp. 529-536.

[80] Baumann, BM, Washington, G, Glenn, BC & Rizzoni, G 2000, 'Mechatronics design and control of hybrid electric vehicles', *IEEE/ASME Transactions on Mechatronics*, vol. 5, no. 1, pp. 58-72.

[81] Schouten, NJ, Salman, MA & Kheir, NA 2003, 'Energy management strategies for parallel hybrid vehicles using fuzzy logic', *Control Engineering Practice*, vol. 11, pp. 171-177.

[82] Alonso, JM, Alvarruiz, F, Desantes, JM, Hernandez, L, Hernandez, VM & Molto, G 2007, 'Combining neural networks and genetic algorithms to predict and reduce diesel engine emissions', *IEEE Transactions on Evolutionary Computation*, vol. 11, no. 1, pp. 46-55.

[83] Jeon, S, Jo, S, Park, Y & Lee, J 2008, 'Multi-mode driving control of a parallel hybrid electric vehicle using driving pattern recognition', *Journal of Dynamic Systems, Measurement and Control*, vol. 124, pp. 141-149.

[84] Moreno, J, Ortuzar, ME & Dixon, JW 2006, 'Energy-management system for a hybrid electric vehicle, using ultracapacitors and neural networks', *IEEE Transactions on Industrial Electronics*, vol. 53, no. 2, pp. 614-623.

[85] Mohebbi, M, Charkhgard, M & Farrokhi, M 2005, 'Optimal neuro-fuzzy control of parallel hybrid electric vehicles', in *Proceedings of the Vehicle Power and Propulsion, 2005 IEEE Conference*, pp 26-30.

[86] Lin, C, Peng, H, Grizzle, JW, Liu, J & Busdiecker, M 2003, 'Control system development for an advanced-technology medium-duty hybrid electric truck," in *Proceedings of the International Truck and Bus Conference, SAE Technical Paper 2003-01-3369.*

[87] Lin, C, Peng, H, Grizzle, JW & Kang, J 2003, 'Power management strategy for a parallel hybrid electric truck', *IEEE Transactions on Control Systems Technology,* vol. 11, pp. 839-849.

[88] Lin, C, Filipi, Z, Wang, Y, Louca, L, Peng, H, Assanis, D & Stein, J 2001, 'Integrated, feed-forward hybrid electric vehicle simulation in SIMULINK and its use for power management studies', *SAE Technical Paper 2001-01-1334*.

[89] Zhang, H, Zhu, Y, Tian, G, Chen, Q, & Chen, Y 2004, 'Optimal energy management strategy for hybrid electric vehicles', *SAE Technical Paper 2004-01-05*.

[90] Sciarretta, A, Black, M & Guzzella, L 2004, 'Optimal control of parallel hybrid electric vehicles', *IEEE Transactions on Control Systems Technology*, vol. 12, no. 3, pp. 352-363.

[91] Perez, LV, Bossio, GR, Moitre, D & Garcia, GO 2006, 'Optimization of power management in a hybrid electric vehicle using dynamic programming', *Mathematics and Computers in Simulation,* vol. 73, pp. 244-254.

[92] Delprat, S, Lauber, J, Guerra, TM & Rimaux, J 2004, 'Control of a parallel hybrid powertrain: Optimal control', *IEEE Transactions on Vehicular Technology*, vol. 53, no. 3, pp. 872-881.

[93] Lewis, FL & Syrmos, VL 1995, *Optimal Control*, Wiley, New York.

[94] Wei, X, Guzzella, L, Utkin, VI & Rizzoni, G 2007, 'Model-based fuel optimal control of hybrid electric vehicle using variable structure control systems', *Journal of Dynamic Systems, Measurement and Control*, vol. 129, pp. 13-19.

[95] Barsali, S, Miulli, C & Possenti, A 2004, 'A control strategy to minimize fuel consumption of series hybrid electric vehicles', *IEEE Transactions on Energy Conversion*, vol. 19, no. 1, pp. 187-195.

[96] Najjafi, G, Ghobadian, B, Tavakoli, T, Buttsworth, DR, Yusaf, TF & Faizollahnejad, M 2009, 'Performance and exhaust emissions of a gasoline engine with ethanol

blended gasoline fuels using artificial neural network', *Applied Energy*, vol. 86, no. 5, pp. 630-639.

[97] Sayin, C, Ertunc, HM, Hosoz, M, Kilicasla, I & Canakci, M 2007, 'Performance and exhaust emissions of a gasoline engine using artificial neural network', *Applied Thermal Engineering*, vol. 27, no. 1, pp. 46-54.

[98] Ghobadian, B, Rahimi, H, Nikbakht, AM, Najafi, G & Yusaf, TF 2009, 'Diesel engine performance and exhaust analysis using waste cooking biodiesel fuel with an artificial neural network', *Renewable Energy*, vol. 34, no. 4, pp. 976-982.

[99] Ho, T, Karri, V, Lim, D & Barret, D 2008, 'An investigation of engine performance parameters and artificial intelligent emission prediction of hydrogen powered car', *International Journal of Hydrogen Energy*, vol. 33, no. 14, pp. 3837-3846.

[100] Ao, GQ, Qiang, JX, Zhong, H, Mao, XJ, Yang, L & Zhuo, B 2008, 'Fuel economy and NOx emission potential investigation and trade-off of a hybrid electric vehicle based on dynamic programming', *Proceedings of the Institution of Mechanical Engineers – Part D – Journal of Automobile Engineering*, vol. 222, no. D10, pp. 1851-1864.

[101] Gray, DL & Hentea, TI 2004, 'Engine emissions modelling for a hybrid electric vehicle', in *Proceedings of the 37th Intersociety Energy Conversion Engineering Conference*, pp. 745-750.

[102] Shepherd, GM & Koch, C 1990, *Introduction to Synaptic Circuits*, Oxford University Press, New York.

[103] Negnevitsky, M 2005, *Artificial intelligence. A guide to intelligent systems*, 2nd edn., Addison-Wesley.

[104] Principe, JC 2000, *Artificial Neural Networks*, Boca Raton, CRC Press LLC.

[105] Jurada, JM 1992, *Introduction to Artificial Neural Systems*, West Publishing Company.

[106] Hebb, DO 1949, *Organization of Behaviour*, Wiley.

[107] McCulloch, WS & Pitts, W 1943, 'A logical calculus of the ideas immanent in nervous activity', *Bulletin of Mathematical Biophysics*, vol. 5, pp. 115-137.

[108] Rumelhart, D & McClelland, J 1986, *Parallel Distributed Processing: Exploitations in the Micro-structure of Cognition*, vol. 1 and 2, MIT Press, Cambridge.

[109] Kohonen, T 1989, *Self-organizing and Associative Memory*, 3rd edn, Springer-Verlag, Berlin.

[110] Albus, JS 1975, ‘A new approach to manipulator control: Cerebellar model articulation control (CMAC)’, *Journal of Dynamic Systems, Measurements and Control*, vol. 97, pp. 220-227.

[111] Hecht-Nielson, R 1990, *Neurocomputing*, Addison-Wesley, Reading.

[112] Hopfield, JJ 1982, ‘Neural networks and physical systems with emergent collecting computational abilities’, *Proceedings of the National Academy of Sciences*, vol. 79, pp. 2554-2558.

[113] Elman, JL 1990, ‘Finding structure in time’, *Cognitive Science*, vol. 14, pp. 179-211.

[114] Jordan, MI 1986, ‘Attractor dynamics and parallelism in a connectionist sequential machines’, in *Proceedings of the 8th Annual Conference of the Cognitive Science Society*, pp. 531-546.

[115] Widrow, B & Hoff, ME 1960, ‘Adaptive switching circuits’, in *Proceedings of the 1960 IRE WESCON Convention Record - Part 4*, pp. 96-104.

[116] Ergezinger, S & Thomsen, E 1995, ‘An accelerated learning algorithm for multilayer perceptrons: Optimization layer by layer’, *IEEE Transactions on Neural Networks*, vol. 6, no. 1, pp. 31-42.

[117] Carpenter GA & Grossberg S 1988, ‘The ART of adaptive pattern recognition by a self-organizing neural network’, *Computer*, vol. 2, no. 3, pp. 77-88.

[118] Dayhoff, JE 1990, *Neural Network Architectures – An Introduction*, Van Nostrand Reinhold.

[119] Watrous, RL 1987, ‘Learning algorithms for connectionist networks: Applied gradient methods of nonlinear optimization’, in *Proceedings of the 1st IEEE International Conference on Neural Networks*, San Diego, CA, vol. 2, pp. 619-627.

[120] Jacobs, RA 1988, ‘Increased rates of convergence through learning rate adaptation’, *Neural Networks*, vol. 1, pp. 295-307.

[121] Haykin, S 1994, *Neural Networks: A Comprehensive Foundation*, McMillan College Publishing Company Inc.

[122] Broomhead, DS & Lowe, D 1988, ‘Multi-variable functional interpolation and adaptive networks’, *Complex Systems*, vol. 2, pp. 321-355.

[123] Yousefizadeh, H & Zilouchian, A 2001, *Intelligent Control Systems Using Soft Computing Methodologies*, CRC Press LLC.

[124] Fausett, L 1994, *Fundamentals of Neural Networks: Architectures, Algorithms and Applications*, Prentice Hall International Inc.

[125] Sheu, KB, Hsieh, LC & Yan, HS 1996, 'Conceptual design of hybrid transmissions for motorcycle applications', *International Journal of Vehicle Design*, vol. 17, no. 4, pp. 430-448.

[126] Sheu, KB & Hsu, TH 2006, 'Design and implementation of a novel hybrid-electric-motorcycle transmission', *Applied Energy*, vol. 83, pp. 959-974.

[127] Sheu, KB 2007, 'Conceptual design of hybrid scooter transmissions with planetary gear-trains', *Applied Energy*, vol. 84, pp. 526-541.

[128] Sheu, KB 2007, 'Analysis and evaluation of hybrid scooter transmission systems', *Applied Energy*, vol. 84, pp. 1289-1304.

[129] Chen, CH & Cheng, MY 2007, 'Implementation of a highly reliable hybrid electric scooter drive', *IEEE Transactions in Industrial Electronics*, vol. 54, no. 5, pp. 2462-2473.

[130] Ceraolo, M, Caleo A, Capozzella, P, Marcacci, M, Carmignani, L & Pallottini, A 2006, 'A parallel-hybrid drive-train for propulsion of a small scooter', *IEEE Transactions on Power Electronics*, vol. 21, no. 3, pp. 768-778.

[131] Khateeb, SA, Farid, MM, Selman, JR & Al-Hallaj, S 2006, 'Mechanical-electrochemical modelling of Li-ion battery designed for an electric scooter', *Journal of Power Sources*, vol. 158, pp. 673-678.

[132] White, B 2007, *GL2 by Island Earth*, viewed 10 July 2007, <http://www.users.bigpond.com/solarbbq/GL2.htm>.

[133] Ambrose, S 2007, 'Design and efficiency testing of a plugin hybrid electric scooter', B.Eng (Hons.) Thesis, School of Engineering, University of Tasmania.

[134] Bug Scooters Australia, *Escape 90CC*, viewed 9 October 2007, <http://www.bugscooters.com.au/escape.htm>.

[135] Dyno Dynamics - 450DS Motor Cycle Dynamometer, viewed 20 May 2010, <http://www.dyno.com.au/dyno/controller/specs/showMOTO450DSPage>.

[136] AutoLogic 2007, *AutoGas emissions analyzer manual*, AutoLogic Document 910-0501.

[137] Microchip Technology Inc. 2008, *28/40/44 – Pin Enhanced Flash Microcontrollers with 10-Bit A/D and nanoWatt Technology*, PIC18F2420/2520/4420/4520 Data Sheet.

[138] National Semiconductor 1995, *LM135/LM235/LM335, LM135A/LM235A/LM335A Precision Temperature Sensors Data Sheet*, Temperature Sensor Datasheet.

[139] LCD control code developed within the School of Engineering, University of Tasmania.

[140] Kiatcharoenpol, T 2004, 'Applications of neural-fuzzy systems to tool condition monitoring in drilling operations', PhD. Thesis, University of Tasmania.

[141] Frost, F 2001, 'Neural network applications to aluminium manufacturing for auto parts', PhD. Thesis, University of Tasmania.

[142] Karri, V & Kiatcharoenpol, T 2003, 'Tool condition monitoring in drilling using artificial neural networks', *Lecture Notes in Computer Science*, vol. 2903, pp, 293-301.

Appendix A

MATLAB-Simulink User-Defined Model Codes

1. Hub Motor Model
2. ICE Model
3. Emissions Model
4. Multi-State Control Model

1. HUB MOTOR MODEL CODES

```
function [motor_torque_available, motor_power_available]= fcn(SC, Tload)


%This block calculates the available torque and power of the DC motor based

%on the manufacturer's data provided.


Tmax = 45;   %Maximum Torque


if SC > 40   %If state of charge is above threshold, 40%

   if Tload < Tmax   %if demanded torque is lower than Tmax

      motor_torque_available = Tload;

      motor_power_available = (-0.800*motor_torque_available^2) + (47.11*motor_torque_available) - 86.03;
%From manufacturer's data

   else   %if demanded torque is over or equal than Tmax

      motor_torque_available = Tmax;

      motor_power_available = (-0.800*motor_torque_available^2) + (47.11*motor_torque_available) - 86.03;
%From manufacturer's data

   end

else   %If state of charge is below threshold

   motor_torque_available = 0;

   motor_power_available = 0;

end
```

2. ICE MODEL CODES

```
function [ICE_power_available, ICE_torque_available]= fcn(Pload, Tload,speed)

%This bloack calculates the engine's available power and torque, based on dyno test data and
%manufacturer's data provided.

Pmax = 2600;  %Maximum engine power, W
Tmax = 98;   %Maximum engine torque, Nm

if Tload < 0   %During braking
   ICE_torque_available = 0;
   ICE_power_available = 0;
else
   if Tload < Tmax   %If demanded road torque is lower than the maximum engine torque
        %Based on manufacturer's and dyno test data.
        ICE_torque_available = -0.057*speed*2 - 2.649*speed + 99.20;
        ICE_power_available =  -20.15*speed^2 + 516.6*speed - 335.8;
   else
        ICE_torque_available = Tmax;
        %Based on manufacturer's and dyno test data.
        ICE_power_available = -0.694*ICE_torque_available^2 + 100.1*ICE_torque_available + 364.4;
   end
end
   ICE_torque_available = Tload;
   ICE_power_available = 2400;
End
function [FE, SFC,throttle_angle]= fcn(Pfinal, Tfinal, Speed)

%Operate the ICE according to the experimental dyno test data for a hybrid electric scooter.

Pmax = 2600; %Maximum engine power, W
```

```
Tmax = 98; %Maximum engine torque, Nm

%Engine throttle Profile; max speed, max torque and max power
vmax_25 = 13.88;
vmax_50 = 20.55;
vmax_75 = 21.04;
vmax_100 = 22.22;

tmax_25 = 15.2;
tmax_50 = 20.4;
tmax_75 = 30.8;
tmax_100 = 55.4;

pmax_25 = 900;
pmax_50 = 1800;
pmax_75 = 2500;
pmax_100 = 2600;

%Set appropriate throttle angle based on torque and speed thresholds

if Tfinal < 0   %braking occurs
   ICE_torque_available = 0;
   ICE_power_available = 0;
   throttle_angle = 0;
else
   if Tfinal < Tmax   %if final torque is less than maximum engine torque
      if Tfinal < tmax_25 && Speed < vmax_25
         throttle_angle = 0.25;
      else
         if Tfinal < tmax_50 && Speed < vmax_50
            throttle_angle = 0.5;
```

```
        else
            if Tfinal < tmax_75 && Speed < vmax_75
                throttle_angle = 0.75;
            else
                throttle_angle = 1;   %WOT
            end
        end
    end
  else   %Demanded torque equal or more than maximum engine torque
        throttle_angle = 1;
  end
end

throttle_angle1 = throttle_angle*100;   %convert to %

%Calculate BSFC to get fuel economy based on throttle angle and test data

switch throttle_angle1
  case 0
    SFC = 0;
    Pfinal1 = 0;
  case 25   %at 25% throttle
    SFC = (-0.036*Tfinal^2) + (1.171*Tfinal) + 236.9;
    Pfinal1 = 58.59*Tfinal/1000*3.5;
  case 50   %at 50% throttle
    SFC = (0.111*Tfinal^2) - (14.84*Tfinal) + 642.2;
    Pfinal1 = 72.13*Tfinal/1000*2.5;
  case 75   %at 75% throttle
    SFC = (0.099*Tfinal^2) - (11.94*Tfinal) + 508.6;
    Pfinal1 = 93.12*Tfinal/1000*3;
  otherwise   %at WOT
    SFC = (0.126*Tfinal^2) - (16.80*Tfinal) + 746.6;
```

```
    Pfinal1 = (98.72*Tfinal)/1000*2;
end


FE = Pfinal1*SFC/3600*1.3564/1000; %l of petrol used
```

3. EMISSIONS MODEL CODES

```
function [COtotal, CO2total, HCtotal, O2total, AF, fuel_used_g]= fcn(fe, sfc, throttle, speed)

%This block calculates the emissions for the hybrid electric scooter; CO, CO2, HC, O2  and A/F ratio
%based on the dyno test data. Inputs are the fuel used, BSFC, throttle position and vehicle speed.

throttle = throttle*100; %convert to %

switch throttle
   case 25   %at 25% throttle
      CO = -0.018*speed + 9.957;
      CO2 = 0.8*(0.022*speed + 4.794);
      HC = 2.168*speed^2 - 10.8*speed + 3549;
      O2 = 0.018*speed + 3.422;
      AF = -0.002*speed^2 + 0.026*speed + 12.87;
   case 50   %at 50% throttle
      CO = 0.011*speed^2 - 0.283*speed + 9.036;
      CO2 = 0.8*(-0.016*speed^2 + 0.519*speed + 5.719);
      HC = -3.864*speed^2 + 60.58*speed + 3714;
      O2 = -0.048*speed + 4.251;
      AF = 0.008*speed^2 - 0.256*speed + 12.96;
   case 75  %at 75% throttle
      CO = 0.003*speed^2 - 0.012*speed + 5.949;
      CO2 = -0.008*speed^2 + 0.189*speed + 7.452;
      HC = -0.625*speed^2 - 58.06*speed + 4469;
      O2 = -0.052*speed + 4.505;
      AF = 0.003*speed^2 - 0.059*speed + 11.65;
   case 100   %at WOT
      CO = 0.05*speed + 5.093;
      CO2 = 1.15*((-0.005*speed^2) + (0.117*speed) + 8.166);
      HC = -1.725*speed^2 - 13.42*speed + 4699;
```

```
        O2 = -0.058*speed + 4.978;
        AF = 0.003*speed^2 - 0.070*speed + 11.50;
    otherwise   %idle conditions
        CO2 = 3.9;
        CO = 3.53;
        HC = 5380;
        O2 = 10.7;
        AF = 17.85;
end

fuel_used_ml=1000*(5.5-fe);   %fuel used in ml
fuel_used_g=0.73722*fuel_used_ml;   %fuel used in grams

%Total emissions in grams
CO2total = CO2/100*fuel_used_g;
COtotal = CO/100*fuel_used_g;
HCtotal = HC/1000000*fuel_used_g;
O2total = O2/100*fuel_used_g;
```

4. MULTI-STATE CONTROL MODEL CODES

```
function [Pmfinal, Tmfinal, Picefinal, Ticefinal, Pbattery]= fcn(Piceavail, Ticeavail, Pmotoravail, Tmotoravail, State, Pload, Tload)


%Based on the selected state (State), power and torque road demand (Pload and Tload) and the

%power and torque available from the ICE and motor, the power splits between the ICE and the motor is calculated

%

%Pmfinal = final provided motor power

%Tmfinal = final provided motor torque

%Picefinal = final provided ICE power

%Ticefinal = final provided ICE torque

%Pbattery = battery power demanded


switch State

  case 1   %Engine State

    Pmfinal = 0;

    Tmfinal = 0;

    if Tload < Ticeavail

      Ticefinal = Tload;

      Picefinal = Pload;  %Insert Engine Map to get power

    else

      Ticefinal = Ticeavail;

      Picefinal = Piceavail; %Insert Engine Map to get power

    end

    Pbattery = 0;


  case 2   %Motor State

    Picefinal = 0;

    Ticefinal = 0;

    if Tload < Tmotoravail

      Tmfinal = Tload;
```

```
        %From manufacturer's data
        Pmfinal = (-0.800*Tmfinal^2) + (47.11*Tmfinal) - 86.03;
        Pbattery = (-0.590*Tmfinal^2) + (47.74*Tmfinal) - 56.24;
    else
        Tmfinal = Tmotoravail;
        %From manufacturer's data
        Pmfinal = (-0.800*Tmfinal^2) + (47.11*Tmfinal) - 86.03;
        Pbattery = (-0.590*Tmfinal^2) + (47.74*Tmfinal) - 56.24;
    end

case 3   %Hybrid State
    if Tload < Tmotoravail
        Tmfinal = Tload;
        %From manufacturer's data
        Pmfinal = (-0.800*Tmfinal^2) + (47.11*Tmfinal) - 86.03;
        Pbattery = (-0.590*Tmfinal^2) + (47.74*Tmfinal) - 56.24;
    else
        Tmfinal = Tmotoravail;
        %From manufacturer's data
        Pmfinal = (-0.800*Tmfinal^2) + (47.11*Tmfinal) - 86.03;
        Pbattery = (-0.590*Tmfinal^2) + (47.74*Tmfinal) - 56.24;
    end
    Ticefinal = Tload - Tmfinal;
    Picefinal = Pload - Pmfinal; %Insert Engine Map to get power

case 4   %Charging State
    Pmfinal = 0;
    Tmfinal = 0;
    Picefinal = Pload; %Insert Engine Map to get power
    Ticefinal = Tload;
    Pbattery = -100;
```

```
    case 5   %Idle Recharging State
        Pmfinal = 0;
        Tmfinal = 0;
        Picefinal = 0;
        Ticefinal = 0;
        Pbattery = -100;

    case 6   %Mechanical Braking State
        Pmfinal = Pload;
        Tmfinal = Tload;
        Picefinal = 0;
        Ticefinal = 0;
        Pbattery = 0;

    otherwise   %Regenerative Braking State
        Tmfinal = Tload;
        Pmfinal = Pload;
        Picefinal = 0;
        Ticefinal = 0;
        Pbattery = -1000;

end



function State = fcn(SC, Tload, Speed,Pload,prev_state)

%This block selects the states based on the threshold values of speed and state of charge.
%Operation States are
%1: Engine State
%2: Motor State
%3: Hybrid State
```

```
%4: Charging State

%5: Idle Recharging State

%6: Mechanical Braking state

%7: Regenerative Braking State

%

%prev_state is the previous state the system was in, State is the current state, SC is the battery's

%instantaneous state of charge [%], Speed is vehicle speed [m/s] and Tload is the demanded road torque [N]


if SC < 40   %If state of charge is below 40%

   if Speed < 0   %if idle

      State = 4;

   else

      State = 5;

   end

else   %if recharging is not needed

   if SC < 50 && (prev_state == 4 || prev_state == 7)   %this is to eliminate engine cycling, thus the range was
set between 40% to 50%

      if Speed < 0   %if idle

         State = 4;

      else

         State = 5;

      end

   else

      if Tload < 0  %if braking occurs

         if SC < 80

            State = 7;

         else

            State = 6;

         end

      else   %no braking

         if Speed < 7.5   %threshold speed 7.5 m/s

            State = 2;
```

```
        else
            if Speed < 13   %threshold speed 13 m/s
                State = 3;
            else
                State = 1;
            end
        end
    end
  end
end
```

Appendix B

Dynamometer Testing Results

1. Throttle Test
2. Ramp Test
3. Modified ECE-15 Cycle Test

1. THROTTLE TEST

Throttle Position	Vehicle Speed		Power		Tractive Force	Fuel Before	Fuel After	Distance	
	m/s	kph	kW	W	N	ml	ml	km	rpm
0.25	2.78	10	0.60	600	230	71	60	0.2	1037.97
0.25	5.56	20	0.80	800	145	69	60	0.2	2195.24
0.25	8.33	30	0.90	900	110	59	51	0.2	3255.44
0.25	11.11	40	0.70	700	59	50	44	0.2	4720.70
0.25	13.89	50	0.90	900	67	44	39	0.2	5344.76
0.5	2.78	10	1.00	1000	400	72	50	0.2	994.72
0.5	5.56	20	1.50	1500	270	49	35	0.2	2210.49
0.5	8.33	30	1.40	1400	178	71	60.5	0.2	3129.45
0.5	11.11	40	1.70	1700	156	59	50	0.2	4335.95
0.5	13.89	50	1.80	1800	132	63	50	0.3	5425.74
0.5	16.67	60	1.40	1400	80	49.5	38	0.3	6963.03
0.5	19.44	70	1.40	1400	70	61	49	0.3	7957.75
0.5	20.56	74	1.50	1500	60	48	32	0.3	9947.18
0.75	2.78	10	1.00	1000	370	73	50	0.2	1075.37
0.75	5.56	20	1.70	1700	310	49	36	0.2	2181.96
0.75	8.33	30	1.65	1650	200	61	48	0.2	3282.57
0.75	11.11	40	2.50	2500	185	47	36	0.3	5376.86
0.75	13.89	50	2.25	2250	160	68	58	0.3	5595.29
0.75	16.67	60	2.10	2100	125	57	43	0.3	6684.51
0.75	19.44	70	1.85	1850	80	42	30	0.3	9201.15
1.00	2.78	10	1.10	1100	385	56	31	0.2	1136.82
1.00	5.56	20	1.75	1750	320	60	37	0.2	2175.95
1.00	8.33	30	2.10	2100	260	76	61	0.2	3213.71
1.00	11.11	40	2.60	2600	235	59	41	0.3	4402.16
1.00	13.89	50	2.50	2500	183	39	22.5	0.3	5435.62

1.00	16.67	60	2.50	2500	150	67	51	0.3	6631.46
1.00	19.44	70	2.10	2100	100	50	35	0.3	8355.63
1.00	22.22	80	1.50	1500	90	78	63	0.3	6631.46

Torque	Fuel Used	time	Volumetric Fuel Rate		Thermal Efficiency	Fuel Economy			BSFC	BSFC
Nm	ml	s	ml/s	m^3/s		ml/km	m^3/km	g/km	kg/kWh	g/kWh
55.20	11.00	259.20	0.042	0.0000000424	0.436	55.000	0.000	40.547	0.188	188.060
34.80	9.00	129.60	0.069	0.0000000694	0.355	45.000	0.000	33.175	0.231	230.801
26.40	8.00	86.40	0.093	0.0000000926	0.300	40.000	0.000	29.489	0.274	273.542
14.16	6.00	64.80	0.093	0.0000000926	0.233	30.000	0.000	22.117	0.352	351.697
16.08	5.00	51.84	0.096	0.0000000965	0.288	25.000	0.000	18.431	0.285	284.939
96.00	22.00	259.20	0.085	0.0000000849	0.363	110.000	0.000	81.094	0.226	225.672
64.80	14.00	129.60	0.108	0.0000001080	0.428	70.000	0.000	51.605	0.191	191.479
42.72	10.50	86.40	0.122	0.0000001215	0.355	52.500	0.000	38.704	0.231	230.801
37.44	9.00	64.80	0.139	0.0000001389	0.377	45.000	0.000	33.175	0.217	217.224
31.68	13.00	77.76	0.167	0.0000001672	0.332	43.333	0.000	31.946	0.247	246.947
19.20	11.50	64.80	0.177	0.0000001775	0.243	38.333	0.000	28.260	0.337	337.043
16.80	12.00	55.54	0.216	0.0000002160	0.200	40.000	0.000	29.489	0.410	410.313
14.40	16.00	52.54	0.305	0.0000003045	0.152	53.333	0.000	39.318	0.540	539.789
88.80	23.00	259.20	0.089	0.0000000887	0.347	115.000	0.000	84.780	0.236	235.930
74.40	13.00	129.60	0.100	0.0000001003	0.522	65.000	0.000	47.919	0.157	156.884
48.00	13.00	86.40	0.150	0.0000001505	0.338	65.000	0.000	47.919	0.242	242.457
44.40	11.00	97.20	0.113	0.0000001132	0.681	36.667	0.000	27.031	0.120	120.358
38.40	10.00	77.76	0.129	0.0000001286	0.539	33.333	0.000	24.574	0.152	151.968
30.00	14.00	64.80	0.216	0.0000002160	0.300	46.667	0.000	34.404	0.274	273.542
19.20	12.00	55.54	0.216	0.0000002160	0.264	40.000	0.000	29.489	0.311	310.507
92.40	25.00	259.20	0.096	0.0000000965	0.352	125.000	0.000	92.153	0.233	233.132
76.80	23.00	129.60	0.177	0.0000001775	0.304	115.000	0.000	84.780	0.270	269.634

62.40	15.00	86.40	0.174	0.0000001736	0.373	75.000	0.000	55.292	0.220	219.810
56.40	18.00	97.20	0.185	0.0000001852	0.433	60.000	0.000	44.233	0.189	189.375
43.92	16.50	77.76	0.212	0.0000002122	0.363	55.000	0.000	40.547	0.226	225.672
36.00	16.00	64.80	0.247	0.0000002469	0.312	53.333	0.000	39.318	0.263	262.600
24.00	15.00	55.54	0.270	0.0000002701	0.240	50.000	0.000	36.861	0.342	341.927
21.60	15.00	48.60	0.309	0.0000003086	0.150	50.000	0.000	36.861	0.547	547.084

CO2 %	CO %	HC ppm	O2 %	A/F Ratio	Lambda
9.921	4.858	3574.375	3.423	12.900	0.878
9.811	4.911	3471.692	3.572	13.015	0.885
9.816	4.996	3636.200	3.609	12.938	0.880
9.773	5.059	3747.400	3.655	12.878	0.876
9.677	5.102	3788.500	3.643	12.878	0.876
8.429	6.412	4028.302	4.393	12.579	0.856
7.507	9.082	3656.333	3.653	11.420	0.777
7.459	9.267	3959.111	3.672	11.253	0.766
7.575	8.956	3925.500	3.682	11.320	0.770
7.419	8.845	3898.500	3.967	11.509	0.783
6.828	10.586	3674.111	3.439	10.763	0.732
7.483	9.950	3547.000	3.263	11.000	0.748
8.163	9.208	3181.250	3.190	11.441	0.778
6.150	7.190	4503.043	4.689	11.897	0.809
5.652	9.294	3764.733	3.806	10.936	0.744
5.889	9.177	4013.571	3.753	10.900	0.741
6.834	7.409	3772.167	4.134	11.943	0.813
6.522	8.188	3674.917	4.098	11.686	0.795
6.436	8.755	3320.182	3.670	11.373	0.774
7.246	8.100	3046.714	3.301	11.614	0.790
5.530	8.055	4661.483	4.915	11.504	0.782
5.312	8.640	4593.949	4.925	11.320	0.770
5.343	9.589	4408.583	3.975	10.630	0.723
5.419	9.428	4133.550	3.962	10.790	0.734
5.730	7.780	4599.917	4.595	11.516	0.783
5.988	8.095	3960.250	4.341	11.600	0.789
6.161	8.602	3491.444	3.553	11.187	0.761
6.269	8.345	3688.700	3.691	11.316	0.770

2. RAMP TEST

Throttle Position	Vehicle Speed			Power		Tractive Force	Tractive Torque
%	m/s	kph	rpm	W	kW	N	Nm
0.25	5.00	18.00	1906.05	800.00	0.80	167.00	40.08
0.25	5.56	20.00	2157.22	900.00	0.90	166.00	39.84
0.25	6.11	22.00	2411.44	1000.00	1.00	165.00	39.60
0.25	6.67	24.00	2735.48	1100.00	1.10	160.00	38.40
0.25	7.22	26.00	2984.16	1200.00	1.20	160.00	38.40
0.25	7.78	28.00	3120.69	1200.00	1.20	153.00	36.72
0.25	8.33	30.00	3194.72	1100.00	1.10	137.00	32.88
0.25	8.89	32.00	3419.34	1100.00	1.10	128.00	30.72
0.25	9.44	34.00	3709.12	1100.00	1.10	118.00	28.32
0.25	10.00	36.00	3862.98	1000.00	1.00	103.00	24.72
0.25	10.56	38.00	4101.93	1000.00	1.00	97.00	23.28
0.25	11.11	40.00	4420.97	1000.00	1.00	90.00	21.60
0.25	11.67	42.00	4863.07	1100.00	1.10	90.00	21.60
0.25	12.22	44.00	4757.35	1100.00	1.10	92.00	22.08
0.25	12.78	46.00	5079.41	1200.00	1.20	94.00	22.56
0.25	13.33	48.00	5134.03	1200.00	1.20	93.00	22.32
0.25	13.89	50.00	5684.11	1300.00	1.30	91.00	21.84
0.25	14.44	52.00	5684.11	1200.00	1.20	84.00	20.16
0.25	15.00	54.00	6121.34	1200.00	1.20	78.00	18.72
0.25	15.56	56.00	6164.45	1100.00	1.10	71.00	17.04
0.25	16.11	58.00	6631.46	1000.00	1.00	60.00	14.40
0.50	6.67	24.00	2672.38	1800.00	1.80	268.00	64.32
0.50	7.22	26.00	2842.05	2000.00	2.00	280.00	67.20
0.50	7.78	28.00	3050.01	2200.00	2.20	287.00	68.88
0.50	8.33	30.00	3338.91	2400.00	2.40	286.00	68.64
0.50	8.89	32.00	3578.12	2500.00	2.50	278.00	66.72

0.50	9.44	34.00	3782.20	2500.00	2.50	263.00	63.12
0.50	10.00	36.00	3994.85	2500.00	2.50	249.00	59.76
0.50	10.56	38.00	4197.12	2500.00	2.50	237.00	56.88
0.50	11.11	40.00	4401.41	2500.00	2.50	226.00	54.24
0.50	11.67	42.00	4692.07	2500.00	2.50	212.00	50.88
0.50	12.22	44.00	4798.64	2400.00	2.40	199.00	47.76
0.50	12.78	46.00	5079.41	2400.00	2.40	188.00	45.12
0.50	13.33	48.00	5364.77	2400.00	2.40	178.00	42.72
0.50	13.89	50.00	5415.04	2300.00	2.30	169.00	40.56
0.50	14.44	52.00	5828.92	2300.00	2.30	157.00	37.68
0.50	15.00	54.00	5995.56	2200.00	2.20	146.00	35.04
0.50	15.56	56.00	6028.60	2000.00	2.00	132.00	31.68
0.50	16.11	58.00	6461.42	1900.00	1.90	117.00	28.08
0.50	16.67	60.00	6693.43	1800.00	1.80	107.00	25.68
0.50	17.22	62.00	7045.92	1700.00	1.70	96.00	23.04
0.50	17.78	64.00	6953.37	1800.00	1.80	103.00	24.72
0.50	18.33	66.00	7485.01	1900.00	1.90	101.00	24.24
0.50	18.89	68.00	7317.47	1600.00	1.60	87.00	20.88
0.50	19.44	70.00	7859.50	1600.00	1.60	81.00	19.44
0.50	20.00	72.00	7751.05	1500.00	1.50	77.00	18.48
0.75	7.22	26.00	2942.12	2100.00	2.10	284.00	68.16
0.75	7.78	28.00	3028.90	2200.00	2.20	289.00	69.36
0.75	8.33	30.00	3327.28	2400.00	2.40	287.00	68.88
0.75	8.89	32.00	3502.53	2500.00	2.50	284.00	68.16
0.75	9.44	34.00	3721.25	2600.00	2.60	278.00	66.72
0.75	10.00	36.00	3978.87	2700.00	2.70	270.00	64.80
0.75	10.56	38.00	4268.52	2800.00	2.80	261.00	62.64
0.75	11.11	40.00	4456.34	2800.00	2.80	250.00	60.00
0.75	11.67	42.00	4584.71	2800.00	2.80	243.00	58.32
0.75	12.22	44.00	4865.00	2800.00	2.80	229.00	54.96
0.75	12.78	46.00	5064.02	2800.00	2.80	220.00	52.80

0.75	13.33	48.00	5280.02	2800.00	2.80	211.00	50.64
0.75	13.89	50.00	5461.20	2800.00	2.80	204.00	48.96
0.75	14.44	52.00	5655.25	2800.00	2.80	197.00	47.28
0.75	15.00	54.00	5935.34	2700.00	2.70	181.00	43.44
0.75	15.56	56.00	6307.97	2600.00	2.60	164.00	39.36
0.75	16.11	58.00	6324.04	2400.00	2.40	151.00	36.24
0.75	16.67	60.00	6585.72	2400.00	2.40	145.00	34.80
0.75	17.22	62.00	6919.78	2400.00	2.40	138.00	33.12
0.75	17.78	64.00	7179.92	2400.00	2.40	133.00	31.92
0.75	18.33	66.00	7116.68	2200.00	2.20	123.00	29.52
0.75	18.89	68.00	7481.64	2200.00	2.20	117.00	28.08
0.75	19.44	70.00	7596.03	2100.00	2.10	110.00	26.40
0.75	20.00	72.00	7957.75	2000.00	2.00	100.00	24.00
0.75	20.56	74.00	8138.61	1800.00	1.80	88.00	21.12
0.75	21.11	76.00	8376.58	1600.00	1.60	76.00	18.24
1.00	7.22	26.00	2937.42	2200.00	2.20	298.00	71.52
1.00	7.78	28.00	3162.02	2400.00	2.40	302.00	72.48
1.00	8.33	30.00	3369.73	2600.00	2.60	307.00	73.68
1.00	8.89	32.00	3476.69	2700.00	2.70	309.00	74.16
1.00	9.44	34.00	3808.16	2900.00	2.90	303.00	72.72
1.00	10.00	36.00	3924.74	2900.00	2.90	294.00	70.56
1.00	10.56	38.00	4263.08	3000.00	3.00	280.00	67.20
1.00	11.11	40.00	4487.45	3000.00	3.00	266.00	63.84
1.00	11.67	42.00	4578.86	2900.00	2.90	252.00	60.48
1.00	12.22	44.00	4807.81	2900.00	2.90	240.00	57.60
1.00	12.78	46.00	5016.84	2900.00	2.90	230.00	55.20
1.00	13.33	48.00	5268.83	2900.00	2.90	219.00	52.56
1.00	13.89	50.00	5494.63	2900.00	2.90	210.00	50.40
1.00	14.44	52.00	5712.24	2900.00	2.90	202.00	48.48
1.00	15.00	54.00	6041.22	2900.00	2.90	191.00	45.84
1.00	15.56	56.00	6189.36	2800.00	2.80	180.00	43.20

1.00	16.11	58.00	6510.88	2700.00	2.70	165.00	39.60
1.00	16.67	60.00	6717.58	2600.00	2.60	154.00	36.96
1.00	17.22	62.00	6813.14	2500.00	2.50	146.00	35.04
1.00	17.78	64.00	7156.25	2500.00	2.50	139.00	33.36
1.00	18.33	66.00	7179.92	2400.00	2.40	133.00	31.92
1.00	18.89	68.00	7639.44	2400.00	2.40	125.00	30.00
1.00	19.44	70.00	7821.72	2300.00	2.30	117.00	28.08
1.00	20.00	72.00	7957.75	1900.00	1.90	95.00	22.80
1.00	20.56	74.00	8248.88	1700.00	1.70	82.00	19.68
1.00	21.11	76.00	8406.07	1500.00	1.50	71.00	17.04
1.00	21.67	78.00	8314.06	1400.00	1.40	67.00	16.08

CO2 %	CO %	HC ppm	O2 %	Air Fuel Ratio	Lambda
3.85	3.71	7090.00	11.73	17.05	1.16
5.34	3.66	7100.00	11.15	16.32	1.11
7.33	3.03	7020.00	9.91	15.73	1.07
8.93	2.70	6614.00	8.16	14.99	1.02
9.61	2.70	6238.00	6.49	14.11	0.96
9.76	2.76	5842.00	5.22	13.52	0.92
9.73	2.85	5516.00	4.44	13.23	0.90
9.75	3.22	5266.00	4.00	12.94	0.88
9.72	3.37	5056.00	3.76	12.79	0.87
9.68	3.41	4884.00	3.64	12.79	0.87
9.67	3.35	4726.00	3.57	12.94	0.88
9.67	3.34	4584.00	3.55	12.94	0.88
9.64	3.42	4441.00	3.52	12.94	0.88
9.41	4.02	4320.00	3.45	12.79	0.87
9.32	4.22	4202.00	3.39	12.64	0.86
9.21	4.35	4093.00	3.32	12.64	0.86
8.92	4.44	4041.00	3.29	12.64	0.86
8.76	4.55	3986.00	3.23	12.49	0.85
8.70	5.17	3802.00	3.17	12.35	0.84
8.36	5.19	3753.00	3.12	12.35	0.84
7.73	5.03	3734.00	3.19	12.35	0.84
2.90	2.86	5670.00	12.70	20.73	1.41
2.90	2.86	5749.00	12.74	20.73	1.41
2.90	2.86	5778.00	12.69	20.58	1.40
2.90	2.86	5778.00	12.69	20.58	1.40
2.91	2.87	5845.00	12.79	20.58	1.40
2.95	3.63	6131.00	12.58	18.96	1.29
2.95	3.63	6131.00	12.58	18.96	1.29
6.92	3.78	6244.00	10.76	16.46	1.12
8.01	3.85	5854.00	8.58	15.14	1.03
8.01	3.85	5854.00	8.58	15.14	1.03
8.21	4.73	5051.00	5.37	13.23	0.90
8.11	4.86	4792.00	4.72	12.94	0.88
8.11	4.86	4792.00	4.72	12.94	0.88
7.33	6.31	4470.00	4.26	12.20	0.83
6.93	7.01	4328.00	4.14	11.91	0.81
6.93	7.01	4328.00	4.14	11.91	0.81
6.35	8.18	4076.00	3.84	11.32	0.77
6.23	8.56	4008.00	3.68	11.17	0.76
6.23	8.56	4008.00	3.68	11.17	0.76
6.29	8.52	3690.00	3.45	11.17	0.76
6.53	8.46	3583.00	3.40	11.17	0.76

6.53	8.46	3583.00	3.40	11.17	0.76
6.76	8.34	3515.00	3.29	11.32	0.77
6.92	7.72	3405.00	3.26	11.47	0.78
6.92	7.72	3405.00	3.26	11.47	0.78
2.97	2.94	5360.00	12.81	21.17	1.44
2.97	2.93	5421.00	12.79	21.02	1.43
2.98	2.93	5577.00	12.81	20.87	1.42
2.98	2.93	5577.00	12.81	20.87	1.42
2.98	2.93	5632.00	12.81	20.73	1.41
3.01	2.94	5648.00	12.81	20.73	1.41
3.01	2.94	5648.00	12.81	20.73	1.41
5.62	4.17	5943.00	11.71	17.35	1.18
6.61	5.67	5766.00	10.01	15.29	1.04
6.61	5.67	5766.00	10.01	15.29	1.04
6.55	7.34	5062.00	6.04	12.49	0.85
6.55	7.31	4800.00	5.12	12.05	0.82
6.55	7.31	4800.00	5.12	12.05	0.82
6.51	7.46	4456.00	4.53	11.76	0.80
6.19	8.54	4319.00	4.38	11.32	0.77
6.19	8.54	4319.00	4.38	11.32	0.77
6.00	9.01	4069.00	3.97	11.02	0.75
6.34	8.90	4005.00	3.77	11.17	0.76
6.59	8.61	3901.00	3.63	11.17	0.76
6.83	8.42	3629.00	3.56	11.32	0.77
7.13	7.43	3521.00	3.57	11.76	0.80
7.23	7.23	3481.00	3.63	11.91	0.81
7.27	7.20	3452.00	3.68	11.91	0.81
7.53	7.35	3505.00	3.69	11.91	0.81
7.56	6.78	3424.00	3.69	12.20	0.83
7.11	6.38	3492.00	3.71	12.20	0.83
3.05	3.16	5812.00	12.62	19.99	1.36
3.06	3.21	5869.00	12.62	19.84	1.35
3.06	3.20	5890.00	12.67	19.84	1.35
3.06	3.20	5916.00	12.71	19.84	1.35
3.06	3.21	5939.00	12.72	19.84	1.35
3.06	3.22	5966.00	12.67	19.70	1.34
3.07	3.23	5946.00	12.70	19.84	1.35
3.13	4.06	6178.00	12.56	18.38	1.25
5.17	5.27	6187.00	11.80	16.46	1.12
6.02	6.77	6005.00	9.94	14.55	0.99
6.21	7.56	5373.00	7.63	13.08	0.89
6.21	7.76	4988.00	6.13	12.35	0.84
6.19	7.93	4735.00	5.35	11.91	0.81
5.91	8.16	4513.00	4.96	11.61	0.79
5.77	9.26	4324.00	4.69	11.32	0.77

5.68	9.64	4193.00	4.42	11.02	0.75
5.69	9.63	4049.00	4.18	11.02	0.75
5.75	9.57	3924.00	3.96	10.88	0.74
5.95	9.52	3838.00	3.80	10.88	0.74
5.96	9.47	3804.00	3.73	10.88	0.74
6.01	9.39	3771.00	3.70	10.88	0.74
6.07	9.27	3736.00	3.70	11.02	0.75
6.42	8.49	3557.00	3.71	11.32	0.77
6.63	8.16	3535.00	3.73	11.47	0.78
6.72	7.83	3579.00	3.70	11.61	0.79
6.66	7.31	3617.00	3.74	11.76	0.80
6.29	7.12	3642.00	4.04	11.91	0.81

3. MODIFIED ECE-15 CYCLE TEST : WOT

Test No.	Throttle Position	Vehicle Speed	Power	Tractive Force	Tractive Torque		CO2	CO	HC	O2	Air Fuel Ratio	Lambda
	%	kph	kW	N	Nm	rpm	%	%	ppm	%		
1	1	13	1.3	370	88.80	1397.98	5.37	8.95	4703	4.21	10.88	0.74
2	1	13	1.6	436	104.64	1460.14	5.37	8.98	4688	4.19	10.73	0.73
3	1	13	1.6	423	101.52	1505.01	5.36	8.98	4673	4.21	10.88	0.74
4	1	14	1.6	413	99.12	1541.45	5.36	8.99	4659	4.23	10.88	0.74
5	1	14	1.6	409	98.16	1556.53	5.36	9.00	4646	4.25	10.88	0.74
6	1	14	1.5	392	94.08	1522.53	5.36	9.01	4628	4.24	10.88	0.74
7	1	14	1.6	407	97.68	1564.18	5.36	9.03	4609	4.21	10.88	0.74
8	1	14	1.6	400	96.00	1591.55	5.35	9.06	4589	4.19	10.88	0.74
9	1	14	1.6	400	96.00	1591.55	5.35	9.08	4572	4.19	10.88	0.74
10	1	15	1.6	391	93.84	1628.18	5.35	9.09	4552	4.20	10.88	0.74
11	1	14	1.5	381	91.44	1566.49	5.35	9.11	4535	4.19	10.88	0.74
12	1	14	1.6	394	94.56	1615.79	5.34	9.12	4516	4.20	10.88	0.74
13	1	15	1.6	403	96.72	1579.70	5.34	9.13	4496	4.21	10.88	0.74
14	1	14	1.5	389	93.36	1534.27	5.34	9.13	4480	4.26	10.88	0.74
15	1	14	1.6	395	94.80	1611.70	5.33	9.14	4464	4.24	10.88	0.74
16	1	14	1.5	383	91.92	1558.31	5.33	9.14	4451	4.23	10.88	0.74
17	1	14	1.6	392	94.08	1624.03	5.33	9.15	4435	4.21	10.88	0.74
18	1	14	1.5	382	91.68	1562.38	5.33	9.17	4422	4.21	10.88	0.74
19	1	14	1.5	377	90.48	1583.11	5.33	9.19	4409	4.20	10.88	0.74
20	1	14	1.5	380	91.20	1570.61	5.33	9.24	4396	4.20	10.88	0.74
21	1	14	1.6	386	92.64	1649.27	5.32	9.24	4381	4.19	10.88	0.74
22	1	14	1.5	371	89.04	1608.71	5.32	9.23	4366	4.20	10.88	0.74
23	1	14	1.5	372	89.28	1604.38	5.32	9.23	4356	4.20	10.88	0.74
24	1	14	1.5	380	91.20	1570.61	5.32	9.24	4346	4.20	10.88	0.74
25	1	14	1.5	377	90.48	1583.11	5.32	9.24	4339	4.23	10.88	0.74
26	1	14	1.6	395	94.80	1611.70	5.32	9.24	4332	4.24	10.88	0.74
27	1	14	1.5	382	91.68	1562.38	5.32	9.25	4326	4.25	10.88	0.74
28	1	14	1.5	381	91.44	1566.49	5.32	9.25	4321	4.23	10.88	0.74
29	1	14	1.5	377	90.48	1583.11	5.32	9.26	4315	4.23	10.88	0.74

30	1	14	1.5	375	90.00	1591.55	5.32	9.26	4308	4.21	10.88	0.74
31	1	14	1.5	381	91.44	1566.49	5.32	9.27	4292	4.21	10.88	0.74
32	1	14	1.6	387	92.88	1645.01	5.32	9.27	4283	4.19	10.88	0.74
33	1	14	1.5	376	90.24	1587.32	5.32	9.27	4276	4.20	10.88	0.74
34	1	14	1.6	380	91.20	1675.32	5.32	9.28	4269	4.20	10.88	0.74
35	1	14	1.5	378	90.72	1578.92	5.32	9.28	4264	4.20	10.88	0.74
36	1	15	1.6	388	93.12	1640.77	5.32	9.28	4260	4.21	10.88	0.74
37	1	14	1.5	384	92.16	1554.25	5.32	9.28	4257	4.21	10.88	0.74
38	1	14	1.4	366	87.84	1521.97	5.32	9.29	4254	4.24	10.88	0.74
39	1	14	1.5	371	89.04	1608.71	5.32	9.29	4252	4.25	10.88	0.74
40	1	14	1.5	378	90.72	1578.92	5.33	9.30	4249	4.25	10.88	0.74
41	1	14	1.5	382	91.68	1562.38	5.33	9.29	4222	4.25	10.88	0.74
42	1	14	1.5	374	89.76	1595.80	5.33	9.29	4211	4.24	10.88	0.74
43	1	14	1.5	386	92.64	1546.19	5.33	9.30	4220	4.24	10.88	0.74
44	1	14	1.4	363	87.12	1534.55	5.30	9.52	4249	4.26	10.88	0.74
45	1	14	1.5	373	89.52	1600.08	5.28	9.65	4261	4.30	10.88	0.74
46	1	14	1.5	368	88.32	1621.82	5.26	9.76	4258	4.24	10.73	0.73
47	1	15	1.6	390	93.60	1632.36	5.24	9.84	4242	4.12	10.73	0.73
48	1	14	1.5	377	90.48	1583.11	5.23	9.88	4220	4.02	10.58	0.72
49	1	33	2	217	52.08	3667.16	5.23	9.91	4197	3.95	10.58	0.72
50	1	32	1.5	170	40.80	3510.77	5.25	9.90	4097	3.90	10.58	0.72
51	1	32	1.7	192	46.08	3522.96	5.27	9.90	4071	3.88	10.58	0.72
52	1	32	1.7	192	46.08	3522.96	5.29	9.90	4064	3.86	10.58	0.72
53	1	32	1.7	198	47.52	3416.20	5.32	9.89	4056	3.82	10.58	0.72
54	1	32	1.8	200	48.00	3580.99	5.34	9.88	4048	3.82	10.58	0.72
55	1	32	1.7	193	46.32	3504.71	5.36	9.88	4041	3.81	10.58	0.72
56	1	32	1.7	199	47.76	3399.04	5.41	9.89	3999	3.81	10.58	0.72
57	1	32	1.7	194	46.56	3486.64	5.41	9.90	3986	3.81	10.58	0.72
58	1	32	1.7	189	45.36	3578.88	5.42	9.90	3975	3.81	10.58	0.72
59	1	32	1.7	192	46.08	3522.96	5.42	9.91	3964	3.78	10.58	0.72
60	1	32	1.8	202	48.48	3545.53	5.43	9.91	3956	3.78	10.58	0.72
61	1	32	1.7	198	47.52	3416.20	5.43	9.91	3949	3.76	10.58	0.72
62	1	32	1.7	198	47.52	3416.20	5.43	9.92	3943	3.76	10.58	0.72
63	1	32	1.7	196	47.04	3451.06	5.46	9.95	3901	3.75	10.58	0.72

64	1	32	1.8	203	48.72	3528.07	5.46	9.95	3895	3.76	10.58	0.72
65	1	32	1.7	192	46.08	3522.96	5.47	9.96	3889	3.76	10.58	0.72
66	1	32	1.6	188	45.12	3386.28	5.47	9.96	3882	3.75	10.58	0.72
67	1	32	1.6	187	44.88	3404.38	5.47	9.96	3855	3.74	10.58	0.72
68	1	32	1.8	200	48.00	3580.99	5.48	9.96	3821	3.88	10.73	0.73
69	1	50	2	145	34.80	5488.10	5.48	9.96	3816	4.00	10.73	0.73
70	1	50	2.2	161	38.64	5436.97	5.49	9.95	3813	4.03	10.88	0.74
71	1	50	2.3	165	39.60	5546.31	5.49	9.81	3810	4.08	10.88	0.74
72	1	50	2.3	166	39.84	5512.90	5.50	9.68	3806	4.08	10.88	0.74
73	1	50	2.3	167	40.08	5479.89	6.23	8.80	3763	4.08	11.32	0.77
74	1	50	2.4	174	41.76	5488.10	6.26	8.70	3758	4.07	11.47	0.78
75	1	50	2.3	167	40.08	5479.89	6.39	8.60	3752	4.08	11.47	0.78
76	1	49	2.3	169	40.56	5415.04	6.52	8.49	3750	4.08	11.47	0.78
77	1	50	2.4	174	41.76	5488.10	6.61	8.44	3752	4.07	11.61	0.79
78	1	50	2.4	174	41.76	5488.10	6.67	8.37	3753	4.06	11.61	0.79
79	1	49	2.3	171	41.04	5351.70	6.70	8.33	3752	4.06	11.61	0.79
80	1	34	2.2	230	55.20	3805.88	6.75	8.30	3751	3.97	11.61	0.79
81	1	34	1.9	199	47.76	3798.92	6.77	8.34	3749	3.83	11.47	0.78
82	1	35	1.9	196	47.04	3857.07	6.76	8.47	3747	3.74	11.47	0.78
83	1	34	1.9	195	46.80	3876.85	6.74	8.64	3722	3.67	11.32	0.77
84	1	34	1.8	189	45.36	3789.40	6.69	9.34	3711	3.60	11.17	0.76
85	1	34	1.8	192	46.08	3730.19	6.40	9.44	3685	3.50	11.02	0.75
86	1	35	1.8	187	44.88	3829.93	6.37	9.46	3679	3.49	10.88	0.74
87	1	35	1.8	192	46.08	3730.19	6.34	9.50	3674	3.49	10.88	0.74
88	1	34	1.7	179	42.96	3778.82	6.31	9.55	3668	3.47	10.88	0.74
89	1	34	1.7	181	43.44	3737.06	6.30	9.57	3664	3.46	10.88	0.74
90	1	34	1.7	176	42.24	3843.23	6.26	9.79	3645	3.42	10.88	0.74
91	1	35	1.8	186	44.64	3850.52	6.26	9.82	3643	3.41	10.73	0.73
92	1	34	1.7	177	42.48	3821.52	6.26	9.85	3641	3.38	10.73	0.73
93	1	34	1.6	165	39.60	3858.30	6.25	9.90	3640	3.38	10.73	0.73
94	1	34	1.7	179	42.96	3778.82	6.25	9.94	3639	3.38	10.73	0.73
95	1	35	1.8	184	44.16	3892.38	6.24	9.98	3639	3.40	10.73	0.73

MODIFIED ECE-15 CYCLE TEST : 75% THROTTLE

Test No.	Throttle Position	Vehicle Speed	Power	Tractive Force	Tractive Torque		CO2	CO	HC	O2	Air Fuel Ratio	Lambda
	%	Kph	kW	N	Nm	rpm	%	%	ppm	%		
1	0.75	15	1.7	417	100.08	1622.08	6.08	7.73	4634.00	4.14	11.32	0.77
2	0.75	15	1.7	419	100.56	1614.34	6.07	7.77	4614.00	4.16	11.32	0.77
3	0.75	15	1.7	415	99.60	1629.90	6.06	7.81	4589.00	4.14	11.32	0.77
4	0.75	15	1.7	408	97.92	1657.86	6.04	7.84	4563.00	4.14	11.32	0.77
5	0.75	15	1.7	411	98.64	1645.76	6.03	7.87	4450.00	4.14	11.32	0.77
6	0.75	15	1.7	407	97.68	1661.94	6.02	7.92	4422.00	4.13	11.32	0.77
7	0.75	15	1.7	405	97.20	1670.14	6.01	7.96	4401.00	4.12	11.32	0.77
8	0.75	15	1.7	412	98.88	1641.77	6.00	8.00	4390.00	4.14	11.32	0.77
9	0.75	15	1.7	413	99.12	1637.79	5.99	8.01	4376.00	4.13	11.32	0.77
10	0.75	15	1.7	404	96.96	1674.28	5.98	8.03	4360.00	4.12	11.32	0.77
11	0.75	15	1.7	412	98.88	1641.77	5.97	8.06	4340.00	4.12	11.32	0.77
12	0.75	15	1.7	399	95.76	1695.26	5.95	8.11	4319.00	4.13	11.32	0.77
13	0.75	15	1.8	420	100.80	1705.23	5.94	8.15	4301.00	4.12	11.32	0.77
14	0.75	15	1.7	403	96.72	1678.43	5.92	8.19	4280.00	4.12	11.32	0.77
15	0.75	15	1.7	408	97.92	1657.86	5.91	8.22	4259.00	4.12	11.32	0.77
16	0.75	15	1.7	401	96.24	1686.80	5.90	8.24	4239.00	4.11	11.32	0.77
17	0.75	15	1.7	404	96.96	1674.28	5.89	8.25	4217.00	4.12	11.32	0.77
18	0.75	15	1.6	392	94.08	1624.03	5.88	8.27	4199.00	4.12	11.32	0.77
19	0.75	15	1.6	389	93.36	1636.55	5.87	8.28	4179.00	4.11	11.32	0.77
20	0.75	15	1.7	399	95.76	1695.26	5.87	8.30	4160.00	4.10	11.32	0.77
21	0.75	15	1.7	385	92.40	1756.91	5.86	8.34	4145.00	4.09	11.32	0.77
22	0.75	15	1.7	397	95.28	1703.80	5.85	8.37	4126.00	4.08	11.32	0.77
23	0.75	15	1.6	388	93.12	1640.77	5.84	8.39	4110.00	4.09	11.32	0.77
24	0.75	15	1.7	405	97.20	1670.14	5.84	8.41	4096.00	4.08	11.32	0.77
25	0.75	15	1.6	391	93.84	1628.18	5.83	8.43	4082.00	4.10	11.32	0.77
26	0.75	15	1.7	400	96.00	1691.02	5.83	8.45	4068.00	4.09	11.32	0.77
27	0.75	15	1.7	396	95.04	1708.10	5.82	8.45	4059.00	4.09	11.32	0.77
28	0.75	15	1.7	400	96.00	1691.02	5.82	8.45	4045.00	4.08	11.32	0.77
29	0.75	15	1.7	401	96.24	1686.80	5.82	8.45	4032.00	4.09	11.32	0.77

30	0.75	15	1.7	397	95.28	1703.80	5.82	8.45	4022.00	4.08	11.32	0.77
31	0.75	15	1.6	391	93.84	1628.18	5.82	8.46	4015.00	4.09	11.32	0.77
32	0.75	15	1.6	393	94.32	1619.90	5.82	8.48	4010.00	4.09	11.32	0.77
33	0.75	15	1.6	384	92.16	1657.86	5.82	8.50	4003.00	4.08	11.32	0.77
34	0.75	15	1.6	395	94.80	1611.70	5.82	8.51	3997.00	4.08	11.32	0.77
35	0.75	15	1.7	400	96.00	1691.02	5.82	8.52	3991.00	4.08	11.32	0.77
36	0.75	15	1.6	381	91.44	1670.92	5.82	8.54	3974.00	4.08	11.32	0.77
37	0.75	15	1.7	397	95.28	1703.80	5.81	8.56	3966.00	4.08	11.32	0.77
38	0.75	15	1.6	386	92.64	1649.27	5.81	8.59	3961.00	4.08	11.17	0.76
39	0.75	15	1.7	404	96.96	1674.28	5.81	8.66	3958.00	4.08	11.17	0.76
40	0.75	15	1.6	391	93.84	1628.18	5.81	8.68	3954.00	4.08	11.17	0.76
41	0.75	15	1.6	381	91.44	1670.92	5.80	8.69	3950.00	4.08	11.17	0.76
42	0.75	15	1.7	398	95.52	1699.52	5.80	8.68	3945.00	4.08	11.17	0.76
43	0.75	15	1.5	371	89.04	1608.71	5.80	8.70	3939.00	4.08	11.17	0.76
44	0.75	15	1.7	396	95.04	1708.10	5.80	8.74	3934.00	4.08	11.17	0.76
45	0.75	15	1.5	363	87.12	1644.16	5.79	8.91	3932.00	4.05	11.17	0.76
46	0.75	15	1.6	390	93.60	1632.36	5.75	9.59	3933.00	4.00	10.88	0.74
47	0.75	32	1.9	208	49.92	3634.55	5.66	9.36	3811.00	3.76	10.88	0.74
48	0.75	32	1.7	191	45.84	3541.41	5.67	9.36	3800.00	3.74	10.88	0.74
49	0.75	32	1.6	185	44.40	3441.19	5.69	9.35	3785.00	3.73	10.88	0.74
50	0.75	32	1.7	198	47.52	3416.20	5.71	9.32	3772.00	3.73	10.88	0.74
51	0.75	32	1.7	199	47.76	3399.04	5.73	9.27	3755.00	3.74	10.88	0.74
52	0.75	32	1.8	203	48.72	3528.07	5.76	9.23	3741.00	3.73	10.88	0.74
53	0.75	32	1.7	191	45.84	3541.41	5.78	9.21	3728.00	3.71	10.88	0.74
54	0.75	32	1.7	198	47.52	3416.20	5.80	9.18	3715.00	3.70	11.02	0.75
55	0.75	32	1.7	194	46.56	3486.64	5.83	9.16	3702.00	3.70	11.02	0.75
56	0.75	32	1.8	202	48.48	3545.53	5.84	9.17	3691.00	3.70	11.02	0.75
57	0.75	32	1.8	199	47.76	3598.98	5.85	9.19	3685.00	3.70	11.02	0.75
58	0.75	32	1.7	195	46.80	3468.76	5.86	9.20	3677.00	3.70	11.02	0.75
59	0.75	32	1.7	190	45.60	3560.04	5.87	9.19	3671.00	3.70	11.02	0.75
60	0.75	32	1.8	205	49.20	3493.65	5.88	9.18	3663.00	3.70	11.02	0.75
61	0.75	32	1.7	190	45.60	3560.04	5.89	9.18	3654.00	3.68	11.02	0.75
62	0.75	32	1.7	196	47.04	3451.06	5.90	9.18	3647.00	3.68	11.02	0.75
63	0.75	32	1.7	197	47.28	3433.55	5.92	9.18	3611.00	3.67	11.02	0.75
64	0.75	32	1.7	194	46.56	3486.64	5.93	9.18	3592.00	3.66	11.02	0.75

65	0.75	32	1.7	197	47.28	3433.55	5.93	9.18	3582.00	3.68	11.02	0.75
66	0.75	32	1.7	193	46.32	3504.71	5.93	9.17	3564.00	3.68	11.02	0.75
67	0.75	32	1.7	194	46.56	3486.64	5.94	9.16	3550.00	3.73	11.02	0.75
68	0.75	32	1.7	192	46.08	3522.96	5.95	8.99	3539.00	3.83	11.17	0.76
69	0.75	32	1.8	202	48.48	3545.53	5.95	8.96	3533.00	3.93	11.32	0.77
70	0.75	32	1.7	195	46.80	3468.76	5.96	8.90	3533.00	3.98	11.32	0.77
71	0.75	51	2.4	167	40.08	5718.14	5.98	8.80	3533.00	4.00	11.32	0.77
72	0.75	51	2.2	157	37.68	5575.49	6.01	8.67	3534.00	4.06	11.47	0.78
73	0.75	51	2.2	156	37.44	5611.23	6.55	8.52	3535.00	4.04	11.61	0.79
74	0.75	50	2.2	159	38.16	5505.36	6.62	7.93	3536.00	4.07	11.76	0.80
75	0.75	50	2.2	160	38.40	5470.95	6.64	7.76	3535.00	4.05	11.91	0.81
76	0.75	50	2.2	159	38.16	5505.36	6.68	7.75	3535.00	4.06	11.91	0.81
77	0.75	50	2.2	159	38.16	5505.36	6.73	7.68	3535.00	4.06	11.91	0.81
78	0.75	50	2.3	165	39.60	5546.31	6.99	7.59	3534.00	4.06	11.91	0.81
79	0.75	50	2.2	160	38.40	5470.95	7.10	7.54	3533.00	4.06	12.05	0.82
80	0.75	50	2.2	158	37.92	5540.20	7.08	7.50	3532.00	4.05	12.05	0.82
81	0.75	50	2.2	162	38.88	5403.41	7.10	7.46	3530.00	4.03	12.05	0.82
82	0.75	50	2.3	164	39.36	5580.13	7.15	7.41	3507.00	4.05	12.05	0.82
83	0.75	29	1.4	170	40.80	3276.72	6.90	8.53	3428.00	3.49	11.47	0.78
84	0.75	31	1.9	229	54.96	3301.25	6.89	8.58	3422.00	3.48	11.32	0.77
85	0.75	31	1.8	210	50.40	3410.46	6.86	8.63	3417.00	3.47	11.32	0.77
86	0.75	31	1.8	207	49.68	3459.89	6.82	8.70	3412.00	3.46	11.32	0.77
87	0.75	31	1.8	209	50.16	3426.78	6.78	8.78	3406.00	3.44	11.32	0.77
88	0.75	31	1.8	208	49.92	3443.26	6.74	8.83	3401.00	3.43	11.32	0.77
89	0.75	31	1.7	198	47.52	3416.20	6.69	8.90	3396.00	3.44	11.17	0.76
90	0.75	31	1.8	205	49.20	3493.65	6.65	8.97	3393.00	3.45	11.17	0.76
91	0.75	31	1.8	204	48.96	3510.77	6.61	9.04	3391.00	3.44	11.17	0.76
92	0.75	31	1.6	188	45.12	3386.28	6.59	9.06	3388.00	3.44	11.17	0.76
93	0.75	31	1.7	194	46.56	3486.64	6.59	9.07	3387.00	3.44	11.17	0.76
94	0.75	31	1.6	188	45.12	3386.28	6.59	9.08	3385.00	3.42	11.17	0.76
95	0.75	31	1.6	182	43.68	3497.91	6.58	9.11	3384.00	3.44	11.17	0.76
96	0.75	31	1.7	196	47.04	3451.06	6.57	9.15	3383.00	3.44	11.17	0.76
97	0.75	31	1.7	192	46.08	3522.96	6.56	9.20	3382.00	3.44	11.17	0.76
98	0.75	31	1.6	186	44.64	3422.69	6.55	9.23	3382.00	3.44	11.17	0.76
99	0.75	31	1.7	190	45.60	3560.04	6.54	9.26	3382.00	3.44	11.17	0.76

100	0.75	31	1.6	184	44.16	3459.89	6.52	9.30	3382.00	3.44	11.17	0.76
101	0.75	31	1.6	188	45.12	3386.28	6.51	9.36	3382.00	3.44	11.02	0.75
102	0.75	31	1.7	193	46.32	3504.71	6.50	9.41	3383.00	3.44	11.02	0.75
103	0.75	31	1.6	181	43.44	3517.24	6.47	9.31	3384.00	3.44	11.02	0.75

MODIFIED ECE-15 CYCLE TEST : 50% THROTTLE

Test No.	Throttle Position	Vehicle Speed	Power	Tractive Force	Tractive Torque		CO2	CO	HC	O2	Air Fuel Ratio	Lambda
	%	kph	kW	N	Nm	rpm	%	%	ppm	%		
1	0.5	13	1	291	69.84	136.73	6.29	5.18	7341.00	11.30	15.43	1.05
2	0.5	14	1.6	394	94.56	161.58	7.44	5.71	7139.00	9.24	14.11	0.96
3	0.5	14	1.5	376	90.24	158.73	7.83	6.18	6825.00	7.13	12.94	0.88
4	0.5	14	1.5	371	89.04	160.87	7.85	6.43	6486.00	5.79	12.20	0.83
5	0.5	14	1.5	376	90.24	158.73	7.91	6.48	6213.00	4.99	11.91	0.81
6	0.5	14	1.5	367	88.08	162.62	7.92	6.47	6004.00	4.53	11.76	0.80
7	0.5	14	1.5	365	87.60	163.52	7.93	6.51	5831.00	4.29	11.61	0.79
8	0.5	15	1.5	370	88.80	161.31	7.93	6.76	5701.00	4.16	11.61	0.79
9	0.5	15	1.5	362	86.88	164.87	7.91	7.01	5568.00	4.05	11.47	0.78
10	0.5	15	1.5	359	86.16	166.25	7.81	7.21	5449.00	3.98	11.47	0.78
11	0.5	15	1.5	364	87.36	163.96	7.70	7.43	5322.00	3.90	11.32	0.77
12	0.5	15	1.5	356	85.44	167.65	7.64	7.48	5214.00	3.87	11.32	0.77
13	0.5	15	1.5	354	84.96	168.60	7.62	7.47	5119.00	3.85	11.32	0.77
14	0.5	15	1.5	355	85.20	168.12	7.61	7.46	5023.00	3.82	11.47	0.78
15	0.5	15	1.4	353	84.72	157.80	7.60	7.45	4937.00	3.82	11.47	0.78
16	0.5	15	1.5	362	86.88	164.87	7.59	7.45	4864.00	3.83	11.47	0.78
17	0.5	15	1.4	352	84.48	158.25	7.59	7.46	4800.00	3.82	11.47	0.78
18	0.5	15	1.5	359	86.16	166.25	7.58	7.47	4742.00	3.83	11.47	0.78
19	0.5	15	1.4	350	84.00	159.15	7.58	7.48	4679.00	3.84	11.47	0.78
20	0.5	15	1.5	354	84.96	168.60	7.58	7.48	4639.00	3.84	11.61	0.79

21	0.5	15	1.4	351	84.24	158.70	7.58	7.47	4587.00	3.88	11.61	0.79
22	0.5	15	1.4	353	84.72	157.80	7.58	7.47	4544.00	3.87	11.61	0.79
23	0.5	15	1.4	352	84.48	158.25	7.58	7.47	4500.00	3.89	11.61	0.79
24	0.5	15	1.5	356	85.44	167.65	7.58	7.46	4453.00	3.89	11.61	0.79
25	0.5	15	1.4	350	84.00	159.15	7.58	7.46	4437.00	3.89	11.61	0.79
26	0.5	15	1.5	353	84.72	169.07	7.58	7.46	4417.00	3.90	11.61	0.79
27	0.5	15	1.5	354	84.96	168.60	7.58	7.46	4348.00	3.90	11.76	0.80
28	0.5	15	1.4	350	84.00	159.15	7.58	7.46	4307.00	3.90	11.76	0.80
29	0.5	15	1.4	344	82.56	161.93	7.58	7.45	4290.00	3.92	11.76	0.80
30	0.5	15	1.4	352	84.48	158.25	7.58	7.40	4274.00	3.91	11.76	0.80
31	0.5	15	1.4	350	84.00	159.15	7.59	7.43	4216.00	3.93	11.76	0.80
32	0.5	15	1.5	353	84.72	169.07	7.59	7.45	4180.00	3.92	11.76	0.80
33	0.5	15	1.4	349	83.76	159.61	7.58	7.46	4166.00	3.93	11.76	0.80
34	0.5	15	1.5	354	84.96	168.60	7.58	7.46	4158.00	3.92	11.76	0.80
35	0.5	15	1.5	353	84.72	169.07	7.58	7.46	4144.00	3.93	11.76	0.80
36	0.5	15	1.4	344	82.56	161.93	7.58	7.47	4086.00	3.93	11.76	0.80
37	0.5	15	1.4	343	82.32	162.40	7.58	7.47	4055.00	3.92	11.91	0.81
38	0.5	15	1.4	349	83.76	159.61	7.58	7.47	4047.00	3.95	11.91	0.81
39	0.5	15	1.4	345	82.80	161.46	7.58	7.47	4039.00	3.94	11.91	0.81
40	0.5	15	1.4	350	84.00	159.15	7.58	7.47	4030.00	3.93	11.91	0.81
41	0.5	15	1.4	349	83.76	159.61	7.58	7.48	4021.00	3.93	11.91	0.81
42	0.5	15	1.4	348	83.52	160.07	7.59	7.48	3959.00	3.93	11.91	0.81
43	0.5	15	1.4	347	83.28	160.53	7.59	7.48	3945.00	3.94	11.91	0.81
44	0.5	15	1.4	347	83.28	160.53	7.59	7.48	3936.00	3.94	11.91	0.81
45	0.5	15	1.4	343	82.32	162.40	7.59	7.48	3929.00	3.94	11.91	0.81
46	0.5	15	1.4	343	82.32	162.40	7.59	7.48	3921.00	3.95	11.91	0.81
47	0.5	15	1.4	349	83.76	159.61	7.59	7.49	3916.00	3.93	11.91	0.81
48	0.5	15	1.4	347	83.28	160.53	7.58	7.49	3873.00	3.93	11.91	0.81
49	0.5	15	1.4	344	82.56	161.93	7.58	7.56	3857.00	3.95	11.91	0.81
50	0.5	15	1.4	344	82.56	161.93	7.58	7.56	3850.00	3.93	11.91	0.81
51	0.5	15	1.4	346	83.04	160.99	7.58	7.58	3847.00	3.94	11.91	0.81

52	0.5	15	1.4	344	82.56	161.93	7.57	7.60	3845.00	3.94	11.91	0.81
53	0.5	15	1.4	342	82.08	162.88	7.57	7.60	3841.00	3.94	11.91	0.81
54	0.5	15	1.4	341	81.84	163.36	7.57	7.60	3836.00	3.95	11.91	0.81
55	0.5	15	1.4	348	83.52	160.07	7.57	7.59	3832.00	3.95	11.91	0.81
56	0.5	15	1.4	343	82.32	162.40	7.57	7.58	3827.00	3.95	11.91	0.81
57	0.5	15	1.4	342	82.08	162.88	7.57	7.56	3821.00	3.94	11.91	0.81
58	0.5	15	1.4	343	82.32	162.40	7.58	7.55	3799.00	3.95	11.91	0.81
59	0.5	15	1.4	336	80.64	165.79	7.58	7.54	3760.00	3.95	11.91	0.81
60	0.5	15	1.4	344	82.56	161.93	7.59	7.53	3752.00	3.94	11.91	0.81
61	0.5	15	1.4	343	82.32	162.40	7.59	7.53	3749.00	3.95	11.91	0.81
62	0.5	15	1.4	339	81.36	164.32	7.59	7.53	3741.00	3.95	11.91	0.81
63	0.5	15	1.4	340	81.60	163.84	7.59	7.53	3737.00	3.95	11.91	0.81
64	0.5	15	1.4	343	82.32	162.40	7.60	7.54	3731.00	3.94	11.91	0.81
65	0.5	15	1.4	341	81.84	163.36	7.59	7.90	3726.00	3.93	11.91	0.81
66	0.5	15	1.4	344	82.56	161.93	7.59	8.16	3721.00	3.90	11.76	0.80
67	0.5	15	1.4	345	82.80	161.46	7.56	8.40	3716.00	3.87	11.61	0.79
68	0.5	15	1.4	338	81.12	164.81	7.54	8.38	3710.00	3.82	11.61	0.79
69	0.5	15	1.4	343	82.32	162.40	7.52	8.33	3658.00	3.80	11.61	0.79
70	0.5	15	1.4	341	81.84	163.36	7.50	8.31	3648.00	3.79	11.61	0.79
71	0.5	15	1.4	339	81.36	164.32	7.48	8.33	3644.00	3.76	11.61	0.79
72	0.5	15	1.4	341	81.84	163.36	7.46	8.36	3638.00	3.74	11.61	0.79
73	0.5	15	1.4	339	81.36	164.32	7.44	8.38	3632.00	3.69	11.61	0.79
74	0.5	32	1.6	179	42.96	355.65	7.43	8.40	3625.00	3.67	11.61	0.79
75	0.5	32	1.6	184	44.16	345.99	7.42	8.41	3578.00	3.65	11.61	0.79
76	0.5	32	1.6	181	43.44	351.72	7.41	8.40	3567.00	3.64	11.61	0.79
77	0.5	32	1.6	178	42.72	357.65	7.41	8.40	3559.00	3.63	11.61	0.79
78	0.5	32	1.6	184	44.16	345.99	7.41	8.39	3550.00	3.61	11.61	0.79
79	0.5	32	1.6	183	43.92	347.88	7.41	8.37	3543.00	3.61	11.61	0.79
80	0.5	32	1.6	179	42.96	355.65	7.43	8.16	3537.00	3.59	11.61	0.79
81	0.5	32	1.6	180	43.20	353.68	7.46	8.18	3498.00	3.57	11.61	0.79
82	0.5	32	1.6	180	43.20	353.68	7.47	8.21	3483.00	3.57	11.61	0.79

83	0.5	32	1.6	182	43.68	349.79	7.49	8.23	3477.00	3.57	11.61	0.79
84	0.5	32	1.6	178	42.72	357.65	7.50	8.24	3474.00	3.56	11.61	0.79
85	0.5	32	1.6	180	43.20	353.68	7.52	8.23	3469.00	3.57	11.61	0.79
86	0.5	32	1.6	182	43.68	349.79	7.54	8.24	3464.00	3.56	11.61	0.79
87	0.5	32	1.5	176	42.24	339.11	7.55	8.25	3459.00	3.54	11.61	0.79
88	0.5	32	1.6	181	43.44	351.72	7.57	8.25	3455.00	3.52	11.61	0.79
89	0.5	32	1.5	174	41.76	343.01	7.59	8.24	3450.00	3.54	11.61	0.79
90	0.5	32	1.6	177	42.48	359.67	7.61	7.98	3445.00	3.53	11.76	0.80
91	0.5	32	1.5	176	42.24	339.11	7.63	8.00	3423.00	3.52	11.76	0.80
92	0.5	32	1.7	186	44.64	363.66	7.66	8.02	3388.00	3.52	11.76	0.80
93	0.5	32	1.5	173	41.52	344.99	7.69	8.04	3377.00	3.51	11.76	0.80
94	0.5	32	1.6	180	43.20	353.68	7.72	8.05	3370.00	3.51	11.76	0.80
95	0.5	32	1.5	174	41.76	343.01	7.76	8.01	3351.00	3.51	11.76	0.80
96	0.5	32	1.6	182	43.68	349.79	7.78	7.83	3342.00	3.55	11.91	0.81
97	0.5	50	2.1	151	36.24	553.35	7.43	8.39	3299.00	3.81	11.76	0.80
98	0.5	51	1.8	129	30.96	555.19	7.50	8.14	3298.00	3.82	11.91	0.81
99	0.5	51	1.9	132	31.68	572.72	7.59	7.94	3296.00	3.82	11.91	0.81
100	0.5	51	1.9	136	32.64	555.87	7.96	7.64	3295.00	3.83	12.05	0.82
101	0.5	50	1.9	135	32.40	559.99	8.00	7.51	3293.00	3.82	12.20	0.83
102	0.5	50	1.9	135	32.40	559.99	8.08	7.37	3291.00	3.86	12.20	0.83
103	0.5	50	1.9	137	32.88	551.81	8.30	7.02	3288.00	3.86	12.35	0.84
104	0.5	50	1.9	139	33.36	543.87	8.40	6.88	3286.00	3.87	12.49	0.85
105	0.5	50	1.9	140	33.60	539.99	8.63	6.64	3258.00	3.86	12.49	0.85
106	0.5	49	1.9	140	33.60	539.99	8.72	6.59	3265.00	3.83	12.49	0.85
107	0.5	49	1.9	140	33.60	539.99	8.75	6.32	3263.00	3.83	12.64	0.86
108	0.5	49	1.9	139	33.36	543.87	9.06	6.08	3263.00	3.82	12.79	0.87
109	0.5	34	1.8	196	47.04	365.41	8.51	7.51	3166.00	3.45	12.05	0.82
110	0.5	34	1.6	167	40.08	381.21	8.47	7.55	3162.00	3.43	12.05	0.82
111	0.5	34	1.5	164	39.36	363.92	8.46	7.56	3158.00	3.43	12.05	0.82
112	0.5	34	1.5	163	39.12	366.15	8.44	7.60	3153.00	3.42	12.05	0.82
113	0.5	34	1.6	165	39.60	385.83	8.42	7.75	3149.00	3.42	12.05	0.82

114	0.5	35	1.5	160	38.40	373.02	8.41	7.75	3144.00	3.41	12.05	0.82
115	0.5	34	1.5	156	37.44	382.58	8.41	7.74	3140.00	3.40	12.05	0.82
116	0.5	34	1.5	158	37.92	377.74	8.40	7.72	3134.00	3.41	12.05	0.82
117	0.5	35	1.5	157	37.68	380.15	8.40	7.72	3115.00	3.41	12.05	0.82
118	0.5	34	1.5	156	37.44	382.58	8.40	7.74	3107.00	3.39	12.05	0.82
119	0.5	34	1.5	159	38.16	375.37	8.39	7.85	3101.00	3.38	11.91	0.81
120	0.5	35	1.5	158	37.92	377.74	8.39	7.86	3096.00	3.38	11.91	0.81
121	0.5	34	1.5	161	38.64	370.70	8.38	7.85	3091.00	3.38	11.91	0.81
122	0.5	34	1.5	154	36.96	387.55	8.37	7.84	3087.00	3.38	11.91	0.81
123	0.5	34	1.5	159	38.16	375.37	8.36	7.86	3083.00	3.39	11.91	0.81
124	0.5	35	1.5	155	37.20	385.05	8.36	7.91	3083.00	3.39	11.91	0.81
125	0.5	35	1.5	153	36.72	390.09	8.35	7.92	3083.00	3.37	11.91	0.81

MODIFIED ECE-15 CYCLE TEST : 25% THROTTLE

Test No.	Throttle Position	Vehicle Speed	Power	Tractive Force	Tractive Torque		CO2	CO	HC	O2	Air Fuel Ratio	Lambda
	%	kph	kW	N	Nm	rpm	%	%	ppm	%		
1	0.25	14	0.6	154	36.96	155.02	9.79	3.72	3922.00	4.09	13.52	0.92
2	0.25	14	0.6	158	37.92	151.10	9.79	3.72	3922.00	4.09	13.52	0.92
3	0.25	15	0.7	173	41.52	160.99	9.81	3.71	3821.00	4.08	13.52	0.92
4	0.25	15	0.7	180	43.20	154.73	9.82	3.72	3664.00	4.12	13.67	0.93
5	0.25	14	0.7	170	40.80	163.84	9.82	3.72	3664.00	4.12	13.67	0.93
6	0.25	15	0.7	177	42.48	157.36	9.82	3.74	3603.00	4.13	13.67	0.93
7	0.25	15	0.7	179	42.96	155.60	9.81	3.82	3493.00	4.13	13.67	0.93
8	0.25	15	0.7	176	42.24	158.25	9.81	3.82	3493.00	4.13	13.67	0.93
9	0.25	15	0.7	170	40.80	163.84	9.81	3.78	3443.00	4.13	13.82	0.94
10	0.25	15	0.7	168	40.32	165.79	9.82	3.49	3352.00	4.14	13.96	0.95
11	0.25	15	0.8	182	43.68	174.90	9.82	3.49	3352.00	4.14	13.96	0.95
12	0.25	15	0.7	173	41.52	160.99	9.82	3.49	3306.00	4.15	13.96	0.95

13	0.25	15	0.7	171	41.04	162.88	9.84	3.50	3233.00	4.16	13.96	0.95
14	0.25	15	0.7	169	40.56	164.81	9.84	3.50	3233.00	4.16	13.96	0.95
15	0.25	15	0.7	178	42.72	156.47	9.86	3.48	3199.00	4.14	13.96	0.95
16	0.25	15	0.7	173	41.52	160.99	9.89	3.31	3145.00	4.18	14.11	0.96
17	0.25	15	0.7	166	39.84	167.78	9.89	3.31	3145.00	4.18	14.11	0.96
18	0.25	15	0.7	175	42.00	159.15	9.91	3.32	3131.00	4.19	14.11	0.96
19	0.25	15	0.7	169	40.56	164.81	9.95	3.32	3050.00	4.16	14.11	0.96
20	0.25	15	0.7	168	40.32	165.79	9.95	3.32	3050.00	4.16	14.11	0.96
21	0.25	15	0.7	166	39.84	167.78	9.98	3.22	3036.00	4.15	14.26	0.97
22	0.25	15	0.7	175	42.00	159.15	10.03	3.20	3015.00	4.20	14.26	0.97
23	0.25	15	0.7	172	41.28	161.93	10.03	3.20	3015.00	4.20	14.26	0.97
24	0.25	15	0.7	167	40.08	166.78	10.06	3.18	2979.00	4.20	14.26	0.97
25	0.25	15	0.7	169	40.56	164.81	10.12	3.14	2951.00	4.22	14.41	0.98
26	0.25	15	0.7	179	42.96	155.60	10.12	3.14	2951.00	4.22	14.41	0.98
27	0.25	15	0.7	178	42.72	156.47	10.13	3.17	2942.00	4.20	14.41	0.98
28	0.25	14	0.6	162	38.88	147.37	10.15	3.17	2929.00	4.18	14.41	0.98
29	0.25	15	0.7	165	39.60	168.80	10.15	3.17	2929.00	4.18	14.41	0.98
30	0.25	15	0.7	178	42.72	156.47	10.16	3.16	2923.00	4.20	14.41	0.98
31	0.25	15	0.7	176	42.24	158.25	10.16	3.16	2878.00	4.25	14.41	0.98
32	0.25	15	0.7	167	40.08	166.78	10.16	3.16	2878.00	4.25	14.41	0.98
33	0.25	15	0.7	167	40.08	166.78	10.16	3.15	2879.00	4.27	14.41	0.98
34	0.25	15	0.7	172	41.28	161.93	10.17	3.03	2871.00	4.26	14.55	0.99
35	0.25	15	0.7	177	42.48	157.36	10.17	3.03	2871.00	4.26	14.55	0.99
36	0.25	14	0.6	158	37.92	151.10	10.17	3.03	2869.00	4.26	14.55	0.99
37	0.25	15	0.7	169	40.56	164.81	10.18	3.03	2863.00	4.27	14.55	0.99
38	0.25	15	0.7	175	42.00	159.15	10.18	3.03	2863.00	4.27	14.55	0.99
39	0.25	15	0.7	172	41.28	161.93	10.18	3.04	2859.00	4.27	14.55	0.99
40	0.25	15	0.7	169	40.56	164.81	10.19	3.02	2854.00	4.26	14.55	0.99
41	0.25	15	0.7	174	41.76	160.07	10.19	3.02	2854.00	4.26	14.55	0.99
42	0.25	15	0.7	169	40.56	164.81	10.19	3.02	2852.00	4.26	14.55	0.99
43	0.25	15	0.7	174	41.76	160.07	10.20	3.01	2848.00	4.27	14.55	0.99
44	0.25	15	0.7	175	42.00	159.15	10.20	3.01	2848.00	4.27	14.55	0.99
45	0.25	14	0.7	166	39.84	167.78	10.20	3.01	2845.00	4.25	14.55	0.99
46	0.25	14	0.6	155	37.20	154.02	10.21	3.01	2825.00	4.25	14.55	0.99
47	0.25	15	0.7	169	40.56	164.81	10.21	3.01	2825.00	4.25	14.55	0.99
48	0.25	15	0.7	176	42.24	158.25	10.21	3.01	2823.00	4.27	14.55	0.99

49	0.25	14	0.6	158	37.92	151.10	10.22	3.01	2821.00	4.28	14.55	0.99
50	0.25	15	0.7	170	40.80	163.84	10.22	3.01	2821.00	4.28	14.55	0.99
51	0.25	15	0.7	168	40.32	165.79	10.22	3.01	2820.00	4.28	14.55	0.99
52	0.25	15	0.7	167	40.08	166.78	10.22	3.14	2818.00	4.26	14.41	0.98
53	0.25	15	0.7	166	39.84	167.78	10.22	3.14	2818.00	4.26	14.41	0.98
54	0.25	15	0.7	176	42.24	158.25	10.21	3.14	2817.00	4.27	14.41	0.98
55	0.25	15	0.7	164	39.36	169.83	10.21	3.15	2813.00	4.25	14.41	0.98
56	0.25	15	0.7	169	40.56	164.81	10.21	3.15	2813.00	4.25	14.41	0.98
57	0.25	15	0.7	180	43.20	154.73	10.21	3.49	2811.00	4.19	14.26	0.97
58	0.25	32	0.9	101	24.24	354.55	10.22	3.84	2690.00	3.74	13.96	0.95
59	0.25	33	0.9	94	22.56	380.96	10.22	3.84	2690.00	3.74	13.96	0.95
60	0.25	33	0.7	76	18.24	366.48	10.22	3.91	2652.00	3.57	13.82	0.94
61	0.25	33	0.7	73	17.52	381.54	10.23	4.10	2577.00	3.43	13.67	0.93
62	0.25	33	0.7	72	17.28	386.83	10.23	4.10	2577.00	3.43	13.67	0.93
63	0.25	33	0.7	72	17.28	386.83	10.23	4.09	2550.00	3.38	13.67	0.93
64	0.25	33	0.8	84	20.16	378.94	10.25	3.74	2528.00	3.34	13.82	0.94
65	0.25	33	0.8	87	20.88	365.87	10.25	3.74	2528.00	3.34	13.82	0.94
66	0.25	33	0.7	79	18.96	352.56	10.26	3.85	2479.00	3.33	13.82	0.94
67	0.25	33	0.7	79	18.96	352.56	10.27	4.21	2452.00	3.30	13.67	0.93
68	0.25	33	0.7	81	19.44	343.85	10.27	4.21	2452.00	3.30	13.67	0.93
69	0.25	32	0.7	78	18.72	357.08	10.27	4.24	2443.00	3.29	13.67	0.93
70	0.25	32	0.7	80	19.20	348.15	10.28	4.19	2393.00	3.25	13.67	0.93
71	0.25	32	0.7	78	18.72	357.08	10.28	4.19	2393.00	3.25	13.67	0.93
72	0.25	32	0.7	79	18.96	352.56	10.28	4.18	2383.00	3.25	13.67	0.93
73	0.25	32	0.7	84	20.16	331.57	10.28	4.16	2375.00	3.26	13.67	0.93
74	0.25	32	0.7	81	19.44	343.85	10.28	4.16	2375.00	3.26	13.67	0.93
75	0.25	32	0.7	77	18.48	361.72	10.28	4.16	2371.00	3.26	13.67	0.93
76	0.25	32	0.7	83	19.92	335.57	10.28	4.22	2345.00	3.25	13.67	0.93
77	0.25	32	0.7	84	20.16	331.57	10.28	4.22	2345.00	3.25	13.67	0.93
78	0.25	32	0.7	82	19.68	339.66	10.28	4.30	2326.00	3.22	13.67	0.93
79	0.25	32	0.7	81	19.44	343.85	10.27	4.24	2316.00	3.22	13.67	0.93
80	0.25	32	0.7	81	19.44	343.85	10.27	4.24	2316.00	3.22	13.67	0.93
81	0.25	32	0.7	80	19.20	348.15	10.27	4.38	2312.00	3.23	13.52	0.92
82	0.25	32	0.7	77	18.48	361.72	10.26	4.44	2305.00	3.22	13.52	0.92
83	0.25	32	0.7	79	18.96	352.56	10.26	4.44	2305.00	3.22	13.52	0.92
84	0.25	32	0.7	83	19.92	335.57	10.26	4.30	2302.00	3.22	13.67	0.93

85	0.25	32	0.7	81	19.44	343.85	10.25	4.31	2295.00	3.22	13.67	0.93
86	0.25	32	0.7	81	19.44	343.85	10.25	4.31	2295.00	3.22	13.67	0.93
87	0.25	32	0.7	82	19.68	339.66	10.25	4.31	2291.00	3.23	13.67	0.93
88	0.25	32	0.7	81	19.44	343.85	10.25	4.31	2268.00	3.22	13.67	0.93
89	0.25	32	0.7	79	18.96	352.56	10.25	4.31	2268.00	3.22	13.67	0.93
90	0.25	32	0.7	78	18.72	357.08	10.25	4.30	2261.00	3.22	13.67	0.93
91	0.25	32	0.7	75	18.00	371.36	10.25	4.30	2249.00	3.21	13.67	0.93
92	0.25	45	0.7	60	14.40	464.20	10.25	4.30	2249.00	3.21	13.67	0.93
93	0.25	45	0.8	63	15.12	505.25	10.25	4.35	2245.00	3.19	13.67	0.93
94	0.25	46	0.8	62	14.88	513.40	10.25	4.27	2236.00	3.19	13.67	0.93
95	0.25	46	0.8	61	14.64	521.82	10.25	4.27	2236.00	3.19	13.67	0.93
96	0.25	47	0.8	64	15.36	497.36	10.25	4.29	2232.00	3.20	13.67	0.93
97	0.25	48	0.9	67	16.08	534.48	10.23	4.63	2228.00	3.25	13.52	0.92
98	0.25	48	0.9	68	16.32	526.62	10.23	4.63	2228.00	3.25	13.52	0.92
99	0.25	49	0.9	67	16.08	534.48	10.19	4.74	2226.00	3.27	13.52	0.92
100	0.25	49	0.9	66	15.84	542.57	9.86	4.73	2225.00	3.32	13.52	0.92
101	0.25	50	0.9	65	15.60	550.92	9.86	4.73	2225.00	3.32	13.52	0.92
102	0.25	50	0.9	64	15.36	559.53	9.90	4.49	2225.00	3.35	13.67	0.93
103	0.25	51	0.9	67	16.08	534.48	10.29	4.10	2225.00	3.39	13.82	0.94
104	0.25	51	0.9	66	15.84	542.57	10.29	4.10	2225.00	3.39	13.82	0.94
105	0.25	51	0.9	66	15.84	542.57	10.34	3.87	2226.00	3.42	13.96	0.95
106	0.25	52	0.9	64	15.36	559.53	10.32	4.22	2227.00	3.43	13.82	0.94
107	0.25	30	0.6	75	18.00	318.31	10.32	4.22	2227.00	3.43	13.82	0.94
108	0.25	31	0.7	84	20.16	331.57	9.82	4.79	2228.00	3.40	13.52	0.92
109	0.25	32	0.8	87	20.88	365.87	9.70	5.19	2227.00	3.31	13.38	0.91
110	0.25	33	0.8	86	20.64	370.13	9.70	5.19	2227.00	3.31	13.38	0.91
111	0.25	34	0.8	85	20.40	374.48	9.73	5.17	2226.00	3.29	13.38	0.91
112	0.25	35	0.8	85	20.40	374.48	9.75	5.14	2225.00	3.23	13.38	0.91
113	0.25	36	0.8	80	19.20	397.89	9.75	5.14	2225.00	3.23	13.38	0.91
114	0.25	37	0.8	81	19.44	392.98	9.78	4.89	2224.00	3.20	13.38	0.91
115	0.25	37	0.8	76	18.24	418.83	10.06	4.07	2221.00	3.23	13.67	0.93
116	0.25	37	0.7	69	16.56	403.65	10.06	4.07	2221.00	3.23	13.67	0.93
117	0.25	37	0.7	71	17.04	392.28	10.50	3.85	2202.00	3.25	13.82	0.94
118	0.25	36	0.6	61	14.64	391.36	10.58	3.82	2200.00	3.25	13.82	0.94
119	0.25	36	0.6	60	14.40	397.89	10.58	3.82	2200.00	3.25	13.82	0.94
120	0.25	36	0.6	62	14.88	385.05	10.59	3.82	2197.00	3.24	13.82	0.94

121	0.25	36	0.6	64	15.36	373.02	10.63	3.83	2188.00	3.17	13.82	0.94
122	0.25	36	0.6	64	15.36	373.02	10.63	3.83	2188.00	3.17	13.82	0.94
123	0.25	36	0.6	61	14.64	391.36	10.65	3.93	2152.00	3.15	13.82	0.94
124	0.25	36	0.7	66	15.84	422.00	10.64	4.05	2142.00	3.13	13.82	0.94
125	0.25	35	0.6	65	15.60	367.28	10.64	4.05	2142.00	3.13	13.82	0.94
126	0.25	35	0.6	62	14.88	385.05	10.63	4.17	2142.00	3.16	13.67	0.93
127	0.25	35	0.6	65	15.60	367.28	10.53	4.42	2140.00	3.19	13.67	0.93
128	0.25	35	0.6	64	15.36	373.02	10.53	4.42	2140.00	3.19	13.67	0.93
129	0.25	35	0.6	64	15.36	373.02	10.47	4.48	2140.00	3.19	13.67	0.93
130	0.25	35	0.6	66	15.84	361.72	10.36	4.45	2140.00	3.25	13.67	0.93
131	0.25	35	0.6	64	15.36	373.02	10.36	4.45	2140.00	3.25	13.67	0.93
132	0.25	35	0.6	65	15.60	367.28	10.32	4.46	2141.00	3.25	13.67	0.93
133	0.25	35	0.6	64	15.36	373.02	10.25	4.45	2143.00	3.26	13.67	0.93
134	0.25	35	0.6	59	14.16	404.63	10.25	4.45	2143.00	3.26	13.67	0.93
135	0.25	35	0.6	64	15.36	373.02	10.24	4.46	2144.00	3.26	13.67	0.93
136	0.25	35	0.6	66	15.84	361.72	10.20	4.47	2147.00	3.26	13.67	0.93
137	0.25	35	0.6	62	14.88	385.05	10.20	4.47	2147.00	3.26	13.67	0.93
138	0.25	35	0.6	64	15.36	373.02	10.20	4.47	2148.00	3.26	13.67	0.93

Appendix C

Component Data Sheets

1. SLA Battery
2. Microcontroller Wiring diagram
3. Throttle Position Sensor

HGHL1235W

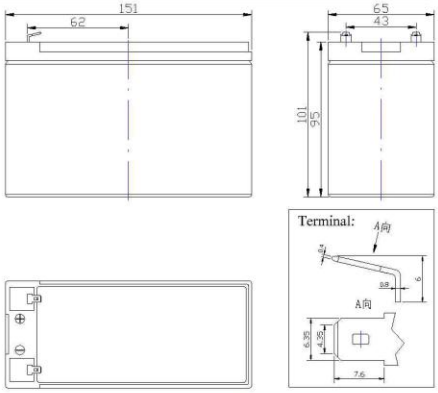

Specifications

Nominal Voltage	12V	
Capacity	35W@15 minute rate to 1.50V per cell	
	8Ah @10 hour rate to 1.75V per cell	
Dimension	Total Height (with terminals)	101mm(3.98inches)
	Height	95mm(3.74inches)
	Length	151mm(5.94inches)
	Width	65mm(2.56inches)
Weight		Approx.2.63kg (5.80lbs)

Discharge characteristics 77℉(25℃)

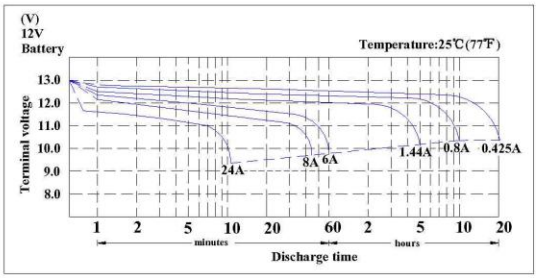

Characteristics

Capacity 77℉(25℃)	20 hour rate (425mA)	8.5AH
	10 hour rate (800mA)	8AH
	5 hour rate (1.44A)	7.2AH
	1hour rate (6A)	6AH
Internal Resistance	Full charged Battery 77℉(25℃)	14mΩ
Capacity affected by Temperature (20 hour rate)	104℉(40℃)	102%
	77℉(25℃)	100%
	32℉(0℃)	85%
	5℉(-15℃)	65%
Self-Discharge 77℉(25℃)	Capacity after 3 month storage	91%
	Capacity after 6 month storage	82%
	Capacity after 12 month storage	64%
Max. Discharge Current 77℉(25℃)	120A (5s)	
Terminal: Standard	F2	
Terminal: Optional	F1	
Charging (Constant Voltage): Cycle	Initial Charging Current 1.6A Or Small 14.5V~14.9V/77℉(25℃)	
Charging (Constant Voltage): Float	13.6V~13.8V/77℉(25℃)	

Duration of discharge vs. Discharge current

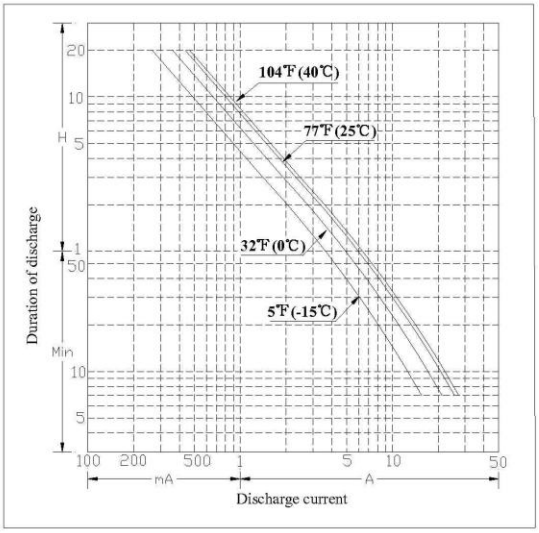

Constant Power Discharge Watts Per Cell @ 77℉(25℃)

Cut off voltage V/cell	5min	10min	15min	20min	30min	40min	50min	60min	90min
1.75	64	40	31	24	18.4	15.2	12.4	10.8	7.6
1.70	65	41	32	25	19.3	15.8	12.8	11.0	7.7
1.67	66	42	33	26	20	16.2	13.2	11.2	7.8
1.60	67	43	34	27	20.8	17	13.7	11.5	7.8
1.50	68	44	35	28	21.5	17.6	14	11.8	8.1

Note The above data are average values, and can be obtained within 3 charge/discharge cycles. These are not minimum values.

FULLRIVER HGHL BATTERIES

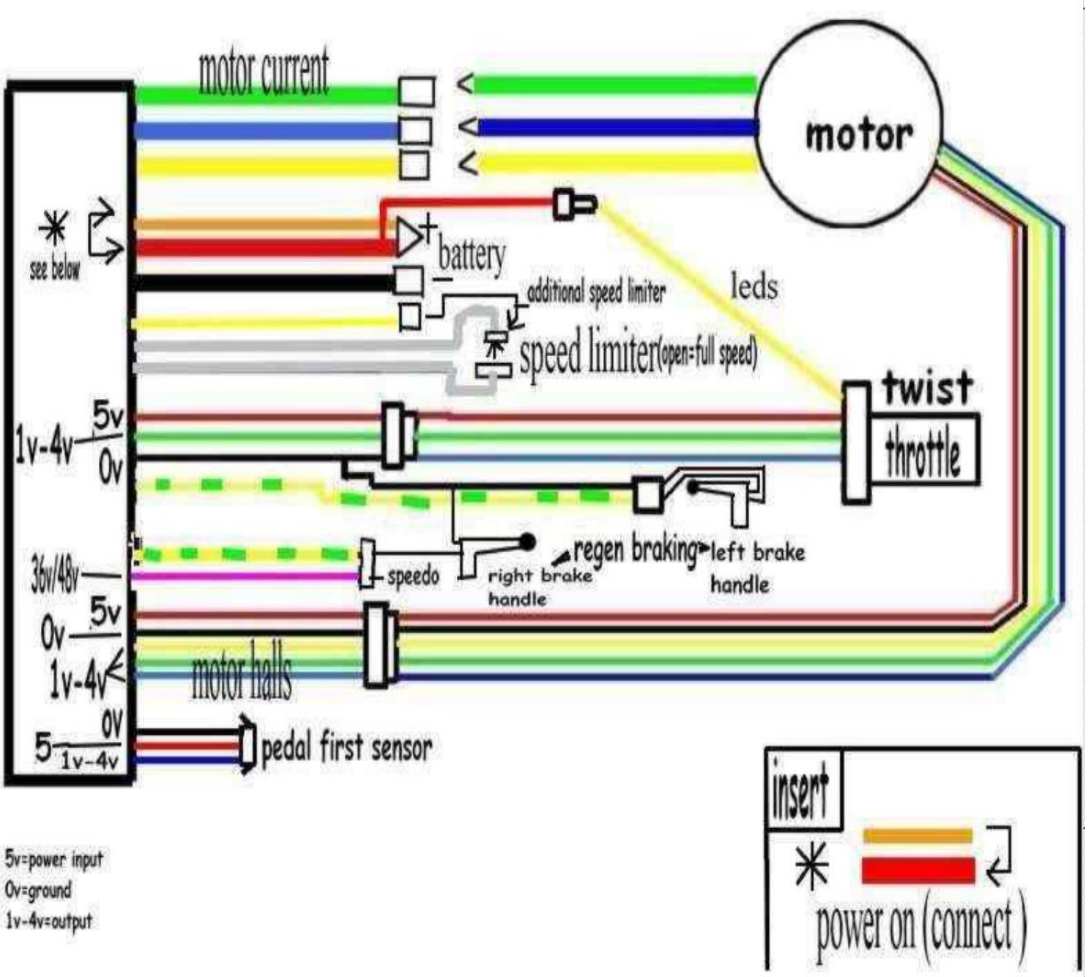
motor current
motor
see below
battery
additional speed limiter
leds
speed limiter(open=full speed)
twist
throttle
1v-4v
5v
0v
36v/48v
speedo
regen braking
right brake handle
left brake handle
5v
0v
1v-4v
motor halls
0v
5
1v-4v
pedal first sensor
5v=power input
0v=ground
1v-4v=output
insert
power on (connect)

Throttle-valve angular-position sensor

Measurement of angles up to 88°

φ / R

- Potentiometic angular-position sensor with linear characteristic curve.
- Sturdy construction for extreme loading.
- Very compact.

Application
These sensors are used in automotive applications for measuring the angle of rotation of the throttle valve. Since these sensors are directly attached to the throttle-valve housing at the end of the throttle-shaft extension, they are subject to extremely hostile underhood operating conditions. To remain fully operational, they must be resistant to fuels, oils, saline fog, and industrial climate.

Design and function
The throttle-valve angular-position sensor is a potentiometric sensor with a linear characteristic curve. In electronic fuel injection (EFI) engines it generates a voltage ratio which is proportional to the throttle valve's angle of rotation. The sensor's rotor is attached to the throttle-valve shaft, and when the throttle valve moves, the sensor's special wipers move over their resistance tracks so that the throttle's angular position is transformed into a voltage ratio. The throttle-valve angular-position sensor's are not provided with return springs.

Design
The position sensor 0 280 122 001 has one linear characteristic curve.
The position sensor 0 280 122 201 has two linear characteristic curves.
This permits particularly good resolution in the angular range 0°...23°.

Explanation of symbols
U_A Output voltage
U_V Supply voltage
φ Angle of rotation
U_{A2} Output voltage, characteristic curve 2
U_{A3} Output voltage, characteristic curve 3

Accessories for 0 280 122 001	
Connector	1 237 000 039

Accessories for 0 280 122 201	
Plug housing	1 284 485 118
Receptacles, 5 per pack, Qty. required: 4	1 284 477 121
Protective cap, 5 per pack, Qty. required: 1	1 280 703 023

Characteristic curve 1.
A Internal stop, L Positional tolerance of the wiper when fitted, N Nominal characteristic curve, T Tolerance limit,
φ_W Electrically usable angular range.

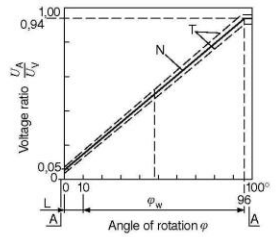

Characteristic curves 2 and 3.
A Internal stop,
φ_W Electrically usable angular range.

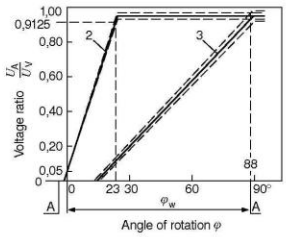

Technical data / Range

Part number		0 280 122 001	0 280 122 201
Diagram		1; 2	3
Useful electrical angular range	Degree	≤ 86	≤ 88
Useful mechanical angular range	Degree	≤ 86	≤ 92
Angle between the internal stops (must not be contacted when sensor installed)	Degree	≥ 95	–
Direction of rotation		Optional	Counterclockwise
Total resistance (Terms. 1–2)	kΩ	2 ±20 %	–
Wiper protective resistor (wiper in zero setting, Terms. 2–3)	Ω	710...1380	–
Operating voltage U_V	V	5	5
Electrical loading		Ohmic resistance	Ohmic resistance
Permissible wiper current	µA	≤ 18	≤ 20
Voltage ratio from stop to stop Chara. curve 1		$0.04 \le U_A/U_V \le 0.96$	–
Voltage ratio in area 0...88 °C Chara. curve 2		–	$0.05 \le U_{A2}/U_V \le 0.985$
Chara. curve 3		–	$0.05 \le U_{A3}/U_V \le 0.970$
Slope of the nominal characteristic curve	deg^{-1}	0.00927	–
Operating temperature	°C	–40...+130	–40...+85
Guide value for permissible vibration acceleration	$m \cdot s^{-2}$	≤ 700	≤ 300
Service life (operating cycles)	Mio	2	1.2

Dimension drawings.

A Plug-in connection,
B O-ring 14.65 x 2 mm,
C Fixing dimensions for throttle-valve housing, **D** Clockwise rotation [1]),
E Counterclockwise rotation [1]), **Ö** Direction of throttle-valve opening.
[1]) Throttle valve in idle setting.

F O-ring 16.5 x 2.5 mm, **G** 2 ribs, 2.5 mm thick,
H Plug-in connection, **I** Blade terminal,
K This mounting position is only permissible when the throttle-valve shaft is sealed against oil, gasoline, etc., **Ö** Direction of throttle-valve opening,
L Fixing dimensions for throttle-valve potentiometer.

0 280 122 001

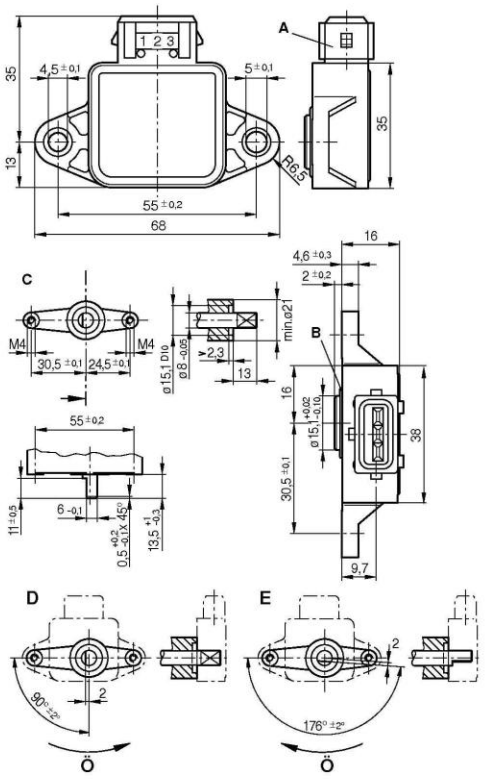

0 280 122 201

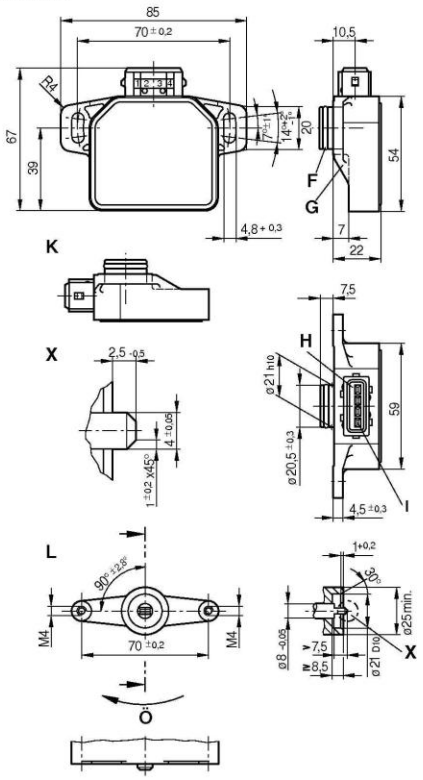

Diagram 1.

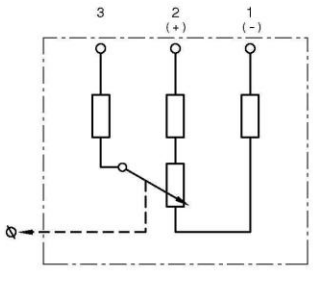

Diagram 2.

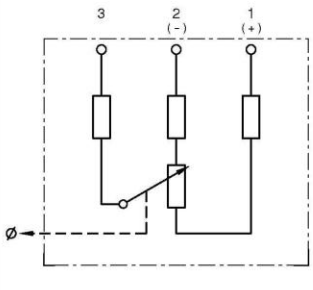

Diagram 3.
Throttle valve in idle setting.